Cyprus
University of
Technology

Faculty of Engineering
and Technology

Doctoral Dissertation

ADVANCED FIBRE OPTIC SENSORS DEVELOPED USING FEMTOSECOND LASER INSCRIPTION

Antreas Theodosiou

Limassol, September 2018

CYPRUS UNIVERSITY OF TECHNOLOGY

FACULTY OF ENGINEERING AND TECHNOLOGY

DEPARTMENT ELECTRICAL ENGINEERING, COMPUTER ENGINEERING AND INFORMATICS

Doctoral Dissertation

ADVANCED FIBRE OPTIC SENSORS DEVELOPED USING FEMTOSECOND LASER INSCRIPTION

Antreas Theodosiou

Limassol, September 2018

Approval Form

Doctoral Dissertation

ADVANCED FIBRE OPTIC SENSORS DEVELOPED USING FEMTOSECOND LASER INSCRIPTION

Presented by

Antreas Theodosiou

Supervisor: Dr. Kyriacos Kalli, Associate Professor

Signature ____

Member of the committee: Dr. Andreas Othonos, Professor

Signature ____

Member of the committee: Dr. Stavros Pissadakis, Principal Researcher

Signature ____

Cyprus University of Technology

Limassol, Semptember 2018

Copyrights

This thesis is dedicated to my family for their
endless support and love and to the memory
of my uncle who's no longer with us

Acknowledgements

First I would like to kindly thank my supervisor Professor Kyriacos Kalli for his expert advice and encouragement throughout this project and for giving me the opportunity to work with him and trust me to be part of the Photonics and Optical Sensing Research Laboratory at the Cyprus University of Technology.

I would like to thank Professor Michael Komodromos from Frederick University and Dr. Andreas Stassis from Mechanical Engineering in Cyprus University of Technology for their support. I greatly appreciate Dr. Udi Shafir and Dr. Garry Berkovic from Soreq NRC (Israel), Prof. Christophe Caucheteur and Dr. Xuehao Hu from the University of Mons (Belgium), Professor Ursula Gibson and her group from Oslo (Norway), Professor Yosuke Mizuno and his group from Japan, and Dr. Carlos Marquez and his group from Aveiro, Portugal, for their wonderful collaboration and help, and the opportunity given to me to be involved in their exciting research projects.

I would also like to thank all my colleagues and friends that I met and collaborated with during my PhD project starting with Dr. Amedee Lacraz, Dr. Charalambos Koutsides, Marios Kofinas, Michalis Polis, and Andrea Ioannou, for their wonderful collaboration, and for all the knowledge shared with me. Your support was valuable and I appreciate that you were always willing to help me all these years.

Finally, special thanks to my parents, George and Augi Theodosiou and to my siblings Gabriella, Katerina, and Theodosi Theodosiou, and my nephew Klairia for their endless support and love.

Abstract

Currently optical fibres are widely used for telecommunications and sensing applications due to their immunity to electromagnetic fields, and their light weight and small design. In particular for sensing purposes, different types of specialised fibres have been development either with special designs, such as microstructure patterns or using different kinds of materials. In this way, the sensitivity of the fibres can be enhanced or become unresponsive to specific parameters. However, not all the speciality fibres are photosensitive and efficiently processed with conventional UV lasers to manufacture sensing structures; as a result, most of the 'alternative' material or designs fibres are not fully exploited.

On the other hand, the femtosecond lasers modify materials using a different principle. The material photosensitivity is not required to induce refractive index changes in the fibres, indeed minimising linear absorption is desirable and the greater the transparency of the material the better for femtosecond laser processing. In this case it is multi-photon absorption that occurs at the laser focus that is important for laser-induced material modifications. In this thesis, we present the development and manufacturing of advanced fibre optic sensors using a femtosecond laser operating at 517 nm. A wide range of different optical fibres processed allows for the fabrication of not only fibre Bragg grating (FBG) sensors but also chirped gratings, Fabry-Perot cavities, and Mach-Zehnder interferometers (MZIs).

I summarise several examples that a unique to femtosecond laser inscription. The precise and accurate control of the inscription parameters during the fabrication of sensors in a multi-mode optical fibre can lead to control of the coupling between a Bragg grating and the higher order modes of a low loss polymer optical fibre (POF). A result is that we are able to inscribe single-peak FBG sensors as an array in the multi-mode optical fibre. We demonstrate this by inscribing FBGs in a low loss POF, in which it is not possible to inscribe gratings using conventional UV-laser sources, and hence demonstrate applications using polymer fibres over several tens of meters, which exceed the operating length of POF-based sensors by three orders of magnitude at an operating wavelength of 1550 nm.

We show the inscription of FBGs in conventional silica fibre inscribed and characterised by exposing the fibre to different femtosecond laser pulse conditions, whereas interferometric structures, such as Fabry-Perot cavities, MZIs, and waveguide Bragg gratings were written using similar inscription parameters, producing compound optical sensors that are able to sense properties such as curvature and refractive index. Moreover, traditional methods for detecting refractive index changes, such as tilted-FBGs, were further studied and for which we developed a flexible inscription method that allowed for the selective control of the range and position of radiation and cladding modes across the wavelength spectrum, applied to refractive index sensing.

We explored other fibre materials, such as phosphate fibres for bio-sensing applications that were laser-processed for the inscription of different structures (FBGs, Fabry-Perot cavities, chirped gratings) and characterised under different conditions (temperature and humidity). Finally, an important step was made in the processing of novel fibres such as silicon-core/glass cladding fibre, and polymer fibres with unique mechanical characteristics, which were processed and characterised showing their sensing superiority compared with other optical sensors.

The content of this thesis contains several novel pieces of research in the field of optical fibre sensing, and femtosecond laser processing of optical fibres that contribute to the better understanding of how one should process different optical fibre materials, with a focus on the difficulties and obstacles that were faced. In conclusion, new routes for industrial processing of materials are enhanced and motivated by the results of this thesis.

Keywords: Femtosecond Laser, Fibre Bragg Gratings, Polymer Fibres, Waveguides, Optical Fibre Sensing

Table of Contents

LIST OF TABLES

LIST OF FIGURES

LIST OF ABBREVIATIONS

MM	multimode
SM	single-mode
FBG	Fibre Bragg grating
POF	Polymer optical fibre
PMMA	Polymethyl methacrylate
CYTOP	Cyclic transparent optical polymer
mPOF	microstructured polymer optical fibre
SI	Step Index
GI	Gradient Index
C	Carbon
O	Oxygen
H	Hydrogen
FTTH	Fibre to the home
AIBN	azobisisobutyronitrile
UV	Ultraviolet
He-Cd	Helium and Cadmium
PbP	Point by Point
Pl-b-Pl	Plane by plane
fs	femtosecond, 10^{-15} s
nm	Nanometer, 10^{-9} m
nJ	Nanojoule, 10^{-9} J
mm	Millimeter, 10^{-3} m
mJ	Millijoule, 10^{-3} J
μm	Micrometer, 10^{-6} m

1 Introduction and Thesis Structure

1.1 Introduction

The immunity to electromagnetic interference, their small size and weight, high sensitivity, broad bandwidth, and low losses are only some of the advantages of optical fibre sensors compared to other conventional (non-fibre) sensing methods. To date fibre optical sensors have found applications in many aspects of our lives, starting from communication systems networks, to more specialised areas such as biomedical, civil, mechanical, and space applications. However, as with all the optical sensing systems, not all the fibres are appropriate for all potential applications. For this reason, a large number of research groups and companies all over the world are working on the development of speciality optical fibres for specific purposes such as detecting gases, the detection of chemical and biological materials (e.g. DNA), resistance to high temperatures, high elasticity etc., using a variety of materials and fibre structures [1]–[5].

One of the most common, efficient, and indeed trustworthy categories of optical fibre sensors are the Bragg grating based sensors. They are formed by periodically modifying the refractive index of the fibre core, typically parallel to the fibre axis, although tilt can be readily introduced. The first gratings were inscribed using holographic inscription methods that were replaced several years later with the phase mask method, which requires less configuration and alignment effort [6]. In 1990 a new method was presented, the so-called Point-by-Point inscription method, which offers flexibility on the gratings period and faster inscription duration [7]. However, the above techniques cannot provide complete control of the grating parameters and enough laser-material interaction flexibility to be applied to any fibre optic material.

With these caveats in mind, the correct processing of the different materials for the utilisation and the development of “optimal” optical fibre sensors is a critical and vital choice. In this thesis we present the application of a novel, patent-pending inscription method that is tailored for use with femtosecond laser systems, which we have termed the “Plane-by-Plane inscription method”, and that is applicable for the inscription Bragg grating sensors and waveguides using similar laser parameters, offering stability and flexibility in the laser modification of materials and sensor development. The particular method offers unique flexibility compared to the other methods to control all the important Bragg grating inscription parameters, such as spatial and optical parameters and that can be employed to readily inscribe uniform Bragg gratings and also chirped gratings, Fabry-Perot cavities, controlling the mode excitation of multimode fibres, tilted fibre Bragg gratings etc. The method may also be applied to a wide range of optical fibres, regardless of their design and their host material.

This thesis has extensively explored different of optical fibre sensor structures in many different materials, starting from conventional single-mode glass fibres, CYTOP polymer fibres, boron-doped fibres, phosphate fibres, and silicon-core fibres. The fibre designs are single- or multi-mode, with solid core or microstructure fibre designs.

The content of the current research has not only scientific impact but also offers an industrially-related interest since most of the work is currently world leading and opens the route to the commercialisation and the use of these speciality optical fibre sensors to industrial environments.

1.2 Thesis Structure

This thesis is divided into three distinct research sections. The first consists of three chapters, (Chapters 3-5) with a focus on new developments in polymer optical fibre sensing technology. The second research area is related to the development of optical sensors based on glass and soft glass fibres and contains two chapters Chapter 6 and Chapter 7, whereas the third research area explores the development of optical fibre sensors in new materials (Chapter 8 and 9).

The contents for each chapter are as follows: Chapter 2 contains the operating principals of the optical fibre sensors that will be presented in later chapters of this PhD thesis, along with the governing equations and theoretical aspects of the particular sensors. An introduction to polymer optical fibres and their use as sensing components is presented in Chapter 3. Their advantages and disadvantages compared to their glass counterparts are summarised. Here we also report on the latest research regarding the inscription of fibre Bragg gratings in POFs, with an emphasis on the inscription methods, designs, materials and sensitivities for different environmental parameters and perturbations. Chapter 4 presents our innovative work and first reported, regarding the inscription of ‘single-peak’ fibre Bragg gratings (FBGs), chirped gratings, and Fabry-Perot cavities in a multimode gradient index CYTOP polymer fibre, using a new femtosecond laser inscription method. The chapter concludes with the characterisation of the optical devices for different physical perturbations such as axial strain, relative humidity, and temperature. Chapter 5 shows for the first time the use of long length (several metres long) POFBGs arrays that are two orders of magnitude longer compared with existing POFBG sensors, for applications in different fields and prepares the route to practical sensing applications.

A shift of focus leads to the development of optical fibre sensors in glass and softglass optical fibres in Chapter 6. More particularly, innovate basic study is presented related to the inscription of FBG sensors in single-mode glass fibre. The laser parameters, such as pulse energy and the number of pulses used to control the grating characteristics such as cladding mode excitation, refractive index change, grating strength, and the order of the gratings are reported. We also present research related to control of the excitation of fibre cladding modes, regarding their strength and position in the wavelength spectrum, of tilted-FBGs, inscribed in boron-doped glass fibre. The chapter concludes with our findings related to the inscription of different optical sensors within soft-glass bioresorbable phosphate optical fibre and their characterisation for temperature and exceptionally high humidity environment for extended time periods. In Chapter 7 we consider the potential of using the fibre cladding as a waveguide-supporting structure and consider the inscription of waveguides for monolithic devices integrated directly into the cladding. The results confirm that is possible to couple the evanescence light from the fibre core to the fibre end face or other parts of the fibre cladding region using cladding waveguides. The inscription parameters to achieve the maximum coupling between the waveguide and the fibre core are presented, while different optical sensing structures such as waveguide Bragg gratings and Mach-Zehnder interferometers were utilised and characterised for various environmental measurands. Finally, integration of multi-core fibres that are now so topical are considered, and novel results of bringing a single core single mode fibre with three FBG arrays written in three different cores of a four-core fibre is presented, supported by their response in reflection for bending and strain.

For the last part of the thesis, we consider grating inscription in two new materials of importance and report our findings in the last two experimental chapters. Chapter 8 leads to a potentially disruptive step in grating technology, as the first ever work on the inscription of FBGs in a silicon-core fibre and their characterisation as strain and temperature sensors is presented. This key step could link optical fibre components with silicon chip technology. Chapter 9 describes a unique work analysing the mechanical properties, the grating inscription, and characterisation of the FBG under temperature, and humidity of a new, ultra-low Young's modulus polymer fibre.

The thesis concludes with Chapter 10; remarks regarding the work presented in this thesis are considered, as are future trends and directions for femtosecond-laser inscription of Bragg gratings.

2 Theoretical Background

2.1 Single-, and Multi-Photon Absorption

In the 19th century Niels Bohr and Ernest Rutherford introduced the Rutherford-Bohr model (later known as the Bohr model) that defines that the photon energy (E_{ph}) is proportional to its frequency,

$$E_{ph} = hf = \frac{hc}{\lambda} \ , \quad (2.1)$$

where h is Planck's constant (6.62607x10^{-34} J.s^{-1}), f is the photon frequency and c is the speed of light (2.998x10^{8} m.s^{-1}). Initially, the atoms were considered to consist of a cloud of negatively charged electrons surrounding a small and positively charged nucleus and moving around the nucleus at specific orders according to their energy [8]. Rutherford in 1911 proposed the planetary-atom model, and according to the classical physics electrons lost energy as they moved around the nucleus, spiralling inwards, giving up energy through their orbit, and finally collapsing into the nucleus. This assumption predicts that all atoms are unstable. However, later experiments showed that the electrons emit and absorb light at particular discrete frequencies. In 1913 Niels Bohr improved Rutherford's planetary-model by proposing a new model, the so-called Bohr model. He suggested that electrons move in orbits around the nucleus without radiating, as they are at resonance, and can only gain or lose energy by jumping from one allowed orbit to the other by absorbing or emitting energy with a specific frequency, determined by the energy difference of the orbits, according to the Planck relation,

$$\Delta E = E_1 - E_2 \ , \quad (2.2)$$

More specifically, as shown in Fig. 1(a), in an atomic transition, the excitation of an electron from the valence band (VB) to the conduction band (CB), requires a photon energy equal to or greater than the energy gap between the two bands. Conversely, the electron is emitting a photon at specific energy when it returns from the conduction band to the valence band as follows,

$$hf = \frac{hc}{f} = E_{CB} - E_{VB} \ , \quad (2.3)$$

In this way, the absorption bands for each material affect how light interacts with the material, through either linear or non-linear absorption. An outcome of this interaction may be a refractive index change in a transparent material, the generation of optical breakdown or material ablation. If we consider, "conventional" methods for modifying the refractive index of optical materials that are based on processes related to material photosensitivity then the laser radiation wavelength should be within the wavelength range of absorption features (bands) of the material. This holds for linear absorption phenomena, where non-linear affects are not present.

In contrast, when extremely high-intensity photons are focused into or on the material, then non-linear process can be activated. For example, with multi-photon absorption, an electron could be excited to the CB by multiple photons as shown in Fig. 1(b), even if the photon energy is far smaller than the band gap energy. Multiple photons can be absorbed simultaneously giving enough energy for electron promotion. This requires that the pulse duration is <1 ps, which minimises hydrodynamic motion and heat transfer, and should be less than the time needed for the electron to transfer energy to the lattice. Moreover, multi-photon absorption is realised for only a small portion of the focused beam that exceeds the material damage threshold. Therefore, when the pulse intensity is extremely high ($10^{11} - 10^{13}$ W/cm^2) and the pulse duration is much lower than the thermal diffusion time (>1 ns), sub-micron or nano-scale refractive index modifications with the minimal thermal damage become possible, as shown in Fig.2(a&b). Importantly, the multi-photon based inscription methods have the advantage of being applicable to any transparent material, in sharp contrast to the photosensitive-related methods.

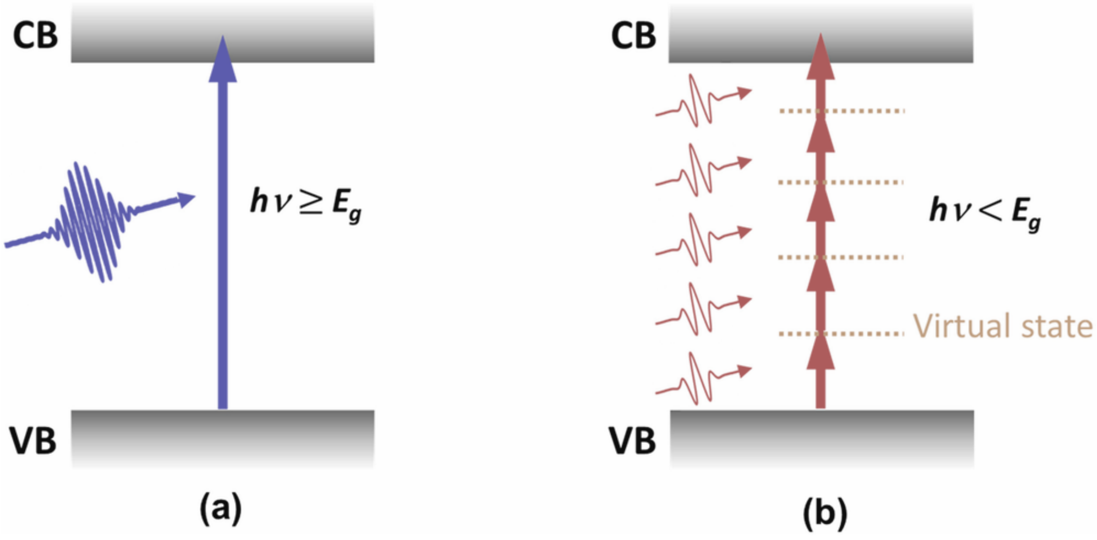

Figure 1: Schematic illustration of a) Single-photon absorption and b) Multi-photon absorption for the transition of an electron from the valence band to the conduction band [9].

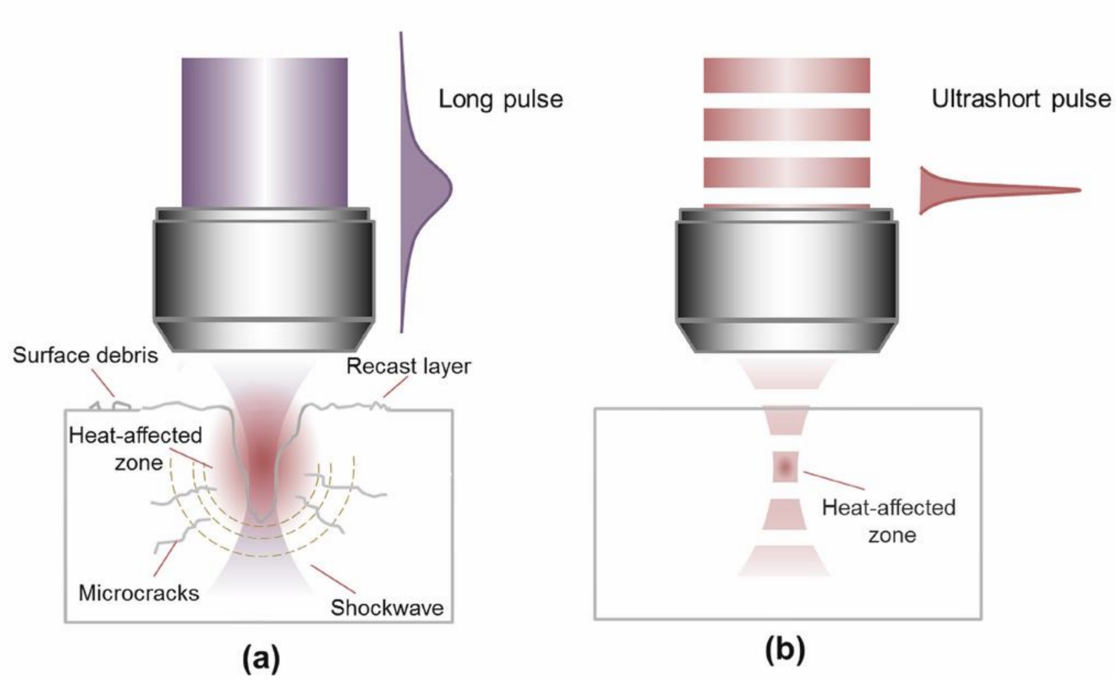

Figure 2: Laser processing of transparent material using a) Long pulses and b) Ultra-short pulses [9].

2.2 Waveguide Theory

In this section presented, the basic theory related to the propagation of the light in cylindrical geometries, such as the optical fibres and the waveguides inscribed and employed in this thesis.

Maxwell's equations govern the propagation of the light in a medium as follows,

$$\nabla x E = -\frac{\partial B}{\partial t} \ , \quad (2.4)$$

$$\nabla x B = \mu_o \left(J + \varepsilon_o \frac{\partial E}{\partial t} \right), \quad (2.5)$$

$$\nabla . E = \frac{\rho}{\varepsilon_o} \ , \quad (2.6)$$

$$\nabla . B = 0 \ , \quad (2.7)$$

where E is the electric field, B is the magnetic field, μ_o is the permeability of free space, ε_o is the permittivity of free space, J is the electric current density, and ρ is the electric charge density.

The wave equations for the electric and magnetic fields that describe the propagation of electromagnetic waves through a medium or in a vacuum are extracted by taking the curl of the equations (2.4 – 2.7) and have the following form,

$$\left(\frac{\nabla^2}{\sqrt{\mu_o\varepsilon_o}}-\frac{\partial^2}{\partial t^2}\right)E=0\ ,\quad (2.8)$$

$$\left(\frac{\nabla^2}{\sqrt{\mu_o\varepsilon_o}}-\frac{\partial^2}{\partial t^2}\right)B=0\ ,\quad (2.9)$$

The Fourier transformation of the electric field is given by,

$$\tilde{E}(r,\omega)=\int_{-\infty}^{\infty}E(r,t)e^{i\omega t}dt\ ,\quad (2.10)$$

while Maxwell's equations can be employed to solve the wave equation in the frequency domain,

$$\nabla^2\tilde{E}+n^2(\omega)k_0^2\tilde{E}=0\ ,\quad (2.11)$$

where n is refractive index, and $k_0=2\pi/\lambda$ is the free-space wavenumber.

Assuming that the optical fibre and the written waveguides are cylindrically symmetrical, the wave equation may be modified to account for cylindrical coordinates,

$$\frac{\partial^2 E_z}{\partial r^2}+\frac{1}{r}\frac{\partial E}{\partial r}+\frac{1}{r^2}\frac{\partial^2 E_z}{\partial\varphi^2}+\frac{\partial^2 E_z}{\partial z^2}+n^2k_0^2E_z=0\ ,\quad (2.12)$$

where r is the radius, φ the azimuthal angle, and z the vertical position while the refractive index define as,

$$n=\begin{cases}n_2 & 0<r\leq a\\ n_1 & r>a\end{cases}\ ,\quad (2.13)$$

where a is the radius of the core.

For waveguides that are spatially close enough (approximately one wavelength of transmitted light) so that their evanescent fields may couple through overlapping in the two waveguiding media (such as waveguides inscribed in chapter 7), the light will periodically transfer from one waveguide to the other. In this way, formally one can solve Maxwell's equations in both waveguides to determine the modes of the system. However, these modes differ from the case where each waveguide is in isolation and the exact analysis can be complicated. To make the calculations more tractable, we can assume that the coupling between the two waveguides is weak. With this assumption, an approximate analysis can be undertaken, using the coupled mode theory.

Subsequently, the electric field may be expressed as a linear combination of the normal modes of the initial waveguide, where the amplitude coefficients A_m vary with the propagation distance, to account for the energy exchange between the waveguides,

$$E = \sum_m A_m(z) E_m(x,y) e^{i(\omega t - \beta_m z)} \quad , \quad (2.14)$$

where m is an integer and denotes the mode number, and E_m is normalized amplitude of the modes. To solve the coupled mode equations, equation (2.14) is substituted into equation (2.10). Assuming a slowly varying amplitude due to the weak coupling (neglecting d^2A_m/dz^2) and the fact there are only two waveguides that support normal modes $E_1(x,y)\exp(i(\omega t - \beta_1 z))$ and $E_2(x,y)\exp(i(\omega t - \beta_2 z))$, the coupled mode equations for co-directional coupling are as follows,

$$\frac{d}{dz}A_1 + ikA_2 e^{i\Delta\beta z} = 0 \ , \quad (2.15)$$

$$\frac{d}{dz}A_2 + ikA_1 e^{i\Delta\beta z} = 0 \, , \qquad (2.16)$$

where $\Delta\beta = \beta_1 - \beta_2$. The equations (2.15) and (2.16) for the case of phase matching between identical waveguides with the same propagation constant ($\Delta\beta = 0$), are solved as,

$$A_1(z) = A_1(0)\cos kz \quad , \quad (2.17)$$

$$A_2(z) = -iA_1(0)\sin kz \quad , \quad (2.18)$$

where $A_1(0)$ is the light amplitude at the launch point z=0 for waveguide 1, whereas the light amplitude in waveguide 2 is $A_2(0) = 0$. The coupling ratio is normalised and defined as the power in the cross port divided by the sum of the power at the two output ports,

$$r = \frac{P_2}{P_1 + P_2} = \frac{|A_1(z)|^2}{|A_1(z)|^2 + |A_2(z)|^2} = \sin^2 kz \quad , \quad (2.19)$$

where the coupling coefficient is,

$$k = \frac{k_0^2}{2\beta}\left(n_{wg}^2 - n_{bulk}^2\right) \iint E_1(x,y)E_2(x,y)dxdy \ , \quad (2.20)$$

where n_{wg} and $n_{bulk}$is the refractive index in the waveguides, and in the bulk (in this case the cladding), respectively, assuming a step refractive index profile. The integration in equation (2.20) is carried out over waveguide 2. The power coupling ratio for the phase-matched case results in sinusoidal oscillation of power between waveguides. The beat length L_{beat} for full power oscillation is inversely related to the coupling coefficient,

$$L_{beat} = \frac{\pi}{k} \ , \qquad (2.21)$$

2.4 Fibre Bragg Grating Theory

The fibre Bragg grating (FBG) is an optical device that operates as a wavelength selective mirror, and is spectrum is viewed mainly in reflection and detected as a single peak at a specific resonance wavelength. If viewed in transmission one can consider that it is a notch in the transmission spectrum, as shown in Fig. 3. The resonance wavelength reflected by a FBG satisfies the Bragg condition that accounts for the period between any two consecutive index changes written along the core, Λ, of the fibre and the effective refractive index change, n_{eff} as given below:

$$m.\lambda_{Bragg} = 2.n_{eff}.\Lambda \quad (2.22)$$

where m is the order of the grating..

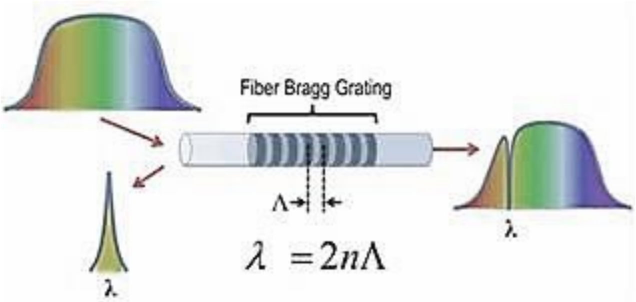

Figure 3: Schematic diagram of the fibre Bragg grating structure and its spectral signature both in transmission and in reflection spectrum [10].

It is the phase matching between the light reflected from each of the grating planes that results in the coherent backscatter of light. Based on the previous section, the FBGs can expressed as a coupled-wave equation and written as [11],

$$\frac{dA_i}{dz} = -ikA_r e^{i\Delta\beta z} \ , \quad (2.23)$$

$$\frac{dA_r}{dz} = ik^* A_i e^{i\Delta\beta z} \quad , \quad (2.24)$$

where A_i and A_r are the amplitude of waves propagated forward and backward, respectively, and k is the coupling coefficient.

The difference between the propagation constant of forward wave β_i, and backward β_r , is given by [12],

$$\Delta\beta = \beta_i - \beta_r - \frac{2\pi m}{\Lambda} \, , \quad (2.25)$$

Assuming the grating has the maximum reflectivity, then $\Delta\beta = 0$, and equations (2.23) and (2.24) become,

$$\frac{dA_i}{dz} = -ikA_r \quad , \quad (2.26)$$

$$\frac{dA_r}{dz} = ik^* A_i \quad , \quad (2.27)$$

By making this assumption one can readily solve the two equations in a similar manner. By differentiating equation (2.26) and eliminating A_r using the equation (2.27), a second order equation appears for A_i as shown below,

$$\frac{d^2 A_i}{dz^2} - k^2 A_r = 0 \quad , \quad (2.28)$$

For a boundary conditions,

$$A_i(L) = 1, \qquad A_r(L) = 0 \quad , \quad (2.29)$$

where L is the total length of the grating, then the solutions of the equation (2.28) are,

$$A_i(z) = \frac{\cosh[k(L-z)]}{B cosh(kL)} \quad , \quad (2.30)$$

$$A_r(z) = \frac{-\mathrm{jsinh}[k(L-z)]}{B cosh(kL)} \quad , \quad (2.31)$$

The effective refractive index change depends on the degree of refractive index modulation and gives a measure of the overall area across the FBG, containing the modified region and the unmodified, and calculated as [11],

$$\delta n_{eff}(z) = \delta n_{dc}(z) + \delta n_{ac}(z) \cos\left[\frac{2\pi}{\Lambda} z + \varphi(z)\right] , \quad (2.32)$$

$$\delta n_{dc} = \frac{\pi}{\lambda}\overline{\delta n}_{\text{eff}} , \quad (2.33)$$

$$\delta n_{ac} = \delta + \sigma - \frac{1}{2}\frac{d\varphi}{dz} , \quad (2.34)$$

where $\delta n_{dc}(z)$ is the dc index change over the grating length, $\delta n_{ac}(z)$ is the index modulation over the length of the grating and $\varphi(z)$ describes the grating chirp [13], [14]. Moreover, δ is the detuning, σ is the "dc" coupling coefficient, the derivative $\frac{1}{2}\frac{d\varphi}{dz}$ describes possible chirp of the grating period, and $\overline{\delta n}_{\text{eff}}$ is the "dc" index change spatially averaged over a grating period. Note that, for a uniform grating along the z, $d\varphi/dz=0$ and $\overline{\delta n}_{\text{eff}}$ is a constant. The aforementioned factors are given by the following expressions:

$$\delta = 2\pi n_{eff}\left(\frac{1}{\lambda} - \frac{1}{\lambda_D}\right) , \quad (2.35)$$

$$\sigma = \frac{2\pi}{\lambda}\overline{\delta n}_{\text{eff}} , \quad (2.36)$$

By using the equations above, the grating reflectivity (R) is extracted as a function of both the grating length (L) and wavelength (λ), and is given below,

$$R(L,\lambda) = \frac{sinh^2(\sqrt{{\delta n_{dc}}^2 - {\delta n_{ac}}^2}L)}{cosh^2\left(\sqrt{{\delta n_{dc}}^2 - {\delta n_{ac}}^2}L\right) - \frac{{\delta n_{ac}}^2}{{\delta n_{dc}}^2}} , \quad (2.37)$$

To find the maximum reflectivity (R_{max}) of a uniform FBG when $\delta = 0$, at the phase matching condition $\lambda_B = 2n_{eff}\Lambda$, the equation (2.37) is simplified to,

$$R_{max} = \tanh^2(kL) = \tanh^2\left(\frac{\pi \Delta n_{mod}\eta L}{m.\lambda_{Bragg}}\right) \quad (2.38)$$

where the k is the coupling coefficient, L is the length of the grating, Δn_{mod} is the induced refractive index modulation, η is the mode overlap integral for the forward and backward propagating modes [11], [13]. The FBGs could be observed in reflection spectrum as a peak of intensity with strength R or as a transmission loss in transmission spectrum indicated as $T=1-R$.

The modulation of the refractive index induced by the laser irradiation is given by solving the equation (2.38) for, Δn_{mod} [15],

$$\Delta n_{mod,AC} = \frac{k.\lambda_{Bragg}}{\pi\eta} \quad (2.39)$$

The parameter η can be estimated from the expression,

$$\eta = \frac{\pi^2 d^2 NA^2}{\lambda_{res}^2 + \pi^2 d^2 NA^2} \quad (2.40)$$

where d is the core diameter and NA is the numerical aperture of the fibre. Using the parameters of SMF28 (d= 8.2 μm, NA= 0.14) at 1.55 μm wavelength, the η parameter is equal to 0.84. The effective refractive index, $\Delta n_{eff,DC}$ is mean modulation of the refractive index and is related to the shift of the resonance wavelength from the anticipated or design resonance wavelength given by equation (2.22). The $\Delta n_{mod,AC}$, is the actual modulation of the refractive and related to the strength of the grating or in other words to the reflectivity of the grating. Figure 4 showing more clearly the difference between the two parameters.

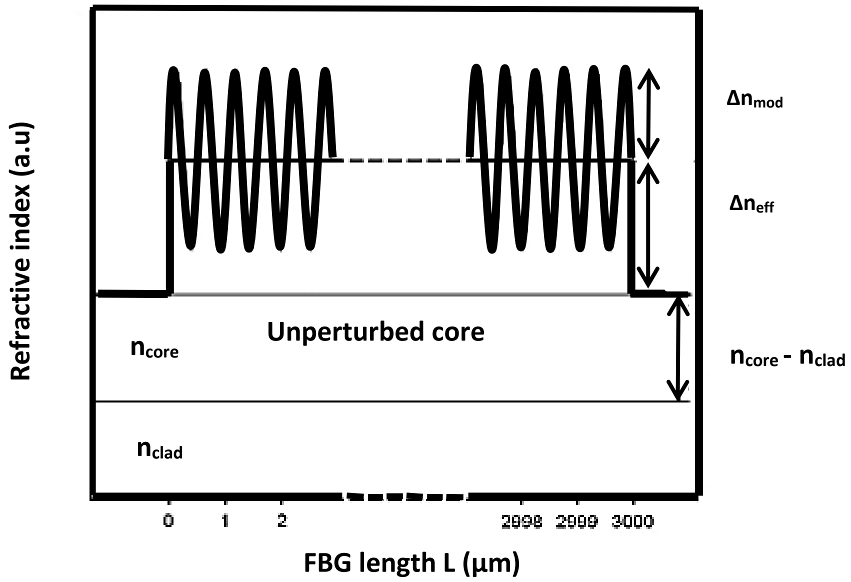

Figure 4: Clarification of the refractive index measurands related to the fibre Bragg gratings [15].

2.4 Fibre Bragg Gratings in Multimode Mode Fibres

Given that we will use multimode fibres having a gradient index profile, we here consider how this affects the location of the Bragg peaks. The refractive index profile for a graded-index fibre given by [16],

$$n(r) = \begin{cases} n_o\sqrt{1-2\Delta(r/a)^2} & (0 < r < a) \\ n_o\sqrt{1-2\Delta} = n_a & r \geq a \end{cases} , \quad (2.41)$$

where n_o and n_a are the refractive indices at $r = 0$ and $r = a$ respectively and

$$\Delta = \frac{n_0 - n_a}{n_0} , \quad (2.42)$$

The normalised frequency, V, is defined as

$$V = 2\pi . a . \frac{NA}{\lambda_o} , \quad (2.43)$$

$$NA = \sqrt{n_o^2 - n_a^2} , \quad (2.44)$$

where NA is the numerical aperture of the fibre which can be simplified based on the equation (2.41) as [16],

$$NA = n_o\sqrt{2\Delta} , \quad (2.45)$$

From the equation (2.41) and (2.42) the number of modes, M_{number}, for a graded index fiber are,

$$M_{number} = \frac{V^2}{4} , \quad (2.46)$$

After that, we compute the refractive index for each particular principal mode using the expression below [16],

$$n_m = n_o\sqrt{1 - 4\Delta . m/V} , \quad (2.47)$$

where *m=1, 2,....M-1*. Furthermore, between two consecutively principal modes, there is one cross-coupled mode [13]. The resonance Bragg wavelengths of principal and cross-coupled modes calculated as follows

$$\begin{cases} \lambda_m = 2n_m\Lambda \\ \lambda_m^{cross} = (n_m + n_{m+1})\Lambda \end{cases} \quad (2.48)$$

Based on the previous equations, we compute the multiple Bragg peak spectrum of a gradient index fibre with core diameter 62.5 μm, NA=0.19, and refractive index in the centre of the core 1.344. This value corresponds to the manufacturer values of CYTOP polymer fibre, GI-CYTOP by Chromis. We initially calculate the number of modes supported by the particular fibre using the equations (2.41) - (2.46) and their respective refractive indices using the equation (2.47). Subsequently, we can calculate the refractive indices of the cross modes as follows,

$$n_{cross,m} = \frac{n_m + n_{m+1}}{2} \qquad (2.49)$$

As the core refractive index is $n_o = 1.3477$, the cladding-core difference is $\Delta \approx 0.01$ and $\lambda = 1560$ nm, the particular fibre supports 140 modes; however, only the lowest mode numbers carry most of the light.

2.4 Tilted Fibre Bragg Gratings

The tilted-FBGs (TFBGs) or blazed FBGs are governed by the same principles as with the uniform FBGs, however now the refractive index modulations are written at an angle with respect to the fibre core, as shown in Fig. 5. In this way, the light propagating through the fibre core is diffracted and coupled to a wide different range of cladding modes that are observed as narrow wavelength dips in the transmission spectrum, as shown in Fig. 6. The tilt angle sets the coupling range and wavelength position of the cladding modes. These particular fibre gratings have found numerous applications for sensing smaller perturbations of the surrounding environment such as refractive index changes, Ph variations, etc.

The TFBGs are mainly fabricated using the phase mask inscription method and holographic approaches [17]–[19]. To achieve the required tilt angle of the grating either the fibre is fixed with a specific tilt with respect to the normal of the diffraction pattern created by the phase mask or the phase mask is rotated with an angle. The latter has the adverse affect of reducing the fringe visibility.

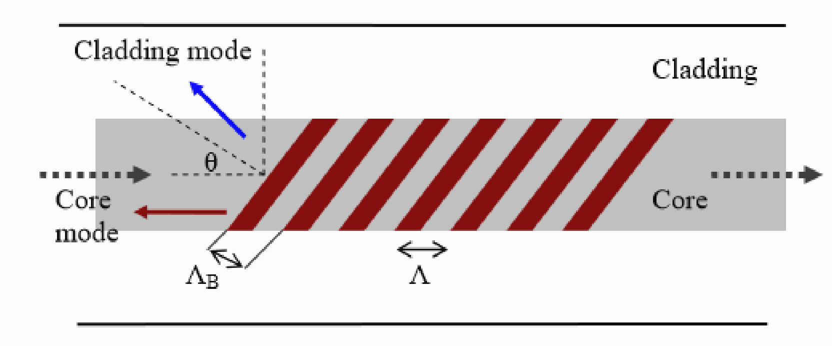

Figure 5: Schematic diagram of a tilted fibre Bragg grating [20].

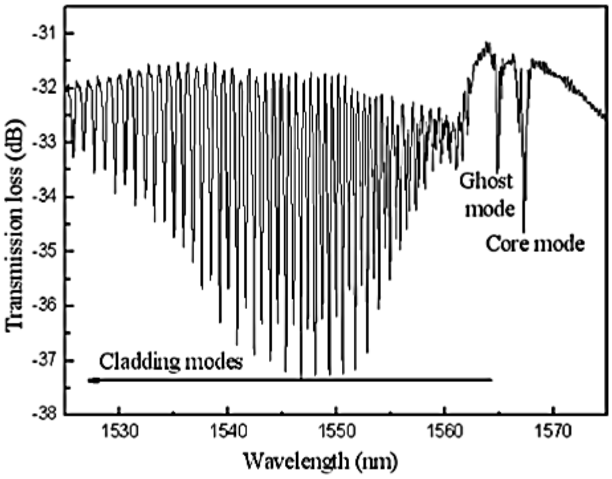

Figure 6: Transmission spectrum of TFBG with tilt angle less than 5 degrees [21].

The coupling between the core mode and a cladding mode and the coupling wavelength ($\lambda_{coupling}$) of a tilted FBG described as follows [22],

$$\beta_{core} + \beta_{cladding} = \frac{2\pi}{\Lambda} cos\theta \ , \quad (2.50)$$

$$\lambda_{coupling} = \left(n_{eff,core} + n_{eff,cladding}\right) \frac{\Lambda}{cos\theta} \ , \quad (2.51)$$

where β_{core} and $\beta_{cladding}$ are the propagating constants for a core and a cladding mode, respectively, Λ is the period of the grating, θ is the angle of the tilt and $n_{eff,core}$ and $n_{eff,cladding}$ are the effective refractive index of the core and cladding, respectively.

2.5 Fibre Fabry-Perot Cavities

The classic bulk optic Fabry-Perot (FP) cavity or etalon interferometer consists of a pair of highly reflective mirrors separated by a specific length to form a cavity that cab be operated as a resonant device, as shown in Fig. 7. When highly temporally coherent light is incident on the cavity, it experiences multiple reflections between the mirrors. When the multiple reflections are brought together by a focusing lens, they interfere coherently, and narrow fringes are observed. The distance between the two mirrors controls the difference between two consecutive fringes.

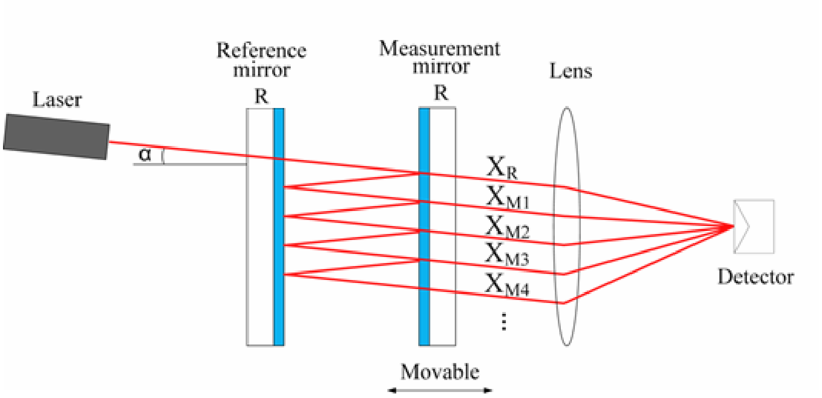

Figure 7: Schematic diagram of a Fabry-Perot interferometer [23].

The FP cavity can be constructed in several ways [24]–[26], tailored for different purposes and applications such as humidity, temperature, and strain sensors, for the development of fibre lasers, as a communications filters, detecting magnetic fields etc. [26]–[30]. However, in this thesis we will only focused on the construction of FP using fibre Bragg gratings instead of traditional, bulk reflective mirrors and other free space components, as shown in Fig. 8(a). This scheme allowed the utilisation of a more compact and stable design for sensing and telecommunication purposes, and fibre laser configurations.

It is critical that the two FBGs operate at the same resonance wavelength. The transmitted intensity of FP is given by,

$$I = \frac{t_1 t_2 e^{-lL_{eff}}}{I - \left(2\cos\left(2kL_{eff}\right)\sqrt{r_1}\sqrt{r_2}e^{-lL_{eff}}\right) + r_1 r_2 e^{-2lL_{eff}}} \;, \quad (2.52)$$

where r_{12} and t_{12} are the reflection and transmission coefficients, respectively, L_{eff} is the effective length of the cavity and l is the attenuation of the fibre [31]. It is noted that the effective length is the summation between the physical length between the two FBGs (d) and the penetration depth of the FBGs ($L_{eff,FBG1}$), as shown below,

$$L_{eff} = d + L_{eff,FBG1} + L_{eff,FBG2} \;, \quad (2.53)$$

$$L_{eff,FBG} = \frac{v_g \tau_{1,2}}{2} \;, \quad (2.54)$$

where v_g is the group velocity, and $\tau_{1,2}$ are the group delays for the corresponding FBGs.

According to the wavelength of the FBGs, the cavity length, and the effective refractive index value, the wavelength difference between two consecutive maxima of the FP interference pattern, the Free Spectral Range (FSR) is given by,

$$\Delta\lambda_{FSR} = \frac{(\lambda)^2}{2n_{eff}L_{eff}} \ , \qquad (2.55)$$

where λ is the operating wavelength, n_{eff} is the effective refractive index, and L_{eff} is the effective length of the cavity. Another important characteristic of the Fabry-Perot cavities is the Finesse and is calculated as shown below,

$$finesse = \frac{\Delta\lambda_{FSR}}{\delta\lambda} = \frac{4R}{(1-R)^2} \ , \qquad (2.56)$$

where $\delta\lambda$ is the full width at half maximum of the fringes.

The Bragg grating is similar to a concatenated array of interleaved, Fabry-Perot cavities, with each cavity having an ultra-low reflectivity mirror and for which the “cavity” period between the two consecutive FBG periods is so small that according to the equation (2.55), the FSR of the shortest “cavity” is in the micrometre range, whereas there are effectively as many FSRs as grating planes. Similarly to the Fabry-Perot there are a large number of propagating fields in the grating structure, and those that are weakly reflected coherently add to produce the characteristic resonance, according to the optical path difference between the Bragg planes.

The shorted form of a fibre Fabry-Perot (FFP) is the π-shifted FBGs, which utilises two FBGs inscribed in line along the fibre’s optical axis, as in Fig. 8(a), but with *d* equal to the half of the grating periods [32], [33]. The transmission spectrum of a π-shifted FBG is shown in Fig. 8(b); the typical FBG spectrum is divided by a sharp resonance peak which splits the FBG in two dips. In contrast, Fig.8(c) presents a typical reflection spectrum of FFP cavity with physical distance between the two FBGs d=4 mm.

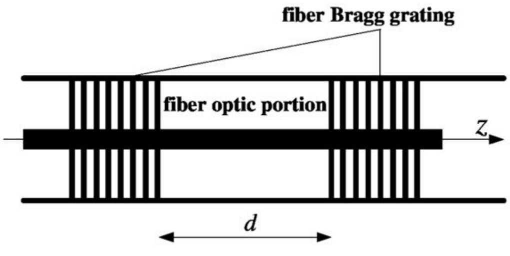

a)

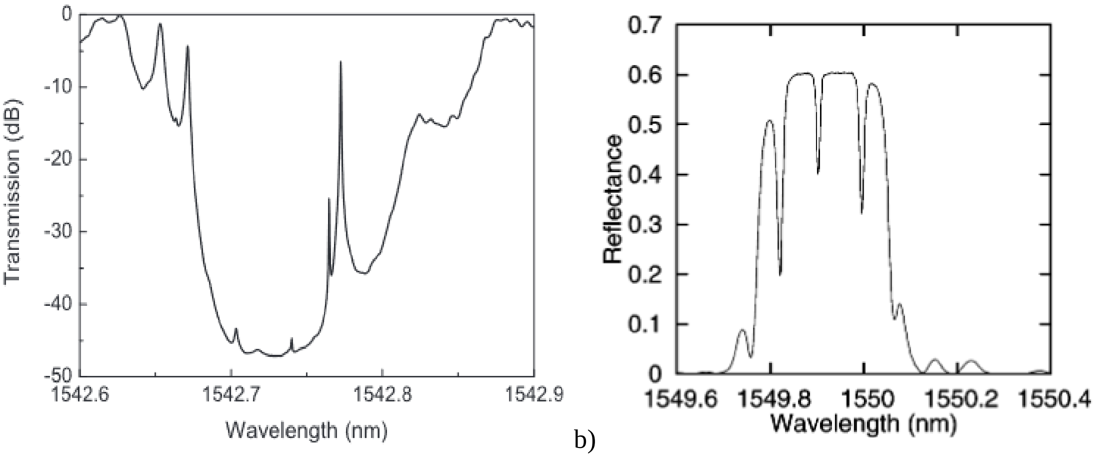

b) c)

Figure 8: a) A Fibre Fabry-Perot schematic diagram for a cavity utilised in a fibre optic cable using two identical fibre Bragg gratings [34], b) π-shifted FBG transmission spectrum [32], and c) Typical reflection spectrum of a fibre Fabry-Perot cavity spectrum with distance *d=4mm* between the two FBG [35] .

2.6 Mach-Zehnder Interferometers

The Mach-Zehnder interferometers (MZI) are another form of an interferometer where the light is separated in two pathways with intensities I_1 , and I_2, for path 1 and path 2, respectively, as showin in Fig. 9(a). One of the two arms is always the reference arm while the other one is used as a sensing arm [36], [37]. At the point where the sensing and reference arm combined, the interference between the light travelling in the two pathways forms a typical interference pattern, as shown in Fig.9 (b) for different optical path differences. The MZI intensity output is described as,

$$I = I_1 + I_2 + 2\sqrt{I_1 I_2} cos\left(\frac{2\pi\ OPD}{\lambda}\right) \ , \quad (2.58)$$

where λ is the operating wavelength [38]. This interference pattern is characterised by the FSR, which is dependent on the optical path difference (OPD) between the two arms. When the sensing arm detects a disturbance, then there is a change in the OPD between the two arms which results in a relative phase shift between the light beams propagating in the two arms and subsequently a shift in the interference pattern.

The optical path (OP) for each arm and the OPD are computed as follows [39]–[41],

$$OP = n_{eff} L \ , \ (2.59)$$

$$OPD = \left(n_{eff1} L_2\right) - \left(n_{eff2} L_2\right) \ , \ (2.60)$$

where n_{eff}, is the effective refractive index and L is the physical length of the waveguide. The phase difference is given as,

$$\Delta\varphi = \frac{2\pi}{\lambda} OPD \ , \quad (2.61)$$

where the phase difference satisfies the condition,

$$\varphi = (2m+1)\pi \ , \quad (2.62)$$

Here m, is the order of the mode and is an integer, and intensity dips appear at wavelengths located at,

$$\lambda_m = \frac{2\Delta n_{eff} L}{2m+1} \ , \quad (2.63)$$

The FSR of the interference fringe pattern is given by,

$$\Delta\lambda_{FSR} = \frac{\lambda^2}{\Delta n_{eff} L} \ , \quad (2.64)$$

Typical transmission spectra for Mach-Zehnders having different path lengths are presented in Fig.9(b). The FSR decreases as the length of the MZI increases, as expected. Another characteristic of interferometers, such as the MZI, is the fringe visibility which is defined as follows,

$$V = \frac{I_{max} - I_{min}}{I_{max} + I_{min}} \ , \quad (2.65)$$

where the I_{max} and I_{min} are the maximum and minimum intensity of the interference pattern fringe. The optimum fringe visibility is achieved if the coupling ratio is precisely 50/50 for both the couplers shown in Fig. 9, and this places strict requirements for the femtosecond laser inscription of cladding MZIs. The fringe visibility is equivalent to the Q-factor, which is calculated in terms of wavelength as,

$$Q = \frac{\lambda_c}{\Delta\lambda} \ , \quad (2.66)$$

where λ_c is the centre wavelength of the fringe and $\Delta\lambda$ is the full width at half maximum bandwidth of the fringe.

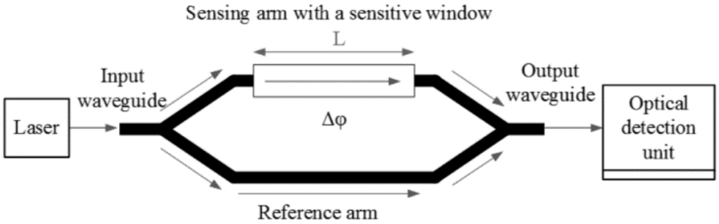

a)

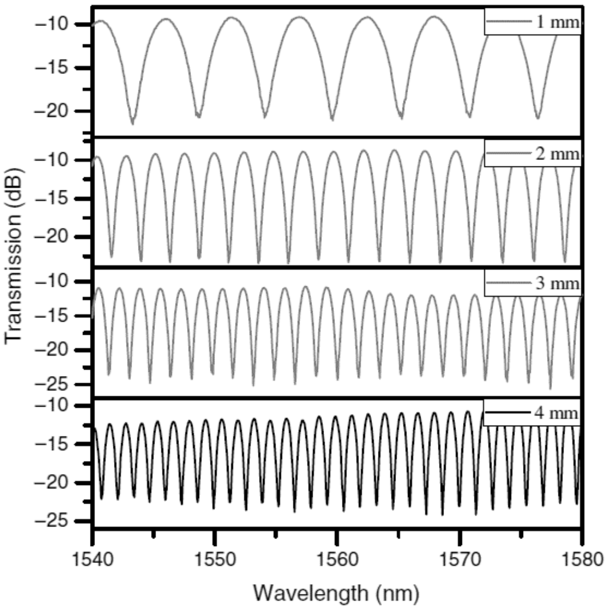

b)

Figure 9: a) A schematic diagram of a Mach-Zehnder interferometer scheme for biomedical applications [41] b) Mach-Zehnder spectrum profile for different lengths [36].

3 Polymer Optical Fibre Sensors – The State of the Art

3.1 Introduction

Originally, POFs were developed as an option for low-cost solutions for future transmission networks. Existing transmission networks operate with glass fibres, with the exception of the last section, the so-called ‘last mile’ to the home, which consists typically of copper cables. Due to the rapid growth of the internet and the higher bandwidth demands, copper cables are being steadily replaced with higher bandwidth solutions, such as optical fibres, either glass or polymer fibres. However, due to the plenty of wires, junctions and connections to be replaced, the solution required to be a low cost, efficient, with minimal installation and maintaince effort. The use of multimode (MM) POFs may provide a good solution since glass fibres are a relatively costly solution. In particular single-mode fibres require careful handling and termination, and high-level training is required for general handling and splicing. The fabrication expenses of POFs are more or less the same as with the glass fibres, but the handling and maintenance costs are much lower. Specifically, the large core diameter of MM-POFs makes coupling of the light to and from the fibre far easier, while their cleaving and connectorisation do not require specialised equipment and well-trained technicians. Initially, the first large core step-index POFs did not support significantly high bandwidths (1 Gbps) than copper cables (10Gbps for Cat6a and Cat7), but this greatly improved with the formation of a tailored refractive index profile and the development of the graded index POF (100Gbps) [42]–[50].

From the sensing point of view, the large-core MM-POFs often lead to various interrogation problems. Typically FBGs inscribed in MM fibres are characterised by multiple peaks at the Bragg wavelength in reflection or multiple dips in transmission [16], [51], [52]. This is because of the high number of propagation modes supported by these large-core fibres having marginally different refractive index values. With conventional inscription methods, such as the phase mask or the interferometric methods using UV laser sources, most of the core modes are triggered and detected in the spectrum as multiple peaks. This will cause interrogation problems as almost all sensing interrogators are designed for use with single peak FBGs. For that reason, several research groups have worked and are still working on the development of single mode POFs, mainly based on polymethylmethacrylate (PMMA) polymers. However, the smaller fibre core in POFs creates its own problems, as will be discussed.

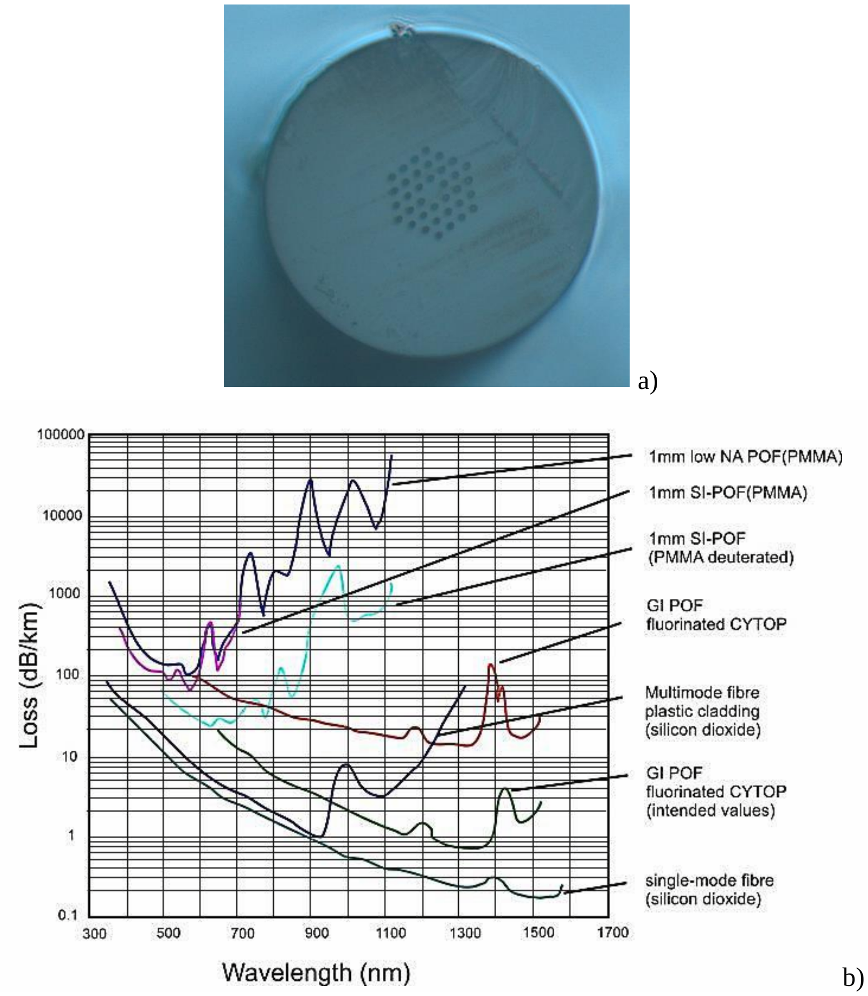

a)

b)

Figure 10: a) Cross section of microstructure polymethylmethacrylate (PMMA) fibre by Kiriama LTD, and b) Attenuation loss comparison between different polymers and common silica single mode fibre.

There are two key designs that are used for the formation of single-mode POFs. The fibres are either fabricated using dopants in the fibre core to increase the refractive index value compared with the cladding region, and referred as step index (SI) fibres, or without dopants (generally) and using microstructured patterns around the core to 'trap' the light inside the core, known as microstructured fibres (mPOFs) [53], [54]. The region around the core is full of air holes that run parallel to the fibre longitudinal axis, and the air-fill fraction determines the average refractive index in that region, thereby immitating the role of the cladding; a cross-sectional image of a microstructured POF is shown in Fig.10(a). We note that if the ratio of the air-holes diameter to the spacing between the air-holes is less than 0.42, then the microstructured fibre is single mode [55]–[57]. As noted, the majority of POF is made using PMMA. The main advantages of PMMA compared to silica fibres are the improved mechanical properties. PMMA fibres have a Young's modulus 25 times lower compared to glass (~3 GPa compared with ~70 GPa), which allows for a larger strain range, and this translates to a larger wavelength tuning range, more than ten times compared to silica, if the fibre incorporates a FBG filter. The maximum wavelength shift reported with a PMMA-FBG was in excess of 70 nm, by inducing strain [58]–[60]. POFs are fundamentally safer to insert into the human's body and perform biomedical measurements due to their high elasticity and soft material properties. Moreover, PMMA fibres have been found to be more sensitive to temperature than the silica fibres, and have also shown sensitivity to other parameters such as to humidity and enhance the interactions with chemical elements like glucose [61]–[63].

The main drawback of PMMA-POF is the exceptionally high attenuation losses which can reach ~100 dB/m, within the 1300 nm to 1650 nm wavelength window often used for optical communication applications. Hence POF can be highly restricted in its potential uses. As Ma et al. [64] showed, the absorption in this particular window come mostly from the overtones of fundamental molecular vibrations. Specifically, the highest energy vibrations occur for molecules having high spring constants and/or small masses and the smallest reduced mass occurs when one of the atoms is hydrogen. For example, the C-H overtone bonds results in high transmission absorption for the second and third harmonics at the wavelengths 1729 nm and 1176 nm, respectively, and for the O-H bond at 1438 nm for the second harmonic [64], [65]. The losses at shorter wavelengths, mostly in the visible region, are much lower at ~0.2 dB/m (Fig.10(b)). However, this the majority of the optical devices operate in near-infrared region 1300 nm - 1650 nm, the region where POF losses are very high. This limits the operating length for FBGs in PMMA-POF when used in the near infrared, and there is a practical length limit of only 10 centimetres, which severely restricts the use of POF to real-world applications. Clearly alternative polymer materials are needed, if POF based FBG sensors or filters are to be used practically and beyond the laboratory environment.

We also note that PMMA-POFs are hydrophilic and display high water absorption. This adversely impacts the use of FBG POF sensors and their applications; a fact that suggests that they be acceptable only for certain uses, such as when FBGs are used to measure relative humidity changes. The presence of humidity also causes cross sensitivity problems, since the water absorption response of the POF interferes with strain or the temperature measurements [61], [66]–[69]. Recent studies have shown that alternative materials may be used to solve this issue, such as the cyclic olefin copolymer (TOPAS) polymers. TOPAS fibres, unlike PMMA, are an inert chemical material and their immunity to water absorption is much higher compared to PMMA. Unfortunately, the material losses remain at high levels for near infrared use, and so do not offer a true alternative to PMMA [70]–[73].

On the other hand, there is an excellent polymer fibre that was developed by Ashasi Glass LTD and Keio University [74]–[76] in 1997, called cyclic transparent optical polymers (CYTOP). The particular fibre was designed specifically to operate at infrared wavelengths for short distance communication systems, such as the Fibre-to-the-Home (FTTH) networks. With this material, the hydrogen bonds, which are responsible for the high transmission losses in the infrared wavelengths, were removed using a fluorination process, and the losses decreased to ~30 dB/km at 1300 nm, while theoretically it is possible to have similar performance with the silica fibres, as better shown in Fig. 10(b) [77]. At the same time, CYTOP-POFs show similar behaviour with TOPAS POFs and glass fibres when placed in environments with high water content. Here it is important to note that conventional UV lasers have yet been used to modify CYTOP and inscribe FBGs, whereas this can be readily achieved using fs laser inscription methods, where the high material transparency is well suited to modification via multi-photon absorption. However, as already discussed the key application of the CYTOP fibre means that is only commercially available as a multi-mode gradient index fibre; this makes FBG inscription and sensor interrogation complicated.

The rest of the chapter is structured as follows. The second section is a literature review of the photosensitivity of polymer fibres and the current inscription methods used for the development of POFBGs. The third section is focused on the sensitivities of the POFBGs to different environmental parameters such as humidity, temperature, and strain; whilst the last section contains conclusions and remarks regarding polymer optical fibre sensing technology.

3.2 Fibre Bragg Grating Inscription in Polymer Optical Fibres

3.2.1 Photosensitivity of POFs

The photosensitivity or photo-reactivity of PMMA polymers were firstly studied over 40 years ago by Tomlinson et al. [78], Kaminow et al. [79], Moran et al. [80], and Bowden et al. [81] using PMMA slabs. However, it was difficult to reach ultimate conclusions, since it was clear that a variety of mechanisms were taking place, and dependent on the radiation wavelength, the power of the laser source, and how the samples were prepared. Tomlinson et al. [78] in 1970 prepared un-doped PMMA slab samples with azobisisobutyronitrile (AIBN), and varied their oxidation levels to produce peroxides. After several hours of exposure, the refractive index change saturated at ~$3x10^{-3}$. From their results, they concluded that the oxidation products in the polymer absorbed the UV radiation and produced free radicals, which cross-linked with adjacent polymer chains. The cross-linkage is known to draw the polymer chains closer together, increasing the material density and hence increasing the refractive index. Later Bowden et al. [81] in 1974 reported on similar results; however they stated that the refractive index increase was due to an increase in material density resulting from the polymerisation of residual monomers and not from crosslinking and this was shown to be correct in 1985 by Marotz et. al. [82]. Kaminow et al. [79] in 1971 and Moran et al. [80] in 1973 reported on reduced inscription times by increasing the ambient temperature to 40 ^{o}C, but the maximum refractive index change saturated as a result and was lower than reported in the previous studies.

Another paper in 1971 by Laming et. al. [83] reported on the poly-degradation or de-polymerisation using UV laser light of 488 nm. Mitsuoka et al. [84] irradiated PMMA samples with 260 nm, 280 nm, 300 nm, 320 nm, 400 nm and 500 nm laser light sources and they reported a threshold wavelength for the photo-degradation of PMMA to be around 320 nm by observing of chain scission of the main polymer backbone. Recently, in 2014 Rodriguez et al. [85] reported the inscription of FBGs in PMMA fibres having applied stress during the inscription process. The stress applied to samples enables photo-degradation effects in polymers that increase the photosensitivity. But then again after the gratings were inscribed the authors removed the phase mask and continued to irradiate the gratings and found that the refractive index change was positive, indicating that photo-polymerisation also occurred during the inscription process.

The photosensitivity of the material could be increased by adding dopants or copolymers into the PMMA samples as reported by Peng et al. in 1999, and Yu et al. and 2004 [86], [87]. Studies continue in this subject area while researchers aim to increase the photosensitivity in POFs and reduce the inscription time.

On the other hand, the photosensitivity of the CYTOP studied for a first time in 2001 by Liu et al. [88] and Kawase et al. [89]. The CYTOP fibre samples were exposed using UV laser operating in wavelengths 355 nm, 457.9 nm, 488 nm, and 514.5 nm. For the first study, Liu et al [88] noted 1.6% diffraction efficiency after 20 minutes of exposure using UV light at 355 nm, however this was after the fibre was compressed between two glass plates and it is not clear what process was affecting the squeezed fibre core. In the second study [89] the samples were exposed only for 10 minutes and the corresponding diffraction efficiencies observed were 0.80%, 0.67% and 0.45% for 457.9 nm, 488 nm and 514.5 nm, respectively. Again, it was unclear what process was responsible for the material modification. Since then, at least to the time writing this thesis, no other studies were reported on the photosensitivity of CYTOP POFs.

3.2.2 Current Fibre Bragg Grating Inscription Methods for POFs

Most of the inscription methods proposed for FBG inscription require that the fibre is photosensitive. The first inscriptions in POFs performed using the phase mask inscription were demonstrated by Peng et al. [87]; this method requires less configuration effort, eases alignment, and offers better reproducibility in results [87]. The laser beam, usually UV radiation operating at 325 nm, is incident on the phase mask and the phase mask divides the monochromatic incident beam into two outgoing beams as shown in Fig. 11 (in this example the beam is incident from above). The two diffracted interfere and form a diffraction pattern in the region where they are overlapped; the fibre is placed in this triangular diffraction region. The FBG is imprinted into the core, with the largest index change corresponding to the regions where the light intensity is highest. Based on the photosensitivity mechanism the fibre absorbs the radiation at the areas where the diffraction maxima exist leading to a positive modulation on the refractive index of the material. The periodicity of the modulation depends on the pitch of the phase mask gratings. Usually, the configuration employed for the FBG inscription is the +1/-1 configuration, with the laser beam directed normally to the phase mask. With this configuration, the resulting fringe period is exactly one-half of the phase mask grating period. Normally the most of the diffractive light of the phase mask is contained in the zeroth and first diffraction order [90]. However, to obtain high quality first order gratings, it is important to suppress the zeroth-order diffraction otherwise it will contribute to the intereference pattern forming higher order gratings. Thefringe visibility of the interference pattern will not be uniform and as a result the grating periods will not uniformly inscribed. Typically zeroth order suppressed to less than 1% of the transmitted power [91].

A more detailed inscription setup diagram is shown in Fig. 12 where a low power continuous wave helium-cadmium (He-Cd) laser was used for the FBG inscription in a microstructured POF fibre. The inscription setup consists two plano-convex cylindrical lenses with 10 cm focal lengths, one in the usual position of the phase mask, which served to focus the light down toward the core, and the other at a distance of 56.5 cm from the mPOF. The second lens was used to expand the diameter laser beam from 1.8 mm to 1 cm [92].

The typical inscription time is 60 to 270 minutes for mPOF, while step index fibre requires a shorter time, typically 45 to 100 minutes [93]–[101], as the scattering of the hole structure is now absent. The particular inscription method is affected by the photosensitivity of the material, and the duration of the inscription is related to the laser wavelengthand, in the case of microstructure fibre, the fibre geometry[102], [103].

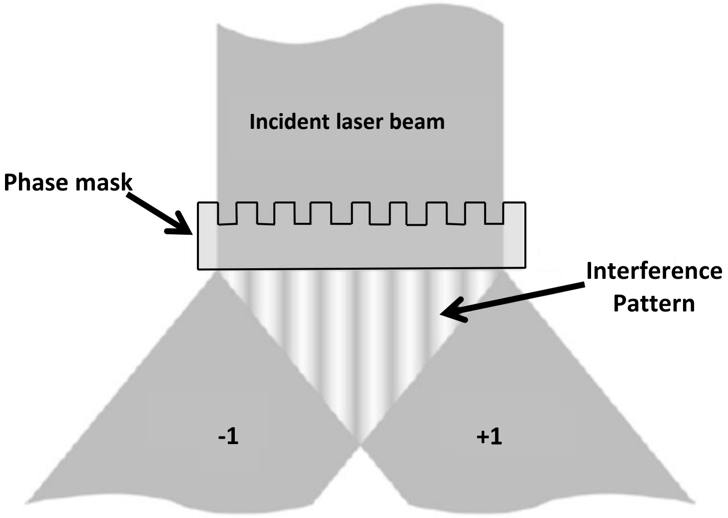

Figure 11: FBG inscription process using the two beam diffraction pattern created using the phase mask +1/-1 configuration [90].

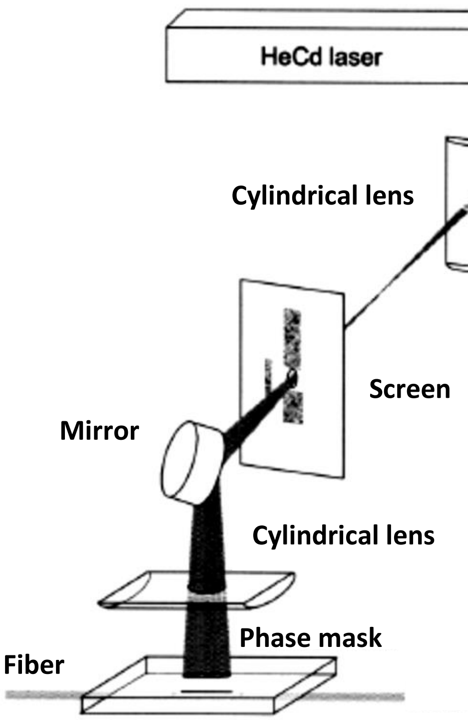

Figure 12: Experimental setup of the phase mask inscription method for FBG inscription using a He-Cd UV laser, mirrors to guide the laser beam and cylindrical lens to adjust the size of the beam [92]

The phase mask inscription method is also suitable for POFBG inscription with femtosecond lasers. In this case the refractive index modulation, depends on multi-photon absorption. From the literature [104] shown that the required inscription time decreased significantly. Only 120 seconds is enough for FBGs with ~94% reflectivity.

In 1990 a new inscription method presented for glass telecommunication fibres by Hill et al. [7] and later Malo et al. [105] the so-called Point-by-Point (*PbP*) inscription method. The main advantage of this approach is the flexibility on selecting the gratings period allowing the inscription of gratings at different wavelengths and potentially chirped gratings. The first inscriptions with this method were made by attaching the fibre sample to a motorised rotary stage from one end, and the other end was attached to a pulley and a counterweight; as the motor turned the fibre was translated in front of the laser beam slit. The laser could be set ‘ON’ either by stopping the motor at each inscription point and perform single laser shot or by continuous motor turns and laser flashes synchronised at regular intervals. However, this method was implemented using a UV laser and the inscription process was laborious. A newer version of the PbP method was proposed by Martinez et. al. in 2004 [106] using a femtosecond laser. By carefully selecting the speed of the translation stage, single laser pulses hit the fibre core at a specific rate creating small points or volume pixels (voxels) to modify the refractive index with minimum thermal damage. The fs PbP is method can be very fast and flexible method regarding grating period. However the alignment requirements are critical, and as a result, the alignment process requires much higher time and careful and accurate stage movements.

3.3 POF-FBG Sensitivity

3.3.1 Strain and Pressure Sensitivity

As already discussed POFs have interesting viscoelastic characteristics. Typical Young's modulus values range from 1.8 - 3.1 GPa for PMMA, 2.6 - 3.0 GPa for TOPAS, and 1.4-1.6 GPa for CYTOP, which is significantly lower than the 73.1 GPa of silica fibres; potentially offering a higher tunability range, lower fracture failure and higher wavelength tuning (73 nm) compared with the glass fibres [59], [60], [98], [107], [108]. Hysteresis is a typically problem with these fibres [109], [110]. It is usually observed when the gratings left under strain for extended time or when exposed to high strain levels approaching the elastic limit of the fibre [109], [110]. The strain sensitivity for POFBGs is typically ~1.5 pm/με at 1550 nm and ~0.7 pm/με at 830 nm, for either PMMA or TOPAS fibres [94], while as we will show later in chapter 4, for CYTOP-FBGs is ~1.44 pm/με at 1550 nm.

3.3.2 Temperature Sensitivity

As one may anticipate silica FBGs can operate at temperatures up to 1000 ^{o}C whilst maintaining its structural integrity, whereas the organic polymer material has a severely limited maximum operating temperature, typically 78 ^{o}C for PMMA [73], and up to 135 ^{o}C for TOPAS [111]. On the other hand, the sensitivity of the POFBGs is significantly higher, specifically, for the PMMA-FBG the response found to be -109 pm/^{o}C [108] while for TOPAS-FBGs is -78 pm/^{o}C [112]. The polymer FBGs (PMMA and TOPAS) show up to 10 times the sensitivity of silica fibre FBGs and the negative wavelength-temperature response has been shown to compensate between strain and temperature, minimising cross sensitivity issues [113]. It is important to note that there is no evidence if the relative humidity kept constant during the experiments. In contrast as we will show in chapter 4 for CYTOP-FBGs the response to temperature found to be 17.62 pm/^{o}C which is positive and very similar to the glass fibres and as Liu et al. [114] report in their work in 2002, where the fibre CYTOP slabs shown better thermal stability than the PMMA.

However, due to the POF fabrication process, the polymer molecules align in the axial direction, creating anisotropic material properties. Thus, birefringence appears in the fibre cross-section when its mechanical properties are perturbed. It is also possible to induce small cracks in the radial direction of the fibre, therefore, it is important to anneal POFs before measurements to remove, or reduce, the effects of the internal stresses that appear during the drawing process. This annealing process can be made before or after the FBG inscription process, with little effect on the grating profile [63], [108], [115].

Finally, the hydrophilic nature of PMMA fibres requires that one must consider the relative humidity in order to extract the correct POFBG temperature response. A standard method to calibrate the sensor for temperature, whilst keeping the humidity constant, is to use a climate chamber [63].

3.3.3 Water Absorption and Relative Humidity Sensing

As briefly discussed in the previous section, one interesting characteristic of the POFs is their hydrophilic properties. I will first discuss PMMA polymers, as they are the most often used for POF, and have the tendency to absorb water and this absorption results in a shift of the Bragg grating resonance wavelength. This behaviour achieved based on two mechanisms. The first relates to the grating pitch change due to the swelling of the polymer through water intake, and the second relates to the change in refractive index due to the increased water content [116]. Several experiments were performed comparing the response of PMMA-FBGs and silica-FBGs with the samples mounted inside a climate chamber operating at constant temperature, and the relative environmental humidity was increased in controlled steps [63], [117]. The results reported 35.2 pm/%RH for the PMMA fibres, whereas for silica the change was only 0.28 pm/%RH. Furthermore, the humidity sensitivity of the POFBGs may vary from sample to sample, since the core/cladding fibre diameter may vary, and the material of the outer cladding will also control the amount and rate of water absorption.

In some cases, the humidity sensitivity of the POFs could be considered a disadvantage, since the absorption usually causes cross-sensitivity issues with other parameters, such as temperature and strain. Other polymer fibres like TOPAS and CYTOP shows lower water absorption behaviour similar to that of the silica fibres, and overcome these cross-sensitivity issues [73], [118]. However, as we will discuss in detail in the next chapter, if the fibre consisted by a hydrophilic surrounding jacket, this may influence the response of the FBG even if the core is not absorbing water and as a result a significant humidity response can be obtained with CYTOP fibres.

3.4 Conclusions

This chapter introduced polymer optical fibres, briefly describing the key materials used for the manufacture of POFs, the usual designs and their optical and mechanical characteristics. We also presented the most common FBG inscription methods in such fibres and their potential compared to their glass counterparts when used as sensing elements. For a better comparison between the POFs, their mechanical characteristics and their sensing responses were summarised in Table 1; with blue highlighted domains were exploited during the studies presented in this thesis and were not exploited before.

We note that POFs are fundamentally safer for bio-sensing applications and in vivo measurements and in combination with their unique characteristics are highly promising as sensing elements and filters. Nevertheless, at the time of writing there remain several obstacles to the commercialisation of the devices. The many different procedures of the polymers preparation make the full understanding of the photosensitivity mechanisms difficult while the sensing responses in the literature are varying significantly.

As a commercial product, there is only one commercial supplier of single-mode POF, the Paradigm Optics, with a supplier of mPOF, Kiriama Pty of Sydney Australia (currently out of business). This explains the lack of single-mode POF components such as couplers and pigtailed devices. Moreover, the studies limited only on PMMA and more recently on TOPAS fibres since other POFs such as CYTOP, Zeonex, or Polycarbonated polymers could probably improve the characteristics of polymers and may fit better for certain applications but their absorption bands may be limiting the development for FBG sensors.

Table 1: Comparison between different polymer fibres with respect to the silica fibre.

	PMMA	**TOPAS**	**CYTOP** *(This work)*	**Silica**
Young's Modulus (GPa)	1.8-3.1	2.6-3	1.4-1.6	73.1
Loss (1550 nm) (dB/Km)	~100 x10^3	~100 x10^3	200	0.2
FBG inscription	Yes	Yes	Yes	Yes
Strain (pm/με)	1.5	1.5	1.43	1
Temperature (pm/ºC)	-109	-78	17.62	10
Thermal Stability	Low	Low	High	High
Humidity	High	Low	Low	Low

4 Inscription and Characterisation of Fibre Bragg Gratings in CYTOP

This chapter presents the experimental details on the femtosecond laser inscription method used to inscribe FBGs, chirped gratings, and Fabry-Perot cavities in a multimode gradient index CYTOP polymer fibre. The direct-write, *plane-by-plane* (*Pl-by-Pl*) inscription method offers unique flexibility and controllability of the spatial inscription parameters compared to all other inscription methods, such as the phase mask and point-by-point method when dealing with FBGs in multimode fibres. Specifically, was we achieved the inscription of 'single peak' FBGs in a multimode fibre, which is not feasible with the other methods. All optical devices were characterised and their sensitivity response reported under different physical perturbations such as axial strain, relative humidity, and temperature.

The work presented in this chapter was published in the IEEE Journal of Lightwave Technology and the IEEE Photonics Technology Letters.

4.1 Introduction

We have identified that silica FBG sensors are widely used as point sensors in a variety of applications, from the measurement of strain and temperature to more complicated quasi-distributed sensing, such as vibration mode shape monitoring, ultrasonic detection, and structural health monitoring. The applications typically require arrays of gratings [119]–[123]. The low loss of silica fibres for the telecommunication window (1260 – 1650 nm) is ~0.2 dB/km. Therefore silica fibres are used exclusively when optical sensors are required for measurements over moderate and long distances. Moreover, the single mode behaviour of standard fibres is well understood and avoids some problems that would otherwise be encountered if multimode fibres were used. For example, FBG sensors in multimode optical fibre display multiple peak spectra, with overlapping Bragg modes that exchange power due to spatial mode mixing in the fibre core as external fields perturb the fiber. We have explored how the evolution of the POFs offers an alternative to glass fibres, however the extremely high loss (~100 dB/m) encountered in the near infrared is a problem, as is the lack of access to commercial, low loss, single mode polymer fibres. So far, all single mode POF has been developed in universities undertaking research in this area and POF promises exceptional optical sensing capabilities if the two aforementioned disadvantages can be overcome. Optical sensors based on POFs can prove to be especially useful for medical applications, where the insertion of plastic-based catheters into the human body is acceptable. Moreover, there are many useful applications such as physical, chemical and bio-sensors that can be used to measure temperature, pressure, glucose levels, and antibody biomolecules [124]–[127]. The POF transmission loss is detrimental to the sensor performance, even for short-range applications. All the currently commercialised and certified polymer optical fibres are available only as step or gradient index multimode fibres; their development is driven by the FTTH applications, where the large fibre core diameters allow for easy and efficient coupling using low-cost connectors and sockets.

In general, the inscription of fibre Bragg gratings in multimode fibres results in the excitation of a large number of higher order modes producing a multi-peak FBG wavelength spectrum [15]. This effect is acceptable for some applications where low-resolution measurements can be tolerated. However, the occurrence of randomly overlapping Bragg modes causes problems for conventional optical fibre sensor demodulation equipment, as peak tracking algorithms can no longer know which peak to track. This issue is exacerbated if more than one multimode FBG is present, such as in a sensor array. Hence there is a need to develop FBG sensors arrays in multimode POF that can overcome these problems. We have already noted the low-loss benefits of perfluorinated POF as the optical absorption is shifted to 7.7–10 μm, and is associated primarily with C–C, C–F and C–O bonds; moreover, CYTOP exhibits low scattering loss due to its highly amorphous nature. However, CYTOP does not currently have a commercial single-mode fibre design. Nevertheless, we can use the low-loss advantages of CYTOP and, through FBG inscription via a femtosecond laser inscription process, address methods to control the multi-peak FBG reflection spectrum typical for multimode fibres.

In this chapter, a gradient index CYTOP fibre was used consisted of a 62.5 μm core diameter, with a cladding layer of 20 μm and an additional polyester and polycarbonate outer jacket of 490 μm to protect the fibre. We inscribe individual grating planes transversely across the fibre core resulting in a modified, 2D refractive index sheet, building the grating in a step-wise process and by doing so have full control of the index change and grating length. In this way, we can efficiently optimise the coupling between the FBG and the lower order fibre modes.

4.2 Plane-by-Plane fs-laser Inscription Method for 'Single Peak' FBGs

4.2.1 Experimental Inscription Setup

The inscription setup utilised for the plane-by-plane method consisting a femtosecond laser system (HighQ Laser femtoREGEN) operating at 517 nm, with 220 fs pulse duration and an air-bearing translation stage system (Aerotech) for accurate two-axis motion. The laser beam was focused from above using a long working distance microscope objective (Mitutoyo, x50, NA 0.42) as shown in Fig. 13 and the focal length was controlled using a third translation stage. The fibre samples were fixed carefully on a glass slide and immersed in refractive index matching oil and covered with a thin cover slip. This method is used to overcome any curvature effects that arise from the cylindrical shape of the fibre acting as a lens. The laser pulses at the exit of the laser could be controlled with an attenuator and energies could be varied from a few nJ to μJ/pulse, whereas the repetition rate was set using a l pulse picker that could set the repetition rate of the laser from 1-100 kHz. For the CYTOP inscriptions presented in this chapter, the laser pulse energy was limited to 60nJ/pulse and the repetition rate to 2 kHz. All the components of the system were synchronised using a personal computer, and the stages were controlled using G-code programming that could be adapted to our requirements.

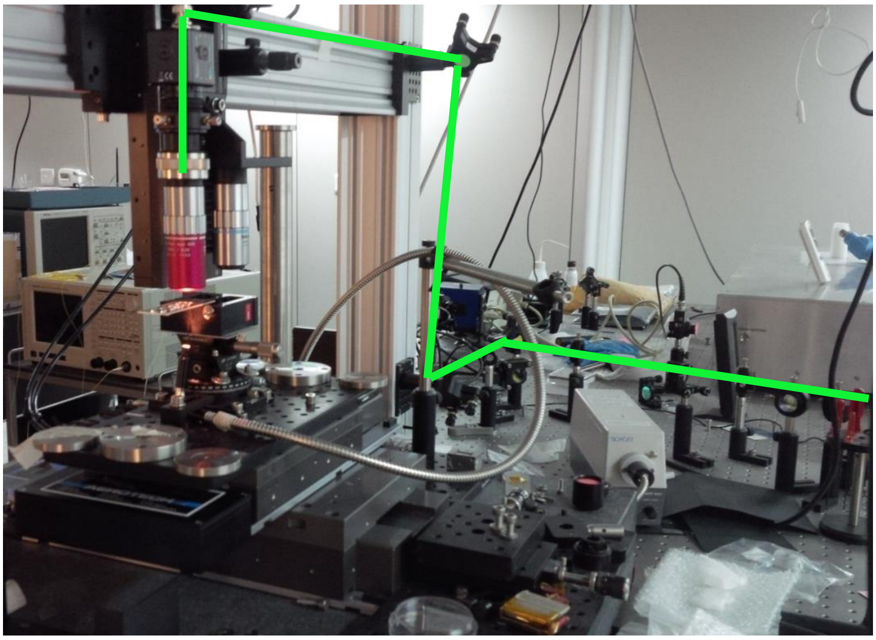

Figure 13: Inscription setup for *Pl-by-Pl* femtosecond laser inscription method.

4.2.2 Working Principles of the Plane-by-Plane Inscription Method

The key advantage of this inscription method compared to the phase mask and the PbP methods is the flexibility to control all the spatial inscription parameters of the gratings such as period, spatial extent of the index change (width, depth, length), and modulation of the refractive index. As shown in Fig.14 the fibre sample moved along the y-direction, transverse to the core, creating three-dimensional sheets or planes of a modulated refractive index with length (y-direction), depth (z-direction), and width (x-direction) while the laser beam kept constant and focused in the centre of the fibre core. An external shutter controlled when and where inscription occurred, in this case it was closed during the diagonal stage movements. The length of the plane and the grating period were set by the stage motion parameters, whereas the depth of the inscription is a variable of the laser power, repetition rate and final focusing lens.

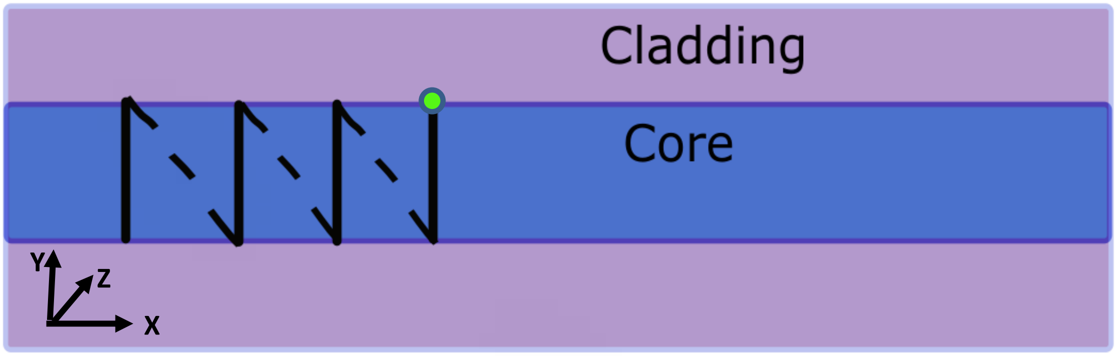

Figure 14: Schematic diagram of the FBG inscription in fibre core using the Plane-by-Plane femtosecond laser inscription method.

A series of inscriptions were performed by keeping the laser repetition rate constant at 10 kHz, and the pulse energy was changed. Following the inscription, the inscription depth was measured using an optical microscope (Zeiss M1). As expected, the depth of the inscription increased with increasing energy; Fig. 15(a) shows the linear relationship between the depth of the inscription and the pulse energy.

Similarly, we kept the laser energy constant (56 nJ) and the inscription depth was measured for different repetition rates (Fig. 15(b)). A linear increase of the inscription depth was observed only for repetition rates exceeding 10 kHz, below this rate the depth modification followed a logarithmic shape.

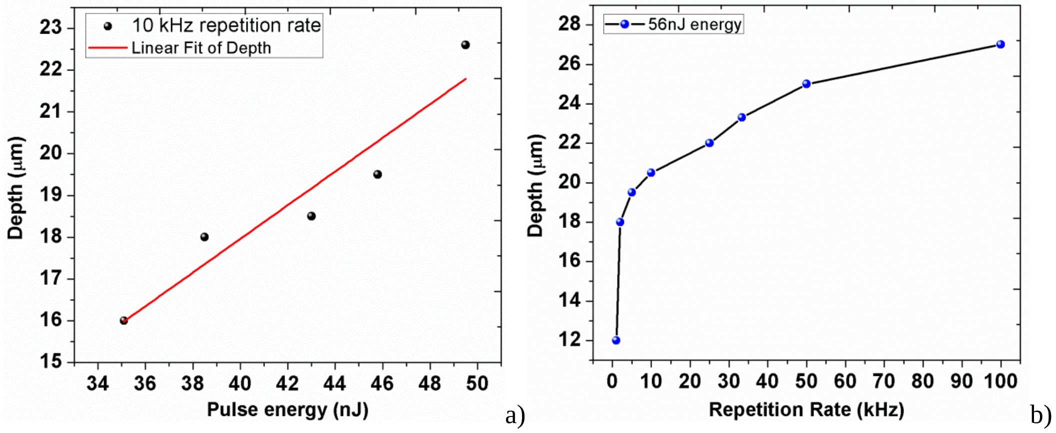

Figure 15: Measured depth of the femtosecond laser inscribed plane in respect to a) Pulse energy vs depth, and b) Repetition Rate vs depth.

4.3 Fibre Bragg Gratings in CYTOP Fibre

Given the flexibility of the *Pl-by-Pl* method, we considered the contribution of the inscription parameters to the excitation of the higher order spatial modes in the fibre core. FBG inscriptions were performed having plane widths of 5 μm, 15 μm, and 30 μm, and located at the centre of the 62.5 μm diameter multimode gradient index fibre core, as shown in Fig. 16. The grating lengths were varied by inscribing 300, 500 and 1000 planes. We selected a plane-period of 2.2 μm to ensure that the duty cycle of the grating was optimum. The reflection spectrum for each case was measured and characterised using a broadband light source (Thorlabs ASE730), a circulator and commercial FBG demodulator with optical resolution ~169.5 pm (Fig. 17).

As the grating length increases the gratings become stronger with reduced bandwidth, Fig. 17 (a-c), but increases the overlap integral between the grating structure and spatial fibre modes resulting in the presence of more Bragg modes. To compare the strength of the gratings in terms of recoverable reflectivity, we interrogated all the gratings with an Ibsen spectrometer (I-MON 512, having a 169.5-pm optical resolution), while keeping the capture integration time constant (10 μs). We observe that the multi-peak, grating reflection spectra, are dependent on the width of the fs-laser inscribed planes and the grating length, as anticipated. The gratings having a longer length and wider planes are more multimode in behaviour; with the presence of short wavelength peaks for all grating inscriptions that consisted of 1000 planes (2.2 mm in length), regardless of the plane width, Fig. 17 (a). These multiple peak spectra are difficult to track using conventional grating demodulators, as they can exchange power, resulting in apparent and sudden wavelength shifts that are in fact inaccurate. If we compare the reflection spectra for the shorter gratings, 500 and 300 planes (grating length 1.1 mm and 0.65 mm, respectively), there is significantly less Bragg mode excitation, Fig. 17 (b, c); we observe the appearance of a strong central mode and the suppression of other Bragg modes. In Fig. 18 the FBG having 300 planes with 5-μm plane width is recovered with a high resolution (10 pm) optical spectrum analyser (Advantest Q8384). Here we observe the cleanest spectrum, with a Bragg peak that is readily tracked using the commercial demodulator. The combination of the physical attributes of the grating with the fibre’s gradient index profile works together to optimise the grating wavelength spectrum. Of course, there will still be sensitivity to the launch conditions and the illumination of the grating, but in general, the FBG spectrum is rarely buried in the noise, and a recoverable signal is always possible. This will be acceptable for low resolution sensor measurements.

Another important optical property that needs to be considered for sensing applications and communication systems is the birefringence, which could result from the asymmetry of the fibre core, and any birefringence induced during the transverse inscription process [128]–[130]. Using a linear polariser between the source and the FBG samples we controlled the input state of polarisation of the source and measured the transmitted amplitude spectrum for different polarisation angles in the range 0°-360°. The wavelength shift as a function of polarisation angle is presented in Fig. 19(a-f) for a grating with 300 planes and 500 planes. The maximum wavelength shifts attributed to the birefringence were 70 pm and 130 pm for 5 µm plane width, 115 pm and 140 pm for 15 µm plane width and 70 pm, and 320 pm for 30 µm plane width, respectively. We note that higher birefringence was obtained for longer grating length for the same plane width, as expected. The results show that the best grating regarding grating strength, single peak spectra, and birefringence compromise corresponded to a grating with a 15 µm plane width, or less, across the fibre core; hence we consider that the optimum inscription parameters for gratings correspond to 300 – 500 planes (~0.65 – 1.1 mm) with 15 µm plane width, or less.

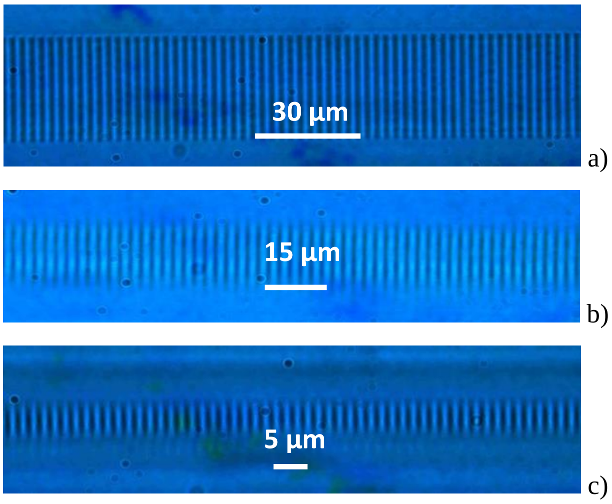

Figure 16: Microscope images of FBGs inscribed in low loss multimode gradient index CYTOP fibre using the *Pl-by-Pl* inscription method with planes having (a) 30 µm, at (b) 15 µm and at (c) 5 µm width, across the centre of the core.

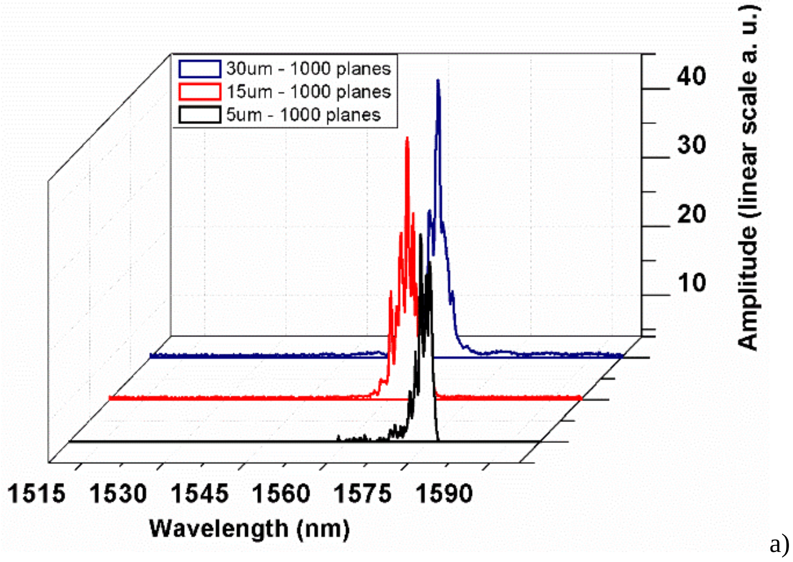

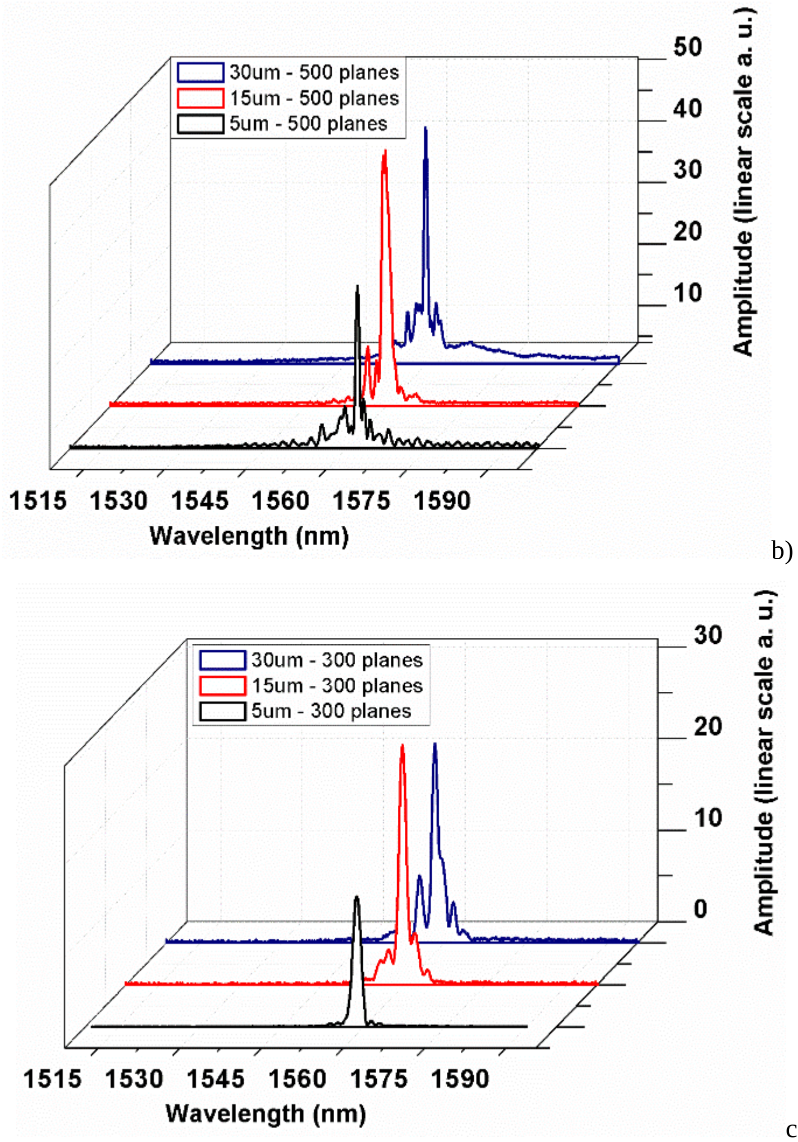

b)

c)

Figure 17: FBG reflection spectra written in CYTOP multimode fibre for (a) 1000 planes having widths of 30 µm, 15 µm and 5 µm; (b) 500 planes having widths of 30 µm, 15 µm and 5 µm; (c) 300 planes having widths of 30 µm, 15 µm and 5 µm. All spectra were recovered using a commercial spectrometer with 10 µs exposure time.

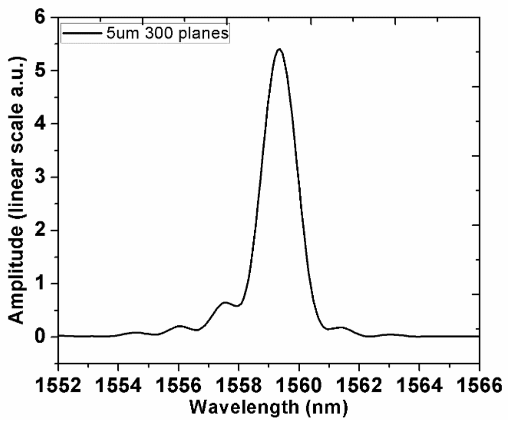

Figure 18: FBG spectrum for 300 planes having 5 µm width recovered using an OSA with 10-pm optical resolution, confirming a single strong Bragg peak.

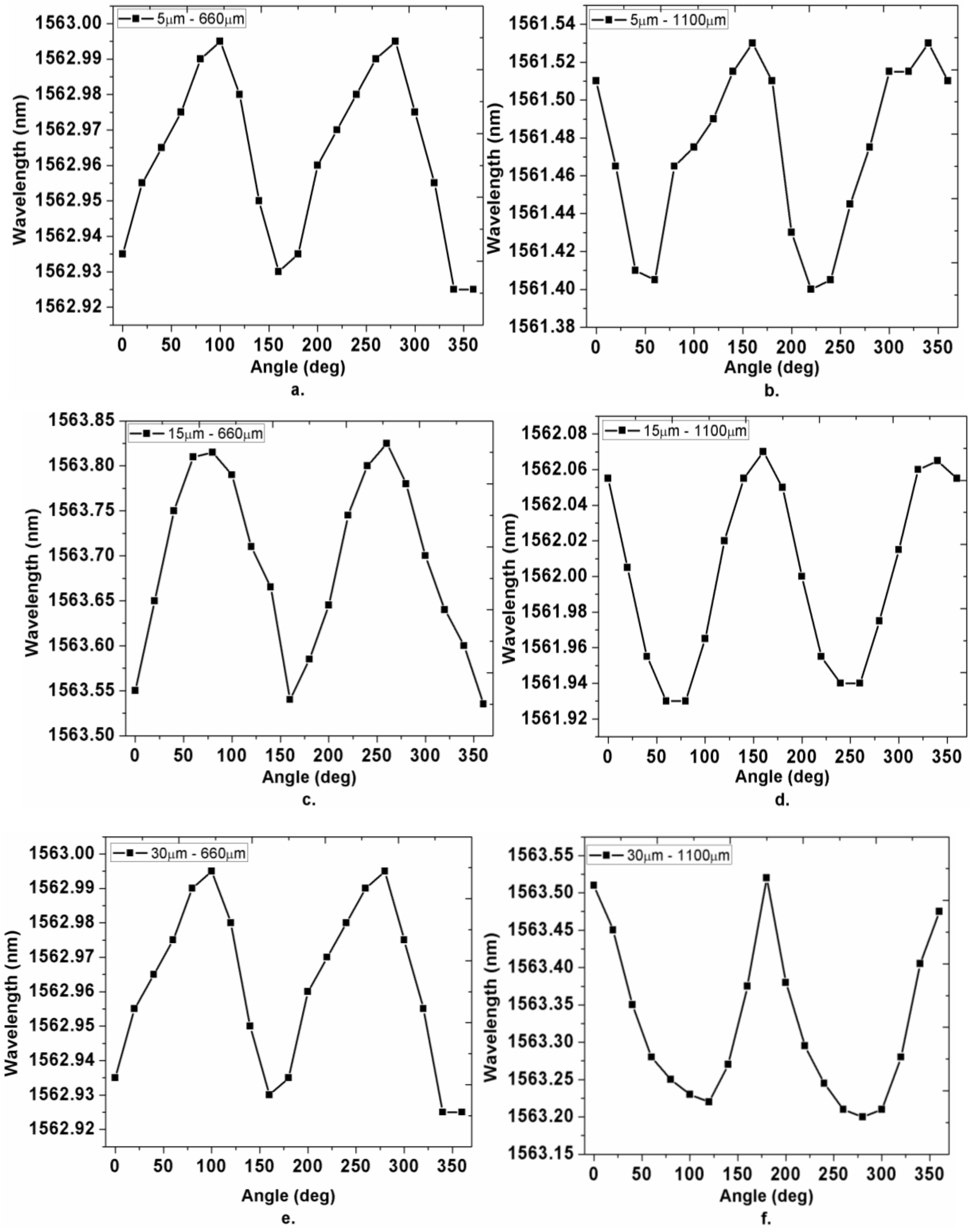

Figure 19: Polarisation measurements (a. 5 μm plane width and 660 μm grating length, b. 5 μm plane width and 1100 μm grating length, c. 15 μm plane width and 660 μm grating length, d. 15 μm plane width and 1100 μm grating length, e. 30 μm plane width and 660 μm grating length, f. 30 μm plane width and 1100 μm grating length).

4.4 Thermal Response

The temperature response of an FBG may be expressed with the following equation,

$$\Delta\lambda_B = \lambda_B(\alpha_\Lambda + \alpha_n)\Delta T, \qquad (4.1)$$

where is α_Λ the thermal expansion and α_n thermo-optic coefficient. The thermal expansion of the material affect the grating period, whereas the thermo-optic coefficient affect the refractive index. There are a few reports on the thermal characteristics of the CYTOP fibre, with the exception of reference [88], for a CYTOP strap embedded in silicon or polymer substrates, where the substrate contribution overwhelmed the CYTOP thermal measurement. The results confirmed a higher thermal stability compared to FBGs in PMMA. In this section, we characterise the thermal response and measure the thermal sensitivity of a 'single-peak' FBG inscribed in a CYTOP multimode gradient index fibre. A single mode glass fibre (SMF28) was connected to the polymer sample using UV glue and the POFBG placed inside a climate chamber (Memmert HCP). The relative humidity of the chamber was set to 23%, and the temperature was linearly increased from 36 °C up to 60 °C for 80 minutes and snapshots of the spectrum were performed every minute. The temperature response of the FBG is shown in Fig. 20. Figure 20(a) with the blue line is the temperature of the climate chamber as measured by its temperature sensor and the black shows the CYTOP-FBG response. The sensitivity was found to be 17.62 pm/°C, which is approximately double the temperature response of the silica FBGs (10 pm/°C) [131]. Figure 20(b) shows the reflection spectrum of the grating for different temperatures. Comparing the spectra in Fig.20(b), we observe an amplitude decrease for increasing temperature; at 60 °C the grating almost disappears.

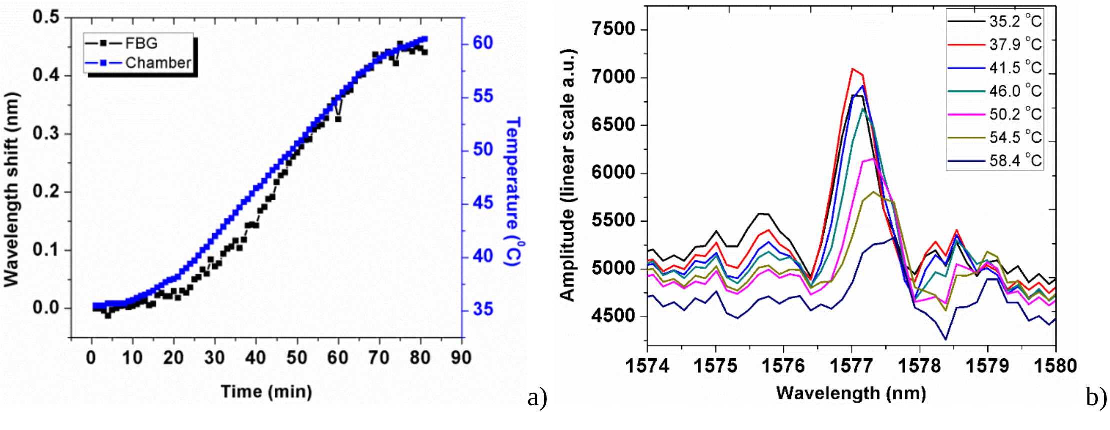

a) b)

Figure 20: Thermal response of the 'single-peak' FBG inscribed in a multimode gradient index CYTOP fibre using the *Pl-by-Pl* inscription method, a) The response of the grating as the temperature increases in the climate chamber, b) Selected spectra at different chamber temperatures.

4.5 Strain Response

The following expressions give the FBG strain response,

$$\frac{\Delta\lambda_B(\varepsilon)}{\lambda_B} = (1 - p_e)\varepsilon, \quad (4.2)$$

$$\varepsilon = \frac{\Delta L}{L_0}, \qquad (4.3)$$

where ε is the strain, p_e is the elasto-optic coefficient, L_0 is the initial length of the sample and ΔL is the difference between the initial and strained sample length.

In order to observe the strain sensitivity of the particular CYTOP gratings, the samples were fixed in two manual stages using epoxy glue, and the axial strain was applied in steps of 700 με up to 12600 με. Increasing the applied strain enhances the presence of side peaks (Fig.21(a)), as the grating now couples to higher order core modes. The strain response of the CYTOP fibre was measured to be ~1.43 pm/με at 1550 nm. It is important to note that the maximum measured wavelength shift was ~18 nm at ~1.33% strain, beyond which the grating signal was lost and return after the grating released.

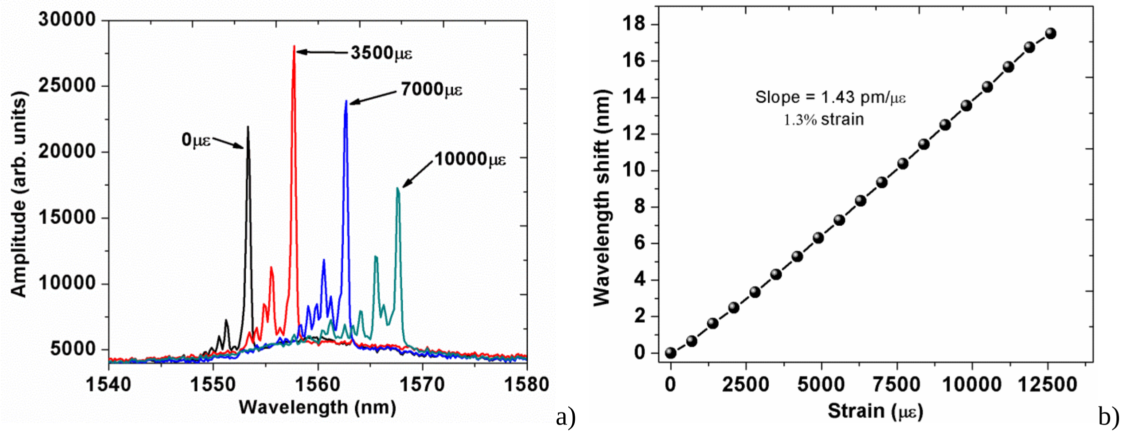

Figure 21: Reflection spectrum of the FBG inscribed in multimode gradient index CYTOP fibre with 300 planes, as measured by a commercial spectrometer and b) Wavelength shift of a CYTOP POFBG when elongated to 1.3% of its total length.

4.6 Hydrostatic Pressure

A slightly different approach was made in order to measure the hydrostatic response of the CYTOP POFBG (Fig 22(a).). The POFBG placed in a hydraulic system (MN151-001, Think-Lands; Fig. 22(b)), in which the hydrostatic pressure *P* can be controlled from 0.1 MPa (atmospheric pressure) to 0.5 MPa, and the reflection spectrum of the POFBG was measured as shown in Fig 22(a).

The FBG-reflected spectra were measured around the dip before and after the pressure *P* was abruptly (within 20 s) increased from 0.1 MPa (atmospheric) to 0.5 MPa, as shown in Fig. 23. Although the linewidth of the dip was slightly reduced, the Bragg wavelength shift was negligibly small. The pressure was subsequently maintained at 0.5 MPa, the Bragg wavelength shifted as time proceeded (Fig. 24(a)). Figure 24(b) shows the wavelength shift of the Bragg wavelength when remaining at 0.5 MPa for approximately 150 min. The Bragg wavelength increased with time and, approximately 150 min later became almost constant. The total Bragg wavelength shift was approximately 0.5 nm. The positive dependence of the Bragg wavelength on pressure was the same for other POF types [132], [133] but the wavelength shift having a time constant of over several tens of minutes was first observed in this measurement. Such a long time constant appears to be caused by the structure of the PFGI-POF, which is composed of two different polymer materials (CYTOP (core and cladding; pressure strength: 30 MPa) is known to be mechanically much weaker than polycarbonate (over-cladding; pressure strength: 86 MPa)). If consider that the Bragg wavelength dependence on pressure without considering the time constant (i.e., when the Bragg wavelength is measured at each pressure after waiting for a sufficiently long time for the signal to be constant) is linear, the dependence coefficient is estimated to be ~1.3 nm/MPa (corresponding to ~860×10^{-6}/MPa). This value is ~5.2 and ~13 times larger than those of the FBGs in an SM-PMMA-POF [132] and MM-mPOF [133], respectively.

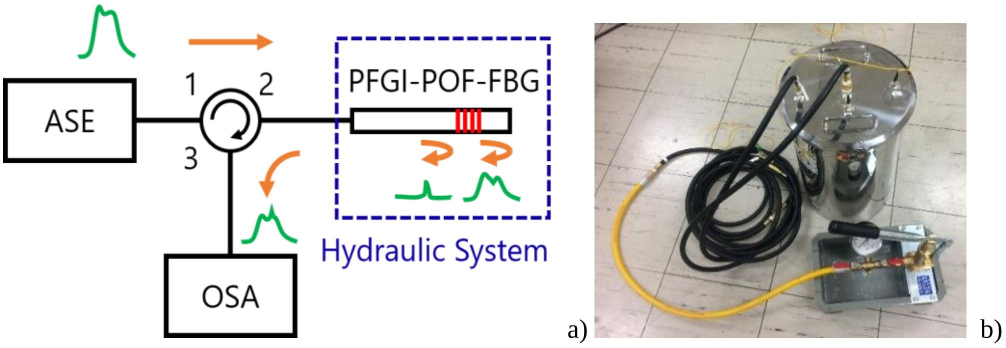

Figure 22: a) Schematic diagram of the experimental setup for measuring the hydrostatic pressure of a CYTOP POFBG in reflection and b) Hydraulic system MN151-001 by Think-Lands.

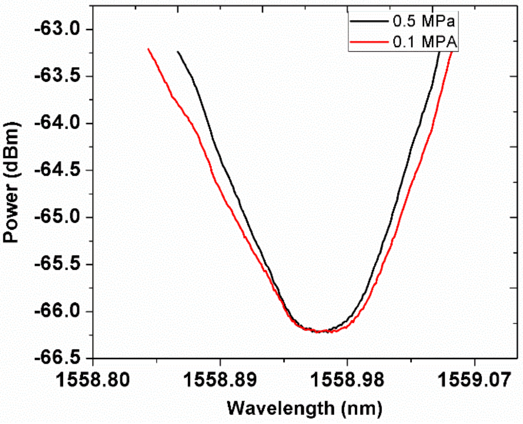

Figure 23: FBG-reflected spectra around the sharp dip measured at 0.1 MPa (red) and 0.5 MPa (black).

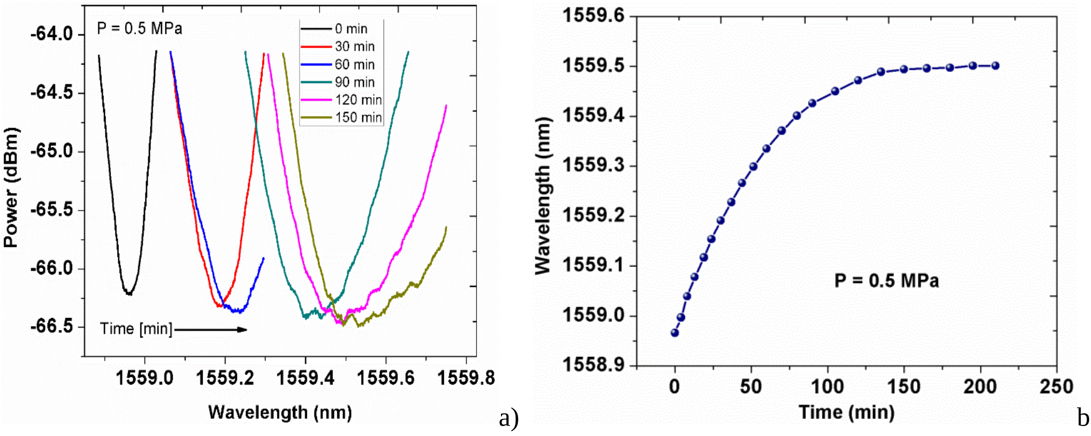

Figure 24: (a) Temporal dependence of the FBG-reflected spectrum at 0.5 MPa. (b) Temporal dependence of the Bragg wavelength at 0.5 MPa.

4.7 Humidity Response

One important parameter that must be taken into account when measuring different physical parameters with POFBGs is the contribution of the relative environmental humidity, which we characterise by placing the sample in a climate chamber to measure the response whilst keeping the temperature constant at 30 ^{o}C. We measured the response of the grating spectrum from 30% to 90% RH by programming the climate chamber to change the RH percentage for one hour and then stabilise at intervals 55, 75, and 95% for 5 hours to find the absorption time of the fibre. After 5 hours at 95%RH, the RH of the chamber was programmed to decrease for 1 hour at the same intervals and remain for 6 hours. The grating period changed as a result of swelling of the polyester and polycarbonate coating. The corresponding humidity sensitivity was measured to be ~37.6 pm/%RH as shown in the Fig. 25. From the results we observed that the absorption time was ~2 hours while the diffuse time was found to be ~3 hours.

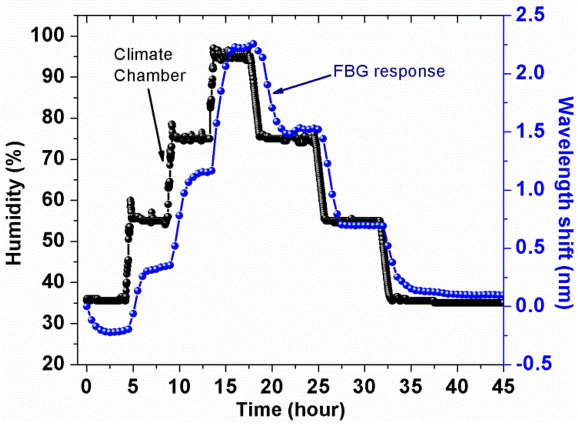

Figure 25: Humidity response of a POFBG inscribed in a CYTOP fibre with a 62.5 μm core diameter and 490 μm outer polyester and polycarbonate jacket.

4.8 Chirped Gratings

For the inscription of chirped FBGs (CFBGs), the 15 μm width planes were chosen to ensure a strong back-reflection, whilst also offering spectra similar to those with 5 μm width plane. The CFBG consisted of 2000 periods with a total length of ~4.5 mm. The grating period was increased in steps of 7.65 pm for each plane; this gives a period difference between the initial and final wavelength of $\Delta\Lambda$=0.0153 μm. The initial period was ~2.3 μm for a 4th order CFBG with a resonance wavelength centred at 1560 nm. The reflected spectrum of the resultant chirped grating is shown in Fig. 26(a). The full-width at half-maximum (FWHM) of the chirped grating is ~10 nm translated to ~2.22 nm/mm. Using an optical vector analyser (OVA CTe Luna Technologies) with wavelength resolution 1.25 pm and fast scanning rate (less than 1 second to analyse a range of a few tens of nm) we obtained the group delay (GD) curves as computed from the Jones matrix using the eigenanalysis [134], [135]. The GD of the chirped grating was measured to be ~40 ps, depicted in Fig. 26(b). In the transmitted amplitude spectrum, the transmission depth was found at ~4 dB (~60% reflectivity) while some ripples up to 30% of the maximum intensity were observed; this could be improved by increasing the period number whilst also making the CFBG stronger.

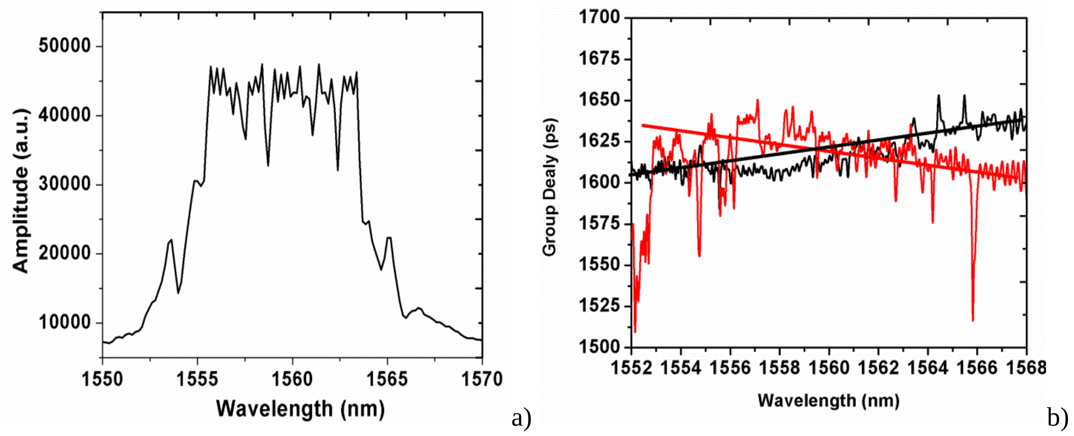

Figure 26: a) Chirped grating inscribed in a multimode CYTOP fibre measured using spectrometer (IBSEN I-MON 512) with ~169-pm optical resolution and b) Group-delay curves of chirped gratings in reflected spectra measured from both sides.

4.9 Fibre Fabry-Perot Cavities

The Fabry-Perot (FP) cavity was made by inscribing two identical 4th order FBGs with a grating length of ~660 μm and planes of width15 μm and the FBGs were physically separated with a cavity length of 3 mm. The FP cavity illuminated with a broadband light source (Thorlabs ASE730), and then through a circulator, the reflected amplitude spectrum was recorded with an optical spectrum analyser (Advantest Q8384) with a 10 pm optical resolution, as shown in Fig. 27, 28 and 29. The total cavity length is given by the summation of the gap between the FBGs and the effective length of the FBGs [136]. According to this, the Free Spectral Range (FSR) should be at ~245 pm for single mode fibres. From the reflection spectrum we found 230-240 pm, any small difference may be attributed to the higher order modes contribution that changes the value of the effective length of the FBGs and the resolution of the OSA whereas the finesse of the cavity is 4 indicating a reflectivity of 65% for each FBG (Fig. 28(b) inserts).

The strain sensitivity of FP cavity was experimentally measured by mounting the sample between two manual stages. We performed elongation steps of 629 με up to 5040 με, and the FP strain sensitivity was measured to be ~1.35 pm/με. The FP wavelength shift, during the application of axial strain is shown in Fig. 27(a) and selected strained cavity reflection spectra are shown in Fig. 27(b).

The FP was also placed in the climate chamber, and by keeping the humidity constant at 48%, we observed its response for temperatures between 40 and 60 °C with steps of 10 °C, as shown in Fig. 28(a). The temperature response was found to be 26.4 pm/°C. It is important to note that no FSR change was noted, as both FBGs respond in the same manner to both strain and temperature excursions and thus only detuning of the cavity wavelength and an intensity decrease is observed as the temperature is increased. Figure 28(b) presents the reflection spectrum of the cavity for 40, 50, and 60 °C.

Finally, by keeping the temperature of the chamber constant, we increase the relative humidity from 60% to 90% with steps of 10%. For each step, we keep the RH constant for 2 hours. The FP wavelength shift with respect to humidity is shown Fig. 29(a) while the reflection spectrum for 60% and 90% is shown in Fig. 29(b). The sensitivity of the cavity for the humidity was found to be 22.18 pm/%RH.

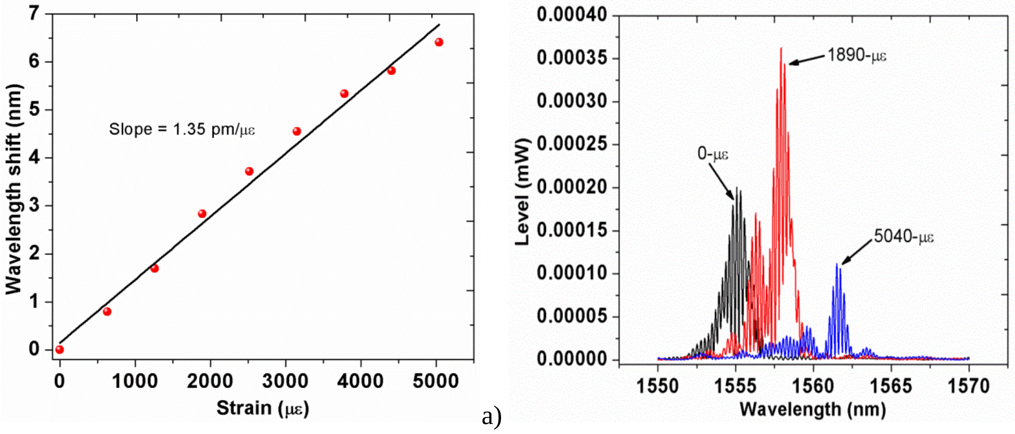

a) b)

Figure 27: Stain response of a Fabry-Perot cavity inscribed in a multimode gradient index CYTOP fibre, a) the wavelength shift of the cavity in respect to the axial strain, b) selected spectra for 0, 1890, and 5040 με axial strain.

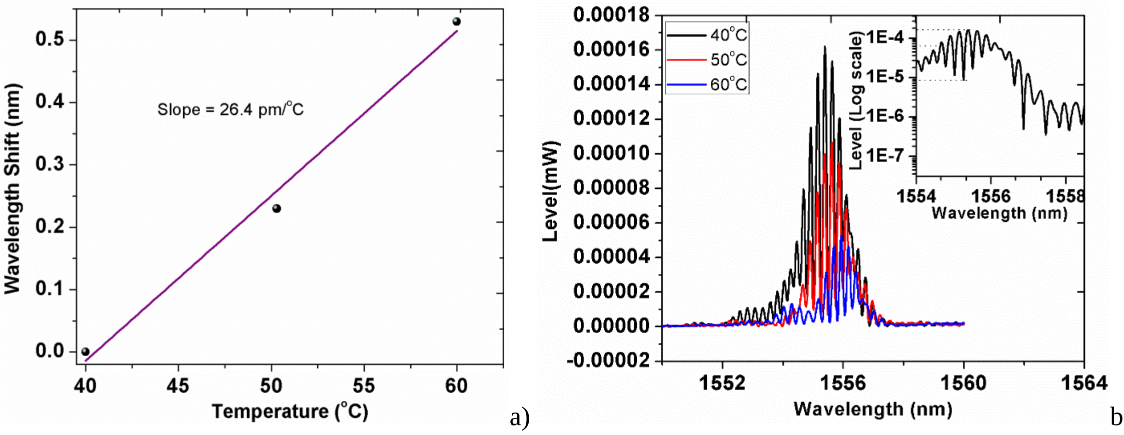

a) b)

Figure 28: Temperature response of a Fabry-Perot cavity inscribed in a multimode gradient index CYTOP fibre, a) the wavelength shift of the cavity in respect to the temperature, b) selected spectra for 40, 50, and 60 °C.

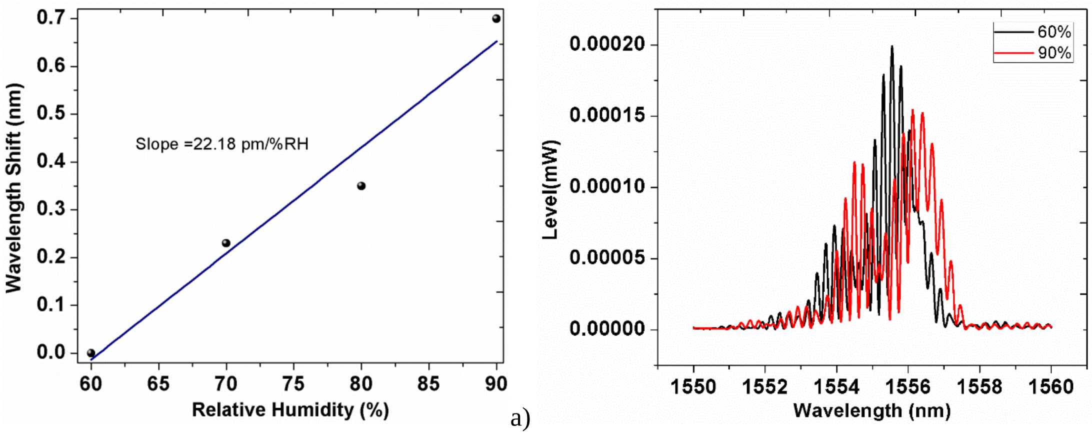

a) b)

Figure 29: Humidity response of a Fabry-Perot cavity inscribed in a multimode gradient index CYTOP fibre, a) the wavelength shift of the cavity in respect to the relative humidity changes, b) selected spectra for 60, and 90% relative humidity.

4.10 Conclussion

This chapter summarises research to inscribe usable 'single-peak' fibre Bragg grating in a multimode gradient index CYTOP POF to overcome the multiple peaks spectra and the mode-mixing issues. Using the plane-by-plane femtosecond laser inscription method we control the spatial parameters of the gratings to minimise the excitation of the higher order modes and as a result minimise the multiple peak reflection spectra. The 'single-peak' FBGs were characterised for strain, humidity, temperature, and pressure. The corresponding sensitivities were found to be 1.43 pm/με, 17.62 pm/^{o}C, 37.6 pm/%RH, and 1.3 nm/MPa for strain, temperature, humidity, and pressure, respectively. Regarding birefringence, the single peak gratings showed less than 70 pm wavelength for a polarisation angle range of 0 to 360 degrees.

Furthermore, developed FP, and chirped gratings for the first time in CYTOP and both structures were characterised in reflection. The FP was calibrated for strain, temperature, and humidity with sensitivities 1.35 pm/με, 26.4 pm/^{o}C, and 22.18 pm/%RH, respectively. The chirped grating has a 10-nm reflection spectrum with only 4.5 mm grating total length while its group delay was 40 ps.

This work has significance to both sensing and telecommunication applications, and the results are very promising as CYTOP polymer fibre offers advantages over other polymer fibres and it is the only certified POF for use in FTTH applications. This work paves the way for the practical realisation of polymer optical fibre sensors and their implementation in real-world applications.

5 Applications Using Multiple POFBG Arrays

This chapter presents the use of CYTOP POF sensors for several applications related to mechanical, and civil engineering and in the medical field. To date, POF applications with lengths exceeding several centimetres were not possible, due to the high material losses. The evolution of CYTOP POFBGs shows that a practical route to commercialisation exists, as we will in this section, where the POF length is no longer limiting factor the development of POF-based sensors.

Briefly, the first section relates to the direct mode shape capture of a free-free metal beam, when excited at its first resonance frequency, using a 6-m long multiple POFBG-array. The second section shows the possibility of detecting damage (location and degree) by measuring the vibration modes of carbon cantilever beam, when small weights are added at different positions to its surface. In both cases we focus on the recovery of time-dependent wavelength shifts of the POFBG-array.

The third and final section focusses on a medical application, for monitoring the foot health condition and gait pattern whilst walking, and this is especially relevant for the older citizens or sufferers of cerebral palsy. In this case the POFBG array is embedded in a shoe-sole, and we dynamically measure the response of the gratings to the human gait.

5.1 Mode Shape Capturing a Free-Free Metal Beam

The experimental results for measuring the mode shape of a vibrating free-free metal beam are presented. A 6-m long CYTOP POFBG array compared with that of a similar FBG array inscribed in glass fibre.

The particular work was published in IEEE Journal of Lightwave Technology and in IEEE Photonics Technology Letters and presented as oral presentation at the SPIE Photonics Europe conference in April 2016.

5.1.1 Introduction

The FBG array directly measured the vibration response of a freely suspended metal beam that was excited at the first resonance frequency. A freely suspended beam, or a free-free system, is fundamentally different from a cantilever, as it is a suspended structure with free-floating ends. The dynamics describe the body motion of the surface of numerous vehicles, such as space- and aircraft, and the hull motion of ships [137], [138]. Free-free surface vibrations lead to fluctuations that are uniform across the surface, in contrast to cantilevers. In the latter case, a point sensor mounted close to the fixed end would display greater sensitivity to lower frequencies, whereas the opposite would be true for sensors far from the fixing point [119], [120]. An analysis of the free-free motion will help clarify the behaviour of the beam under vibration.

5.1.2 *Motion Analysis of a Free-Free System*

The governing equation of motion of a free-free system is given by Newton's second law [139]–[141] :

$$M\ddot{x} + C\dot{x} + Kx = F(t), \qquad (5.1)$$

where F is the external force, and $M, C,$ and K are represent the mass, attenuation and the stiffness, respectively. For free vibration with no absorbing term (C=0) and (F(t)=0) the equation is:

$$M\ddot{x} + Kx = 0\,, \qquad (5.2)$$

The free vibration (with associated natural frequencies) is described as follows,

$$x(t) = \hat{x}e^{i\omega t}\,, \qquad (5.3)$$

Taking the second derivative

$$\ddot{x}(t) = \hat{x}(i\omega)^2 e^{i\omega t} = -\hat{x}\omega^2 e^{i\omega t}, \quad (5.4)$$

and substituting into Equation (5.2) we arrive at,

$$\left(-M\omega^2\hat{x}e^{i\omega t}\right) + \left(\hat{x}Ke^{i\omega t}\right) = 0, \quad (5.5)$$

$$\hat{x}e^{i\omega t}\left(K - \omega^2 M\right) = 0, \quad (5.6)$$

The above equation is valid for all *t*, and simplifies,

$$(K - \omega^2 M)\hat{x} = 0, \quad (5.7)$$

This is an eigenproblem with unknowns ω and $\hat{x}$, and has infinite solutions $(\omega_1, x_1), \ldots, (\omega_n, x_n)$. The values $\omega_1^2 \ldots, \omega_n^2$ are the eigenvalues, the $\omega_1, \ldots, \omega_n$ are the natural frequencies and $\widehat{x_1}, \ldots, \widehat{x_n}$ are the mode shapes or eigenvectors.

The eigenproblem solution is solved using linear algebra. Specifically, for the homogeneous linear algebraic equation system (Equation (5.3)), with unknowns $\widehat{x_1}, \ldots, \widehat{x_n}$, a non-zero solution it means that the determinant of the unknown coefficients should be zero,

$$det(K - \omega^2 M) = 0, \quad (5.8)$$

The above equation represents the characteristic equation to find the natural frequencies $\omega_1, \ldots, \omega_n$. To observe the mode shapes, we apply force to the bar, modifying Equation (5.2) as follows,

$$M\ddot{x} + Kx = F(t), \quad (5.9)$$

The harmonic force $F(t)$ applied to the bar is $F(t) = asin(\omega t)$.

5.1.3 *Mode Shape Computation Algorithm*

To recover the mode shape, the following procedure was followed. The beam is excited by a vibrational force given by $F(t) = Asin(\omega t)$ with constant frequency (ω) and peak force (A). The mode shape is recovered at the resonance frequencies of the beam, and the overall mode shape replicated along the length of the FBG array, as each grating acquires a maximum strain value that relates to its position relative to the nodes and antinodes on the bar. Each grating is modulated with respect to time displaying a sine waveform for which $\Delta\lambda_i(t)$ is given by,

$$\Delta\lambda_i(t) = \max\left(\left[\Delta\lambda_i(\varepsilon_i, t) - median\left(\Delta\lambda_i(\varepsilon_i, t)\right)\right]\right) sin(\omega t), \quad (5.10)$$

$$\lambda_i(t) = \begin{bmatrix} \lambda_1(0) + \max\left(\left[\Delta\lambda_1(\varepsilon_1, t) - median\left(\Delta\lambda_1(\varepsilon_1, t)\right)\right]\right) \sin(\omega t) \\ \vdots \\ \lambda_n(0) + \max\left(\left[\Delta\lambda_n(\varepsilon_n, t) - median\left(\Delta\lambda_n(\varepsilon_n, t)\right)\right]\right) \sin(\omega t) \end{bmatrix}, \quad (5.11)$$

where i=1,2,…n and depends on the number of the FBGs, $\Delta\lambda_i(\varepsilon, t)$ is the wavelength variation as given by equation (5.10) with respect to time, and $\lambda_i(0)$ is the resonance wavelength of each FBG when unperturbed. The median is preferred instead of the mean because is less sensitive to outliers. To extract the mode shape at the given resonance frequency one needs to normalize $\lambda_i(t)$ whilst substituting the variable t of the equations (5.10) and (5.11) to a constant value for all the wavelengths, $t = T/4$ is preferred; at that time we extract the maximum wavelength variation (T = period of vibration),

$$\bar{\lambda}_i(n) = \begin{bmatrix} \bar{\lambda}_1 \\ \vdots \\ \bar{\lambda}_N \end{bmatrix}, \quad (5.12)$$

where $\bar{\lambda}_i(n)$ is the discrete normalized value $\lambda_i(t)$ for constant time t. The mode shape, according to the surface displacement, is given by calculating the following sequence,

$$\bar{S}(n) = \sum_{i=1}^{N} \bar{\lambda}_{N-i}\, x(N-i), \quad (5.13)$$

where $x(n)$ gives the real mounting position of each point sensor on the metal beam.

$$x(n) = \begin{bmatrix} x(0) \\ \vdots \\ x(N-1) \end{bmatrix}, \quad (5.14)$$

where N is the maximum number of the FBGs in the array.

5.1.4 Experimental Setup

We inscribed an FBG array, consisting of 6 gratings separated physically by 8 cm and spectrally separated in the wavelength range from 1500-1600 nm, in a 6-metre length of multimode gradient index CYTOP fibre. The grating separation of 8 cm was selected for two reasons, firstly to match the experimental set up for the vibrating beam, and secondly as this distance matches or exceeds the maximum useable fibre length for PMMA POF operating at 1550 nm. Figure 30 shows the FBG reflection spectrum for the array used for this experiment as interrogated with the I-MON 512 (10 μs integrated capture time). The reflection of the six gratings were observed at 1529 nm, 1540 nm, 1548 nm, 1560 nm, 1571 nm, and 1580 nm with average full width at half maximum (FWHM) bandwidth of 1.39 nm.

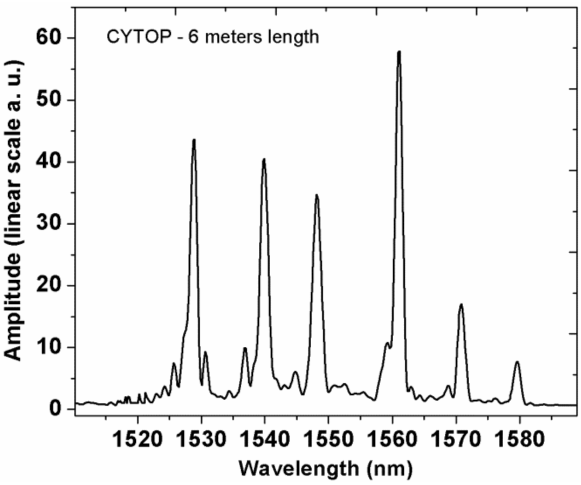

Figure 30: Reflection spectrum of the six-FBG array inscribed in multimode gradient index polymer CYTOP fibre.

The interrogation method used to measure the vibration response of the metal beam shown in Fig. 31, with the FBG array adhered to a steel beam (653 x 50 x 8 mm) using polyimide (Kapton) tape. A broadband light source with an integrated circulator (DL-BP1-1501A SLED) was used to illuminate the sensors that were monitored in reflection. A frequency generator was connected to an exciter through an amplifier, so that the resonance frequencies of the beam could be measured through the excitation of mechanical oscillations, and the polymer and silica fibre sensor arrays were compared at the first resonance frequency. The suspended beam was held with two thin-gauge nylon fibres to minimise any effects on the vibration characteristics of the beam. The exciter was placed at a point close to a node according to simulation results, thereby preventing distortions of the mode shape. At the point where the metal beam deforms downwards, the gratings undergo a wavelength blue shift (compression), whereas gratings undergoing deformation upwards show a redshift (expansion). These wavelength variations, and their associated displacements, lead to sinusoidal waveforms with respect to time for all vibration frequencies. Note that all the measurements performed from the "long side" of the fibre, where the distance between launch point and metal beam was ~6 m, showing the practicality of CYTOP POF.

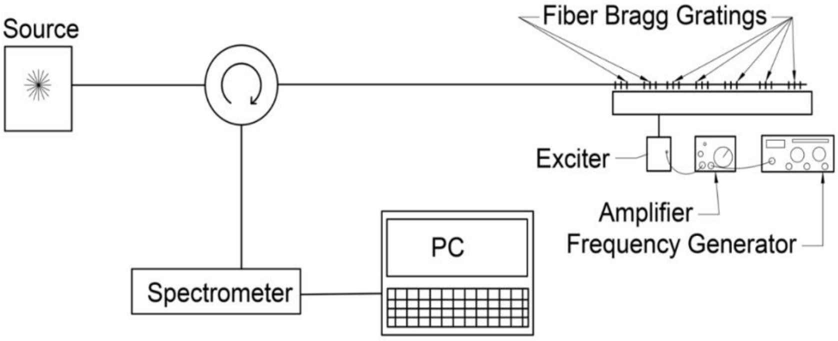

Figure 31: Experimental setup for the interrogation system.

According to the modal analysis based on the finite element analysis (FEA), the first resonance frequency of the beam was 96 Hz, and the corresponding mode shape at that frequency is shown in Fig. 32(a). We monitored the vibrating response of a single FBG sensor, which according to the FEA was far from a node, and as a result no vibrational frequency was missed. We applied the swept sine method to vary the drive frequency in the range of 80 to 120 Hz and extracted the frequency response of the beam; the first resonance frequency was measured to be 96 Hz, in excellent agreement with the FEA. This showed that the support method of the beam, and the addition of the sensor array, did not adversely impact the dynamic characteristics of the free-free beam (Fig. 32(b)). The sine wave peak force was kept constant for all measurements.

We repeated the vibration measurements keeping the force amplitude as before but this time using an FBG array written in a single mode silica fibre (SMF28). The reflection responses of the seven gratings were observed at 1541 nm, 1548 nm, 1556 nm, 1563 nm, 1568 nm, 1569 nm and 1582 nm, as shown in Fig. 33. The silica FBG array was adhered parallel to the polymer array and interrogated using the same scheme.

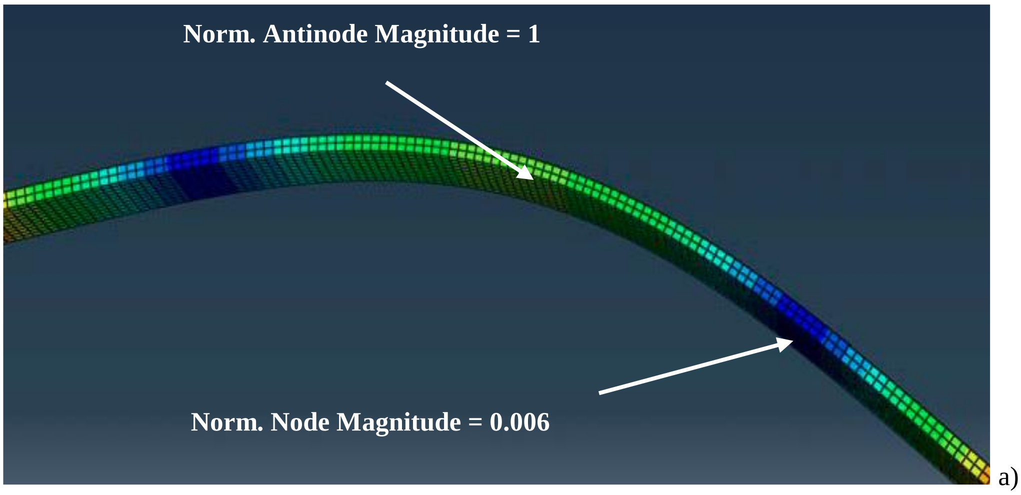

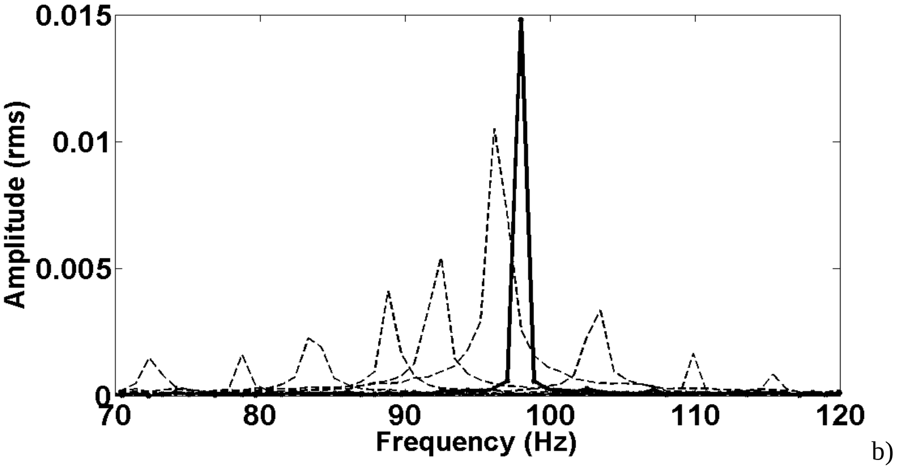

Figure 32: (a) The first mode shape of the metal beam as was taken from finite element analysis, with a calculated resonance frequency at ~96 Hz. (b) The frequency response of the beam using the polymer CYTOP fibre, showing the peak amplitude response with a frequency at 96 Hz for the first mode.

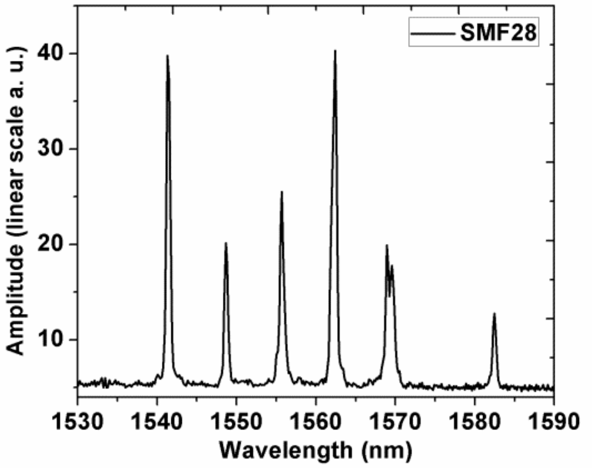

Figure 33: Reflection spectrum of the 7-FBG array in silica glass fibre.

The vibration response of the beam recovered for each FBG point sensor is shown in Figs 34 and 35 for both arrays. In Fig. 34 we observe selected time-dependent wavelength measurements for the POF (Fig. 34 (a, b)) and silica (Fig. 34 (c, d)) FBG arrays, respectively. In accordance with the mode shape shown in Fig. 33(a) the FBGs placed close to the centre of the beam (anti-node position), 1551 nm and 1568 nm in Fig. 34(a), displayed the largest amplitudes of ~60 pm and ~50 pm, respectively. In contrast the lowest wavelength shift, ~35 pm and 20 pm, was recovered for the FBGs 1542 nm and 1580 nm (Fig. 34(b)) that were located away from the anti-node and towards the nodes. On the other hand, the measurements using the silica array were at least a factor of 6 lower as shown in Fig. 34(c, d). In particular, at points towards to the nodes of the beam, where the fluctuations were significantly reduced, the silica array showed an inability to recover the vibration response of the beam, leading to measurements very close to the spectrometer noise floor. This resulted in reduced accuracy and noisy measurements, as shown in Fig. 34(d) and in the subplot of Fig. 35.

In Fig. 35 we observe the composite response, where the red line is the response of the polymer array and the blue line the response of silica. We clearly notice the bell shape of the first mode shape as we expect from the FEA results, and the improved response of the POF-based sensors. In Fig. 36 presented the mode shape of the beam for the particular resonance frequency as measured using the response of the polymer array and the equations described in section 5.1.3.

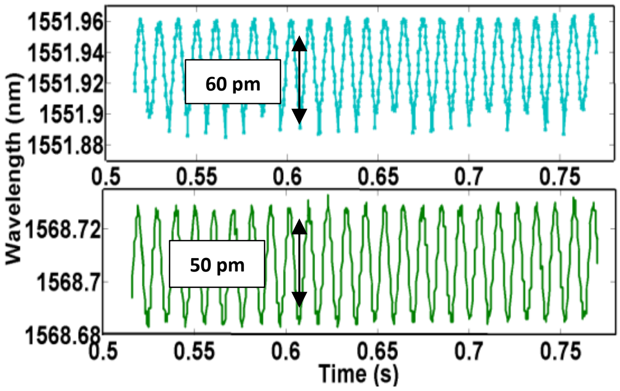

a)

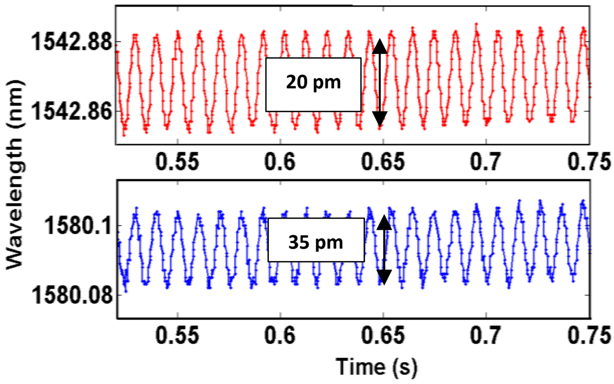

b)

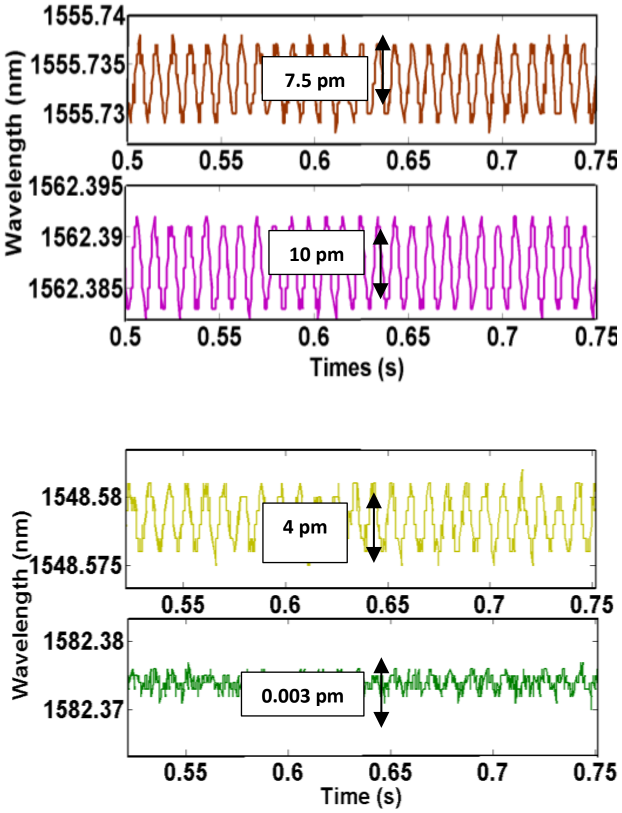

c)

d)

Figure 34: Wavelength versus time for FBGs located at the same physical point on the beam, a) and b) FBGs close to anti-nodes and nodes, respectively, for CYTOP POF, c) and d) FBGs close to anti-nodes and nodes, respectively, for the silica fibre array.

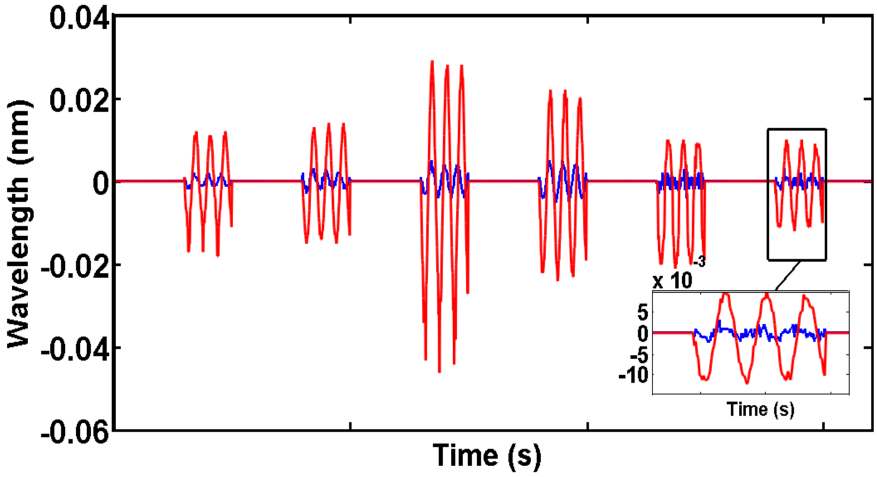

Figure 35: Comparative vibration snapshot of the time-depended wavelength response of the free-free metal beam excited at 96 Hz as measured using a CYTOP and a silica FBG array and plotted according to their position on the metal beam. The red line is the result of the CYTOP array and with the blue line are the results of the silica array.

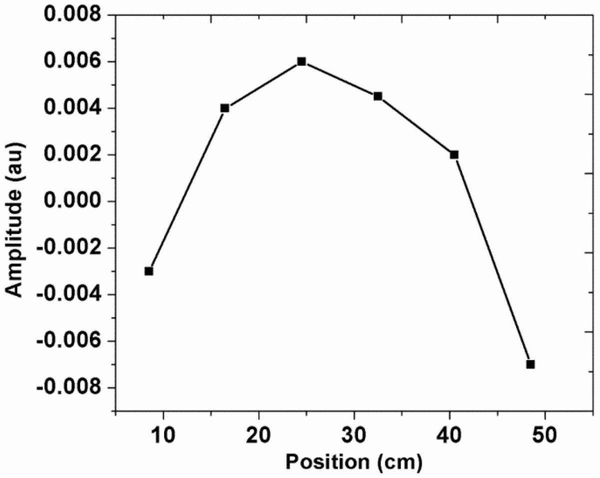

Figure 36: First mode shape of the free-free metal beam as recovered based on the response the CYTOP POF FBG array and the method described in section 5.1.3.

A CYTOP POF sensor array was successfully used to measure the vibration response of a free-free metal beam. The response of the polymer sensor array was compared with that of silica FBG sensor array and showed significant improvements in sensitivity; up to 6-times greater. This shows that POF can perform very well in comparison with silica fibres. This demonstrates the potential for realising practical FBG sensor arrays in multimode POFs. The approach presented in this section is exceptionally flexible, allowing for user selectable Bragg wavelengths, controlled grating strength, and spectral profile. It offers a new and practical way of sensing with CYTOP POF that has yet to be realised using other POF types.

5.2 Carbon Cantilever Beam Health Inspection

In this section a quasi-distributed sensor for cantilever health inspection measurements is used to recover the response of a carbon beam to study how the addition of masses at different positions on the beam that is the rear rotor of a helicopter. We simulate damage through the additional masses at different positions on the beam directly influencing the vibrational behaviour. The polymer-based fibre Bragg gratings, offer accurate and rapid detection of damage points on a structural beam.

This research was published in the IEEE Journal of Lightwave Technology and resulted in an oral presentation at the POF Conference (September 2016) at Birmingham (UK). Later developments were presented as a poster at the Optical Fibre Sensors (OFS-25) Conference (April 2017) at Jeju Island (South Korea).

5.2.1 Introduction

The use of composite materials is on the increase in several industries, principally for aviation, aerospace and marine applications. Carbon fibre composites are typically used where high strength and light weight are paramount. However, composite rotor blades are susceptible to the typical damage characteristics of any composite material such as delamination effects, matrix cracking, and fibre breakage. This has an impact on various properties of the composite rotor blade, affecting the rigidity, degree of deflection and frequency of vibration. Considering this requirement we studied the behaviour of a helicopter rear rotor blade, an essential stabilising component for helicopter flight. In addition to rotating, the tail rotor blades also change pitch angle; counteracting airframe torque with anti-torque tail rotor thrust. The tail rotor can fail if the rotor stops turning or the pitch change mechanism stops functioning. It is vital to inspect the health condition of key components such as air-blades, before, after, and during the flight, as failure occurs on a short time scale. Current inspection and monitoring methods for hollow aluminium air blades [142]–[145], are unsuitable for use with carbon fibre composites. There are no proven methods to reasonably estimate and monitor the rotor health condition when the helicopter is flying. The potential of fibre optic sensors for this type of application is clear, given their small volume, light weight, and immunity to electromagnetic interference, and having no significant influence on the structure under test. Similar health monitoring inspection can be applied to applications such as spacecraft, wind turbines, and civil structures [146]–[148]. We utilized a custom POFBG sensor array to study the behaviour and structural health of the carbon cantilever, by monitoring the wavelength response with respect to the time. In order to mimic signs of rotor damage we attached small weights to different locations on the cantilever beam, from which the dynamic mode shapes of the beam were extracted. Furthermore, we adjusted the degree of 'damage' by using different masses and distinguished between them using the time-dependent wavelength response of the gratings [149]–[151]. Our goal here was to observe the deviation from the normal response, e.g. the degree of deflection.

5.2.2 Experimental Setup

The FBG array consisted of 4 gratings that were physically separated by 8 cm and the fibre sample had a total length of 2 m. The FBGs were spectrally separated with small variations in their periods and hence operating wavelengths of 1548 nm, 1561 nm, 1570 nm, and 1580 nm, and the optimised illumination of the grating array is shown in Fig. 37. The carbon fibre blade from the rear rotor of a helicopter, of dimensions 36 cm x 6 cm, was fixed to the edge of an optical table, with the FBG array mounted along the beam length, (Fig. 38). During the experiment, the beam was gently pushed down and released to excite the first vibration mode of the structure. The demodulator (Ibsen IMON 512HS) captured data at frequencies up to 35 kHz for an integration time of 10 μs; the time response is shown in Fig. 39. We observe that the grating located at the fixed base of the beam (position 1, Fig 39(a)) shows no measurable fluctuation, as expected, whereas amplitude excursions increase as we move to the end of the beam (position 2–4, Fig 39(b–d), respectively), and measure the FBG wavelength shifts according to their physical position, extracting the vibrational beam shape directly.

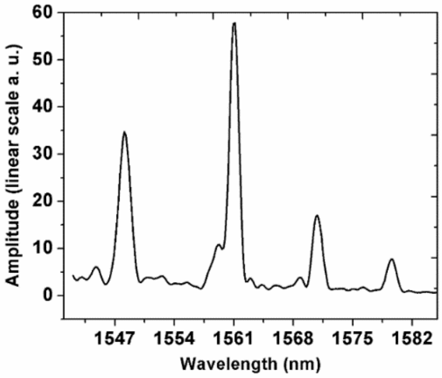

Figure 37: Reflection spectrum of a multiple-FBG array recovered using a commercial FBG demodulator spectrometer.

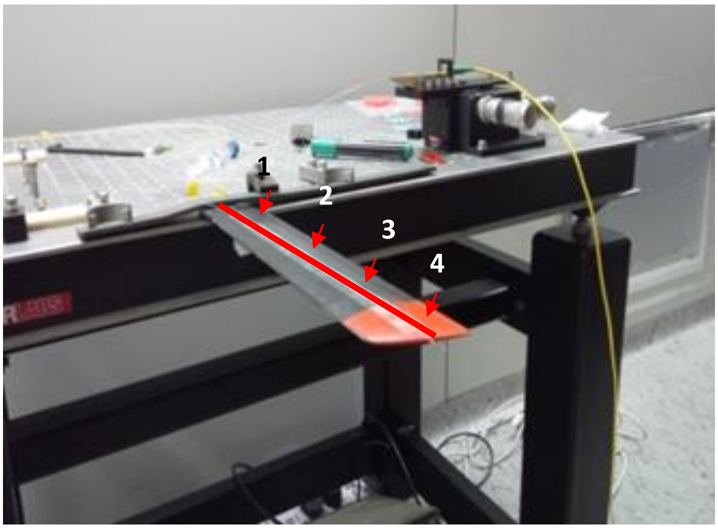

Figure 38: Experimental setup for the cantilever health monitoring system. A multiple FBG sensor array was mounted on a helicopter rear rotor blade. The physical location of the FBGs on the beam is indicated with the numbers 1-4.

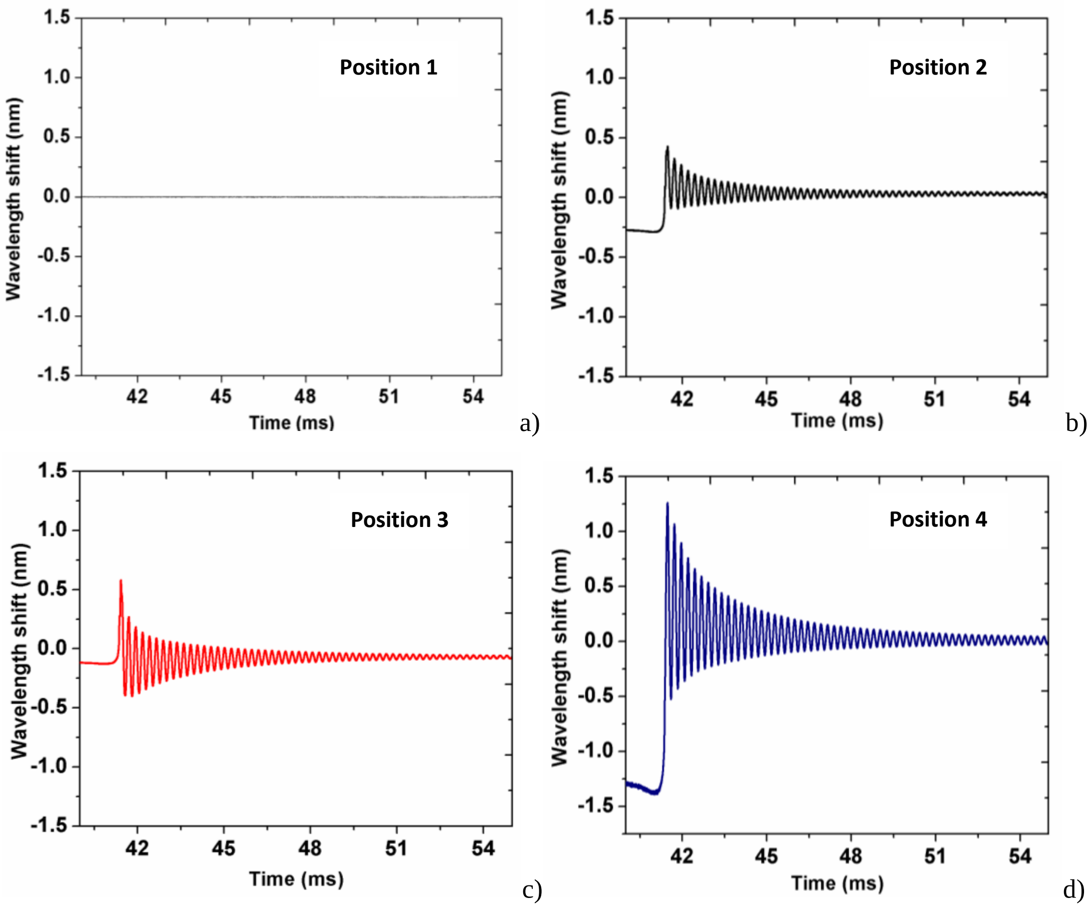

Figure 39: Wavelength response of the polymer FBGs with respect to time for gratings located according to Fig.38, (a) at the base of the beam position 1, (b) position 2, (c) position 3, (d) position 4.

5.2.3 *Results*

We added weights along the length of the beam, close to the FBGs position, to mimic "damage", and compared their respective vibrational displacements with and without the additional masses; all measurements were repeated four times. The normalised vibrational shapes are shown in Fig. 40(a-e) for different time intervals while the reference vibrational shape shown in Fig. 40(a) with no weight added to the beam. The minimum fluctuation was noted when weights were added to position 1 (Fig. 40(b)) and the maximum when weights were added to position 4 (Fig. 40(e)). Comparing Fig. 40(a-e) we observe that significant information regarding the damage position is given by the last point of the vibrational shape, which corresponds to the position of the 4th FBG; in this particular case the maximum sensitivity is at the edge of the beam. It is well known that as damage increases the resonance frequencies of the beam are shifted and this leads to a change in the beam's vibration response; now the contribution of the other FBGs becomes important in identifying the damage position [152], [153]. For example, in our case the FBG in position 2 experiences compression when that in position 4 experiences expansion.

Another important factor for the health condition during the inspection procedure of the beams is the level of damage. For this reason, we attempted to ascertain the level of "damage", repeating our measurements using different masses of, 0 g, 17 g, and 34 g. The weights were fixed securely to position 2 of the beam and we tracked the grating peak that was closest to that point (operating at 1561 nm). From the time-dependent wavelength results shown in Fig. 41(a-c) for the three weights, we observe a gradual shift off the fluctuation normal. The maximum peak-to-peak fluctuation for the first measured period corresponded to a wavelength shift of 1 nm for 0 g, ~0.4 nm for 17 g and ~0.15 nm for 34 g. In Fig. 42 we observe the declining peak-to-peak fluctuation of the POF-FBG when the mass of the weight is increased. It is important to note that, all the measurements refer to the use of the same FBG, with the weights added to exactly the same position in each case. We consider that useful outcomes were extracted regarding the prediction of health condition of the beam. The position of the damage could be detected by the fluctuation of mode shape, whereas the level of the damage could be defined by the maximum peak-to-peak response of the FBG. Clearly a careful calibration is required for each device under test, however, it is often most important to discern that the response of the component has changed from its original behaviour, to be replaced accordingly prior to component failure.

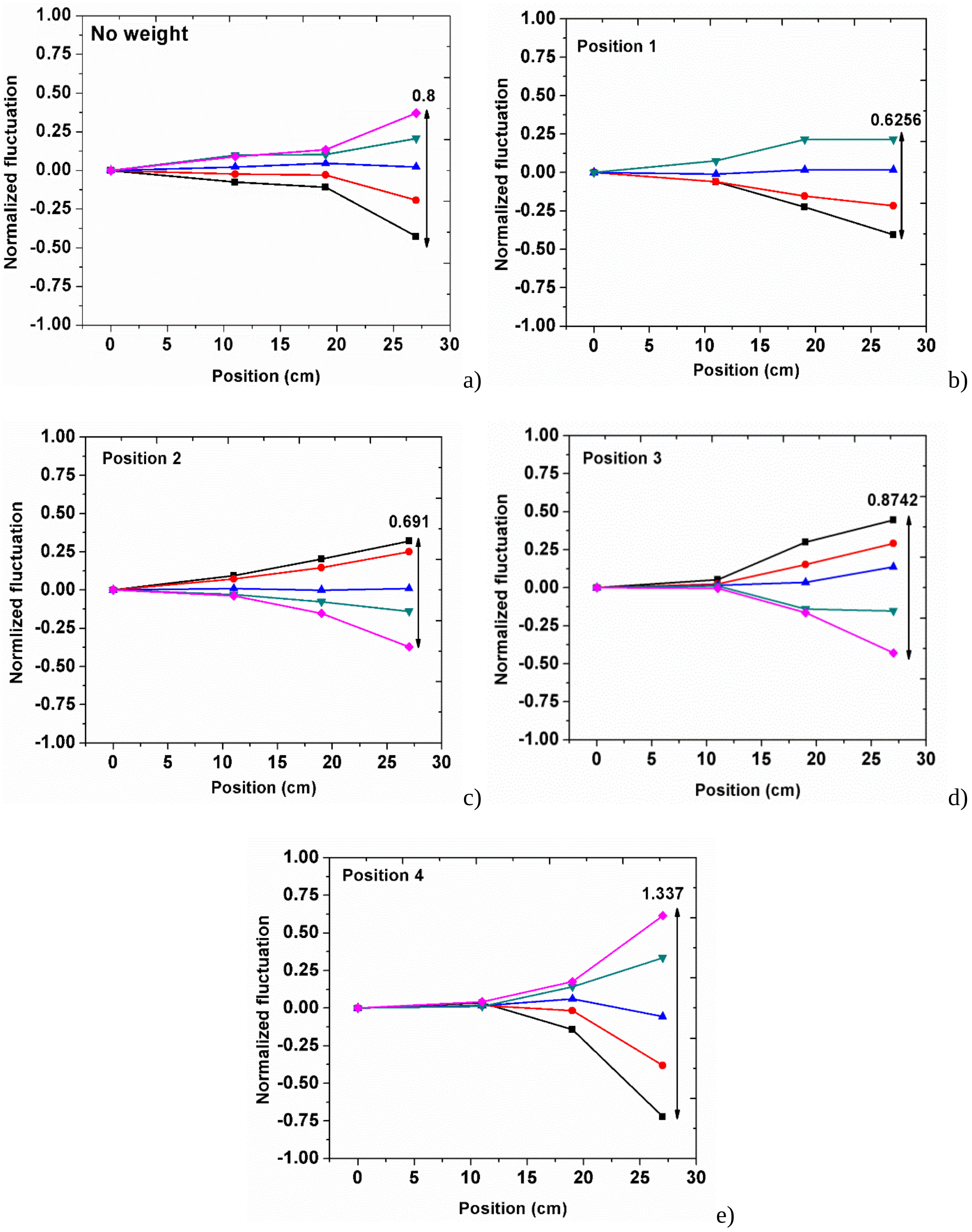

Figure 40: Response of the cantilever with the addition of weights to the beam for (a) No added weight, (b) weight at position 1, (c) at position 2, (d) at position 3, (e) at position 4.

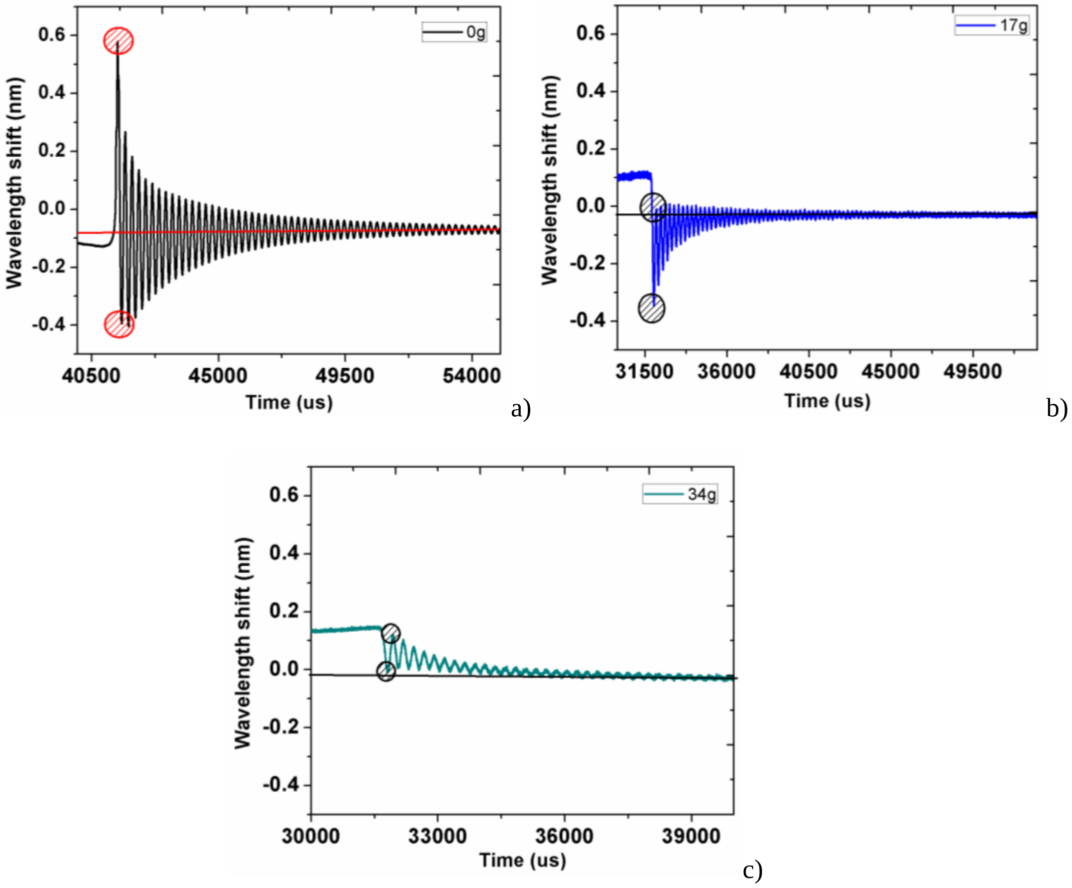

a)

b)

c)

Figure 41: Time-dependent FBG wavelength response for (a) no mass, (b) 17-g mass, and (c) 34-g mass added on the beam at location 2 for the grating operating at 1561 nm.

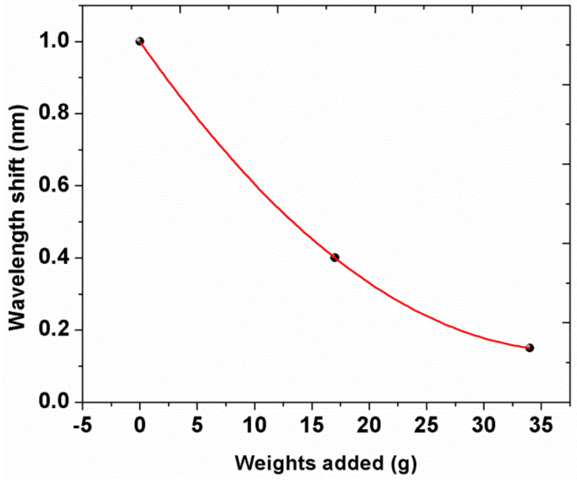

Figure 42: The peak-to-peak fluctuation of the FBG time-dependent response, as the mass of the weights increasing.

5.2.4 Conclusion

The vibrational profile of the structure and the influence of the position of the damage site was extracted by adding small weights to the beam. The results showed higher fluctuation when the weights placed close to the base of the cantilever, and the lower variation when placed close to the edge of the beam compared with the response obtained with no additional weights. Moreover, with different masses we adjusted the “damage” to the beam and we observed the correlation between the magnitude of the fluctuation and the added mass. The proposed method has the potential be employed for real-time monitoring during flight. However, the goal was to show that low-loss CYTOP POFBGs are feasible for such applications and not to present a refined health monitoring method as the current technology is new and will require further refinement to ensure the long-term accuracy and robustness of the method.

Finally, we consider that the gradual development of perfluorinated low-loss POFs combined with FBG technology offers a realistic solution for the use of polymers fibres in real-world industrial applications.

5.3 Insole Measurements for Plantar Pressure Monitoring

In this section, we propose a fibre-optic sensors system based POFBGs to measure foot plantar pressure. The plantar pressure signals are detected by five FBGs, in the same piece of cyclic transparent optical polymer (CYTOP) fibre, which are embedded in a cork insole for the dynamic monitoring of gait. The results using the POF showed a very good response when compared with solutions using silica optical fibres, resulting in sensitivity almost twice as high, with excellent repeatability and ease of handling. The high fracture toughness of POF enables its application in monitoring patients with higher body mass compared to similar systems based on silica fibre. POFs can withstand lower curvature radius (5 mm) than silica fibres (10 mm) and provide the necessary resistance to the system during the gait movement, in order to avoid damage or breakage, as can easily happen using silica optical fibre.

This work was published in MDPI Sensors Journal and presented as an oral presentation at the Biodevices Conference, January 2018 (Portugal). The work was accomplished in collaboration with the Dr. Carlos Marques and his research group in Aveiro (Portugal).

5.3.1 Introduction

Their flexibility and non-brittle characteristics make POF sensors clinically acceptable [154], and numerous applications of POF sensors related to human safety have been proposed [155]. Moreover, applications that point towards the detection of motion impairment experienced an aging population are increasingly important, as they lead to increased health risks; there is a need for the close monitoring of elder citizens and patients. Although the field of e-Health has shown progress, it still faces challenges, which are generally related to the mobility compromise and lifestyle of the monitored patients. In order to overcome these challenges, mobile health monitoring devices need to provide low power consumption, size, and weight. Furthermore, high safety and privacy are also desirable. Therefore, the development of efficient solutions for healthcare sensor applications (regarding size, weight and energy consumption) is an important research focus given the rapid technological advances in healthcare monitoring equipment, microfabrication processes and wireless communication [156].

We have identified that of the key parameters monitored by researchers for biomedical applications is foot plantar pressure [156], [157]. This parameter is an important indicator of the foot health condition and the gait pattern. Information regarding the condition of the spinal cord or regarding the evolution of foot ulcerations (in case of patients with diabetes) can be inferred from the plantar pressure distribution map. In the particular case of diabetes, the patients tend to develop foot ulcerations, which can be detected by high/abnormal forefoot plantar pressure [158]. Hence, accurate and controlled evaluation of the plantar pressure is vital to reduce and eventually avoid the risk of such pathologies. Additionally, by mapping the ground reaction forces or pressures during gait it is possible to understand the effect induced in the body [156]; gait analysis is a systematic examination of body locomotion that can be used in the evaluation of pre-treatment, for surgical decisions and post-operative assessment of patients [156]. The human gait is defined as the period of initial contact of the foot with the ground and lasts until the same foot touches the ground again [159]. A gait cycle is generally divided into two main phases: the stance and swing phases. The stance phase represents approximately 62% of the gait cycle for a person without gait abnormalities and is related to the period that the foot is in contact with the ground [160]. The stance phase starts with the initial contact (IC), at which point the foot touches the ground, followed by the maximum weight acceptance (MA), when the weight of the subject is on the heel region. Following this there is a rotation of the foot with the ankle as a pivot, and when the whole foot is in contact with the ground, the flat foot (FF) phase is reached. As the rotation continues, the heel loses contact with the ground, corresponding to the heel off (HO) phase. Finally, at the instant that the toe is off the ground, the toe off (TO) phase takes place and the swing phase starts [160].

Conventional technologies for plantar pressure assessment are mainly based on electronic or imaging devices. Several of the smart insole implementations, based on piezoresistive sensors and wireless data communication modules, for walking gait rehabilitation monitoring, have been reported [161], [162], offering high resolution data acquisition, robust and wireless communication, real time processing, and low power consumption [161]. Similar features are anticipated for FBG sensors, although drawbacks, including fragility, long-term instability, inconsistency and excessive drift are problematic [163]. Additionally, their output is restricted to a small sensing area requiring the use of more sensors to monitor larger areas [163].

In order to overcome the limitations of conventional technologies, many scientific papers have been published reporting plantar pressure distribution monitoring techniques, and even though optical fibre sensing technology had already been used to monitor static plantar pressure values [164]–[166], the application of FBGs is rarely addressed [156], [163]. To date, there is only a single report on the dynamic, continuous measurements during gait motion and that was based on silica optical fibre technology [167].

5.3.2 POFBG Array Characterisation when Embedded into the Cork-Insole

The key areas of the foot for plantar pressure monitoring are presented in Fig. 43(a), namely heel, midfoot, metatarsal and toe areas [156], [157], [168]. Five POFBGs sensors are distributed within these areas, embedded in the cork insole with 10 mm thickness. Although cork can display characteristics of plastic behaviour following long periods of use, it has several advantages such as thermal isolation, malleability and low Poison ratio (near zero) [169]. The latter prevents the crosstalk between sensors, since the insole will isolate the five pressure sensing points. Furthermore, the low Poisson ratio can diminish the effects of shear stress during the gait on the plantar pressure assessment. The malleability property of the cork enables its application in different types of shoes and the thermal isolation reduces the influence of the body temperature on the sensors response when compared to a gait cycle that generally takes about 1 second to occur [167]. Considering the load pressure applied in the gait movement, the POFBGs were encapsulated in epoxy resin (Liquid Lens^{TM}) cylindrical structures (1 cm diameter and 0.5 cm height). Each sensing element consists of a cylindrical epoxy structure with the POFBG at the middle. The epoxy structure is mainly under axial strain when force is applied and strain is transmitted to the embedded-FBG leading to a wavelength shift proportional to the applied force. To compensate for any temperature change, an FBG temperature sensor [155] was incorporated in the insole, so that the thermal isolation provided by the cork is ensured, minimising body temperature effects or external temperature changes. Figure 43(b) shows a diagram of each sensor position on the cork insole. Figs. 43(c) and (d) show a photograph of the POFBGs array embedded in the cork insole and a zoom of a POFBG in its sensing position.

The POFBG sensors were inscribed as shown in Fig. 35(a) and spectrally separated in the range 1535 nm to 1580 nm. The reflection spectrum of the POFBG array following fs inscription is shown in Fig. 35(b). The spectral full width at half maximum for each grating is between 0.6 and 1.0 nm.

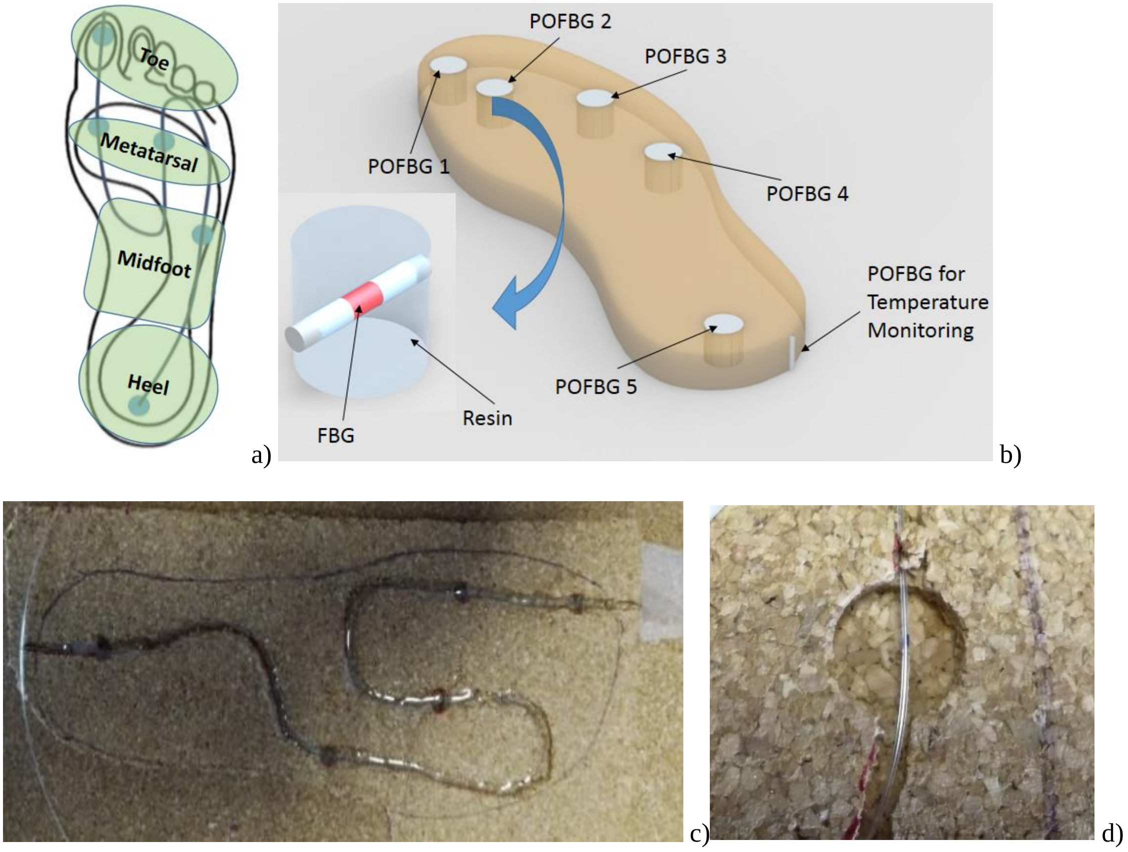

Figure 43: Schematic representation of: (a) foot plantar area designation and sensing points distribution and (b) POFBG-embedded cork insole. (c) Photograph of the POFBGs array embedded in the cork insole. (d) A zoom-in image of one sensing element.

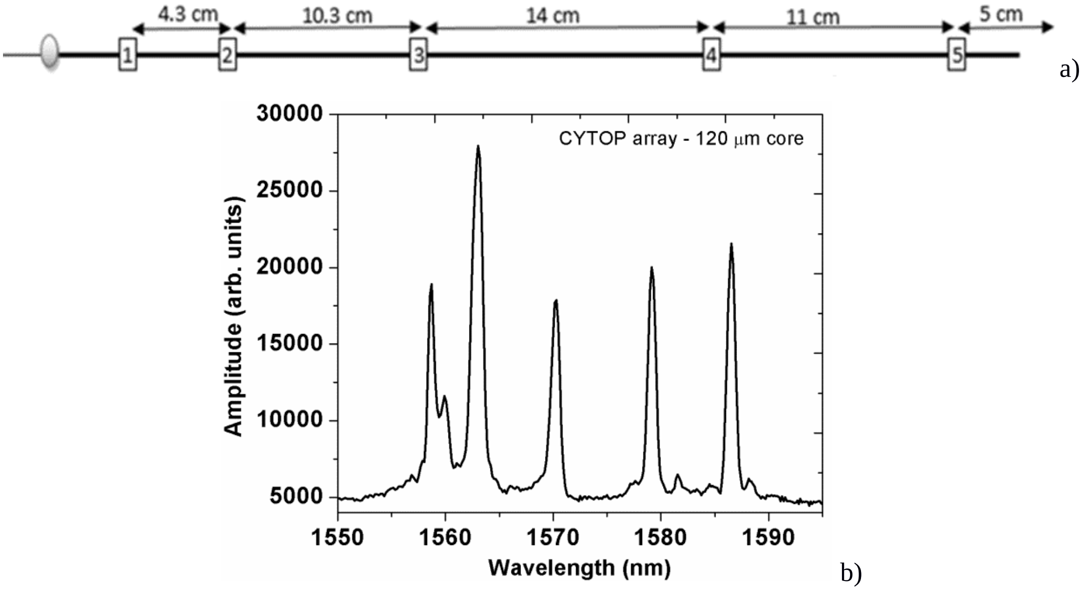

Figure 44: (a) Schematic demonstration of the physical distances between FBGs in the CYTOP fibre. (b) Reflected optical spectrum of the five-FBG array inscribed in 120 μm core diameter, multimode, gradient index CYTOP fibre.

For calibration and plantar pressure monitoring, the POFBG-array was interrogated in reflection using a fixed platform monitoring system as shown in Fig. 45(a). To guarantee a stable fibre connection and monitoring of the POFBG array, the polymer fibre was UV-glued with a silica multimode gradient index fibre for easier coupling and then spliced to a silica single mode fibre to be compatible with our interrogation system. The array of 5 FBG sensing elements were calibrated to different pressure loads ranging from 10 to 1500 kPa with 100 kPa steps as shown in Fig. 45(b). The load sets were applied independently in each sensing point (from POFBG 1 to POFBG 5), using a probe with a diameter of 10 mm. During each load set, the FBG wavelength shift was acquired and compared with the ratio between the applied force of the testing machine and the cross-sectional area of the epoxy resin cylinder. Table 2 summarizes the pressure and temperature sensitivity coefficients for all POFBGs of the array after embedding in the cork-insole and the RMSE of the POFBGs is compared with the load cell of the force platform.

A comparison with the silica FBG-based insole [167] indicates that the proposed POFBG insole presents higher sensitivity, whereas the RMSE for each grating is found to be less than 4% over four circles.

Table 2: Pressure and temperature sensitivities obtained for the 5 POFBGs.

FBG	Pressure Sensitivity (pm/kPa)	Temperature Sensitivity (pm/°C)	RMSE (kPa)
1	8.31±0.20	18.4±0.42	36.59
2	7.99±0.28	18.2±0.47	54.47
3	8.51±0.23	18.9±0.41	42.76
4	7.71±0.31	18.5±0.49	62.81
5	8.20±0.15	18.1±0.45	29.22

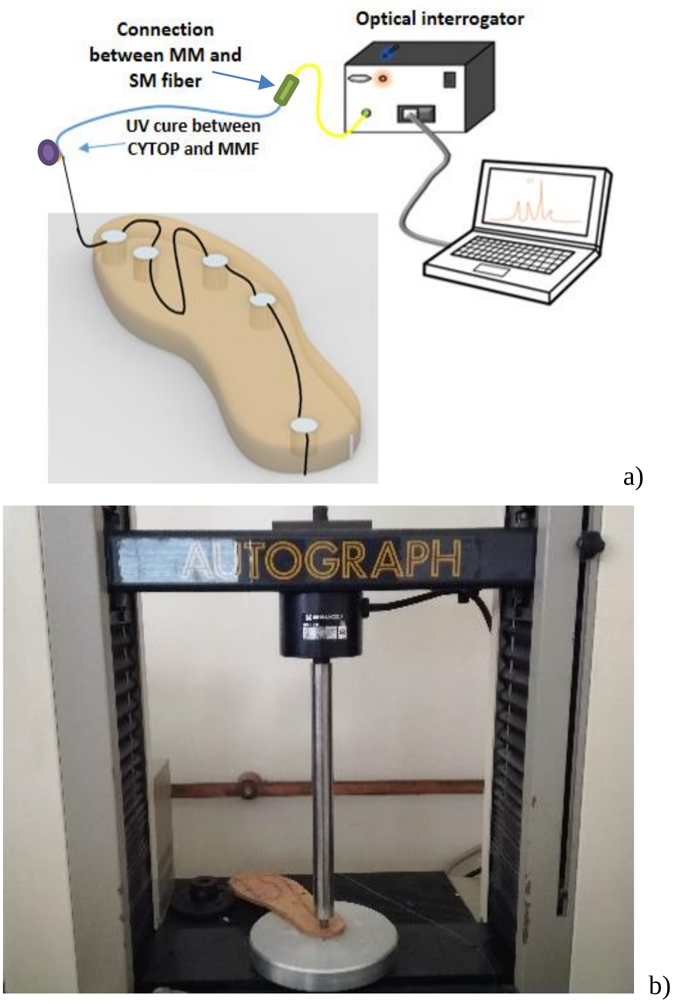

Figure 45: a) Schematic representation of the monitoring system. b) Photograph of the pressure testing platform with the cork insole.

5.3.3 *Force Platform of the Insole POFBG Plantar Pressure Sensor Network*

The pressure induced in the sensing elements during a normal gait movement was analysed with the cork insole fixed on the ground, as showed in Fig. 46(a), and four gait cycles was recorded for each sensor. The feedback of the platform to the displacement of the body centre of mass (BCM) was evaluated using a 55-kg a female subject.

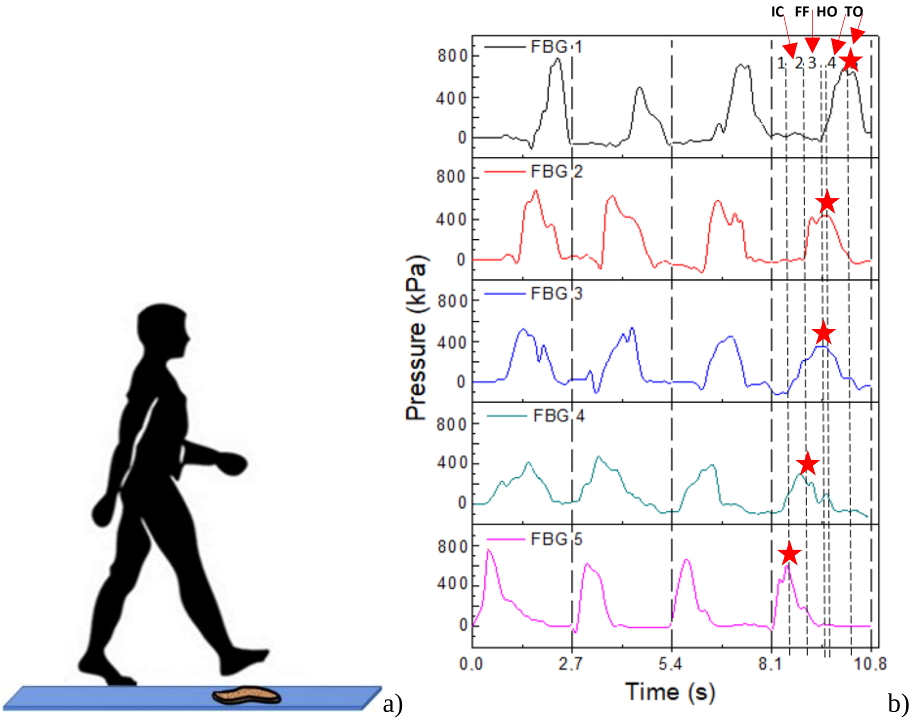

Figure 46: (a) Schematic diagram of the protocol implemented for the gait analysis using the fixed platform. (b) Pressure obtained during the four steps for the 5 POFBGs, where the periods of stance phase (short dashed lines and star symbols) can be observed. IC: initial contact; FF: flat foot; HO: heel off and TO: toe off.

In Fig. 46(b), it is possible to verify that the sensing network response is similar for the four passages, suggesting that the human motion limits the repeatability of the sensors' response. Furthermore, it is possible to confirm the activation time for each sensor, which is related to the stance phase of the gait cycle. POFBG 5, located at the heel region, shows a pressure increase at the start of the cycle (IC phase), and POFBG 4, 3, 2 and 1 are sequentially activated as the TO phase approaches. The dashed lines of the last cycle presented in Fig. 46(b) represent the activation of each POFBG. The slight differences of each POFBG sensor for each passage are directly related to the differences of foot positioning on the platform during the tests.

The second static test correspond to the body centre of mass displacements both in the body frontal plane, by moving it forward and backwards, and in the sagittal plane, with the subject moving the torso from the left to the right and vice-versa. For that purpose, the subject stand on the sensing platform, with one foot on the sensing area and the other levelled in the same horizontal plane, to execute a series of BCM movements (with about 3 seconds duration each). Fig. 47 presents the protocol for the BCM displacement tests. The test starts with the subject standing still at the centre position (C), the next step is moving the BCM to the front on the frontal plane to achieve the anterior (A) position, then back to the centre (C) and then moves to the posterior (P) position. The movement on the frontal plane finishes at the centre (C). The sagittal displacement is executed with the same procedure, however in this case, the BCM is moved to the left (L) and right (R), instead of to the anterior (A) and posterior (P) positions.

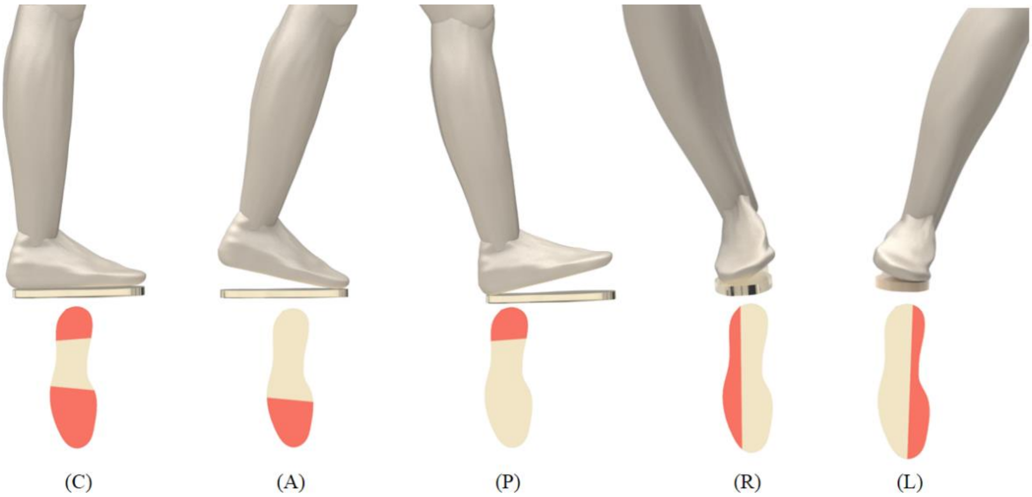

Figure 47: a) Schematic diagram of the protocol implemented for the analysis of the BCM displacement and descriptive pressure increasing on the platform (the subject remained in each position for 3 seconds - the areas with increased pressure are coloured in red).

During the protocol implementation, the Bragg wavelength shift induced in the sensing network was acquired and the correspondent pressures were calculated. Figure 48 presents the response of each sensor, during the different moments of the performed tests.

For the tests on the frontal plane, an increase of the pressures registered by the sensors positioned in the metatarsal and toe areas is evident in the anterior movement, while the sensor placed in the heel section indicates a decrease of the pressure. On the other hand, during the posterior displacement of the BCM, the pressure at heel area is more accentuated, while the pressure values at the toe and metatarsal areas decrease. Regarding the centred position of BCM (C), the areas that are most often actuated in the platform are the metatarsal and midfoot areas, indicating that those zones experience greater ground pressure when sustaining the subject’s body weight whilst standing. It should be also noted that there was a small increase of pressure on the toe and heel regions. During the frontal tests, the behaviour of the 5 POFBGs sensors are as anticipated, since the anterior and the posterior movements activate the heel and toe areas, represented by POFBGs 5 and 1, respectively. However, for body balance reasons, it is not possible to activate only the heel and toe regions, and therefore the sensors on the metatarsal and midfoot regions are also activated, namely POFBGs 2, 3 and 4, especially on the anterior movement, where the subject presents more difficulty to maintain her balance during the 3 seconds of the test. Furthermore, the sensors of the metatarsal and midfoot regions are more distant to the sensor on the heel region when compared to the distance of these sensors to the one at the toe region. For this reason, there is a higher isolation of the posterior movement, which explains the lack of increase on the pressure by POFBGs 2, 3 and 4 when the posterior position is taken.

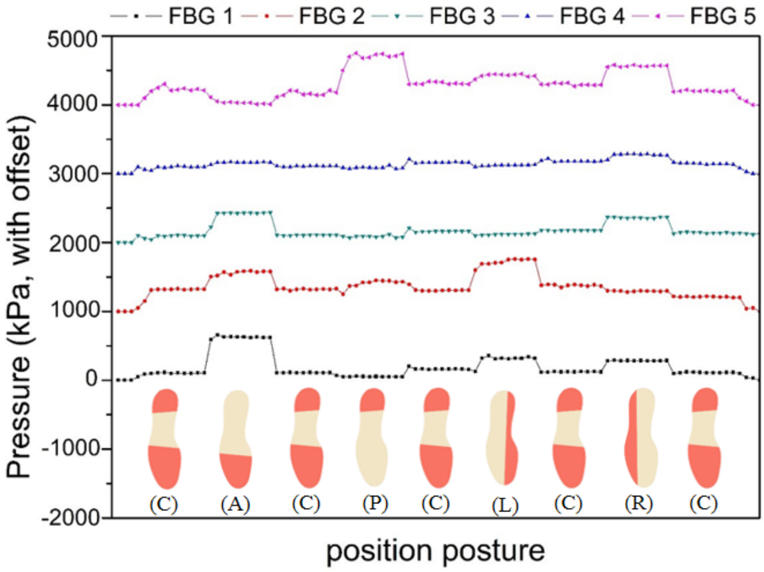

Figure 48: Representation of the pressures detected during the BCM displacements (the pressure on each foot location is coloured to red in the scheme).

Regarding the sagittal plane displacements, the sensors located at the extremities of the platform (FBG 2, FBG 3 and FBG 4) should be the ones presenting a higher variation of the pressure. In fact, it is noticeable that during such movements the sensor placed in position 2 records the increase of pressure, when the BCM is displaced to the left, while the sensors placed in positions 3 and even 4 shows a similar behaviour when the BCM is moved to the right. There is also a lower activation of the sensor at position 1 (toe region) and at position 5 (heel region) due to the characteristic of the BCM displacement, which happens on the whole left and right regions of the foot. The results obtained on both sagittal and frontal plane movements show that the proposed sensor system is able to track the BCM movement on both planes with results similar to the results of reference [167].

5.3.4 In-Shoe Application

From the promising results of the cork insole positioned as a fixed platform during the performed tests, it becomes evident that the method implemented is an adequate solution for pressure monitoring during gait. Moreover, from the analysis of the pressures registered during the stance phase, it is also possible to infer and monitor the plantar pressures of individuals [166]. In order to perform a dynamic and autonomous pressure monitoring during gait, the insole having the five-FBG sensor network was adapted to a shoe, similar to the one developed in [167]. The foot plantar pressure fluctuation during gait is also induced in the instrumented cork sole. Such pressure oscillations resulted in shifts in the reflected Bragg wavelength, and these changes were monitored in the same way as in the previous tests.

After converting the acquired wavelength shift, considering the sensitivity coefficient previously obtained (see Fig. 45), the plantar pressure distribution induced in the cork sole over the gait movement was applied for the 5 POFBGs during 4 gait cycles, as shown in Fig. 49. From the results obtained with the proposed insole sensor network, the repeatability of the data becomes clear, given the similar response of the sensors over the four gait cycles depicted in Fig. 49. Also, it is possible to detect the sequence in which the sensors are activated (maximum amplitude registered), which was also in accordance to what is expected in a gait movement [156], [167].

The POFBG 5 is activated first, at the beginning of the stance phase of the gait cycle, when the heel starts its contact with the floor. With the evolution of the cycle, POFBG 4 (located at the middle-foot and beginning of the metatarsal) is reasonably activated at the start of foot-flat stage during the single support. Following the gait movement, POFBG 2 and POFBG 3, located at the metatarsal positions, present a response at the forefoot contact during the middle of the stance phase. Finally, POFBG 1, located at the toe area, is activated at the toe-off moment, marking the end of the stance phase and the beginning of the swing phase of the gait cycle. The plantar pressure typical curve for the gait movement can be obtained by the addition of the 5 sensors' feedback. The curve obtained represents the vertical ground reaction forces on the stance phase of the gait. On the swing phase, the foot loses contact with the ground the response of each POFBG is near to zero. Figure 49 presents the ground reaction forces obtained with the sum of the five POFBGs showing a RMSE of 160 kPa between the four cycles, which represents an error of only 5% when compared with the average of the sum from the five POFBGs, over four cycles. The description of the dynamic measurements was made to show that the proposed system is capable of detecting the subdivisions of the stance phase discussed on the introduction to this paper, which can aid on the detection of gait-related pathologies. In addition, the detection of the gait phases can be applied on the controllers of wearable robots for gait assistance [170].

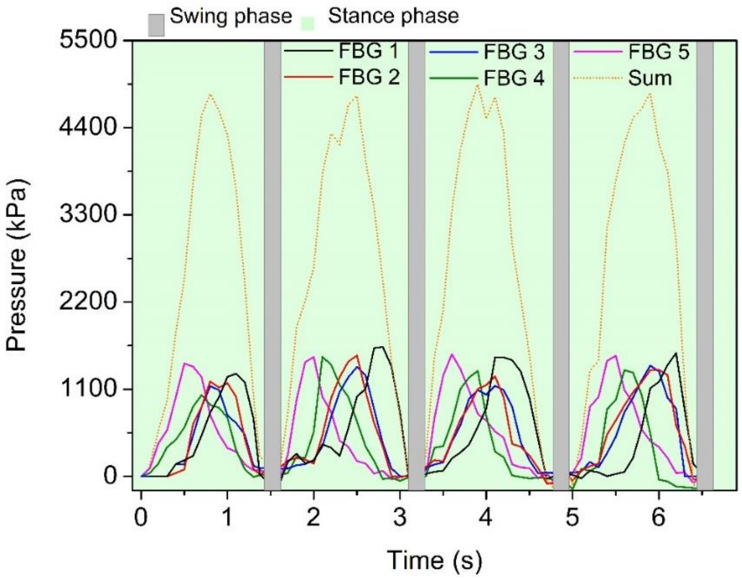

Figure 49: Pressures registered in the cork insole-sensing network for four gait cycles.

The temperature control sensor, the POFBG located in the cork insole, remains constant at 22 ± 0.2°C (after the sensor is properly calibrated), validating the thermal isolation of the cork used for the instrumented sole production.

Finally, any limitations for the maximum allowable velocity that the system is capable of measuring are related to the material response and acquisition frequency of the interrogator. The epoxy resin was tested in frequencies higher than 1 kHz. Since the sampling frequency of 200 Hz is sufficient for acquiring the gait activities, the proposed system is able to cover the velocities employed on human gait. In addition, based on simple stress-strain relations, the proposed sensor system can, in principle, measure the plantar pressure of subjects with body mass higher than 200 kg and according to the calibration results the detection of weights lower than 1 kg is capable.

5.3.5 Conclusion

In conclusion, with the presented architecture, a framework for monitoring the health conditions of citizens and provide automated visual feedback using different state of the art technologies (advanced optical fibre sensors technology, secured energy-efficient wireless broadband access systems, smart actuators, among others) can be developed. The results, using the CYTOP fibre, showed a good response when compared with previously reported solutions using silica optical fibres, almost four times higher than the one obtained for the same application with silica FBGs and good repeatability. A RMSE of 160 kPa was estimated comparing each gait cycle to show the sensor system repeatability. Whereas, the mean RMSE of 45.17 kPa that represents a relative error below 4% is obtained for each POFBG when compared on the reference measurement system of the testing machine, taking advantage of the polymer optical fibre benefits (high flexibility for instance), demonstrates that this is a viable solution for this kind of application. Such higher sensitivity leads to a higher wavelength shift of the POFBGs with the same pressure variation when compared with FBGs in silica fibres, which enable the application of low cost interrogators with lower wavelength measurement resolution (about 5 pm) than its higher cost counterparts (about 0.1 pm). Furthermore, POFs present higher fracture toughness and higher strain limits than SOF, which can enable its application for measuring the plantar pressure of individuals with higher body mass.

6 *Femtosecond Laser Processing of Glass and Soft Glass Fibres*

6.1 Study of FBG Inscribed in SMF28 Fibre Using the *Pl-by-Pl* Femtosecond-Laser Inscription Method

The aim of this work is to study how modifying the inscription parameters (pulse energy and duration, repetition rate, and the translation speed) influence the degree of refractive index modulation for FBGs in a silica glass fibre (SMF28 by Corning); the *Pl-b-Pl* femtosecond laser inscription method is used throughout. Our inscription system consists of a femtosecond laser system (HighQ femtoREGEN) operating at 517 nm with 220 fs pulse duration and a nanometre accuracy air-bearing translation stage (Aerotech), controlled with a personal computer using G-code scripts. The repetition rate of the laser may be regulated using a pulse picker, operating from 1-100 kHz.

6.1.1 *Introduction*

Refractive index modifications induced using femtosecond lasers depend on the material's energy bandgap and the photon energy. The laser wavelength defines whether we have high energy or high-density photon deposition. We must also consider the laser pulse duration and repetition rate; all aforementioned factors impact how the material responds to the deposited laser energy, either separately or with relative contributions. High energy photons lead to intense linear absorption, whereas if the material is highly transmissive (non-absorbing) it can still absorb energy at the laser focus if the pulse duration is short – through non-linear, multi-photon absorption. The pulse duration affects whether the material experiences a local heat affected zone and collateral damage, such as fissures and cracks. The laser repetition rate impacts large scale material thermal loading (this is similar to material annealing). If the repetition rate is faster than the electron diffusion time then the material will be thermally loaded by successive pulses, often leading to less confined index changes. The electron diffusion time in glass is ~1 μs, therefore if the laser repletion rate is close to or beyond 1 MHz, a large-scale heat affected zone will lead to smoothing of the induced index changes [171]; this is a "hot" process. Conversely, a lower repetition rate is considered a "cold" process, with any heating occurring only at the laser focus on a time scale concomitant with the pulse duration. We need to ask how this information impacts our inscription processes, where the laser operates at 517 nm (suggesting a few-photon process in glass), 220-fs pulse duration (well below electron recombination effects and thermal diffusion), up to 100-kHz repetition rate (no expectation of thermal loading, our process is "cold"). Of course, we also need to consider the laser focussing (the numerical aperture of the lens affects the scale and depth of the index change) and dosage; from a practical perspective related to *Pl-by-Pl* FBG inscription, the number of laser pulses/µm is a useful normalisation. The threshold for a single pulse will differ for multiple pulses/µm, as the material is no longer pristine for every subsequent pulse; eventually the index change will saturate for a given number of pulses/µm. We performed a series of FBG inscriptions where the selected variables were precisely controlled, such as the translation stage speed (nm/s resolution), the repetition rate (software controlled), and pulse energy (controlled to nJ level), whereas the wavelength of the laser (517 nm), the pulse duration (220 fs), and the focal lens of system (Mitutoyo x50, NA 0.42) remained unchanged. By carefully modifying the parameters we aimed to study the optimum inscription parameters for FBGs in silica fibre, such as commercial SMF-28 fibre manufactured by Corning. For better comparison, all the gratings were inscribed keeping the same grating length (L) and characterised in transmission (and reflection where necessary). The results are quantitatively presented regarding to the refractive index change (δ_n), the effective refractive index (n_{eff}), and the coupling constant (k).

In general optical fibres are suspended between two fibre clamps in order to position the core relative to the laser beam, prior to any form of laser inscription. However, this can lead to unwanted strain and the clamps can induce birefringence. We instead fix the fibres to a glass slide; this can them be mounted on to the air-bearing translation stage. To overcome curvature effects resulting from the fibre's cylindrical shape, the fibres were immersed in refractive index matching oil and covered using with thin coverslip.

According to the specifications of the lens and for the operating wavelength (λ = 517 nm) of our system, the focal spot size as calculated using the equation below,

$$Spot\ size\ diameter\ (W_o) = \frac{4\lambda f}{\pi D}, \quad (6.1)$$

where f is the focal length, $D = 2.NA.f$ is the pupil diameter and $NA = 0.42$ is the numerical aperture of the particular lens and found to be ~0.878 µm. The lens is a complicated, compound objective, and so the spot size is approximate. An observation, regarding the spot size; it has been shown that femtosecond lasers can beat the diffraction limit producing sub-wavelength features/holes (~20-nm diameter, laser wavelength 800 nm), however this holds true for a single laser pulse. Once there is a collection of pulses that inscribe a line, then the feature size is far larger and is on the same scale as the laser wavelength.

With the *Pl-by-Pl* inscription method, the laser beam moves transversely to the fibre core in a fully controlled three-dimensional motion (as discussed in Chapter 4). The minimum width of the plane is dependent on the beam spot size (~0.8 μm) whereas the depth and the length of the plane are controlled by the system parameters. When we compare this with the PbP method, we note that the *Pl-by-Pl* inscription method relaxes the need for perfect alignment; whilst at the same time maintains the flexibility offered regarding the grating period. PbP inscription demands an alignment of better than 1-μm offset from the fibre axis on two axes (x and y), this equates to better than 1 part in 10,000 on the two axes, and the likelihood of inscribing two identical gratings is low. *Pl-by-Pl* inscription can be monitored in real time and the grating inscription is stopped when the desired grating spectrum is achieved; the inscription characteristics can be fully selected by the system parameters. The *Pl-by-Pl* inscription time is longer (up to tens of minutes), but the fibre alignment takes a couple of minutes.

6.1.2 *Uniform Fibre Bragg Gratings*

SMF-28 has core and cladding diameter 8.2 μm, and 125 μm, respectively, while the refractive index of the core and cladding is 1.44681 and 1.445205 at 1550 nm, respectively. Based on previous studies, the energy gap for the photo-excitation for the particular Ge-doped glass is between 7.1 eV and 7.8 eV; for a femtosecond laser operating at 517 nm this implies three-photon absorption [15], [172].

In order to quantify our experimental results all, the data is normalised to the number of pulses per μm. By doing this we overcome trade-offs between repetition rates and inscription speeds. Moreover, for all inscriptions, the gratings were spatially limited to the core region to avoid, or at least to minimize, additional errors and losses to the grating spectrum; we kept the total grating period number constant. It is important to note that all the gratings were characterised in transmission using a broadband light source

(Thorlabs ASE730) and an optical spectrum analyser (Advantest Q8384) with optical a 10-pm resolution.

We begin our experiments by inscribing gratings for different pulses/μm to identify the most appropriate dosage for FBG inscription in the particular fibre; the pulse energy was kept constant at ~100 nJ. We inscribed equal length gratings with 50, 67, 80, 100, 140, and 200 pulses per μm and Fig. 50 present the transmission depth for each grating. This shows that the grating with the highest transmission depth is measured for 80 pulses/μm (for the particular fibre under test). As the pulse number increases we observe signs of material saturation, the notch depth has decreased to ~5 dB.

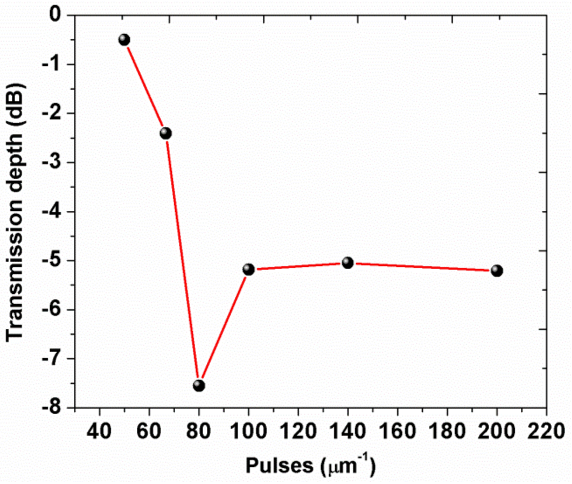

Figure 50: The transmission depth with respect to the number of pulses/μm, for gratings inscribed with the same pulse energy (100 nJ).

The other parameter that will impact the strength of the gratings is the pulse energy; the number of pulses is kept at 80 pulses/μm and a series of inscriptions with different pulse energies are undertaken (85 to 155 nJ/pulse). For pulse energies below the 85 nJ, it was not possible to locate the grating in either the transmission or reflection spectra.

Figure 51(a) shows the refractive index modulation of the core with respect to the pulse energy with ~85 nJ the threshold pulse energy for the particular fibre, whereas the ideal energy is close to ~137 nJ, after which the transmission depth is reduced. This decrease in the transmission depth may be explained by the creation of a negative refractive index change. More specifically, due to the high pulse energy, micro-voids are created as a result the effective refractive index drops. A comparison between a uniform inscription and one with no signs of optical breakdown is presented in Fig. 52. Similarly, in Fig. 51(b), the threshold step at ~96 nJ is observed, while the grating inscribed with 137 nJ pulse energy had the highest transmission depth ~19 dB, which corresponds to ~99% reflectivity; at the higher energies the grating strength decreases.

In contrast, the DC refractive index modulation shown in Fig. 51(c), follows a different behaviour. A positive change is noted up to ~109 nJ and after that follows a negative slope changes up to 136 nJ. After that, for pulse energy 155 nJ, the DC change has a positive slope again. The negative slope may be explained by the micro-voids (RI = ~1) created in the centre of the inscription which drops the DC effective index value. At the same time the material accumulated around the micro-voids, as a result for pulse energies above 136 nJ, the diameter of micro-voids increases ‘enough’, hence the refractive index value of the accumulated material reaches much higher values leading to a positive change again. On the other hand, the accumulated material at energies >136 nJ covers a spatially larger area with the result of period overlapping which explains the transmission depth drop shown in Fig. 51(b).

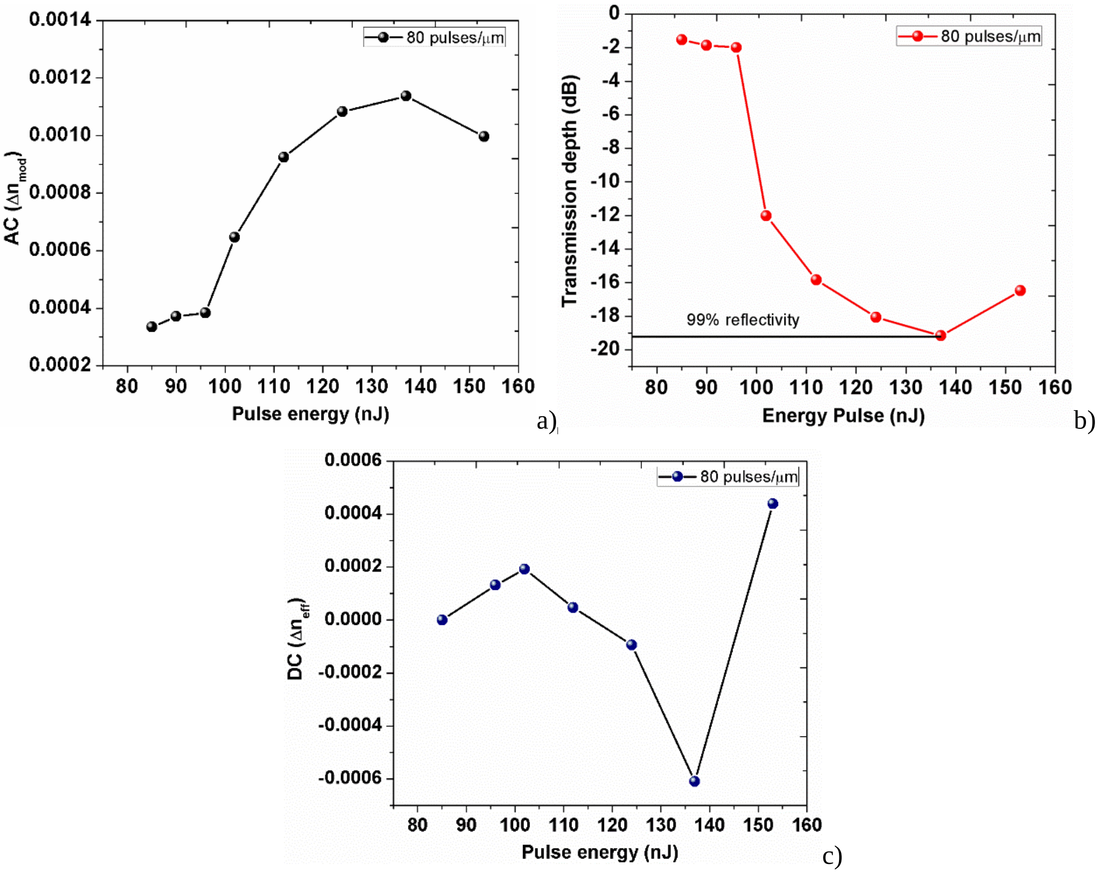

Figure 51: a) The refractive index modulation (AC), b) the transmission depth of the gratings, with respect to the pulse energy and c) the effective refractive index modulation (DC).

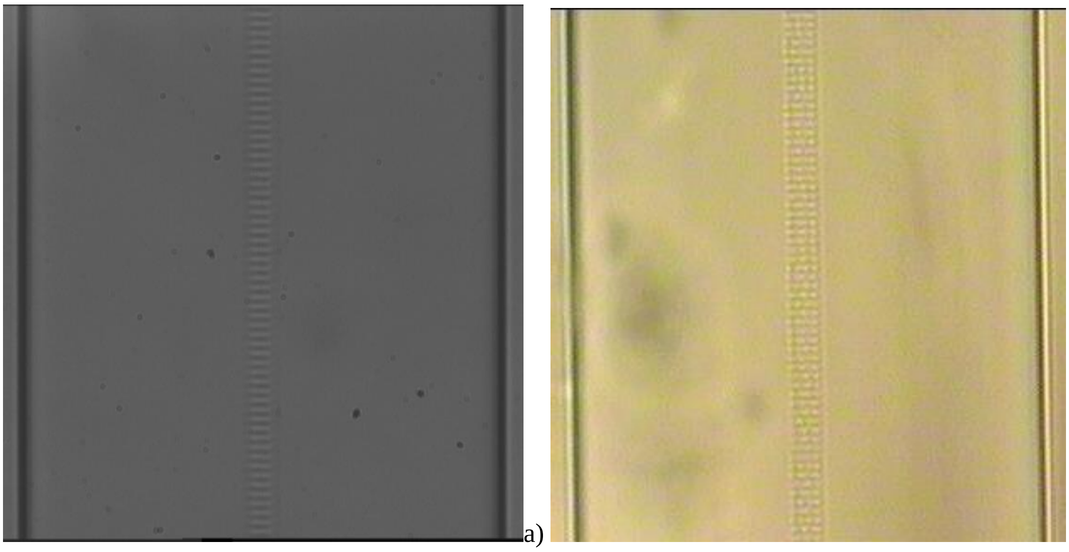
a) b)

Figure 52: Microscope images for comparison between inscriptions with a) 'normal' and b) high pulse energies prior to the onset of optical breakdown.

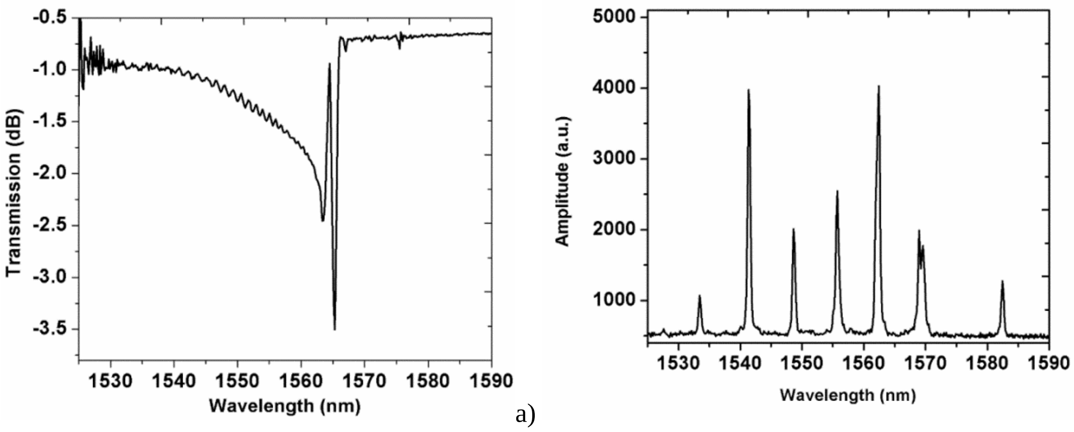

a) b)

Figure 53: a) Transmission spectrum of a 4th order fibre Bragg grating inscribed in SMF28 fibre without removal of the fibre jacket and showing the presence of radiation modes, and b) FBG array inscribed 'blind' in SMF28 using the *Pl-by-Pl* femtosecond laser inscription method for a uniform grating.

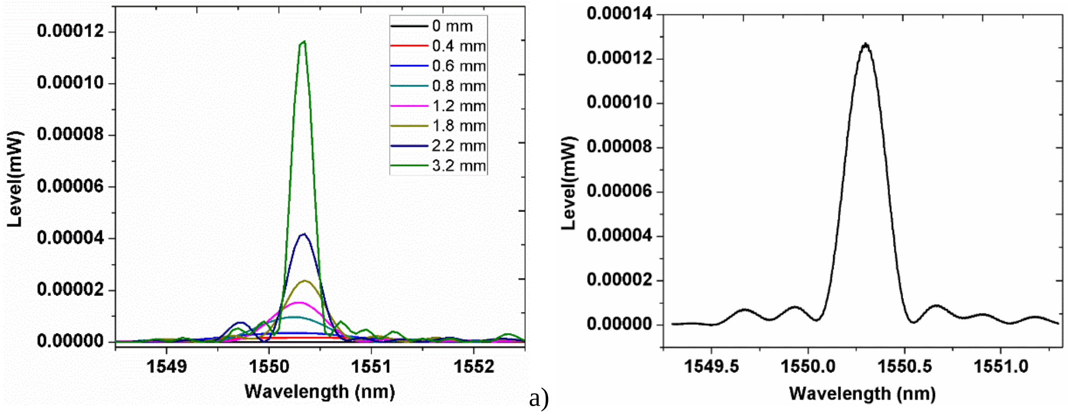

a) b)

Figure 54: a) Fibre Bragg grating growth in reflection as measured during the inscription process, b) The final reflection spectrum of the FBG.

Figure 53(a) shows the transmission spectrum of a 4th order FBG, and Fig. 53(b) the reflection spectrum of a multiple-FBG array, as recovered using a broadband light source, and a commercial FBG spectrometer. The FBG array consisted by eight FBGs physically separated by 8 centimetres and spectrally in the range of 1500-1600 nm. The total length of the gratings was ~2 mm and the average FWHM is ~0.5 nm. The reflection responses of eight gratings were observed at 1534 nm, 1541 nm, 1548 nm, 1556 nm, 1563 nm, 1568 nm, 1569 nm and 1582 nm. All gratings were written "blind" without active monitoring in order to show the capability of the *Pl-by-Pl* inscription method and Fig. 54(a)&(b) shown the grating growth and the final reflection spectrum of a 3.2 mm long grating, respectively.

6.1.3 *Higher Order Uniform Fibre Bragg Gratings*

The *Pl-by-Pl* inscription method has a flexibility advantage compared to other inscription methods; to the grating period is readily modified and one can inscribe gratings at different wavelengths and different orders. It is noted that higher order gratings can be produced as the index profile is top hat (rectangular profile, Fig. 55), and so the grating transmission spectrum has many peaks, all located at higher orders of the original Bragg wavelength. We inscribe gratings with a constant number of periods but with different grating orders. In this way, we expect to study how the duty cycle of the gratings influences the transmission spectrum and in particular coupling to the fibre cladding modes associated with of the gratings.

The resulting spectra obtained and presented in Fig. 56, showing a correlation between the grating order and the cladding mode strength; we inscribe 4th, 8th, and 16th order gratings. We observe that as the order of the grating is increases, the cladding mode coupling is reduced (Fig. 57(a)). For the 4th order grating the cladding mode has a transmission depth of -4.5 dB, decreased to -3.216 dB and -1 dB for the 8th and 16th order respectively. The corresponding duty cycle is ~40%, ~20% and ~10% for 4, 8, and 16th order gratings, respectively.

In addition to the cladding modes, important grating characteristics such as bandwidth and strength also change with the grating order. The full width at half maximum (FWHM) bandwidth was 1.104 nm for the 4th grating, 0.434 nm for the 8th order, and 0.281 nm for the 16th order as shown in Fig. 57(b), while the grating strength also increased. Theoretically, as referred to Erdogan's work [13], both grating characteristics are dependent on the grating length. In our case, the number of periods is the same for all gratings; hence the final total length of the 16th order grating was approximately eight times longer than the 4th order. The FWHM bandwidth of an FBG is evaluated as follows [173],

$$\lambda_{FWHM} = \frac{1.39\lambda^2}{\pi L n_{eff}} \quad , \qquad (6.2)$$

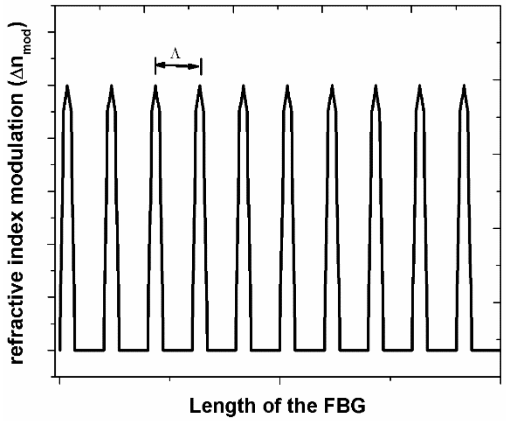

Figure 55: Top hat refractive index change profile for uniform Bragg gratings using the *Pl-by-Pl* femtosecond laser inscription method.

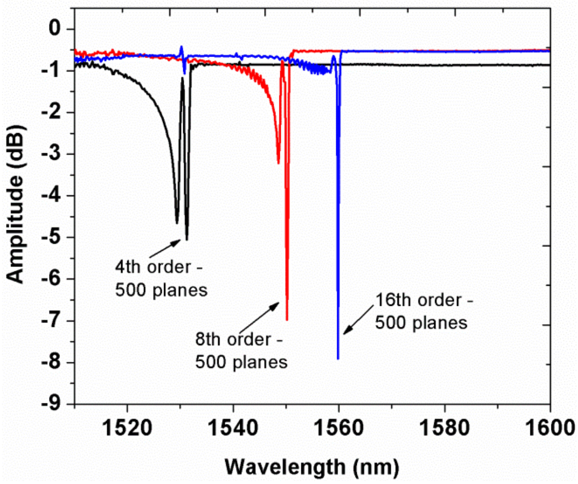

Figure 56: Transmission spectra of 4th, 8th, and 16th order FBGs, to correlating the cladding mode with the duty cycle of the gratings.

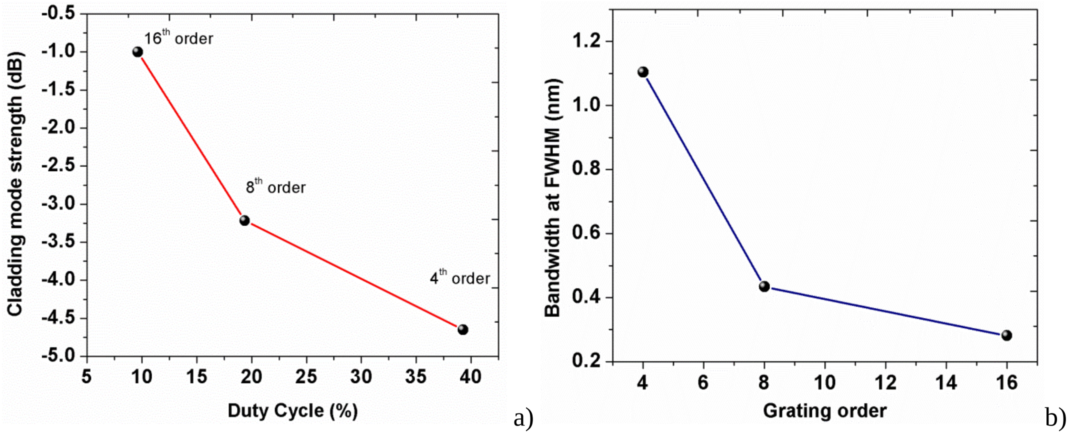

Figure 57: Comparison between 4th, 8th, and 16th order gratings' transmission spectra. a) The strength of the cladding modes with respect to the duty cycle; b) as the grating order increases, the grating duty cycle and the bandwidth decrease, the latter resulting from the longer length as the plane number remains constant.

6.1.4 *Non-Uniform Fibre Bragg Gratings or Chirped Gratings*

A demonstration of the *Pl-by-Pl* inscription flexibility is presented in this section. As mentioned previously, the grating period could be easily controlled to inscribe gratings at any wavelength and order.

$$\Lambda(z) = \Lambda_0 + \frac{\left(\Lambda_{lg} - \Lambda_0\right)}{l_g} z \ , \tag{6.3}$$

where Λ_0 is the period at the start of the grating, Λ_{lg} is the period at the end of the grating and l_g is the grating length.

Instead of the uniform gratings, we proceed to inscribe non-uniform (chirped) gratings. The physical difference between the two is that for the uniform gratings the modulation period is always constant whereas chirped gratings have a constantly increasing period; spectrally, the uniform FBGs are reflected only a single wavelength but the chirped gratings reflect over a range of wavelengths. Figure 58 presents a 10-nm chirped grating with total length ~4.5 mm. The grating is 4th order while the period was initially Λ= ~2.1557 μm and the final period was Λ= ~2.1695 μm.

Based on the results discussed in the previous section, we inscribed 4th, 8th, and 16th order chirped gratings with FWHM bandwidths of 5 nm (Figs. 59(a-c)). From the reflection spectrum of the chirped gratings, we observe that, the slope at the edge of the chirped spectrum is affected by the grating order. More specifically, for 4th order, the slope found to be 1.28 dB/nm, for the 8th order 0.64 dB/nm, and 0.4 dB/nm for the 16th order. It is important to note that all the gratings were inscribed with the same number of periods, so the corresponding total length was ~2 mm, ~4 mm, and 8 mm for 4th order, 8th order, and 16th order respectively.

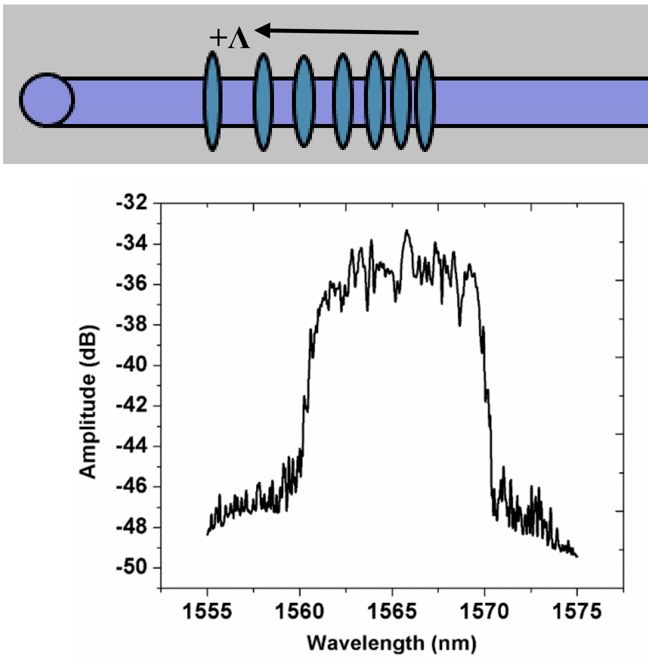

Figure 58: The reflection spectrum of a 10 nm non-uniform fibre Bragg grating or chirped grating inscribed in SMF28 fibre.

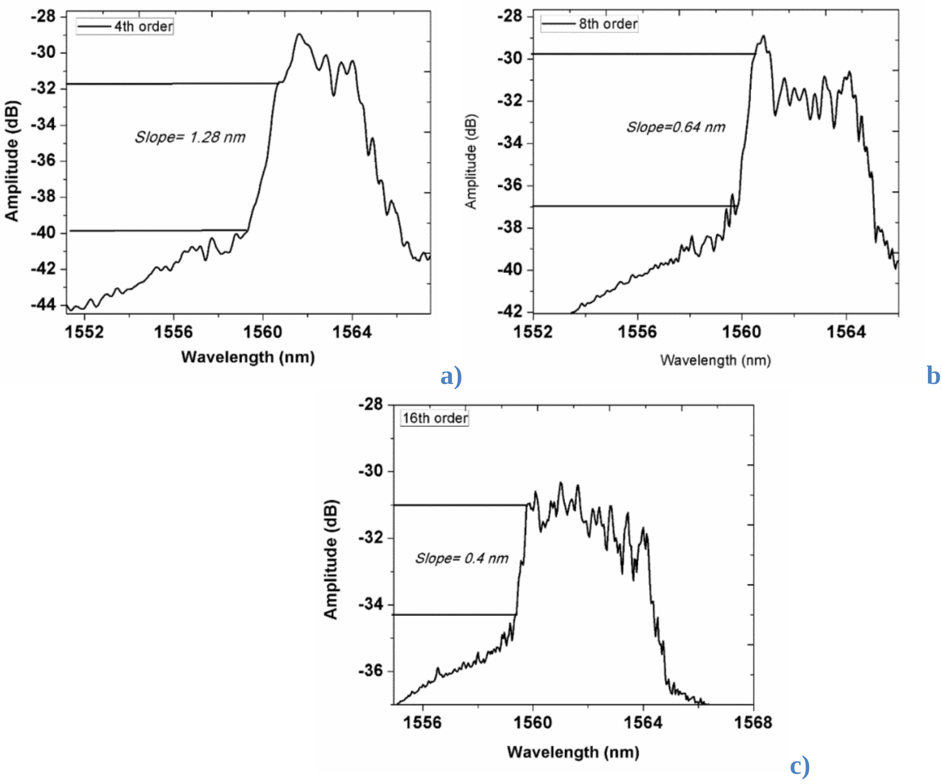

a)

b)

c)

Figure 59: The reflection spectrum of a) 4th order, b) 8th order, and c) 16th order chirped grating inscribed in SMF28 glass fibre using the *Pl-by-Pl* inscription method. The slope of the edge of the chirped grating is noted.

6.1.5 *Fibre Bragg Fabry-Perot Cavities*

Figures 60-62 shows fibre Fabry Perot cavities. Figures 60(a) and 60(b) show the linear and logarithmic reflection spectra for a FFP with FSR ~210 pm with finesse ~17.2, respectively. The FFP consisted of two 1-mm long FBGs operating at 1580 nm, and separated physically by 3 mm.

As the physical distance between the FBGs increases the FSR of the cavities decreases and vice versa, as expected, a physical length reduction from 3 mm to 2 mm, leads to a FSR of 242 pm (Fig.61) and 120 pm for 5mm (Fig.62). In the same way when increased to 5 mm the FSR become 120 pm. Moreover, the finesse for all the cavities remains below 17, indicating that the FBGs are not highly reflective. More specifically, this indicates that the FBG reflectivity is ~94%. One must also consider that as the gratings increase in length, the concomitant grating loss will influence the cavity finesse.

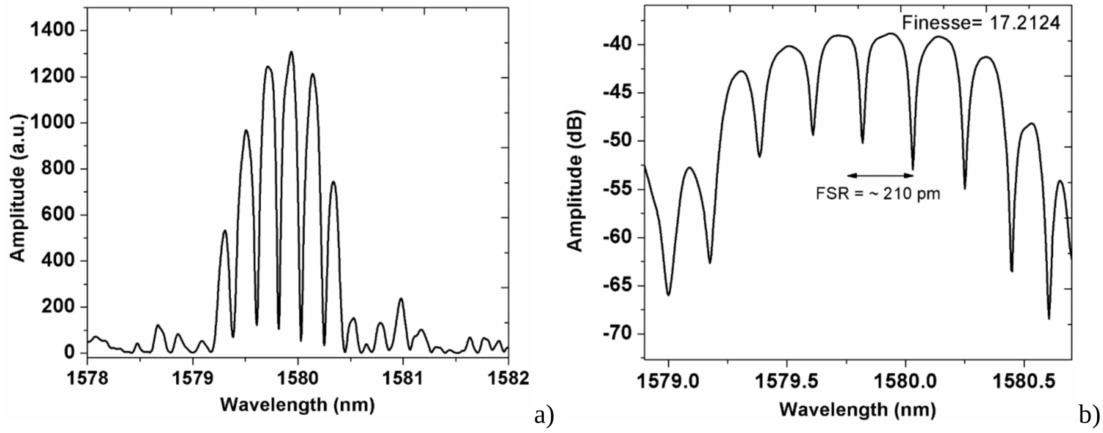

Figure 60: The reflection spectrum of a Fabry-Perot cavity formed from using two identical FBGs inscribed in a single mode SMF-28 fibre. a) Linear and b) logarithm reflection spectrum for the FFP with a physical spacing of 3 mm.

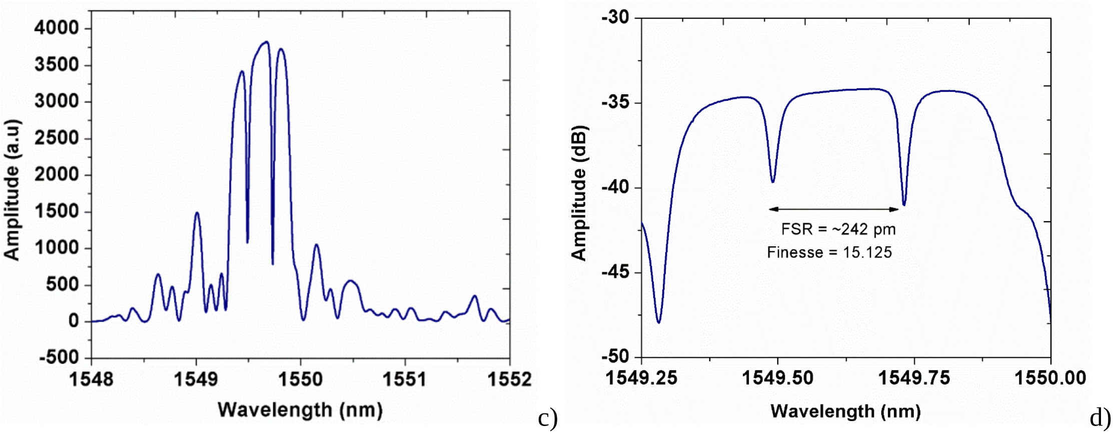

Figure 61: The reflection spectrum of a Fabry-Perot cavity. a) Linear and b) logarithmic reflection spectra of FFP with a physical spacing 2 mm.

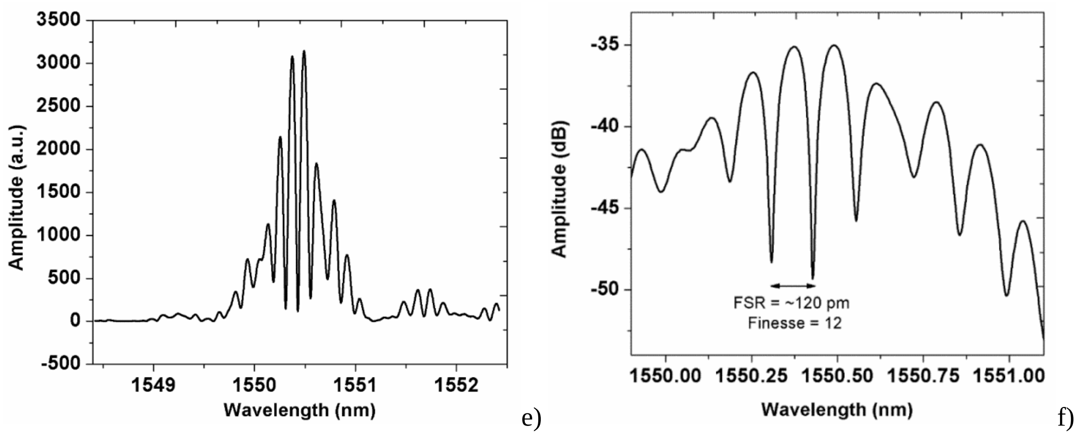

Figure 62: The reflection spectrum of a Fabry-Perot cavity, a) Linear and b) logarithmic reflection spectra for physical spacing 5 mm, and longer FBGs for higher reflectivity.

6.1.6 *Chirped Fibre Bragg Fabry-Perot cavities*

Another important optical component for optical fibre systems that is difficult to produce, is a variable FSR filter. In this section we investigated the inscription of FP using chirped instead of uniform gratings.

We focus on two designs for chirped FP cavities (CFP), the dispersive and the non-dispersive forms. Figure 63(a) shows a schematic diagram of a non-dispersive CFP; the two chirped gratings are inscribed as in section 6.1.4 with the same change in pitch (~3 pm/mm), increasing from right to left with physical distance between them 3 mm. The resulting reflection spectrum with uniform FSR for all dips in the reflection spectrum is shown in Fig. 63(b).

In contrast, for the dispersive CFP (Fig. 64(a)), the two chirped gratings were inscribed with the same characteristics as before but with opposite directions resulting in a range of cavities over the reflection spectrum, with a variation of FSR (Fig. 64(b)). The FSR starts at 140 pm for the higher wavelengths and increases to 800 pm for the lower wavelengths. The reflection spectrum indicates a reduction in the fringe visibility at the lower wavelengths and this may be an indication that the chirped gratings require more periods.

The two designs could be improved by using higher reflectivity chirped gratings (more length) written with lower pulse energy (lower loss) for more homogenous spectrum and improve finesse. With the *Pl-by-Pl* inscription method the length of the chirped gratings and the number of periods is controlled readily and the demands of the CFP in terms of finesse, reflectivity, and FSR could be adapted efficiently.

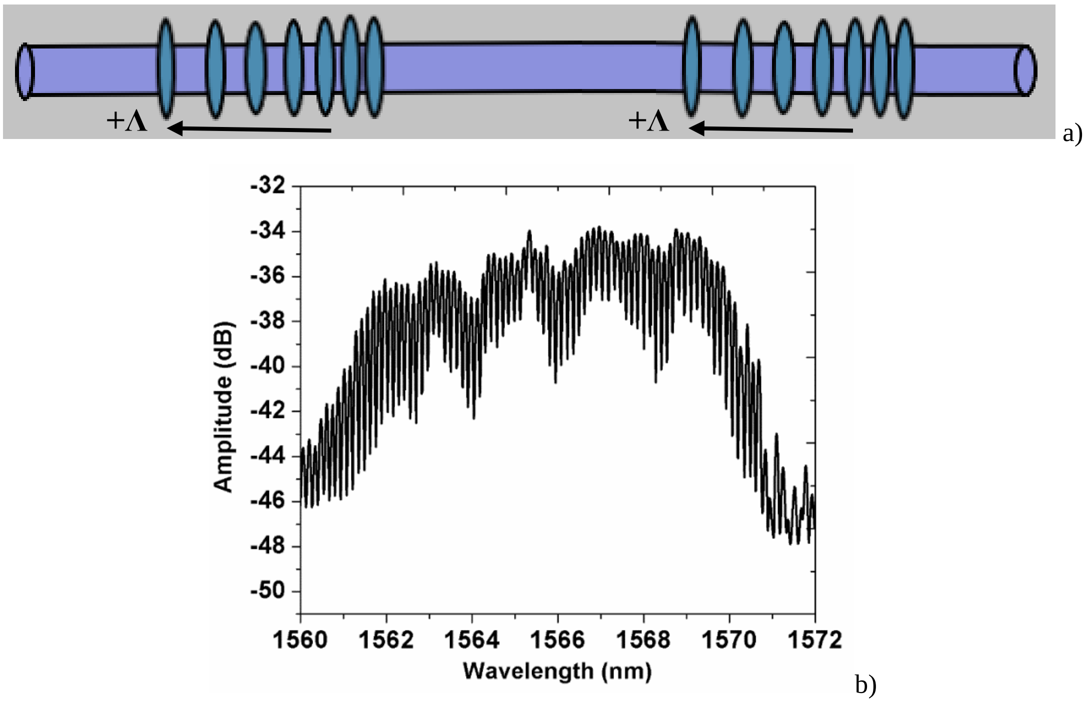

Figure 63: The reflection spectrum of a non-dispersive chirped Fabry-Perot cavity using two 10-nm chirped gratings. The FSR is constant across the whole spectrum (140 pm).

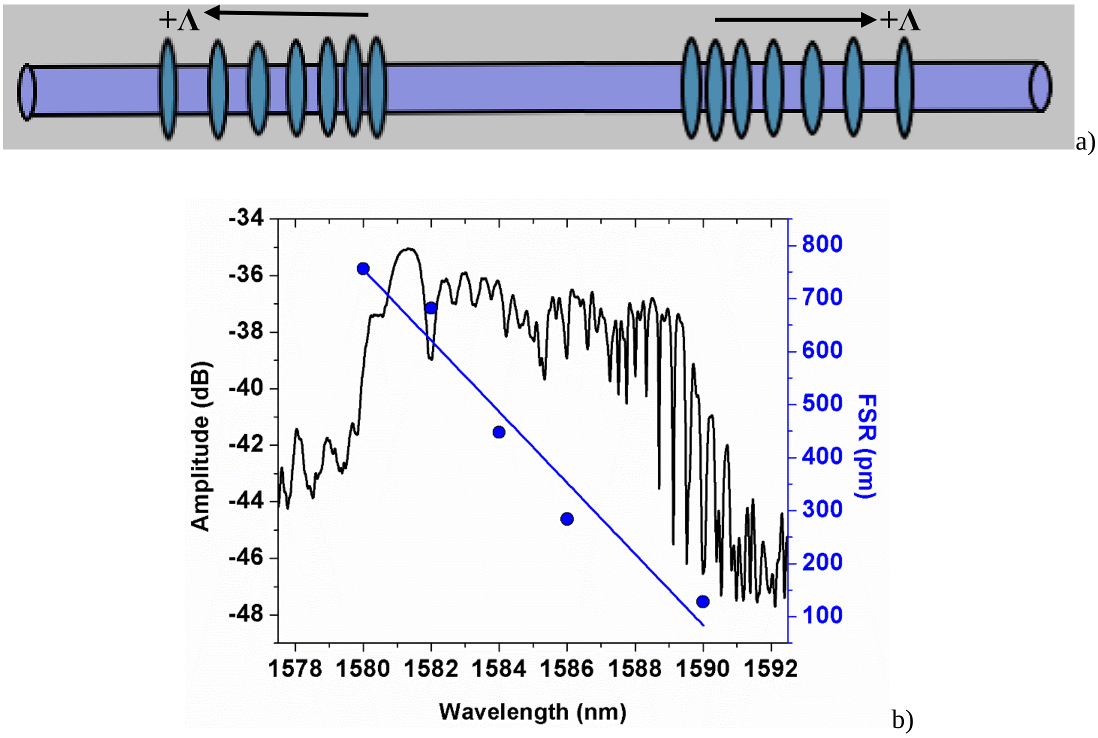

Figure 64: The reflection spectrum of a dispersive chirped Fabry-Perot cavity using two 10-nm chirped gratings, inscribed with chirp in opposite directions. The FSR is variable with wavelength.

6.2 Tilted Fibre Bragg Gratings in Boron-Doped Glass Fibre

In this section, a flexible method for the development of tailored tilted fibre Bragg gratings (TFBGs) using the femtosecond laser is presented. Compared to the conventional UV-laser or existing femtosecond laser fabrication processes based on phase masks, interferometric and PbP methods, the approach is far more flexible and offers several advantages. Laser inscription was made through the fibre coating while the grating planes were controlled to minimize birefringence related to the inscription process, with precise control over the wavelength location and strength of cladding modes. 10th order gratings were produced in the C+L bands so that higher order gratings could be studied at shorter wavelengths.

This work was published in Optics Letters and part of the work was presented as a poster at the Workshop on Specialty Optical Fibres (WSOF) October 2017 in Limassol Cyprus and awarded with the best poster presentation award.

6.2.1 *Introduction*

TFBG technology has seen a huge rise in interest during the last decade mostly due to its lab-around-fibre sensing capabilities. In common with uniform FBGs, TFBGs are created when a photo-inscription process takes place along the propagation axis of the optical fibre core, thereby inducing a permanent and periodic modulation of its refractive index. In addition to the core mode coupling at the Bragg wavelength, controlled tilting of the refractive index modulation with respect to the optical fibre axis promotes light coupling from the core to numerous tens (not to say hundreds depending on the tilt angle value [19] of backward-going cladding modes. They appear as narrowband dips (full width at half maximum ~200 pm) in the transmitted amplitude spectrum. With the inherent birefringence resulting from the tilted grating planes, which break the cylindrical symmetry of the fibre, TFBGs have been used in numerous applications, including in-fibre polarizers [174], bending [175] and twist sensors [176], to name just a few examples. According to the grating’s phase matching conditions, each cladding mode has its own effective refractive index and will be sensitive to surrounding refractive index changes in a narrow range around that particular value. Hence, TFBGs remain very attractive for temperature-insensitive refractometric sensing [177], [178]. Two key approaches have been reported to demodulate the TFBG amplitude spectrum response:

(1) computation of the area delimited by the cladding mode resonances in the amplitude spectrum and (2) computation of the wavelength shift of the most sensitive cladding mode resonance. The latter is located marginally above the cut-off mode whose effective refractive index matches that of the surrounding medium. The second demodulation technique typically yields in aqueous media surrounding refractive index sensitivity of the order of ~20 nm/RIU (refractive index unit) for a cladding mode resonance close to 1550 nm. More recently, it was demonstrated that TFBGs behave as highly sensitive plasmonic biosensors when they are surrounded by a thin gold coating on which bioreceptors are grafted [179]–[183].

TFBGs are classically photo-inscribed using UV irradiation (either with continuous-wave frequency-doubled argon laser or pulsed excimer laser) with the interferometric or phase mask technique. In [184], a 800 nm femtosecond pulses laser was used to manufacture TFBGs using the phase mask technique.

6.2.2 *Experimental Details*

The *plane-by-plane* TFBGs were inscribed in a photosensitive single-mode optical fibre manufactured by the FiberCore [185]. The focused laser inscribed planes had a width of ~800 nm; whereas the other dimensions were controlled by suitable translation stage motion, resulting in a 3-dimensional refractive index change with controlled plane length, depth and grating-plane angle. The energy of pulses at the exit of the laser was measured as 100 nJ/pulse, for a repetition rate of 50 KHz. Initially, the jacket of the fibre was not removed, thus retaining the fibre’s integrity throughout the initial laser processing [186], it was removed for refractometry applications.

6.2.3 *Results*

Following the inscription, the TFBG spectra were recovered using a broadband light source and an optical spectrum analyser (Advantest Q8384, 10-pm resolution). The transmission spectrum of a 10 mm, 7° TFBG is shown in Fig. 65 before and after stripping of the fibre jacket, and we confirm that with the fibre coating the cladding modes are naturally weaker. The maximum peak-to-peak intensity for the cladding modes with the coating was 5 dB, increasing to 15 dB when the fibre was stripped at the grating location.

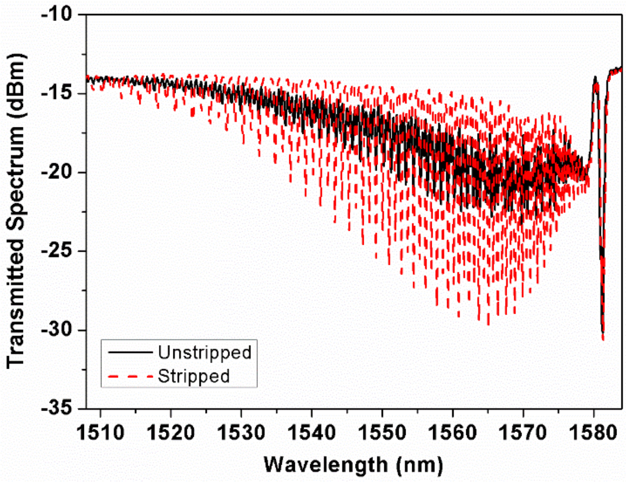

Figure 65: Transmitted power spectrum of a 7° TFBG with a Bragg peak of ~25dB and a maximum cladding mode intensity of ~15 dBm.

Considering the flexibility of our writing technique, we studied the effect of the plane length on the TFBG spectrum. The grating planes were made with a length varying between 4 and 40 µm. Figure 66 shows a microscope image recovered from the inscription set-up, for 7 and 40 µm plane lengths.

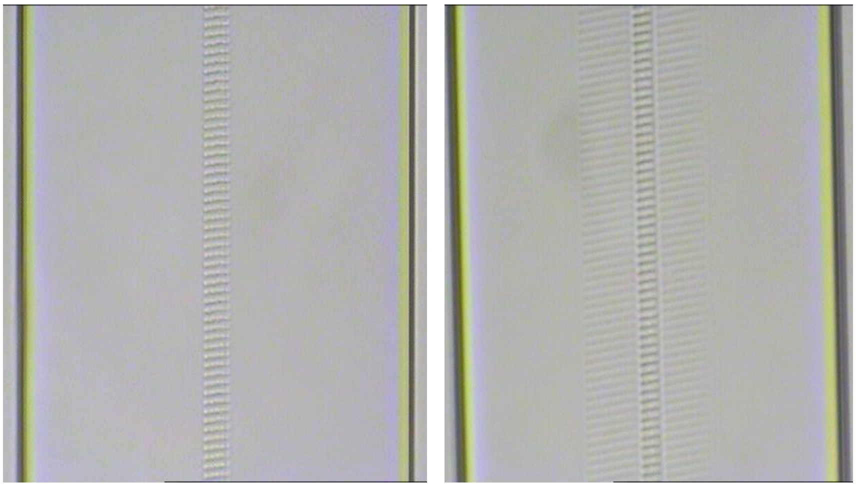

Figure 66: Pictures of 7° TFBGs with 7 and 40 µm plane lengths in fibre with core diameter 8.2 µm.

Figure 67 shows the corresponding transmitted spectra for 2-mm long, 7° TFBGs. It shows that the peak-to-peak amplitude of the cladding mode resonances is enhanced for a plane depth corresponding to the core diameter. For refractive index modulations extending in the cladding region, the cladding mode resonances visibility decreases and the baseline is decreased due to the excitation of radiated modes. We have also studied the effect of the tilt angle on the grating spectrum. Figure 68 shows the spectra obtained for a tilt angle of 0, 7, 14 and 21°, respectively. As observed for conventional TFBGs [19], [186], the depth of the Bragg and cladding mode resonances decreases as the tilt angle value increases. The cladding mode resonances centre of mass (CMR-COM) shifts to shorter wavelengths as expected. Figure 69, shows that the CMR-COM follows a 2nd order polynomial function.

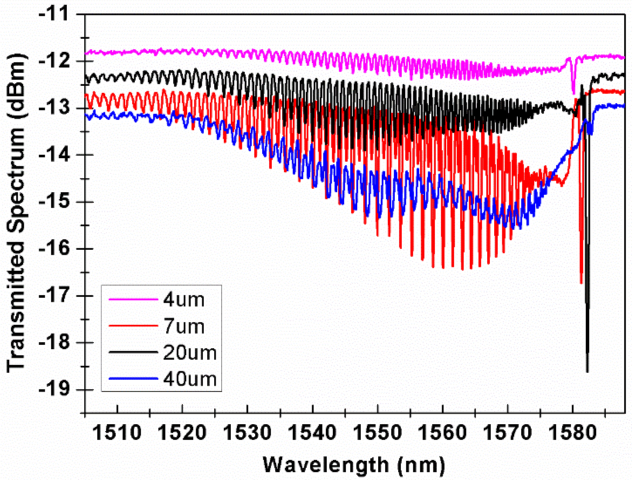

Figure 67: Transmitted amplitude spectra of 7° TFBGs with different grating plane depths. (spectra are offset on the vertical axis for clarity)

The technique highlights an important difference compared to the classical inscription methods: as we rely on a direct writing process, the Bragg wavelength does not shift with the tilt angle value, allowing for precise control in its positioning. Finally, for tilt angle values above 20°, excitation of cladding modes in the range 1340-1440 nm is possible for a simultaneous strong Bragg mode at 1580 nm, which is typically not the case if a phase mask is rotated relative to an optical fibre. These modes are characterized by an effective refractive index value close to 1. Hence, as already reported in [187], this yields the opportunity to use such highly tilted gratings for refractometry in gaseous media.

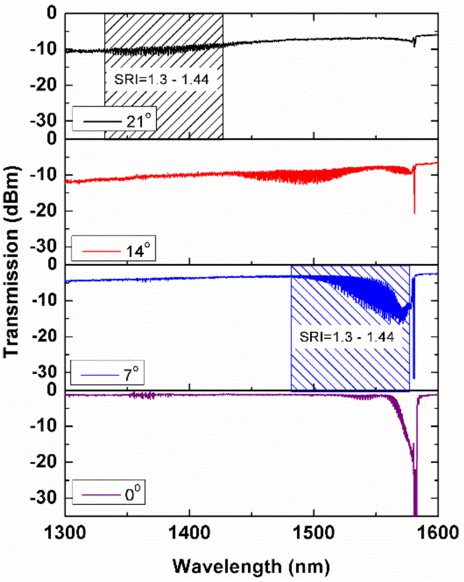

Figure 68: Transmitted amplitude spectra of 0°, 7°, 14° and 21° TFBGs.

The role of laser-induced birefringence has been considered for grating planes corresponding to the fibre core diameter, which offers the strongest cladding mode resonances. Here a polarization controller was placed in the measurement set-up between the optical source and the grating. For all the tested TFBGs, the birefringence is manifested by a maximum shift of the Bragg wavelength of only 8 pm, which is more than an order a magnitude improvement over other femtosecond laser FBG inscription methods, and may be further reduced by controlling the laser inscription energy.

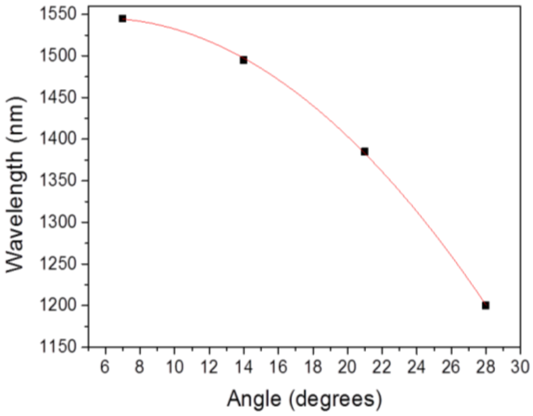

Figure 69: Cladding mode resonance centre of mass shift per angle change, fitting with a 2nd order polynomial function.

It is well known that this value corresponds to $2\Delta n\Lambda$ where Δn is the birefringence and Λ is the grating period. Hence, this gives a laser-induced birefringence of $7.4\text{x}10^{-6}$, which is on the same scale as UV written gratings, quite similar to other photo writing techniques [188].

Another interesting feature of the direct write method is the ability to produce high order gratings operating at ~1550 nm, allowing for the study of the behaviour of higher order cladding modes located at lower wavelengths. Figure 70 depicts the transmitted amplitude spectra of a 4th and 10th order grating at 1580 nm and 1550 nm, respectively. It shows that the wavelength range over which the cladding mode resonances of a particular grating order extend decreases with the grating order. This arises because the wavelength spacing between neighbouring cladding mode resonances decreases, as shown in the insets of Fig. 70.

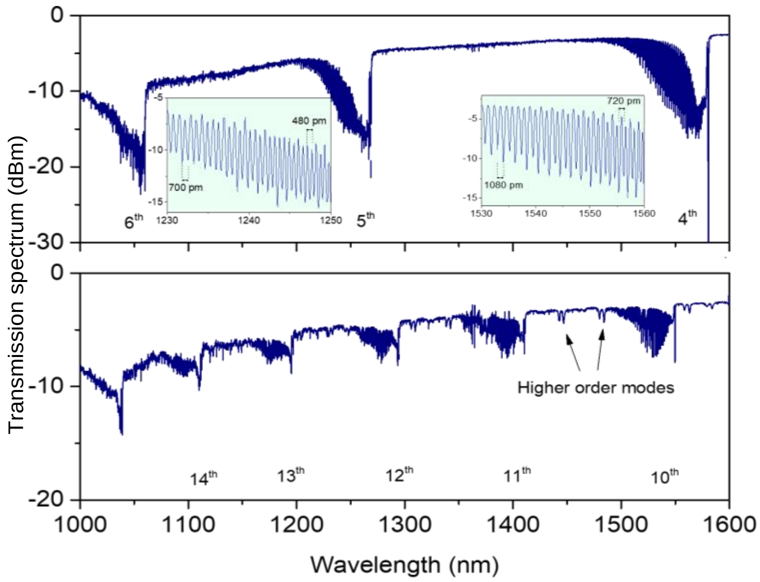

Figure 70: The 4th and the 10th order gratings at 1580 nm and 1550 nm respectively displaying higher order modes at shorter wavelengths. Inset: zoom on the 4th and 5th orders to see the evolution of the wavelength spacing between neighbouring cladding modes.

Finally, we inscribed a 10th order TFBG that was immersed in a salted water mixture whose refractive index was slightly modified by adding small quantities of water. The refractive index of solution was measured with a handheld Abbe refractometer accurate to 10^{-4} RIU. The applied demodulation technique was based on the computation of the wavelength shift of the most sensitive cladding mode resonance in the grating spectrum. Figure 70 depicts the obtained results for the 10th, 11th and 12th grating orders, respectively. A linear regression of the raw data yields a refractometric sensitivity of ~28 nm/RIU for the cladding mode resonance at 1506 nm in the 10th order grating. This sensitivity decreases to ~13 nm/RIU at 1257 nm for the 12th order grating. This differential refractometric sensitivity between grating orders can be beneficial in the process of ultrafine refractometry, as reported in [189]. Moreover, from the obtained data, it is expected that the sensitivity can increase at longer wavelengths (9th order grating at ~1720 nm for instance) provided that adequate source and optical spectrum analyser are used to record them.

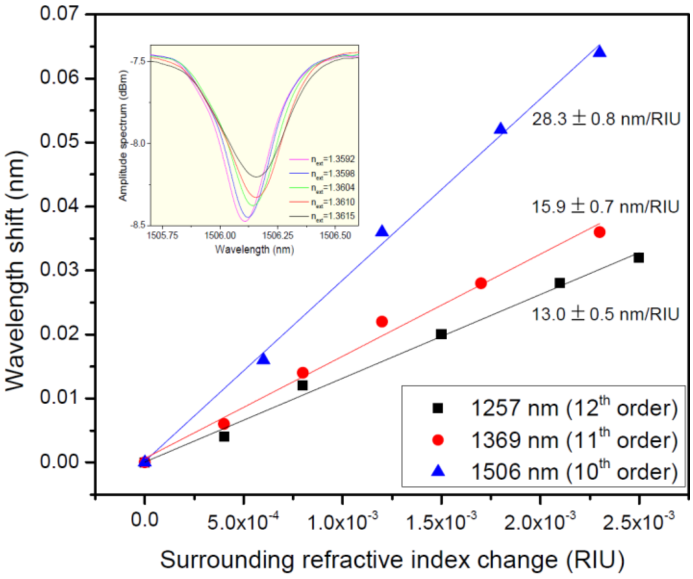

Figure 71: Refractometric sensitivity as a function of the grating order. Inset: wavelength shift of the most sensitive cladding mode resonance for the 10th order grating.

6.2.4 *Conclusion*

The characteristics of TFBGs inscribed using a femtosecond laser along with number of differences with the traditional process were reported. The immense inscription flexibility was confirmed, in particular the grating strength and angle. The low birefringence and the presence of higher order modes with their own set of cladding modes makes these TFBGs quite unique. This will open new paths to explore in regard to refractometric sensing. The index sensitivities were ~28 nm/RIU at ~1510 nm to ~13 nm/RIU at ~1260 nm.

6.3 Studies in Phosphate Glass Fibre

Here there is a focus on developing components in a bioresorbable phosphate fibre, such as uniform FBGs, chirped gratings, and Fabry-Perot cavities. Part of this work was presented as a poster presentation in Workshop on Specialty Optical Fibres (WSOF) October 2017, in Limassol, Cyprus.

6.3.1 Introduction

Optical and optoelectronic technologies have been widely used in biomedicine and healthcare related applications and the research efforts in this field are dramatically expanding in several directions. A recent research line arising from new advances in biomaterials science concerns the development of biomaterial based photonic devices able to degrade in physiological conditions once their functionality has expired. To this aim, different materials able to combine biodegradability with good optical properties have been synthesized.

The first biodegradable optical fibre was based on cellulose [190], while further studies led to the development of spider silk, fibroin and hydrogel based devices [191]–[193]. Hydrogels, in particular, are recognised as the ‘gold standard’ for bioresorbable optical devices thanks to their noticeable resistance, flexibility and transparency [194]. Recently calcium-phosphate glasses (CPGs) have been proposed as a new solution for the manufacture of resorbable devices [195]. These glasses, regarded as promising biomaterials since the 80’s, have been widely studied for the fabrication of bone scaffolds, resorbable composites and as support for neural growth [196]–[198]. CPGs offer superior optical properties in comparison to polymers, as they guarantee a wider window of transparency spanning from around 250 nm to about 2600 nm. Moreover, their refractive index and dissolution kinetics can be tailored by opportunely changing the composition.

CPG based bioresorbable optical fibres are mechanically reliable both in dry and humid environments [199] and to show the lowest attenuation values compared to all resorbable photonic devices reported in literature. These fibres were recently employed for diffuse optics experiments on biological tissues showing the same performances of silica based ones [200], and their photosensitivity in the deep ultraviolet (UV) region was also demonstrated [201].

The aim of this work is the femtosecond laser processing of the phosphate glass fibre to inscribe bioresorbable optical grating sensors. Again, the focus is on demonstrating the key optical filtering elements, such as FBGs, CFBGs and FFP, all characterised in reflection. The components were calibrated to temperature and relative humidity changes, and monitored over extended time periods, with the degradation of the FBG recorded in a high humidity environment for 52 hours.

Due to the high biocompatibility of the core and cladding calcium-phosphate glasses, the sensor developed in this work can be easily integrated into other resorbable biomedical components, such as bioactive scaffolds, resorbable composites, or implants for soft tissue regeneration. Providing that there is a suitable bioresorbable polymeric coating, the sensor could be also implanted as a single fibre for different applications. This paves the way towards the development of multifunctional inorganic structures for the monitoring and regeneration of human hard and soft tissues.

6.3.2 Fabrication and Characterization of the Phosphate Optical Fibre

The bioresorbable phosphate glass optical fibre used for the grating inscriptions was manufactured by preform drawing, with the preform being obtained by the rod-in-tube technique [202], and was sourced from collaborators at the Politecnico di Torino in Italy. In detail, the core glass rod was drawn into a 4-mm diameter cane and inserted into the first cladding tube. The fabricated core/cladding structure was then stretched into a 4 mm diameter rod and subsequently placed in the second cladding tube. The final preform was finally heated above the T_g and below the T_x to draw the optical fibre while the fibre's diameter was monitored during the drawing process.

The core and cladding calcium-phosphate glasses were *ad-hoc* developed for this research with the aim to ensure an exclusive combination of optical and biological functionalities [195]. The glasses proved to be homogeneous, stable against de-vitrification ($\Delta T \sim 200$ °C) and therefore suitable for crystal free fibre drawing; were transparent from UV to near-infrared (NIR) region; soluble in simulated biological environment (PBS, pH = 7.4 at 37 °C) with a dissolution rate of 2-4 μm/day. The above details give an indication that this homogeneous fibre may be well suited to femtosecond laser processing. Table 3 reports the thermal, physical, and optical properties of the manufactured core and cladding glasses.

Table 3: Glass transition temperature (T_g), onset crystallization temperature (T_x), glass stability parameter (ΔT), coefficient of thermal expansion (CTE), density and refractive index at 1533 nm of the manufactured calcium-phosphate core and cladding glasses.

Glass label	Core	Cladding
T_g [°C] ± 3 °C	435	435
T_x [°C] ± 3 °C	658	628
ΔT [°C] ± 6 °C	223	193
CTE [10^{-6} °C^{-1}] ± 0.1 °C^{-}	12.6	12.2
ρ [g cm^{-3}] ± 0.005 g cm^{-3}	2.606	2.600
n ± 0.001	1.514	1.512

The bioresorbable optical fibre has diameters of 15 and 120 μm for the core and the cladding, respectively, with a corresponding numerical aperture (NA) value of 0.08. These parameters were designed in order to achieve a SM behaviour at 1533 nm (V number = 2.390).

A good interface adhesion between the core and cladding was observed, thus proving the noticeable thermo-mechanical compatibility of the two glasses. Furthermore, the near-field imaging of the fibre output recorded using an IR camera highlighted a good confinement of the light beam inside the core of the fibre.

Attenuation loss coefficients of around 1.9 and 4.7 dB/m were measured respectively at 1300 and 633 nm. These values are in line with those typically exhibited by phosphate glass optical fibres [203] and one up to two orders of magnitude lower in the decibel scale than those published so far for bioresorbable optical fibres [204].

6.3.3 Bragg Grating Inscription in Phosphate Glass Fibres

The now familiar inscription setup was to produce the optical component. The pulse energies at the exit of the laser set at ~100 nJ/pulse and the repetition rate was set at 5 kHz using the pulse picker.

For the inscription of the uniform FBG operating at 1560 nm we set the grating's period at Λ= ~2 μm. The grating was 4th order to avoid any index overlap, while the inscription width set at 15 μm which is the diameter of the core and the total period number of periods was 1000 which results to a ~2 mm total length grating. Using an optical circulator, the FBGs illuminated using a broadband light-source (Thorlabs ASE730) and the reflection spectrum of the grating was measured using a commercial FBG demodulator (Ibsen IMON 512 High speed) with optical resolution ~169 pm (Fig. 72(a)).

From the reflection spectrum the FWHM grating bandwidth was 0.5 nm, whereas the effective refractive index was found to be n_{eff} = ~1.515.

In the same manner, we proceed with the inscription of a chirped grating. The initial period was ~2.060 μm for a 4th order FBG at 1561 nm and the final period was ~2.067 μm, corresponding to 1566 nm, giving a 5-nm chirped grating, (Fig. 72(b)). From the reflection spectrum, ripples up to 20% of the maximum reflection spectrum are observed, however this could be improved using a smaller chirp coefficient and higher period number.

Moreover, we proceeded with the inscription of a FPP using two identical FBGs separated by L=3.4 mm. Considering the length of the gratings was ~0.8 mm the effective optical length of the cavity is $L_{cavity} = {\sim}4.2\ mm$. The FSR of the cavity found to be 189 pm, while the finesse of the cavity calculated to be 3.16 as shown from the reflection spectrum in Figs. 73(a-b). This value of finesse corresponds to ~53 % reflectivity, which is logical considering that the gratings have less than 400 periods. As a result, the finesse of the cavity could be improved with stronger FBGs.

It is important to note that the fibre is very fragile and it was manually cleaved with a diamond blade, however, there was almost always a small cleave angle (<10^{o}). The phosphate samples were fusion spliced with a SMF28 pigtail using modified splicer settings on a Fujikura FSM100P+ fusion splicer. The small cleave angle influenced the splice quality, and so the reflection spectra occasionally show high back reflections. More details for the spicing settings are included in Appendix B.

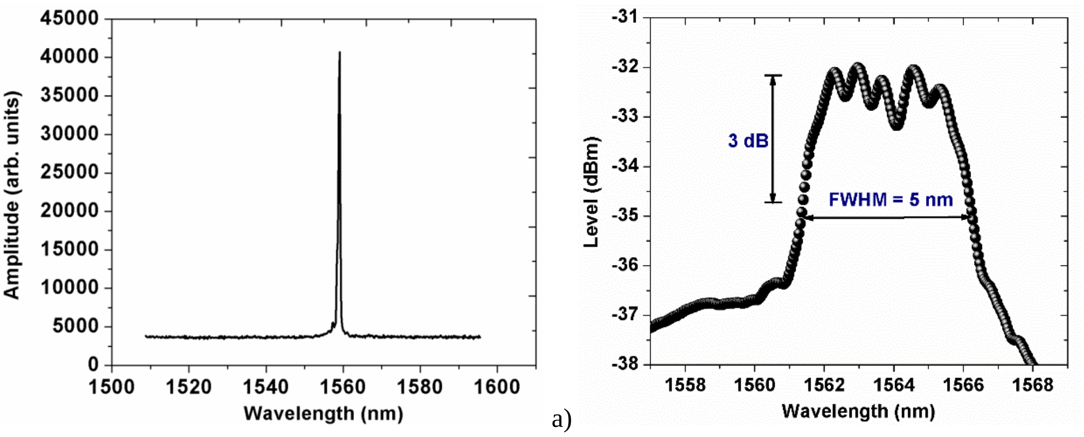

a) b)

Figure 72: a) Reflection spectrum of uniform FBG in the phosphate fibre, as recovered using a commercial FBG demodulator and b) Reflection spectrum of 5-nm chirped grating inscribed in the phosphate fibre.

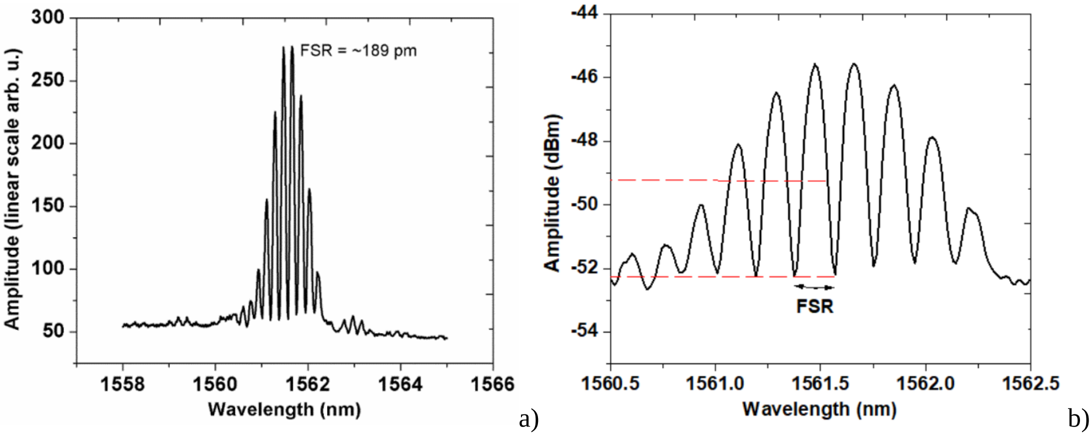

a) b)

Figure 73: Reflection spectra of the Fabry-Perot cavity in the phosphate glass fibre.

6.3.4 Characterisation and Calibration of the Bioresorbable Optical Sensors

The key application of the bioresorbable sensors is insertion in to the human body; as a result it is essential to study the sensor behaviour when inserted in environments with high water content, as one would find in blood vessels. In addition, the response of the sensor to the temperature fluctuations is essential, since cross sensitivity issues could cause inaccuracies with the measurements.

Bearing this in mind, the FBG phosphate sample was placed in our climate chamber and interrogated in reflection, as described in the previous section. We began our characterisation measurements with the temperature sensitivity. The relative humidity of the chamber kept constant at 35%, while the temperature was set to increase from 23 ^{o}C to 73 ^{o}C degrees within one hour. During this period spectral snapshots were recovered and the temperature of the climate chamber sensor was noted (internal sensor). The grating response was 12.7 pm/^{o}C (Fig. 74) whereas the grating amplitude was increased significantly (Fig. 75) for temperatures ranging from 25.3-73.1 ^{o}C; well within the body's operating temperature.

Subsequently, we kept the temperature constant (36 ^{o}C) and increased the relative humidity from 35% to 95%. After four hours the FBG wavelength shifted by only 0.025 nm, which gives a response to humidity of 0.416 pm/%RH (Fig. 76), not surprising as this is a glass-based fibre, and at this level can be neglected. Nevertheless, the grating was kept under these conditions for 52 hours and its reflection spectrum was captured every 6 hours. We observe the grating change in shape, amplitude, and wavelength. More specifically, a significant decrease of the grating magnitude was noted up to 52 hours, and the grating disappears (Fig. 77). Figure 78 presents more clearly the deviation of the amplitude with respect to time, which may be explained by the phosphate fibre dissolving in the high humidity environment. This is similar to a tilted-FBG inscribed in phosphate fibre using a UV laser, reported recently [205].

In addition, the reflection spectra of the grating was recovered using the Zero Crossing Algorithm [206] and shown in Fig. 79. The Bragg grating showed an initial positive wavelength shift over the first four hours, as previously shown in Fig. 76, and then followed a decent wavelength shift at an exponential rate (Fig. 79). In Fig. 79, the blue line is the humidity level inside the climate chamber according to the internal sensor, along with the FBG response (black line). At the first four hours the fibre absorbed a significant amount of the water content, slightly changing the fibre dimensions leading to a physical elongation of the fibre and positive wavelength shift. Following this, the dissolution procedure occurred was a reduction in the cladding's refractive index, reducing the effective refractive index and leading to a negative wavelength shift of the grating. It is noted that due to the connectorisation issues referred previously, only the uniform FBG was characterised, however similar response expected from all the other optical devices since the changes are related to the material properties

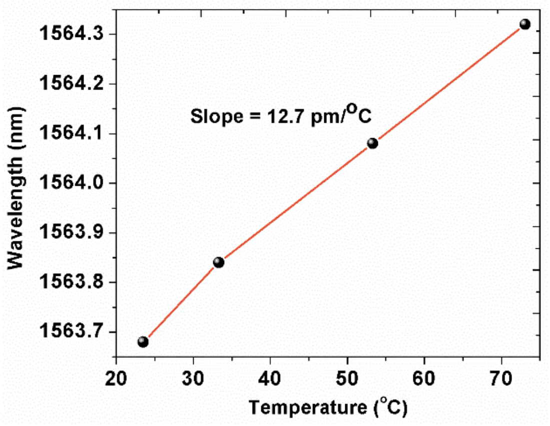

Figure 74: Temperature response of a uniform FBG inscribed in the phosphate fibre.

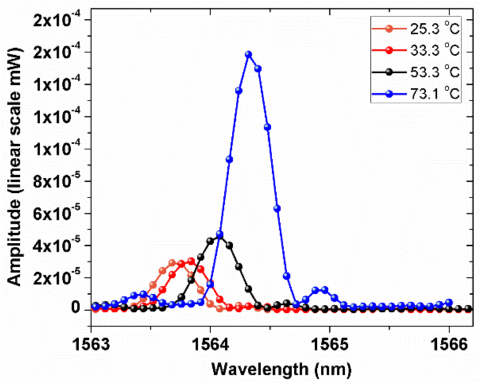

Figure 75: The amplitude change of the uniform FBG inscribed in a phosphate fibre when the temperature was increased ~50°C above room temperature.

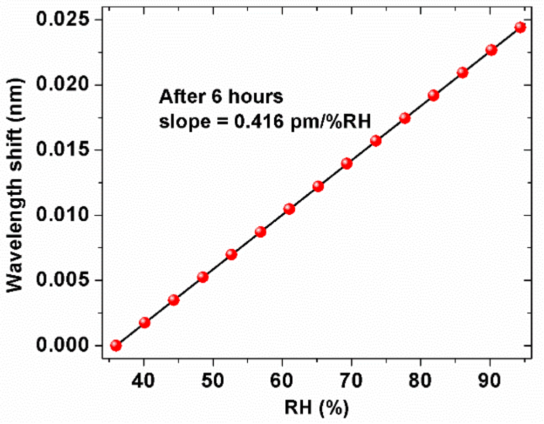

Figure 76: The grating response when the environmental relative humidity changes from 35% to 90% at ~36°C.

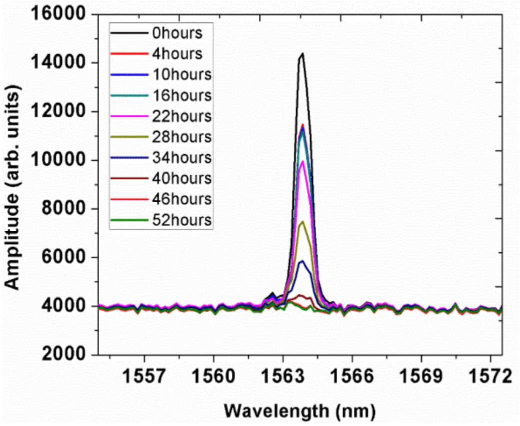

Figure 77: Reflection spectra of a uniform FBG inscribed in the phosphate fibre for different time periods, following insertion into the climate chamber with 95% relative humidity and temperature similar to human body (~36 °C).

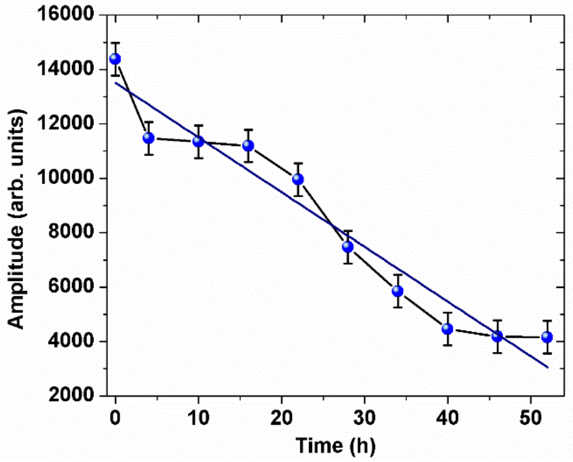

Figure 78: Amplitude modulation of the phosphate FBG when inserted in a climate chamber with high relative humidity levels.

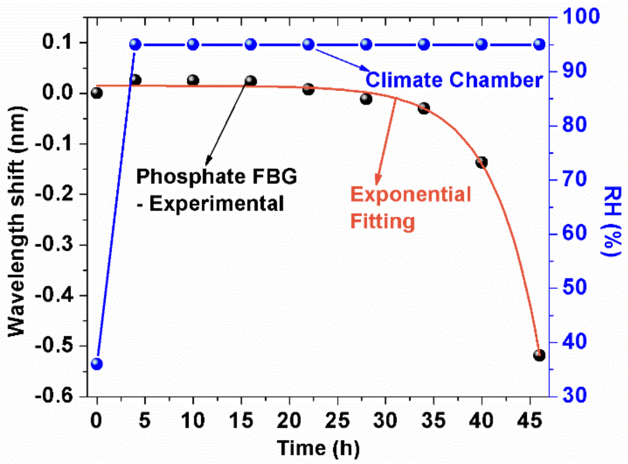

Figure 79: Wavelength shift of the phosphate Bragg grating as monitored for different time intervals when inserted to a climate chamber with relative humidity at 95%.

7 *Waveguide Inscription Using a Femtosecond Laser*

The inscription of integrated fibre devices is critical for the realisation of compact micro-sensors. Here femtosecond laser waveguide inscription is explored in the optical fibre cladding, with the development of evanescent waveguide couplers and monolithic Mach-Zehnder interferometers (MZIs), both incorporating Bragg gratings. New devices are developed for refractive index measurements. Finally, direct bridging waveguides are inscribed between single-core fibre (SMF28) and multi-core fibre (four cores).

Part of the work was presented as oral presentation at SPIE Photonics Europe in 2016 in Brussels.

7.1 Introduction

The use of femtosecond (fs) lasers as a means of directly writing structures and waveguides inside the bulk volume of glassy materials is considered a highly attractive approach, offering great flexibility and a simple, single-step processing. Femtosecond lasers have an inherent capability to perform high-resolution micromachining and inscription in many different transparent materials, including silica optical fibres. This selective material modification allows for the flexible patterning and prototyping of micro- and nano-structures. Using fs lasers the fabrication of photonic crystal arrays, diffractive elements and their templates is possible [106], [207]–[209]. With this in mind, the fabrication of different waveguide structures is explored in optical fibres, optimising the inscription parameters for optimal light coupling from the fibre core to the cladding waveguide, this leads to waveguide Bragg gratings, Mach-Zehnder interferometers and vectorial sensors in a 4-core fibre. Critically the same key laser-inscription parameters for making the FBG components were used for the waveguide inscription, making the method applicable to any type of miniature optical component. This approach ensures reliability and repetition in component manufacture, as the same basic conditions are used to inscribe the MZI and FBG. Moreover, the integrated, compound cladding sensor has a minimal effect on the fibre strength (through the jacket inscription), leading to a robust sensing device. We show that the sensors maintain their unique sensing capabilities, and present various measurement results.

7.2 Cladding Waveguide Inscription

For the inscription of the waveguides the same FBG inscription setup was used. The energy for all the waveguide inscriptions was set to ~105 nJ/pulse as measured at the exit of the laser with a repetition rate of 100 kHz. The waveguide was fabricated by focusing the laser beam to the same depth as the fibre core, but translated to the side of the core, so that light was coupled *evanescently* to the waveguide [210], [211] as shown in Fig 80. Briefly, using a controlled G-code script the waveguide structure begins with a selected coupling length (length 1), a smooth move away of the core having a specific angle creates an S-bend in the middle of the cladding and this is followed by a straight motion (length 2). The process repeated several times with a specific step between each inscription until the waveguide reaches the desirable width. In this way the mode profile of the cladding waveguide can be controlled. A microscope image of two waveguides inscribed parallel to the fibre core are shown in Fig. 81. The fibre core is illuminated with visible light operating at 630 nm, and the light coupled to the cladding waveguides is visible scattering. Note, that for these samples the inscription was stopped 5 μm before the cleave end of the fibre in order to avoid damage to the fibre end face.

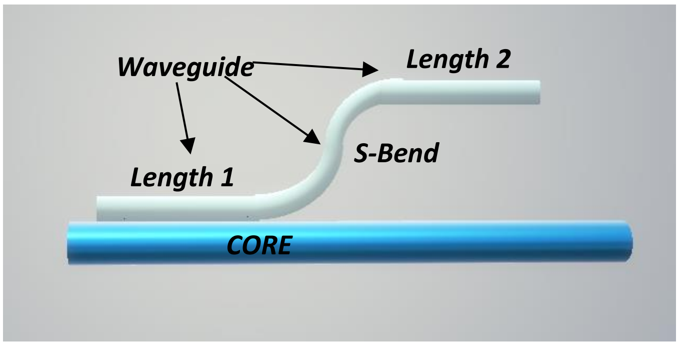

Figure 80: Schematic diagram of the waveguide in the cladding of a silica optical fibre.

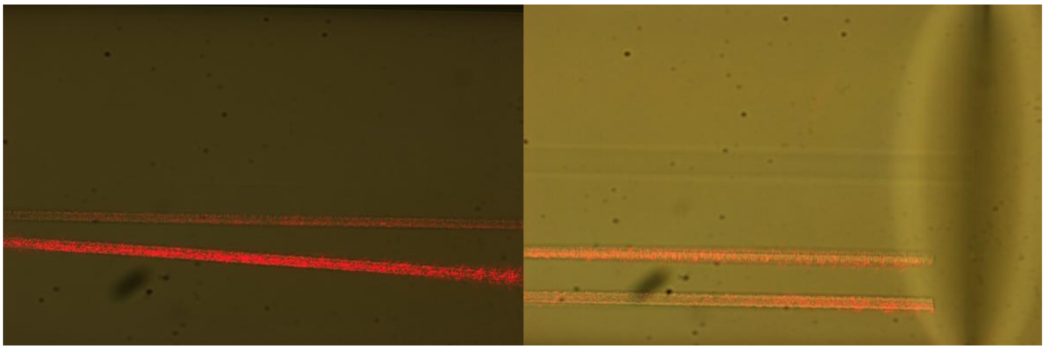

Figure 81: Two cladding waveguides imaged using a microscope, after the fibre core is illuminated with a red laser diode source. Scattering of light in the region of the waveguide is observed.

A series of inscription were performed in order to investigate the optimal conditions to achieve an ideal 50% coupling efficiency for the MZI, extracting light passing through the fibre core, whilst also ensuring a circular beam profile. After each inscription the fibre samples were connected with visible light source operating at 630 nm and the output light profile of the waveguide was captured using a profilometer (Veeco – Wyko NT9100) in intensity measurements mode ((the instrument acts only as a camera system in this mode). The waveguides were 'built-up' having translation steps between each repetition that varied from 0.3 – 0.8 μm. The coupling lengths were selected to be 0.25 mm, 0.5 mm, or 1 mm. The target waveguide size, larger pulse energy and repetition were 6 μm, 110 nJ/pulse, and 100 kHz, respectively. These parameters were kept constant for all inscriptions for better comparison between the waveguide samples. Using this approach the waveguide was developed to the desired final size. Cladding waveguides could be inscribed in any location of the fibre cladding and it was a simple matter to inscribe several waveguides in one fibre. Using this approach, the waveguide was developed to the desired final size. Cladding waveguides could be inscribed in any location of the fibre cladding and it was a simple matter to inscribe several waveguides in one fibre.

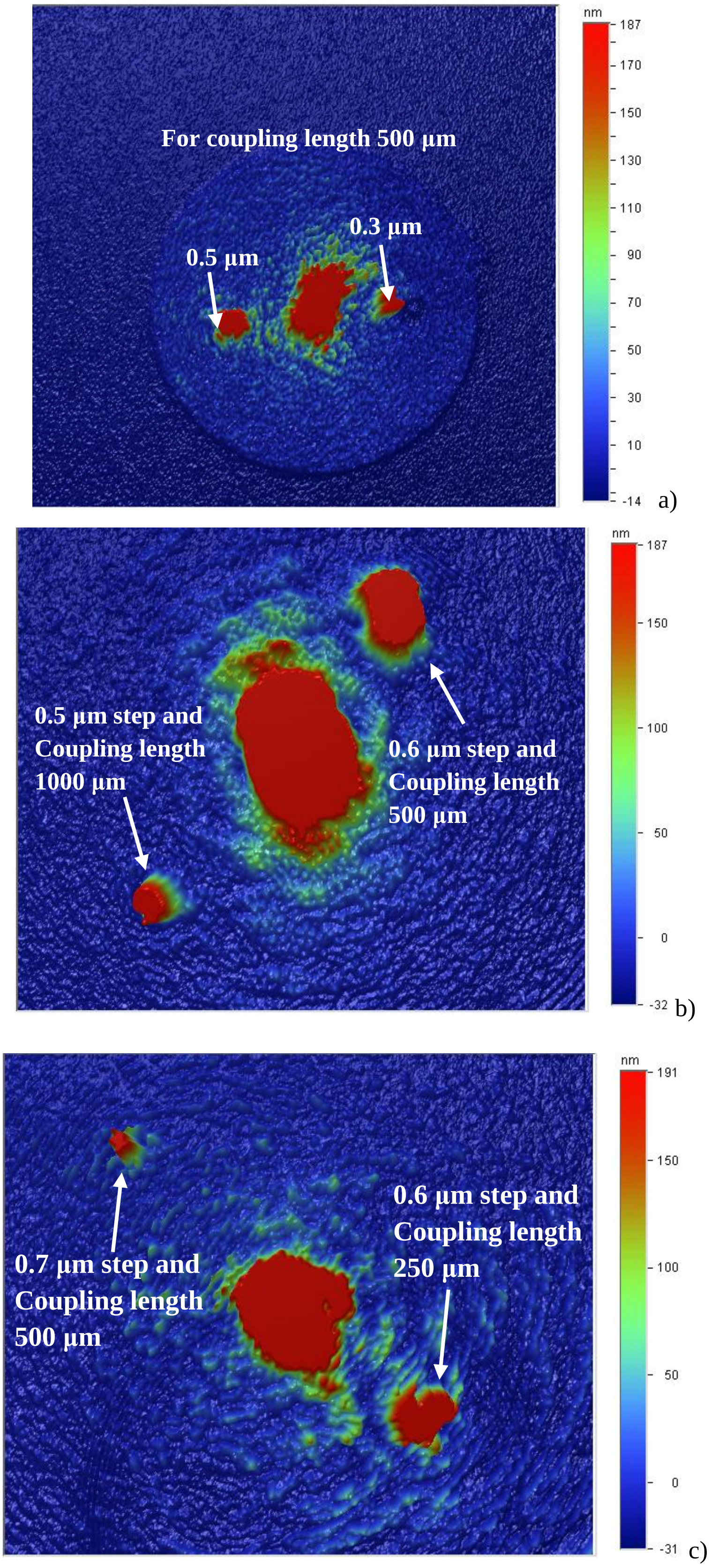

Figure 82: Waveguide inscription on the side of the core of single mode glass SMF28 fibre to find the optimal inscription parameters for optimal coupling between the core of the fibre and the waveguide and circular shape, a) 0.5 and 0.5 µm gap and coupling length 0.5 mm, b) 0.5 and 0.6 µm gap with couling length 1 mm and 0.5 mm, respectively, and c) 0.7 and 0.6 µm gap and coupling length 0.5 mm and 0.25 mm, respectively.

Our inscriptions began with two waveguides having a coupling length of 500 μm and translation step 0.5 and 0.3 μm, respectively. The two waveguides were inscribed on the same sample; one to the left of the core and one to the right, and the output profile of the two waveguides as measured using the profilometer are shown in Fig. 82(a). For 0.5 μm steps the profile of the light is more circular and the light exiting the waveguide is comparatively greater than the 0.3 μm step waveguide. For the next sample (Fig. 82(b)), two waveguides were inscribed again, one with coupling length 1000 μm and a 0.5-μm step and one with the same coupling length as the previous samples (500 μm) but having 0.6-μm step. We observed that the longer coupling length doesn't improve the coupling efficiency of the waveguide. On the other hand, for a 0.6-μm step and 500-μm coupling length, the coupling efficiency exceeded 30% and the shape of the output was similar to the core. For the next inscription sample the coupling length was decreased to 250 μm and the step was kept at 0.6 μm for the one side, whereas for the other side the coupling length was 500 μm but step was 0.7 μm. The results showed no improvement for either waveguide (Fig. 82(c)). It appears that the optimized conditions for the coupling coefficient and waveguide shape are a coupling length of 500 μm and 0.6-μm step between the inscriptions.

It is known that the distance between coupling waveguides should be less than the wavelength of transmitted light for maximal evanescent wave coupling if the coupling length is limited (our case) [212]. This is supported by results derived from side polished optical fibre couplers, which are true evanescent wave couplers. For the side polished coupler, a gap of ~0.3–0.5 μm ensures excellent coupling. To account for the core to waveguide spacing, we control the spacing choosing initially a 0.5-μm gap (readily possible) and then a gap of 0.8 μm towards the core from the other side of the core. The resulting output light is shown in Fig. 83, the smaller gap improves the light coupling to >40% compared to <10% for the waveguide inscribed with the larger gap.

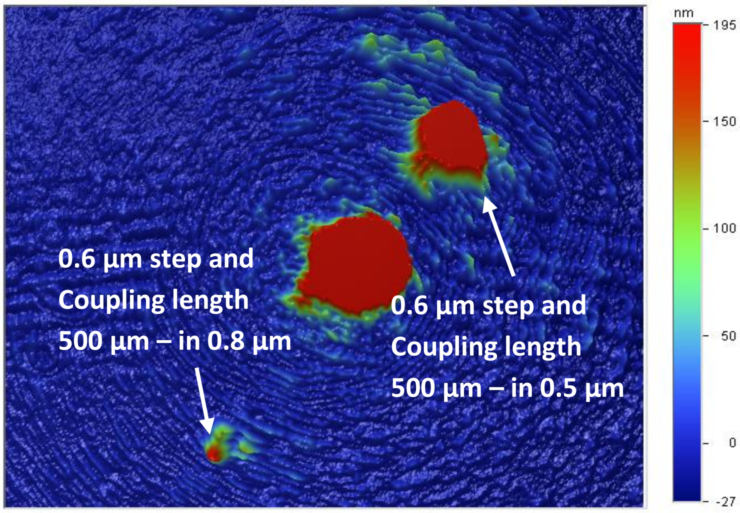

Figure 83: Waveguides inscribed with a coupling length of 0.5 mm and 0.6-µm repetition step. For 0.8-µm gap between waveguide and core leads to a coupling efficiency <10%, whereas reducing the gap to 0.5 µm improves the coupling efficiency to >40%.

7.3 Waveguide Bragg Grating Inscription and Characterisation

7.3.1 *Waveguide Bragg Grating Inscription Details*

Uniform, in-core FBGs have shown high sensitivity to environmental parameters such as temperature and strain. However, FBGs are too far from the cladding/air interface to interact with external media, hence TFBGs or long period gratings that couple light to the cladding and beyond are used to make refractive index measurements [213]–[215]. However, both TFBGs and LPGs generally operate in transmission (they can be made to operate in reflection, with restrictions), limiting sensors for in-vivo biomedical measurements. If we consider that the measurement of refractive index can be related with the different diseases [216]–[218], the development and use of refractive index sensors operating in reflection is important.

For this reason, a method was developed to inscribe a uniform FBG inside to the inscribed waveguide structure. The key is that the inscription properties for the waveguide and FBG are very similar, making this method extremely flexible. For example, if the PbP method was used for the FBG inscription, the laser energy would have to be increased by an order of magnitude compared to the requirements for the waveguide.

The waveguide was inscribed as described earlier and the length was increased to 4.5 mm to ensure enough length for the FBG inscription. Figure 84 shows a microscope image of the Waveguide Bragg Grating (WBG). For the inscription of the WBG, we retained the energy used for waveguide inscription, and increased the repetition rate to 100 kHz. A total of 2000 planes were inscribed across the waveguide with a period of ~2.18 μm. During the grating inscription the sample was connected to an optical circulator, and we illuminated the grating using a broadband light source (Thorlabs ASE730); the reflection spectrum of the grating was recovered using an OSA (Advantest Q8384). Figure 85(a) shows the grating growth in reflection for the WBG during the inscription process and for different grating lengths while Fig. 85(b) shows the final grating reflection spectrum for the total length of 4.5 mm. The grating was located at 1583.6 nm (~0.5 nm bandwidth) and the effective index was n_{eff}=1.4506.

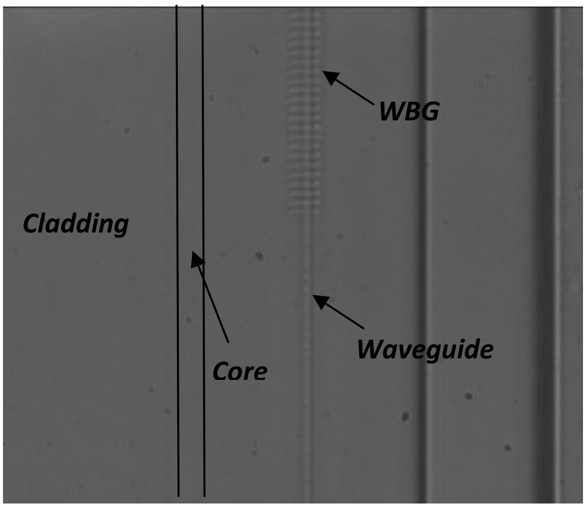

Figure 84: Microscope image that shows the location of the fibre core, the cladding, the laser inscribed waveguide and the WBG.

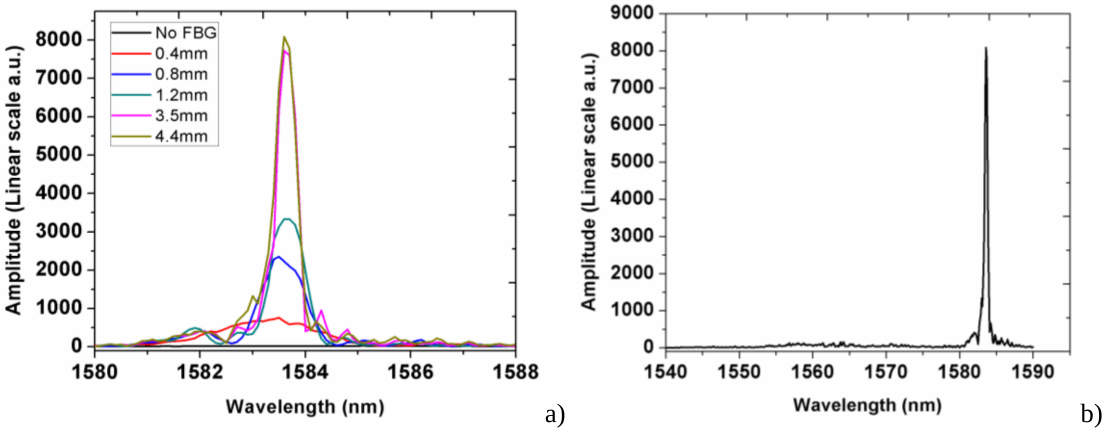

Figure 85: a) Grating growth reflection spectrum and b) final reflection spectrum of the WBG as recovered using the Advantest Q8384 OSA with 10 pm optical resolution.

7.3.2 *Characterisation of the Waveguide Bragg Grating*

To characterise the strain response of the grating we fixed the sample between two manual stages using UV glue and axial strain steps were applied. The response of the WBG to the strain was found to be ~0.8 pm/με as shown in Fig. 86. Measurement of the WBG curvature response is shown in Fig. 87 for three directions (left, right, up) and the linear fit slope sensitivity of the waveguide for each direction varying from 54 pm/m^{-1} for right direction, 29 pm/m^{-1} for left direction, and 8 pm/m^{-1} for up direction. The given directions refer to the position of the fibre sample on the experimental measuring setup and not on the position of the WBG in the fibre. From the results the WBG is located on the lower-right region of the fibre, as shown in the schematic in Fig. 87. Whereas it is clear that the WBG is not centred on the stage, we observe different sensing responses for the different bend directions, as shown in the schematic in Fig.87(right)).

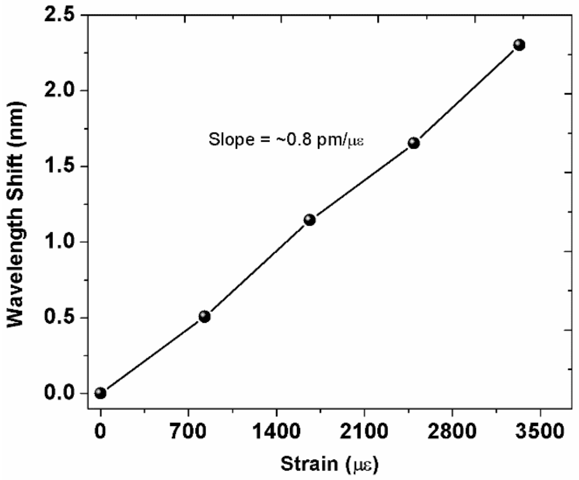

Figure 86: Strain response of the waveguide Bragg grating.

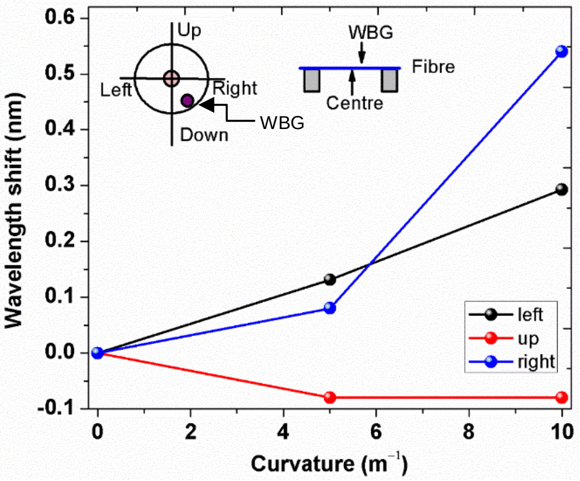

Figure 87: Bend sensing measurements using the WBG inscribed on the side of the core of an SMF28 fibre.

Finally, the WBG was immersed in three different liquids and found to be sensitive to the surrounding refractive index (RI). More particularly, the fibre was immersed in water (RI=1.33), alcohol (RI= 1.361), and index matching oil (RI= 1.518). The first measurements show a negative wavelength shift when the outer refractive index is smaller than the effective refractive of the FBG (alcohol and water), and positive when the refractive index is larger (oil) as shown in Fig. 88. However, more measurements with different RI values are required to complete the sensitivity response of the WBG for refractive index variations.

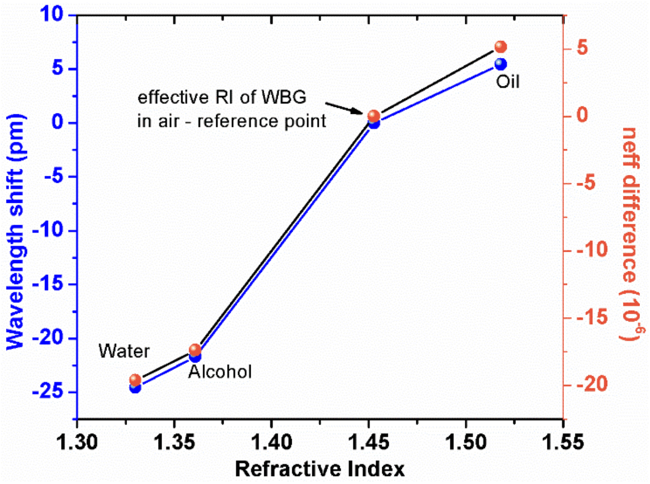

Figure 88: Refractive index measurements using waveguide Bragg grating.

7.4 Mach-Zehnder Waveguide Inscription

7.4.1 *Waveguide Mach-Zehnder Inscription*

By mirroring the previous waveguide so that it now couples back to the core, we arrive at the next waveguide structure, the Mach-Zehnder interferometer (MZI); the schematic diagram of which is shown in Fig. 89. The physical path difference between the waveguide and core is very small since most of the waveguide structure runs parallel to the core except in the S-bend sections, and our calculations estimate that the physical path difference is sub-micron. As a result, the OPD is principally dependant on the refractive index change induced during the waveguide inscription.

The MZI were inscribed with the same inscription setup as before and the repetition step between the waveguide “building” inscriptions was 0.3 μm. Various inscriptions were performed changing the coupling lengths (section 1 and 2, Fig. 89) and S-bend angle, and spectra were captured for different waveguide dimensions. Specifically, the MZI transmission spectra were measured during the inscription process using a broadband light source (1200-1650 nm) and OSA, every 0.9 μm of incremental waveguide width, equivalent to three laser inscription scans.

Figure 90(a-c) shows examples of the MZI transmission spectra for coupling lengths 250, 500, and 1000 μm, respectively, for waveguide sizes ranging from 2.7 - 6.3 μm. By comparing the transmission spectra for all the coupling lengths, two observations are noted. Firstly, as the waveguide size increases the MZI dips are shift to higher wavelengths and secondly, for smaller coupling lengths, the MZI are formed with smaller waveguide dimensions.

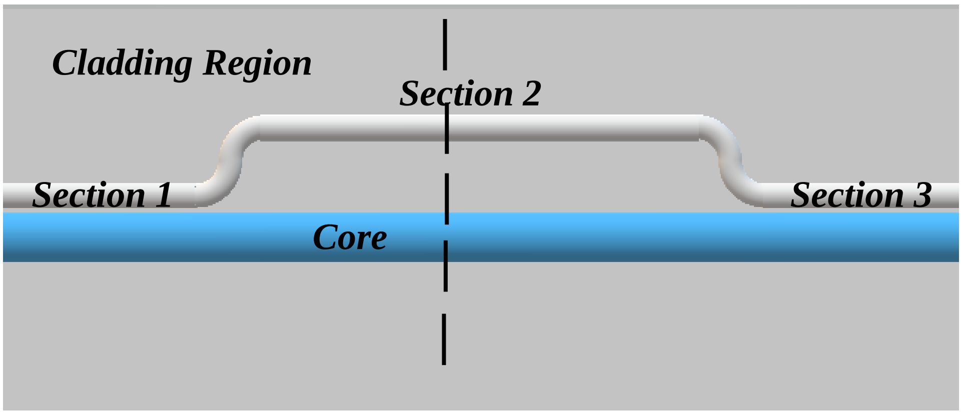

Figure 89: Schematic diagram of the MZI structure inscribed using a femtosecond laser in SMF28.

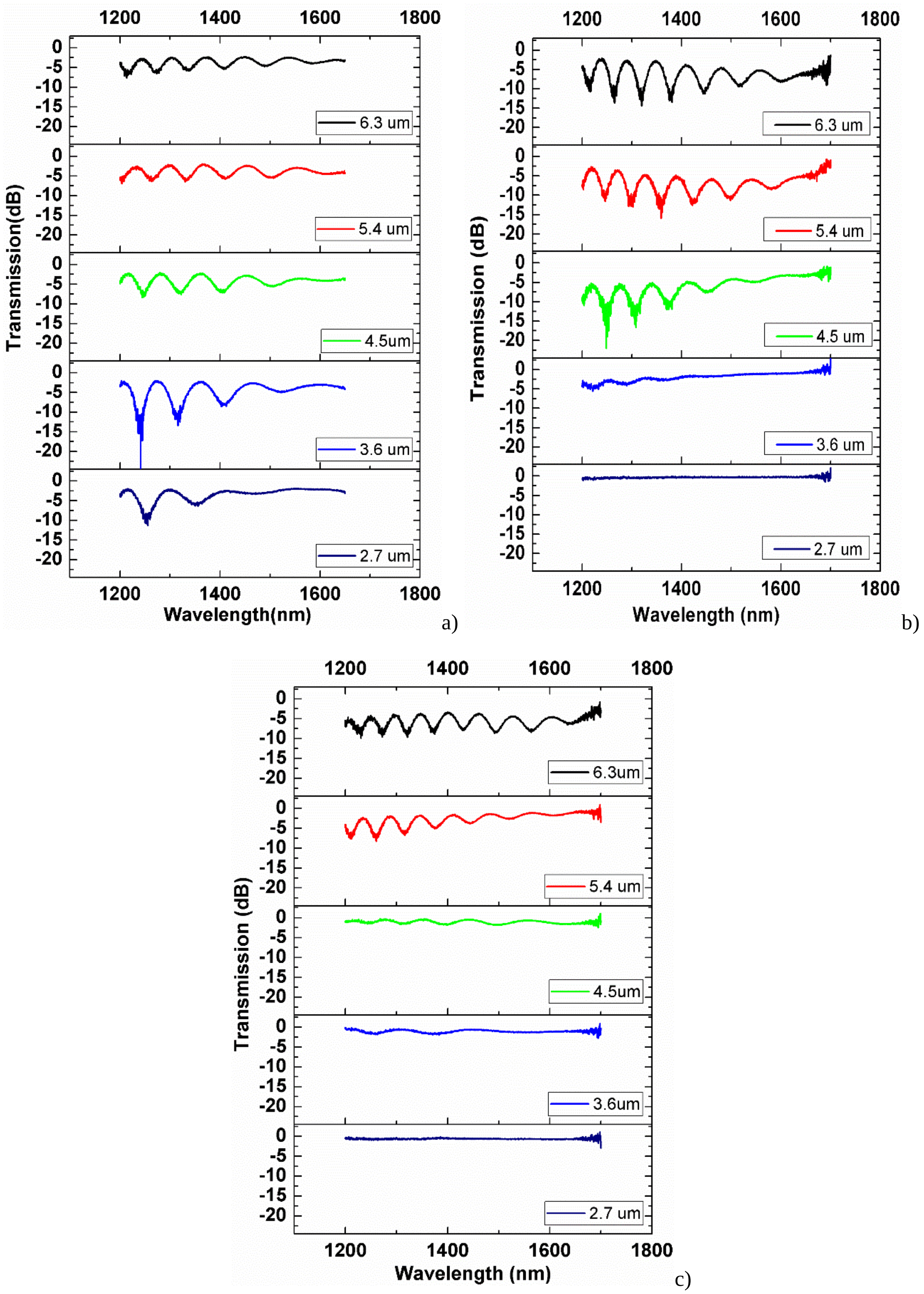

Figure 90: Mach-Zehnder interferometers inscribed with coupling lengths a**)** 250 μm, b) 500 μm, and c) 1000 μm for different waveguide structure dimensions.

As shown in Fig. 90(a-c) for a MZI with waveguide width of 2.7 μm and coupling length 250 μm, there is a ~10 dB notch at ~1250 nm, whereas for larger coupling lengths no further features appear in the spectrum. For coupling lengths of 500 and 1000 μm, the

MZI notches appear for a waveguide width 3.6 μm. However, for a 500 μm coupling length the MZI notches cover all the available spectrum, while for the 1000-μm coupling length significant features appear only in the range 1200 – 1400 nm. It is clear that as the waveguide increases the MZI notches also increase, beginning with lower wavelength notches; this is clearer for the 1000-μm coupling length. This may appear to be in conflict with the waveguide results presented in the section 7.2, where a higher coupling efficiency to the waveguide was achieved with a short 250-μm coupling length and 3.6 μm waveguide size. However, the earlier waveguides were illuminated at 630 nm, and when that is considered the results actually support our MZI study. Therefore, one would anticipate that a MZI operating at 1550 nm would require a waveguide size of at least 4.5 μm and longer coupling lengths.

Figure 91(a-c) shows the FSR of the three MZIs and we observe that as the waveguide size increases the FSR decreases, which is clearly related to the influence of the index change on the OPD, where the overlap between two consecutive inscription repetitions can be >75%. The refractive index increases, simultaneously increasing the OPD and decreasing the FSR. According to the spectral characteristics in Fig.90 and by solving the equation 2.61 in Chapter 2 to n_{eff} as shown below, the estimated refractive index value is ~3.8x10^{-3} for the final MZI structure in all cases, as shown in Fig. 91.

$$\Delta n_{eff} = \frac{(\lambda)^2}{L\,\Delta\lambda_{FSR}}, \quad (7.1)$$

According to the MZI spectrum shown in Fig. 90(c), with waveguide width 6.3 μm and 1 mm coupling length, the refractive index difference was calculated for all the fringes within the range 1250 – 1600 nm. The results shown the refractive index deviates as the wavelength increasing (Fig. 91(d)).

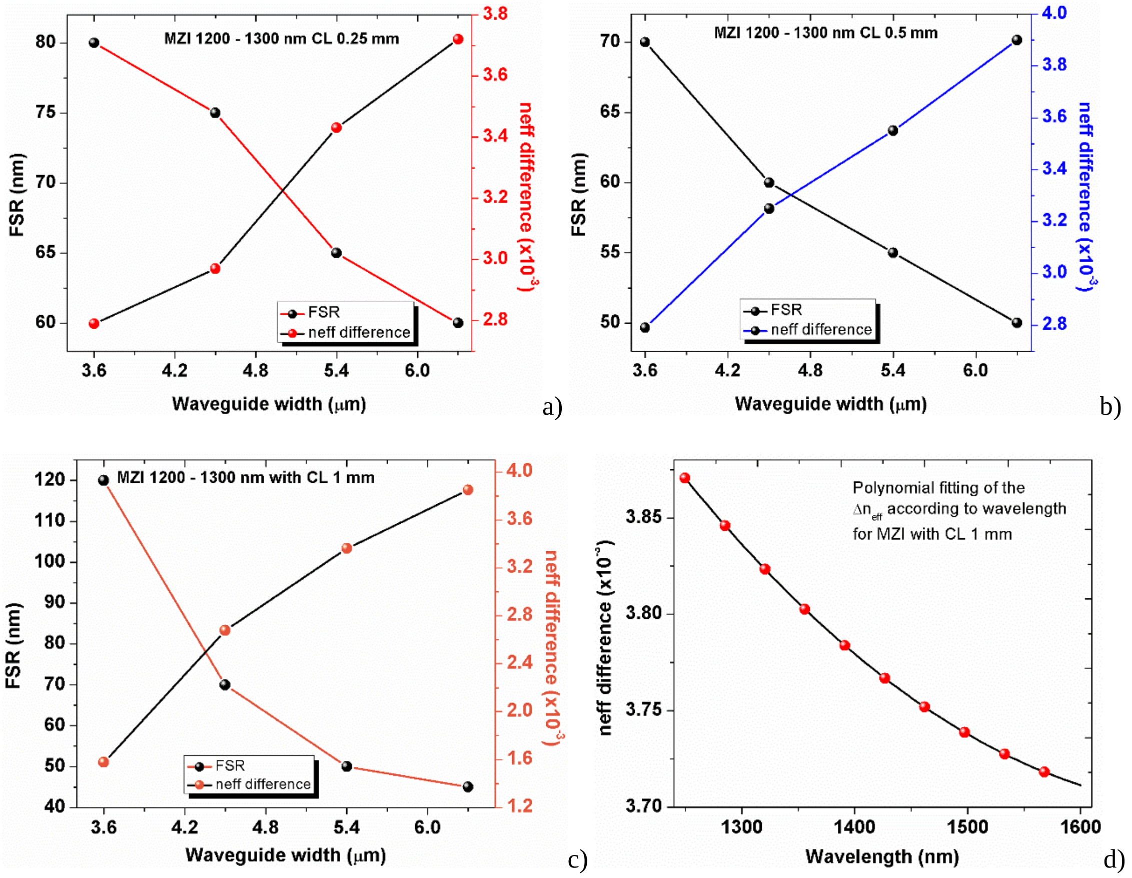

Figure 91: Free spectral range of the MZI and refractive index difference between the core and the waveguide with respect to the waveguide width a) 250 μm b) 500 μm, c) 1000 μm coupling length for MZI fringes at 1200 - 1300 nm region. d) The refractive index difference in respect to the wavelength.

7.4.2 *FBG Inscription in a Waveguide Mach-Zehnder Interferometer*

We continue by incorporating an FBG into the section 2 of the MZI (Fig.89). By keeping the same pulse energy as used for the inscription of the MZI and increasing the number of pulses/μm, a ~4.5-mm long FBG was inscribed. The grating had a period Λ=~2.18 μm and consisted of approximately 2000 periods. Figure 92(a) shows the transmission spectrum of the MZI with the FBG. A zoomed spectrum shown in Fig. 92(b), while the grating reflection spectrum shown in Fig. 92(c) and shows excellent uniformity. The FBG is located at ~1580 nm with ~50% reflectivity and bandwidth (FWHM) ~0.9 nm. The multiple dips appear in the range 1320-1420 nm are associated with the light source.

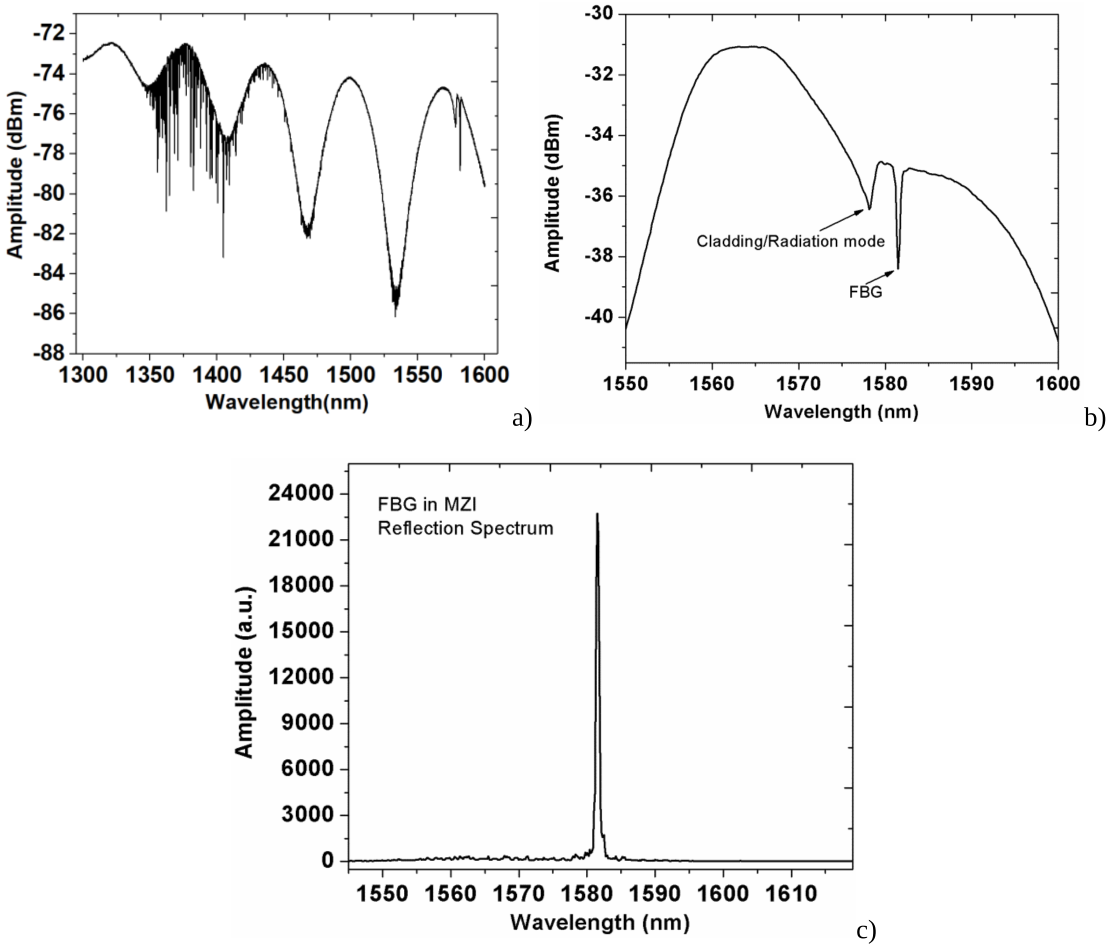
a) b) c)

Figure 92: FBG inscribed in the MZI a) transmission spectrum of FBG and MZI, b) Zoomed picture of the FBG transmission spectrum, and c) the FBG reflection spectrum.

7.4.3 *Humidity and Temperature Sensing Using the FBG-MZI*

The compound sensor has the advantage that each element maintains its basic sensing characteristics, as each sensor operates in a fundamentally different way. In order to justify this marrying of sensors the temperature and humidity response of the FBG-MZI are measured. For our purposes the outer coating of the fibre was removed and placed inside the climate chamber for controlled variation of the temperature and relative humidity. The transmission spectrum of the FBG-MZI before and after removal of the outer jacket is shown in Fig. 93. The black line is the spectrum before stripping and the FBG is observed at a spectral position with no MZI dips. However, once the coating is removed, the transmission dip of the MZI shift to the position of the FBG. The wavelength position of the FBG was 1581.51 nm and 1581.70 nm before and after stripping (and in the climate chamber), respectively. The FBG-MZI was mounted in the chamber using Kapton tape and there is a possibility that a small amount of strain was applied to the fibre sample and as a result the wavelengths shift of the FBG. The ~50 nm wavelength shift of the MZI dip was observed immediately after stripping and is certainly associated with the difference in refractive index once the coating is removed ($RI_{coating}$ = ~1.4682 at 1550 nm for Corning SMF28), and there is no measured change to the FSR. This suggests are refractive index sensitivity of ~107 nm/RIU.

The first temperature experiment was carried out with variations from 49.8 ^{o}C to 57 ^{o}C and keeping the relative humidity constant at 30%. The wavelength shift of the MZI fringe located at ~1560 nm was measured a negative wavelength shift with increasing temperature was noted to be -490 pm/ ^{o}C (Fig.94). In order to confirm the validity of the measurements the response of the FBG was measured (Fig. 95), for which an anticipated positive wavelength shift was recorded with slope ~11 pm/ ^{o}C, which is very similar to an FBG inscribed in the fibre core.

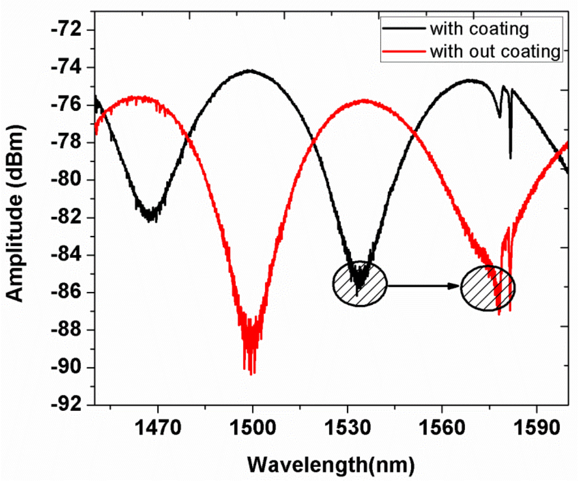

Figure 93: Transmission spectrum of the MZI with and without the outer polymer fibre jacket.

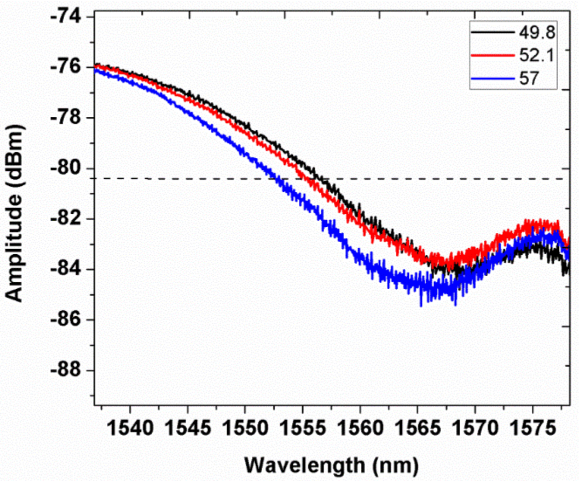

Figure 94: Wavelength shift of the Mach-Zehnder fringe located at ~1560 nm for different temperatures.

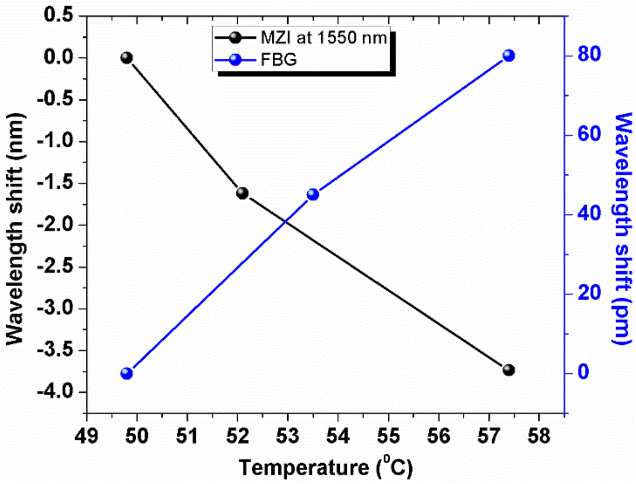

Figure 95: Wavelength shift of the Mach-Zehnder and FBG composite cladding sensor for different temperature values.

For a constant temperature of 50 °C the relative humidity of the chamber was changed from 49% to 75%, and 90% and the transmission spectrum was measured for each case. As shown in Fig. 96, the MZI shows a positive shift with increasing relative humidity. The interrogating source was weak and the dip was at the limit of the measurement dynamic range, therefore the wavelength shift was measured by tracking a point at the middle of the dip. The FBG was not affected by the relative humidity, (Fig. 97 blue), whereas the MZI showed a linear positive shift of 26 pm/%RH. The response of the MZI to the humidity is under investigation. The cause of this sensitivity to humidity is unclear as the index difference of moisture in the chamber is very small indeed.

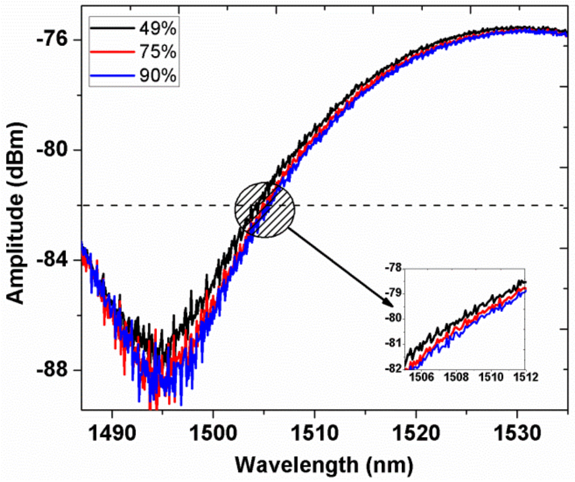

Figure 96: Humidity response of the Mach-Zehnder for relative humidity values 49%, 75%, and 90%.

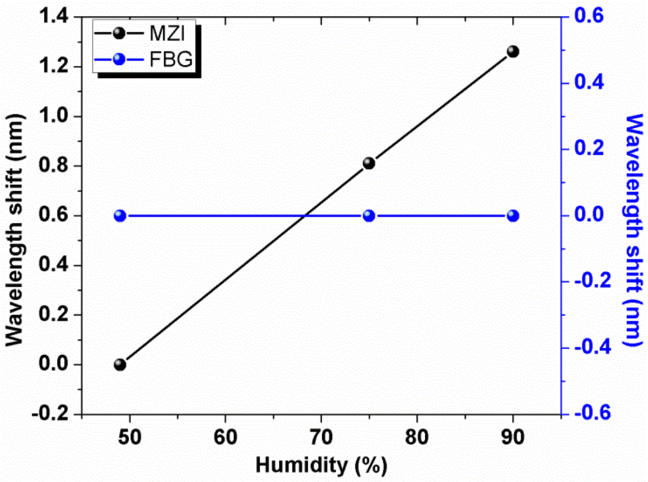

Figure 97: Comparison of the FBG and MZI response to humidity.

The integrated, compound cladding sensor is a robust sensing device and maintains the unique filter sensing characteristics, enabling co-located and complementary measurements. The same *key laser-inscription parameters* are used to develop two critical miniature optical components with a single inscription process, offering reliability and repetition in component manufacture. The FBGs are femtosecond inscribed using the direct-write; *plane-by-plane* method, this ensures that in contrast to other FBG inscription using a fs laser there is no need to change the laser energy as the device type is changed. We consider that this is an important step in the development of compact, smart optical fibre sensors.

7.5 Single Core Coupling with 4-Core fibre for Advanced FBG Sensor Development

7.5.1 *Introduction*

Multiple core fibres offer a possible solution to increase the data density on optical fibres or for the development of new types of vectorial optical sensors. However, a critical problem with this fibre type is the lack of efficient methods for coupling multicore fibre to existing networks or for coupling to single-core fibres and this is essential since all the existing optical equipment is designed for use with single core fibres. For this reason, a number of techniques have been proposed for simultaneously coupling between all the cores and single core fibres. Such methods are referred as either direct coupling techniques, such as tapered methods [219]–[221] and connection via a waveguide module [208], [222] or indirect coupling using lens systems [223]. As noted, the multiple core fibres have important applications in sensing, since the simultaneous interrogation of more than one core could be solve cross sensitivity issues or could be used for shape sensing applications.

A new, direct, and efficient coupling technique was developed to address the aforementioned issues and coupling between a single-core and four-core fibre was demonstrated via femtosecond laser inscribed *bridging waveguides*. Moreover, multiple FBG arrays were selectively inscribed in the cores of four-core fibre and their response recovered via a single-core fibre using conventional optical spectrometers.

7.5.2 *Coupling Waveguides Inscription - Bridging Waveguide*

In order to realise the bridging waveguide method, the following process was followed. Firstly, SMF28 fibre was fusion spliced to the multi-core fibre (Fibercore Ltd), of course the spatially separated cores did not exchange light, and light launched through the SMF28 was not injected into any of the four cores. By inscribing waveguides near to the single fibre core, we evanescently coupled light from that core to one or more cores in the multi-core fibre, thereby acting as bridging waveguides, Fig. 98 and 99; now the cores could transfer light signals between them. The waveguides were stopped a few microns before the core of the other fibre. The end face of the four-core fibre, with one of the cores “bridged” via the waveguide to the single mode fibre, is shown in Fig. 99; the image was captured using the Wyko profilometer. The image shows how only one of the four cores is illuminated and communicates with the single core fibre.

To demonstrate the efficiency of the method and the design of new kinds of optical fibre sensors, we modified the above recipe by *first* selectively inscribing three FBGs in each one of the four cores of the multi-core fibre, using the *Pl-by-Pl* inscription method (prior to waveguide inscription). The gratings consisted of 1000 planes with period of ~2.15 μm that were physically separated by 3 mm. Now the FBGs were monitored (but not yet observed) via the SMF28 fibre that was illuminated with the broadband light source (ASE730, Thorlabs) and connected to the OSA (Advantest Q8384) via a circulator. As the bridging waveguides were inscribed the FBG-array appeared with the increasing waveguide size (Fig. 100). The final spectrum for three of the four cores connected with the SMF28 is shown in Fig. 101. The FBGs where recorded at 1552, 1555, and 1557 nm for the first core, 1572, 1575, and 1577 nm for the second core, and 1582, 1585, and 1587 nm for the third core and the average grating bandwidth was ~1 nm. Particularly for the cases of the cores 2 and 3 (Fig.101), there is a magnitude variation between the gratings that may be explained as follows. The measurements are made in reflection and the source profile is not flat with wavelength (linear scale) and there is loss associated with the waveguides and gratings. On the other hand, the reflection spectrum inhomogeneity of the FBGs in the first core is likely caused by the quality of the inscribed waveguide.

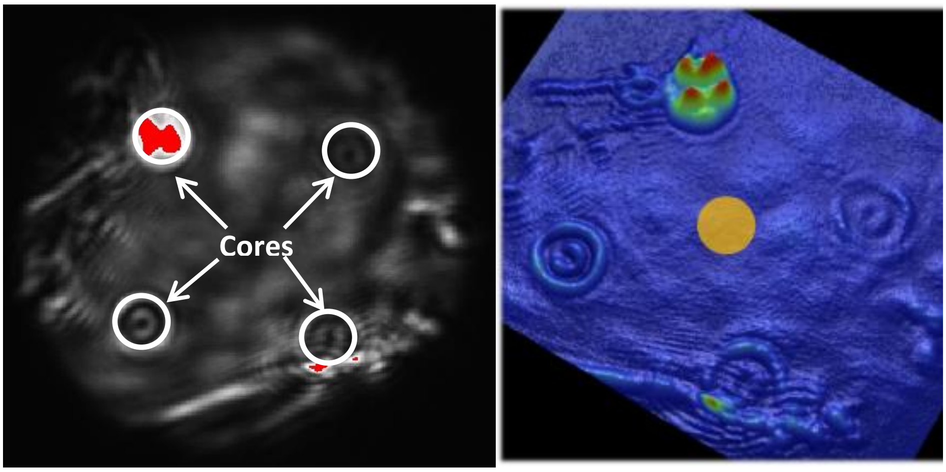

Figure 98: End-face picture of the four-core fibre when one of the four cores connected and red-light passing through the fibre as captured using a profilometer; we observe 1 bright and 3 dark cores.

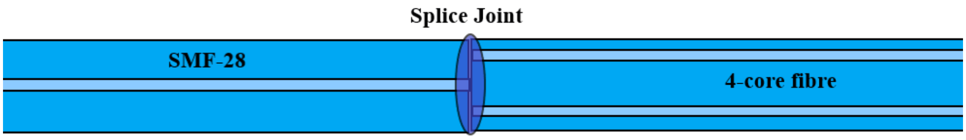

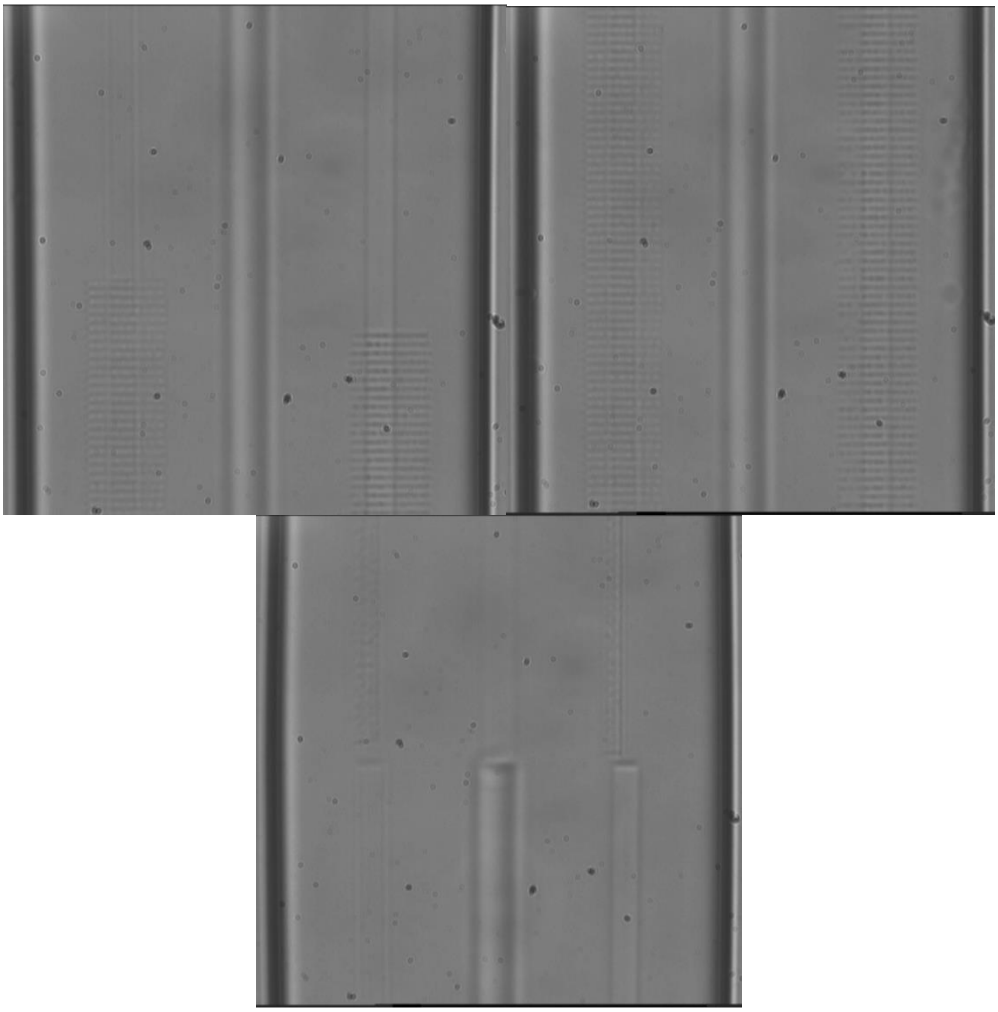

Figure 99: Microscope pictures of the FBGs inscribed in two of the four cores of a four core fibre (upper images) and the coupling point between the cores and the inscribed waveguides (lower images).

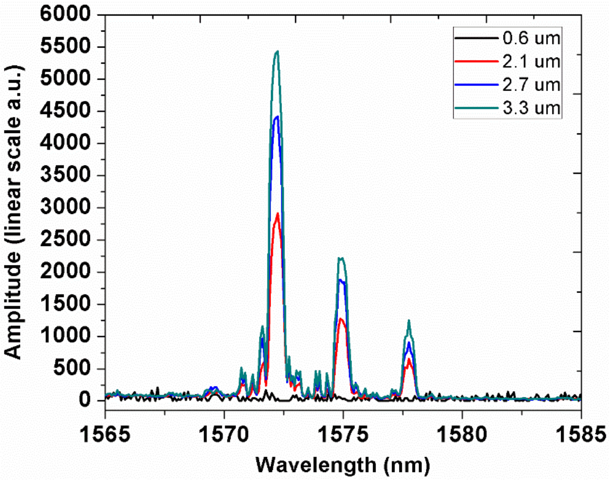

Figure 100: Appearance of the FBG array as the width of the waveguide is increased.

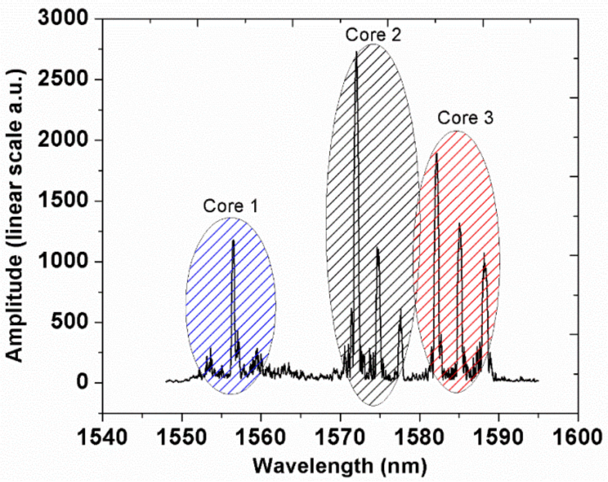

Figure 101: Reflection spectrum of three multiple FBG arrays, each array was inscribed in a different core of the 4-core fibre. The amplitude variation is related to the source profile and waveguide quality and grating loss.

7.5.3 *Response to Fibre Shape and Discussion*

The four-core FBG sensor was monitored in reflection and the response for each core and FBG is shown in Fig.102 with respect to the fibre shapes shown in Fig. 103. In Fig. 103 we observe four shapes; however, by looking the pictures carefully, the shape 1 and shape 2 are essentially the same, but with different angle, and their spectra are indeed similar; shape 3 and 4 are more complicated.

Comparing the reflection spectra of shape 1 and 2 in Figs. 102(a-b), a similar response is observed for cores 1 and 2 but with a variation in magnitude and a response opposite to that of core 3. More particularly, core 1 shows positive wavelength shift and core 2 negative for both cases while the core 3 shown positive wavelength shift for shape 1 and negative for the shape 2. Considering that the fibre shape is same for shape 1 and shape 2, then core 3 is actually indicating the direction of the fibre.

For the reflection spectrums in Fig.102(c-d) the shapes are more complicated. However, the fibre cores are responding in a similar manner to the two previous shapes, since the direction of the shapes is the same as before (up and left). The first core is compressed in both cases, and core 2 is strained in both cases. The FBGs in core 3, were strained, when the fibre experienced an upwards direction, whereas they underwent compression and a negative wavelength shift when the direction was to the left. Moreover, the expansion of the spiral shape could be translated with the magnitude of wavelength shift. For shape 3 the bend less severe than that in the shape 4, which resulted in a smaller wavelength shift.

We observe the potential of vectorial sensing by combining multi-core fibres and FBGs, but we also note that it is necessary to use machine learning techniques if the precise shapes are to be extracted, and this is under development.

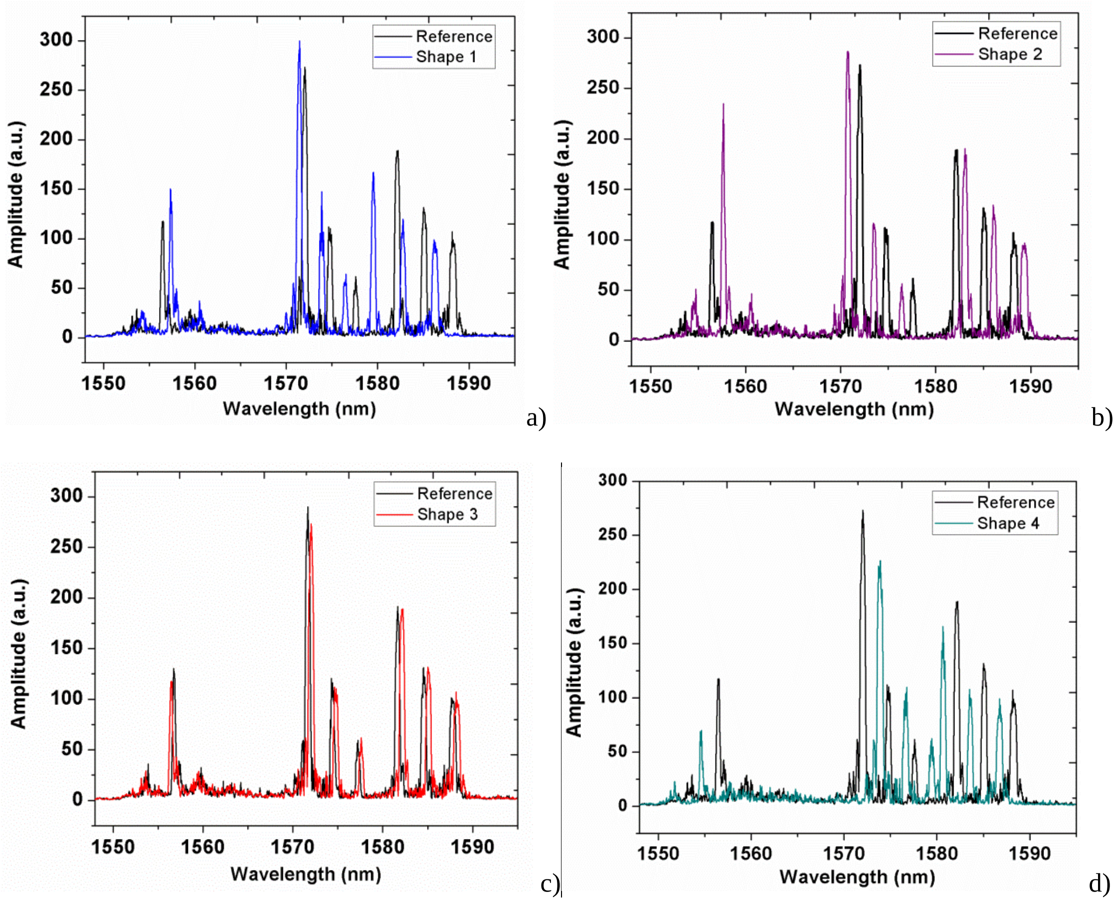

Figure 102: Response of the FBGs inscribed in different cores of the four core when undertaken to non-uniform bending.

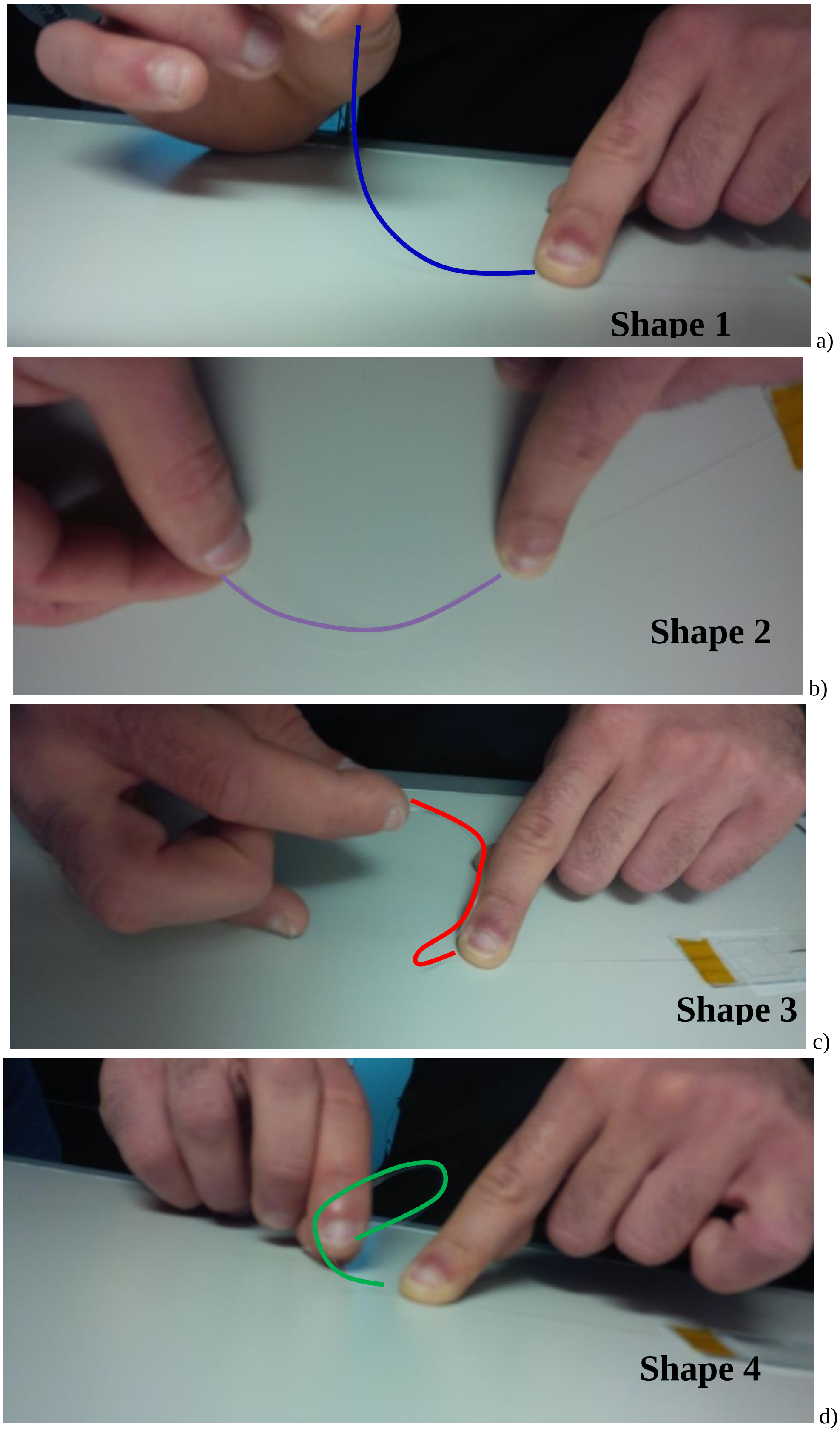

Figure 103: The fibre shapes corresponding to the FBG array responses presented in Fig. 102 a) Shape 1: bend shape with direction upwards, b) Shape 2: bend shape with direction on the left, c) Shape 3: spiral shape with direction upwards, d) Shape 4: spiral shape with direction on the left.

8 Silicon-Core Fibre Optic Sensors

This chapter describes the work on the inscription of FBGs in semiconductor, silicon-core fibres using visible femtosecond laser pulses. The inscribed FBGs were characterised in reflection and calibrated for strain and temperature showing significantly different responses compared to typical glass fibres.

This work was published in Optics Materials Express May 2017 and was presented as an oral presentation at the Workshop in Specialty Optical Fibres (WSOF) in October 2017 in Limassol, Cyprus.

8.1 Introduction

The semiconductor core fibres have emerged recently as an interesting alternative to planar silicon for a variety of optoelectronic application [224]–[226]. These fibres, are produced either by high pressure chemical vapour deposition [227] or by a modified glass-fibre drawing technique [228]. Silicon-core fibres drawn from bulk preforms have been made with lengths up to ~100 m and core diameters down to 12 µm [229], and resonators, tapers and splices have been made of these fibres, using conventional arc-based equipment [230]–[232]. Thermal annealing has been employed to reduce optical losses [233], and dc above-gap radiation has been used to recrystallize fibres, both for introducing high stress levels [234] in silicon cores, or for reducing optical losses in germanium [235] cores.

In addition to the modification of the fibre core, the interface between the core and cladding, or the entire fibre can be modified by appropriate choice of the laser source. Above-gap CW illumination has been used to modify the band-gap [234] and crystallinity [236] of the core and CO_2 lasers allow localized and reproducible heating and cooling of the glass cladding, and several commercial fibre fusion/tapering systems based on this effect are available for conventional fibres. CO_2 lasers have also been used to create tapers in nylon fibres [237] and, more recently, in pure silica glass used for gravity wave detector mirror suspensions [238]. Their use for recrystallization of the core in both silicon-[229] and SiGe-core [239] fibres has been reported. Pulsed lasers have been used extensively for the characterization of semiconductor-core fibres, but they can also be used to modify the stress at the core-cladding interface.

As the research in this thesis has consistently shown femtosecond (fs) lasers provide an alternative route to the traditional UV laser-induced modification of optical fibres [240]; via “direct-write” methods that have been shown to be an extremely flexible inscription process, producing high-resolution structuring of transparent and opaque materials. As has been noted the former process is typically an interaction driven through multi-photon absorption, and realized in the bulk material volume, whereas the latter is limited to laser-induced perturbations confined to the laser’s penetration depth in the material. Given that the typical pulse durations for the laser used in this research is <250 fs, one only needs moderate, average laser powers one can produce extremely intense laser pulses. The combination of the laser wavelength and short pulse duration ensures that rapid absorption takes place in silicon at sub-micron depths and the material absorption coefficient dramatically increases, concomitantly increasing the temperature at the laser focus. As this occurs on a scale comparable to the laser wavelength, it is readily possible to generate extreme temperatures ($10^4 – 10^5$ K) at the focus [241]. However, in contrast to the aforementioned CO_2 modification, the femtosecond process is essentially “cold”, as cooling rates are extremely high and the heat dissipation to the surroundings results in re-solidification of molten material, a process that has been shown to lead to the formation of amorphous silicon [242]–[244]. A significant obstacle for the realization of Bragg gratings using fs lasers, and in particular the point-by-point and line-by-line methods, is the need for precise inscription coinciding with the fibre’s longitudinal axis. This is needed to maximize the overlap between the grating and guided modes; demanding significant penetration into the core material [245]. In contrast, *plane-by-plane* FBG inscription method can readily modify the silicon-glass interface, and leading to stress modulation across the whole core [246], [247].

8.2 Fibre Fabrication

The fibres studied here were produced using a silica preform of 30 mm outer diameter and a 3-mm coated bore was loaded with a bulk silicon rod, and heated above the softening point of the glass, and well above the melting point of silicon. Drawing down the glass formed a coaxial silicon core silica clad fibre with 125 μm outer diameter and a 12 μm core. The fibre was manufactured by Professor Ursula Gibson and her group in Norwegian University of Science and Technology in Norway.

8.3 Fibre Bragg Grating Inscription in Silicon

All femtosecond laser inscription was undertaken at 517 nm and 5 kHz, with 220 fs pulse duration and pulse energies of 100 nJ. At this wavelength there is no penetration into the silicon, and linear absorption dominates, however the ultra-short pulses induce significant thermal loading and introduce strain at the interface between the glass and the core without significantly affecting the properties of the core material. The penetration depth in silicon at this wavelength is limited to ~1 μm, corresponding to an absorption coefficient of ~0.9 μm [248]. In these preliminary experiments, we used a pre-annealed 12 µm, single crystal core fibre [229], and exposed the side of the core to the 100-nJ laser with a focal spot size measured to be ~1 μm. The energy density was 100 kJ/m^2 (10 J/cm^2), a value that can readily result in the projected extreme temperatures at the laser focus. During the inscription process, strong plasma generation in the region of the Si core was observed as the laser swept across the core; this is consistent with the notion of extremely high temperatures in the regions of high fluence. The laser beam was swept transversely across the core at a velocity of 50 μm/s, resulting in a mean exposure of 100 pulses/µm; the fibre was displaced by a controlled step and this motion was repeated to define a periodic modulation along the fibre length. This resulted in the fabrication of a Bragg grating, which was probed in longitudinal reflection through the silicon core.

The periodic modulation of the core region occurred every ~1820 nm, corresponding to an 8th order grating; where it was determined that a silicon refractive index of 3.4408 would result in a grating close to 1565 nm. From the recovered spectra, our estimate for the refractive index of the guided modes was indeed ~3.44, which is close to the expected value; the index would drop slightly due to the overlap between the grating mode and the core/cladding. Due to the large core diameter and depending on the launch conditions it was possible to excite a number of modes, but it is also possible to excite the fundamental as the primary sampled mode. Figure 104(a) shows the spectrum for a 2000-plane FBG with a target reflectivity at 1565 nm where the reflected line-width is ~0.9 nm. In addition to the expected grating reflectivity, we observed significant stress changes in the core material resulting from the grating fabrication, and quasi-periodic stress relief in the glass cladding.

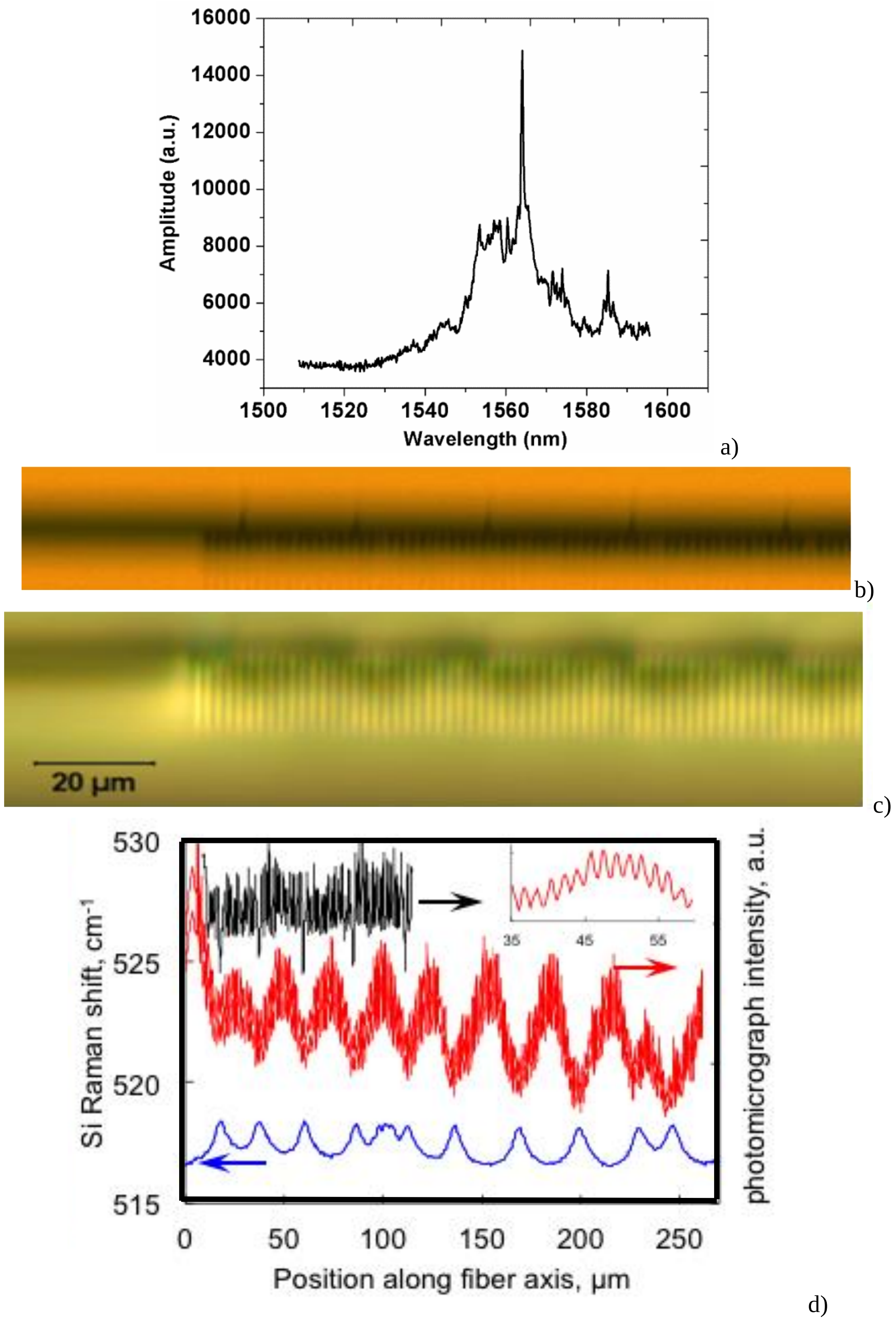

Figure 104: (a) Reflection spectrum from a 2000-plane grating written in the interface region of the silicon-core fibre. (b) Transmission image of fibre grating showing 1.8 µm period and additional features with a spacing of ~20µm. (c) Image of the same region through partially crossed polarizers, showing variations in the stress-induced birefringence. (d) Scans of the intensity vs. position along the images in (a- black curve) and (b- red curve), along with the Raman shift of the silicon peak plotted on the same axis. Insert shows an expanded region of (b) showing the grating period. There is a clear correlation between the crack-like features, the birefringence in the glass and the residual strain in the silicon.

Figure 104(b) is a microscope image of one end of the grating region, using transmitted light, showing the grating period, as well as some sharp aperiodic features extending away from the grating region. Figure 104 (c) is the same part of the fibre imaged through crossed polarizers; the colour variations are due to birefringence. The grating lines in glass, as well as quasi-periodic variations in the stress-induced birefringence can be seen. Figure 104(d) shows intensity plots from the micrographs together with the Raman shift of the silicon peak as a function of position in the same region. The Raman curve was generated by measuring the Raman spectrum every 0.5 μm, and plotting the position of the Si peak (in cm^{-1}) as a function of position along the fibre. The Raman measurements were made by our collaborators, Prof. Ursula Gibson and her group in Norway and noted that the lateral resolution of the Raman measurement was ~4 μm, so stresses associated with the grating period could not be resolved. There is a clear overall increase in the compressive strain in the vicinity of the grating and quasi-periodic Raman shift changes that correlate with the larger features in Fig. 104(a), suggesting possible strain relief through the formation of micro-cracks.

8.4 Silicon FBG Characterisation for Strain and Temperature

The silicon grating was initially connectorised with an SMF-28 pigtail using the UV-glue method in order to be compatible with the optical equipment. A broadband light source was connected to a circulator and the grating was illuminated. The reflection spectrum of the grating was then recovered using the Advantest Q8384 OSA. The grating was glued using super glue between two manual stages and steps of ~900 με up to ~2800 με axial strain were applied along the grating, leading to a response of ~0.23 pm/με as shown in Fig. 105. Compared with silica-FBG counter parts the sensitivity is reduced by a factor of 4. The elasto-optic coefficient (p) of silica is 0.007873, whereas for silicon it is 0.764132, as calculated using the Lorentz-Lorenz equation,

$$p = \frac{(n^2-1)(n^2-2)}{3n^4} \ , \quad (8.1)$$

where n is the refractive index of the core. By solving the strain equation,

$$\Delta\lambda(\varepsilon) = (1-p)\varepsilon \ , \quad (8.2)$$

where ε is the applied strain. Solving the equation (8.2) using the coefficients of the materials, the corresponding wavelength shift for the silica and silicon FBGs is 0.992127 and 0.235868, respectively, for 1 mε, a factor of 4 difference, which confirms our experimental results.

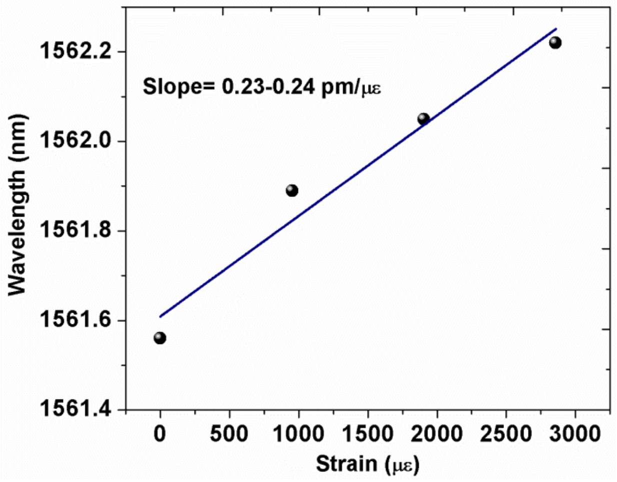

Figure 105: Strain sensitivity of the silicon core FBG with the application of axial strain.

To measure the temperature response of the grating, the sample was placed inside to the climate chamber. The temperature response was found to be 76.64 pm/°C and the wavelength shift of the Bragg grating with the temperature is shown in Fig. 106. Compared to glass, the silicon grating is approximately 11 times more sensitive.

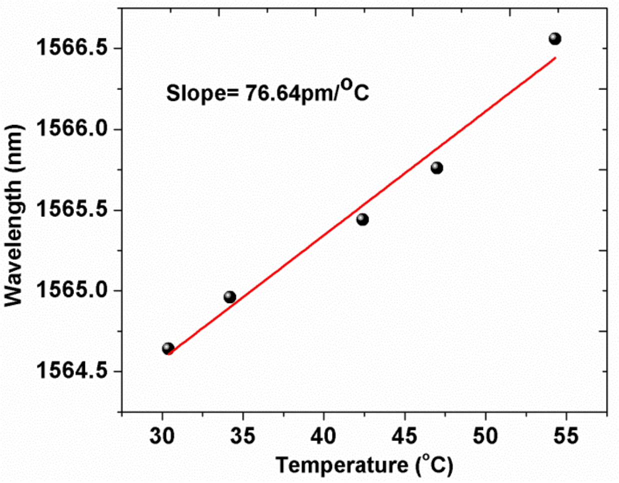

Figure 106: Temperature response of the silicon core FBG when subjected to temperature excursions from 30 to 55 °C.

The thermo-optic coefficient and the thermal expansion of the silica fibre at 30 °C is ~8 x 10^{-3} and 0.5 x 10^{-6}, respectively, whereas for the silicon the corresponding values are 90 x10^{-3} [249] and 3 x 10^{-6}. The wavelength shift of the Bragg grating when subjected to temperature excursions can be evaluated using,

$$\Delta\lambda = (a_n + a_\Lambda)\Delta T \quad , \qquad (8.3)$$

where a_n is the thermo-optic coefficient, a_Λ is the thermal expansion and ΔT is the temperature difference. By solving equation (8.3) the temperature sensitivity for the silicon grating should be ~11 times higher, our measurements indicate an improvement of ~7.6. The difference may be related to the glass fibre cladding surrounding the silicon core for the following reasons. Firstly, the thermal expansion of the glass is 6 times less than for silicon, but this effect is an insignificant contribution to these measurements, as thermo-optic coefficient dominates. Secondly, the value of the thermo-optic coefficients in the two materials assumes that the light traverses pure materials alone. However, in practice the light at 1550 nm sees both the core and cladding materials, which would act to reduce the thermo-optic response of the fibre structure.

8.5 Conclusion

Silicon is an important material; it forms the basis for current electronic chip technology. The ability to couple to optical fibres is an important requirement for optical interconnects that can combine optical and electronic technologies. The material differences between optical fibres and on-chip silicon devices impair advances in high-speed computing. Hence having silicon core fibres and demonstrating the incorporation of key optical components in that fibre is extremely important, as now two issues are being addressed, i) material differences and ii) the capability to incorporate optical filters for off-chip WDM devices. In this work we demonstrated the first FBGs in silicon-core fibres via the introduction of stress through the silicon fibre core, using a femtosecond laser operating in the visible. The period of the stress modification zones was accurately controlled utilising an 8th-order fibre Bragg grating operating at 1565 nm. The strain sensitivity of the silicon grating was found to be ~4 times less than for silica fibre, whereas the temperature sensitivity was ~7.6 times higher. The experimental results were evaluated by comparing the thermal coefficients (thermo-optic and thermal expansion) and the elasto-optic coefficients of the two materials.

9 Polymer Optical Fibres with Unique Properties

This chapter presents our latest achievements measuring the effects of temperature, relative humidity, and pressure on a Bragg grating inscribed on a new type of non-PMMA polymer optical fibre. The fibre was produced using a new, patented method called the Light Polymerization Spinning (LPS) process that was designed to produce fibres having a very low Young's modulus.

Different aspects of this research were presented at three conferences; POF Conference 2016 in Birmingham as an invited, oral presentation, POF Conference 2017 in Aveiro, Portugal as poster presentation, and at the Workshop on Specialty Optical Fibres (WSOF) 2017 in Limassol, Cyprus as poster presentation.

9.1 Introduction

Early in this thesis it was noted that PMMA is still the most employed material for POFs [250], whereas TOPAS is promising because of its hydrophobic structure [251], and the potential of high-Tg TOPAS [111]. Zeonex fibre was proposed as a material with high Tg and good drawability, related to its optimal molecular weight and melt flow that enable a more stable and controllable drawing [252]. In addition, there are the polycarbonate (PC) fibres with Tg of 145 °C and that can survive higher stress compared with other POF materials [250]. This thesis has focussed on CYTOP, as it is an important material that is commonly used and commercially available for POFs and we have noted that it offers significantly lower optical losses than the other polymer materials due to its amorphous nature and the perfluorinated backbone [247]. We noted how POFs are commonly fabricated with the aforementioned materials using a heated extrusion or drawing process. For the former, a preform of the desired material is extruded at temperatures exceeding 200 °C (>Tg) [253]. In the latter process, the preform is heated and pulled under controlled tension, resulting in a drawn fibre thread. However, in both cases an asymmetric temperature profile on the fibre may lead to non-uniform diameter and asymmetric fibre properties that are undesirable. Annealing the fibre can enhance the polymer's thermal stability [250], which can provide a higher repeatability and increase the material drawability. However, the fibre extrusion process is a time-consuming and rather inflexible manufacturing technique.

In this chapter, we consider a POF manufactured using a novel process, known as the light polymerization spinning (LPS) process. In this method, there is no need for polymer preforms, there is instead a process that combines liquid monomers and other additives that are rapidly UV cured as the fibre is produced, which makes the POF manufacturing process highly scalable and customizable, and where fibres with strain limits up to 800% can be fabricated [254], [255]. The room-temperature LPS fabrication process allows for new monomer combinations that are not yet available via more conventional POF manufacture. Therefore, the unique mechanical characteristics of this fibre were studied, including the Young's modulus, storage modulus variations with temperature, humidity, frequency, and the fibre thermal expansion using dynamic mechanical analysis (DMA). An FBG was inscribed using the femtosecond laser inscription method and characterised in reflection, along with its response to temperature, relative humidity, and hydrostatic pressure.

9.2 New Polymer Fibre Fabrication Method

Figure 107 presents the block diagram of the LPS manufacturing process for developing POFs. A liquid mixture of monomers and additives at room temperature are added to a dosing system that regulates the amount of the mixture that is passes a spinneret. The monomer is Bisphenol-Acrylate that has a low molecular weight and high refractive index, which can result in high elasticity and good optical properties. Since the goal is to produce optical fibres, the output of the spinneret defines the fibre shape. This liquid monomer/additive mixture is polymerized with a UV lamp and with a circular cross-section. Following the curing process, the polymer is stretched and texturized to obtain the desired core diameter and cladding thickness. Finally, the manufactured fibre is coiled onto a spool. Table 4 presents the optical characteristics of the LPS-POF analysed in this work. The fibre was manufactured by Oleg Palchik and his company Tescolut LTD in Israel.

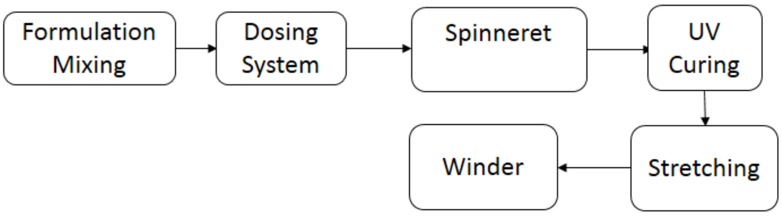

Figure 107: Block diagram of the LPS POF-manufacturing process.

Table 4: LPS-POF optical properties

Properties	Values
Core/Cladding Composition	Acrylate based
Core Diameter (µm)	580
Core Refractive index	1.54
Cladding Thickness (µm)	20
Cladding Refractive index	1.45
Numerical Aperture	0.47
Attenuation at 660 nm (dB/km)	2200

9.3 Mechanical Properties

The DMA measurements were made at Electrical Engineering of Federal University of Espírito Santo, in Brasil, using a DMA 8000 (Perkin-Elmer, USA). DMA is a well-established method for characterising the polymer response with parameter variations, such as temperature, strain, frequency and humidity [256]. An oscillatory load is applied to the polymer with controlled displacement and frequency, as the polymer is a viscoelastic material [257]. For this reason, the LPS-POF response is analysed with respect to its storage modulus that is the real part of the complex Young's modulus of the polymer [258] and its loss factor (tanδ), which is the ratio of the storage and loss modulus of the polymer response [258]. Of course, stress-strain tests were made to obtain the Young's Modulus. Regarding LPS-POF configuration and geometry for the tests, a single cantilever was used for oscillatory load tests, whereas, a tension configuration was used for stress-strain tests.

The LPS-POF Young's modulus was measured to only 15 MPa; this is up to 400 times smaller than for typical polymer materials (Table 5) and certainly the lowest Young modulus reported for any optical fibre. Such a low modulus can provide higher load sensitivity and offers a potentially larger wavelength shift range for sensors based on this type of POF, assuming that one can record FBGs. It would then be possible to obtain sensors for physical parameters such as temperature [250], liquid level [259], acceleration [260] and angle [257] with a sensitivity of a few orders of magnitude greater than for the more conventional POFs.

Table 5: Young modulus for different POF materials

POF Material	Young Modulus (MPa)
LPS-POF	15±1.2
PMMA	4.3×10^3
TOPAS	3.0×10^3
PC	3.0×10^3
Zeonex	2.5×10^3
CYTOP	6.5×10^3

The DMA was made over a range of 25 to 160 °C with a temperature increment of 2 °C/min. Figure 108(a) shows the temperature characterization for the storage modulus and the loss factor between 25 and 35 °C. The peak of the tanδ represents the Tg of the polymer, which, in this case, is ~30 °C. Although it is a rather low Tg, the material storage modulus is stable when the temperature exceeds 60 °C. Therefore, a POFBG could be used as a temperature sensor, with greater stable for temperatures greater than the material Tg. In addition, the decrease of the LPS-POF storage modulus shows a linear behaviour, with a decreasing rate of -0.0124 MPa/°C; it could be used as a high dynamic range, intensity variant temperature sensor, where changes in the fibre's mechanical properties with temperature result in fibre output power variations.

Additionally, strain cycles with different frequencies were performed on the LPS-POF from 0.01 Hz to 100 Hz, in order to obtain the operating limits of the LPS-POF with respect to frequency (Fig. 108(b)). The LPS-POF has a stable frequency response up to 21 Hz, and then, the storage modulus significantly increases. More specifically, for frequencies up to 21 Hz the storage modulus was approximately 15 MPa, while its value increased linearly at a rate of 5.51 MPa/Hz for higher frequencies. This large variation of the material modulus with frequency will limit the use of LPS-POF for applications that involve high frequency oscillatory movement, such as curvature sensors and accelerometers [261]. The large variation of the material modulus at higher frequencies is related to the molecular rearrangement of the polymer, which is influenced by the polymer relation time; it is a viscoelastic material. On the other hand, the storage modulus variations allow this fibre to be used as an accelerometer based on the intrinsic fibre variations. The mechanical features of LPS-POF enable sensors with greater sensitivity than their existing POF counterparts [111], [252], [260], [262].

In Fig. 108(c), the humidity sensitivity of the LPS-POF is analysed using DMA from 75% and 95% RH, at a constant temperature of 26 °C (room temperature) and for a strain cycle frequency of 1 Hz. The variation on the storage modulus was close to 8% and this indicates that the LPS-POF has a hydrophilic polymer chain with similar moisture absorption and swelling effects as PMMA. Although humidity sensitivity may require a relative humidity compensation for temperature and strain measurements applications, it also enables the use of LPS-POF as humidity and moisture sensors, where such high variation on its storage modulus may result in a humidity sensor with high sensitivity.

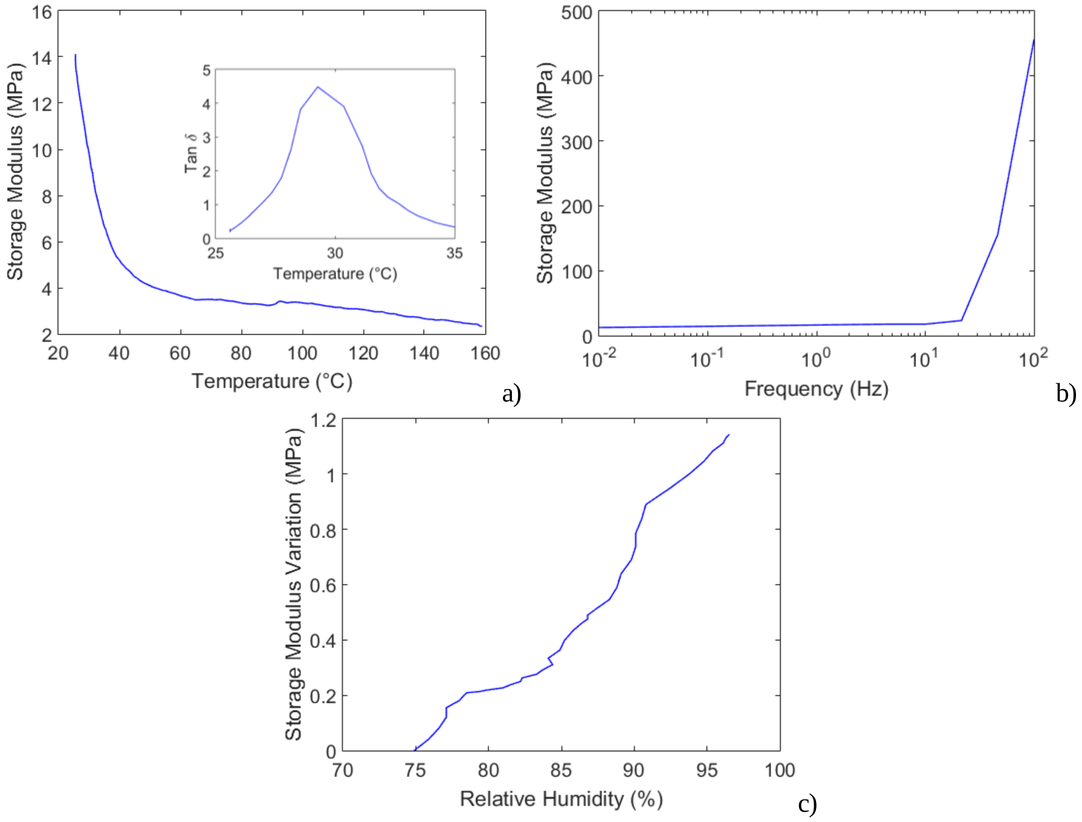

Figure 108: (a) Temperature response of the LPS-POF with respect to its storage modulus and loss factor (tanδ figure inset). (b) Frequency response of the LPS-POF with respect to its storage modulus. (c) Relative humidity response of the LPS-POF with respect to its storage modulus.

9.4 FBG Inscription in LPS-POF

The LPS-POF has a step index refractive index profile with 580 μm core diameter and core refractive index n_1= 1.54; the approximate number of modes are [16],

$$\Delta = \frac{n_1 - n_2}{n_1}, \quad (9.1)$$

$$V = \frac{2\pi a}{\lambda} n_1 \sqrt{2\Delta}\,, \quad (9.2)$$

$$M_{number} \approx \frac{V^2}{2}\,, \quad (9.3)$$

where a is the core radius, n_2 is the cladding index and Δ is the index difference between the core and cladding ($\Delta \approx 0.05$). This particular fibre supports ~190000 principal modes. In order to minimise the excitation of all these modes, the spatial dimensions of the gratings were limited using the *plane-by-plane* inscription method, as detailed described in previous chapters. We selected grating planes with 30 µm width, this is ~19 times smaller than the core diameter and the total grating length was ~4 mm. The microscope image of the grating at the centre of the core is shown in Fig. 109(a). Using the butt-coupling method, the grating was illuminated with a broadband light source (Thorlabs ASE730), and the reflection spectrum was measured using an Ibsen IMON (Fig. 109(b)). The maximum peak wavelength was at 1560.23 nm for a 1.5-nm bandwidth. Due to the high fibre attenuation, the sample length was limited to 4 cm.

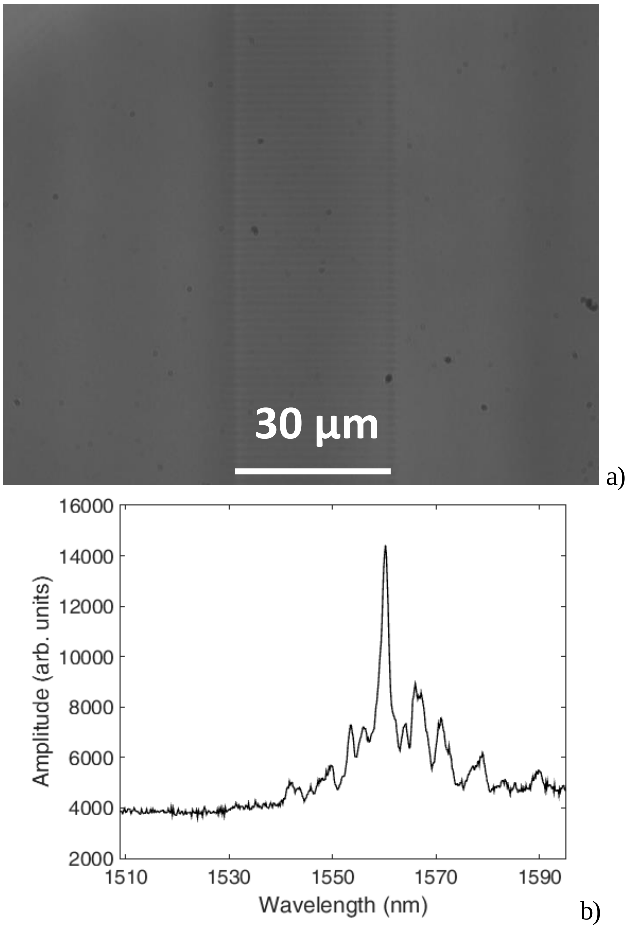

Figure 109: (a) Microscope image of the LPS-POFBG using the well-controlled femtosecond laser inscription method. (b) Reflection spectrum (linear scale) of the LPS-POFBG as measured using a commercial spectrometer (Ibsen IMON).

9.5 Sensing Analysis of the LPS-FBG

In order to characterise the LPS-POFBG with temperature the grating sample was connectorised using the UV-glue method with a multimode angle cleaved gradient index glass fibre in order to establish a sufficiently "stable connection" for the measurements and the other side of the fibre was fusion spliced with a SMF28 pigtailed, finally placed in the climate chamber. The hydrophilic nature fibre meant that we kept the relative humidity constant at 48% for 6 hours to overcome potential cross-sensitivity issues between humidity and temperature. The temperature was increased from 22 °C to 37 °C every hour and snapshots of the reflection spectrum were taken using the FBG demodulator. The wavelength shift of the grating with temperature is shown in Fig. 110, with a sensitivity of –521.3 pm/°C. The POFBG wavelength shift is approximated as follows,

$$\Delta\lambda_B = [(1-p)\varepsilon + (\alpha+\zeta)\Delta T + (\eta+\beta)\Delta H]\lambda_B \ , \quad (9.4)$$

where λ_B is the unperturbed Bragg wavelength, ε is the fibre strain and p is the photo-elastic constant. Furthermore, to account for the temp\erature influence on the wavelength shift, α is the thermal expansion coefficient, ΔT is the temperature variation and ζ is the fibre thermo-optic coefficient. Regarding the humidity term, ΔH is the humidity variation, β is the swelling coefficient and η is the normalized refractive index variation with the humidity.

The grating has a negative response since it is an acrylate-based polymer, and this value is several orders greater than of other POFs. For comparison, the temperature sensitivity of PMMA-FBGs is -109 pm/°C [108], CYTOP-FBGs 17.6 pm/°C[263], Zeonex-FBGs -24.0 pm/°C [252], TOPAS-FBGs -78 pm/°C [251] and PC-FBGs -30.0 pm/°C [250]. The LPS-POFBG has a 4.5 times greater sensitivity compared to PMMA. To ensure the correctness of our results the LPS-POF thermal expansion was measured using DMA for constant stress. The thermal expansion coefficient was estimated as the fibre's length increased with respect temperature, where the ratio between the temperature and length variation gives the thermal expansion coefficient. The results indicate that the thermal expansion is ~4 times lower compared with PMMA (LPS-POF: 1.8×10^{-5} K^{-1} and PMMA: 7.3×10^{-5} K^{-1}) [264], indicates that for LPS-POF the contribution of the thermo-optic coefficient is significantly greater and its negative value augments the measured wavelength shift for acrylate-based POFs (Eq. 9.4). Hence, we can conclude that the 4.5

times higher thermal sensitivity of the LPS-FBG makes sense, given the higher thermo-optic coefficient. However, due to the strong mode mixing during the temperature experiment, the response of the grating at higher temperatures was not possible.

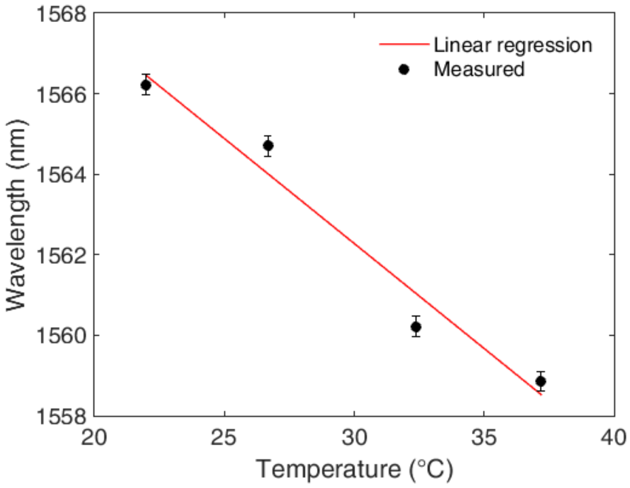

Figure 110: Wavelength shift of the LPS-POFBG for a temperature increase from 22 to 37 °C, with constant humidity.

For the humidity characterisation, the temperature of the climate chamber was kept constant (25±1.5 °C), and the relative humidity was increased from 50% to 90%, in steps of 20%. The transition time for each level was 1-hour, and the relative humidity was kept constant at each level for 6 hours prior to the next humidity step. The resultant grating wavelength shift with humidity change is shown in Fig. 111(a) as a function of time; the black line represents the LPS-POFBG wavelength shift, whereas the blue line shows the humidity variation, as measured using the internal climate chamber sensor. It is clear that the grating largely follows the humidity changes of the climate chamber. For the humidity stabilisation tests, the humidity absorption time was ~1.5 ± 0.25 hours (Fig. 111(b)), while the rejection time was ~ 2 ± 0.25 hours. Figure 112(a&b) shows the wavelength shift for humidity levels between 33 % and 95.5 % for two different modes. As expected from the results presented in Fig. 108(c), the slope of the curve is positive and the humidity sensitivity found to be 167.80 ± 17 pm/%RH for humidity levels 50% to 80% and 347.10 ± 33 pm/%RH for 80% to 95%. The best fit to the data over the measurement range is a simple exponential regression, which could be used to calibrate the sensor response. To our knowledge, this is the highest humidity sensitivity reported with polymer fibres, since TOPAS and Zeonex are almost humidity insensitive [112], whereas CYTOP, PMMA and PC have a humidity sensitivities of 14.7 pm/%RH [263], 39 pm/%RH [265], and 7.31 pm/%RH [262], respectively.

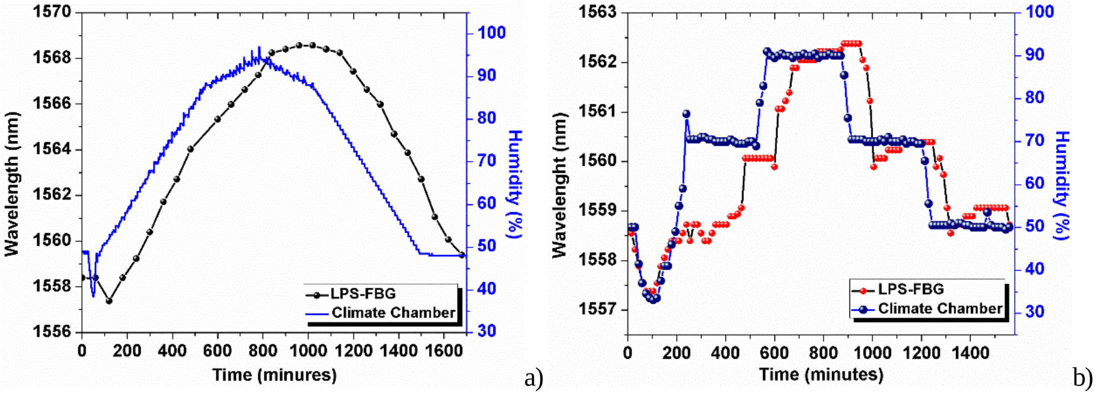

Figure 111: (a) Humidity response of LPS-POFBG in the humidity controlled climate chamber, (b) LPS-POF FBG humidity stabilisation tests.

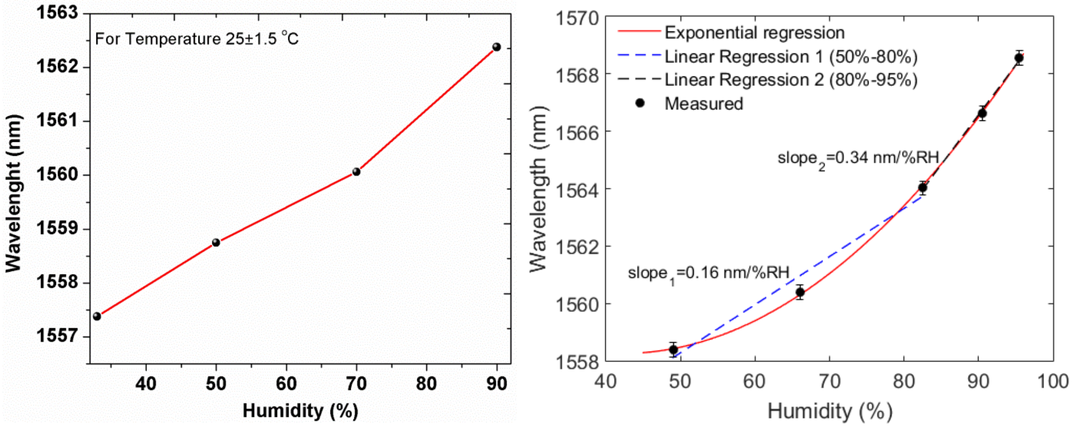

Figure 112: LPS-POFBG wavelength shift with humidity at constant temperature for two different modes.

9.6 Conclusion

This chapter presented the characterization of a novel POF fabricated via the LPS process, and having an ultra-low Young's modulus (~15 MPa). Hence LPS-POF has the potential for strain sensing applications, and the low Tg may not be problematic as the material modulus is stable from 60 to 160°C, potentially leading to high temperature polymer sensors. The LPS-POF displays a high variation in its mechanical response for frequencies >21 Hz, which could have applications to accelerometers, whereas the low storage modulus variation for frequencies <21 Hz could be useful for curvature sensing. In addition, the LPS-POFBG had a high temperature sensitivity of –521 pm/°C; the highest yet reported for POFBGs. The humidity characterisation also showed the highest sensitivity among POFBGs that was related to the lower Young's modulus, and hence greater strain-related swelling. However, connectorisation issues currently limit the use of this fibre, whereas mode mixing issues can be eliminated or largely reduced by using smaller core LPS-POFs or using by decreasing the core diameter using tapering techniques.

10 Summary and Future Directions

This thesis has focussed on the development and inscription of advanced fibre optic sensors using a femtosecond laser system. We have demonstrated a number of key achievements in a range of areas that are related to the capabilities of femtosecond lasers to induce refractive index changes in any transparent material through multiphoton absorption, as explained in chapter 2.

The development of useable polymer optical fibre sensors in a gradient index multimode CYTOP fibre and their demonstration for long length applications was the key achievement with POF. As discussed in the first chapters of this thesis, a significant body of work has already been published regarding the development of optical sensors in polymer optical fibres and their use for numerous applications. These studies were mostly limited to a few polymers, such as PMMA and TOPAS. The great weakness of these particular polymers relates to their high attenuation losses particularly for wavelengths in the range 1300 – 1600 nm, which limits the practical fibre lengths to a few centimetres. Moreover, given there is only one commercial company that manufactures single-mode POF, the future is not very promising for incorporating POF sensing technology in real commercial applications.

On the other hand, for data transfer and telecommunications systems different commercial POFs are available; some of them offer very good optical properties, such as CYTOP. All of these fibres are designed for easy light coupling and so are available as multimode designs. The mixing between the propagation modes of the multimode fibres makes the development of sensors and sensing schemes with the particular fibre extremely difficult. Furthermore, the very low photosensitivity of the promising CYTOP polymer to UV radiation hinders sensor development. However, we have addressed both of these challenges in this thesis.

In chapter 4, we developed, for the first time; usable FBG based optical sensors in a commercial gradient index multimode CYTOP fibre. Using a femtosecond laser inscription method, we had sufficient control of the grating/mode excitation overlap to create ‘single-peak’ FBGs. This achievement allowed for the significant demonstration of POF sensors operating in lengths exceeding six metres. Recent collaborations with a French company Terre Armee have seen them use our sensors in fibre lengths exceeding

60m, for real-world applications, which is a first. The research advanced from the initial ‘single-peak’ POFBGs to more complicated structures such as chirped gratings, fibre Fabry-Perot cavities, and arrays of FBGs distributed along a single POF strand. The POFBGs were characterised and calibrated for temperature, humidity, and strain, with responses very similar to other POFBGs, with the exception of pressure measurements. Polarisation dependent loss and the group delay for the chirped gratings were measured for different inscription conditions and for the first time.

In chapter five, multiple POFBG arrays inscribed in long-length CYTOP fibres were demonstrated as sensing strands for different applications. A POFBG array was used as a quasi-distributed sensor on free-free beams to extract their mode shapes when vibrated at their resonance frequencies and a comparison between the POF array and a silica counterpart was made. The results showed the superiority of the POF sensors, showing six times higher sensitivity to vibration. A POFBG array was used for health condition inspection of a cantilever beam, where we observed the damage position on the beam and the level of the damage by suspending different weights on the cantilever beam surface. Finally, a POFBG array was utilised for plantar pressure monitoring when embedded in a cork insole and the results showed significant sensitivity gain when compared with silica counterparts. There are several issues that must be solved in order to best utilise POF sensors, such as connectorisation issues, strain survivability, long-term and thermal stability etc.; however, we consider that this work is currently the first, most complete in the practical use of POF sensors and is highly promising, opening a route to the commercialisation of the particular sensors. Similar applications would be impossible with other POF-based sensors due to their severe length limitation, as previously described. Additional work is required in the future to improve the strain limits (>1.3%) of these sensors and better solutions for termination of the samples.

The thesis has also focused on the development of different optical sensors in glass and soft glass fibres. As mentioned, the plane-by-plane inscription method offers flexibility and controllability with respect to the inscription conditions, particularly compared to other methods such as the phase mask and the point-by-point inscription. In the first section of chapter six the optimum femtosecond laser parameters, such as the number of pulses, pulse energy, repetition rate and inscription speed were established, and the refractive index change was quantified, according to the resultant FBG spectrum. All the results were normalised to the number of pulses per micron and shown that for the particular fibre that 80 pulses/µm is the optimum 'dosage' for the stronger FBGs. Moreover, it was demonstrated that the order of the gratings affected the strength of the radiation/cladding modes, the bandwidth of the FBGs and the slope FBG peak. These results were experimentally determined by inscribing a series of gratings using different grating order and the same number of periods. Moreover, various optical devices were written, such as chirped gratings, fibre Fabry-Perot cavities, chirped fibre Fabry-Perot cavities, and opposite chirped fibre Fabry-Perot cavities, showing the flexibility of the proposed inscription method. The specific work is the first study of this kind has provided valuable results that could be used to commercially develop specialised femtosecond laser-based FBGs.

We further extended the control afforded by the Pl-by-Pl inscription method to develop tilted FBGs inscribed in a Boron-doped fibre. By controlling the tilt-angle and the spatial extent of the grating we selectively triggered cladding modes changes; as the tilt-angle increased the cladding modes region shifted to smaller wavelengths. It is possible to measure very small refractive indices, such as gasses (work under development and to be reported in a future publication). Finally, chapter six concluded with the inscription and characterisation of optical devices in a soft glass fibre fabricated with phosphate to be biocompatible and used for bio-sensing applications. The reflection spectrum of uniform, non-uniform FBGs and Fabry-Perot cavities was measured, while the behaviour of the gratings for temperature and high humidity was also characterised. A uniform FBG was characterised when the inserted in climate chamber for 52 hours with relative humidity >95%.

Different optical waveguide sensor structures were described and presented in chapter 7. A preliminary study was undertaken in the first section to observe the optimal inscription conditions for waveguide inscription on the side of the fibre in terms of coupling efficiency, and the circular shape. The output light for each waveguide was measured using a profilometer and a laser operating at ~600 nm, for different coupling lengths, inscription gaps, and starting positions. The process was extended by adding the inscription of a Bragg grating on the cladding waveguide and its response characterised for strain, curvature, and some values of refractive index was measured. Furthermore, a compact cladding Mach-Zehnder interferometer was developed, for which a series of inscriptions were utilised to achieve higher fringe visibility, while the structure was further improved with the inscription of a Bragg grating in the MZI waveguide arm. The

Bragg grating was characterised both for reflection and transmission, and the response to temperature, and relative humidity was characterised. The MZI and WBG responded differently to temperature variations, while for the humidity measurements the WBG showed complete insensitivity whereas the MZI responded with a positive wavelength shift. The structure co-locates two unique sensors and offers a structure that could be used to address cross-sensitivity issues that are typical for optical fibre sensors. Finally we presented waveguide inscription as a means to bridge a single core fibre with a four-core fibre. For each single core of the four-core fibre, an FBG array consisting of three FBGs was inscribed prior to the waveguide inscription and the reflection spectrum growth was monitored as the waveguide size increased. The particular work is significant both for communications and sensing. This is one of the few direct methods for linking multiple fibre cores, which is important for spatial division multiplexing, and also for sensing purposes since cross-sensitivity issues could be cancelled through the multicore fibres and also could be used for shape or curvature sensing applications.

The last section of the thesis focused on the development of FBG sensors in novelty or new optical fibres. A semiconductor fibre such as a silicon-core fibre was processed using the femtosecond laser in chapter 8. The high-intensity femtosecond pulses of the laser operating in the visible region were fully absorbed by the silicon core producing locally extremely high temperatures. The suddenly increased temperature induced a stress field thereby modifying periodically the core of the fibre to produce a FBG. The particular FBG sensor shows low sensitivity to strain and almost eight times greater thermal response compared with traditional glass fibres. In chapter 9, an acrylate-based fibre was explored, which was manufactured using a new patented method allowing the development of fibres with unique mechanical properties processed for FBG inscription. The FBGs inscribed in the particular fibre showed very high sensitivities to temperature, humidity, and pressure compared to all the other polymer and glass FBG sensors reported in the literature. In both cases the fibres are completely new and the studies are continuing since issues such as the connectorisation and handling are limiting further characterisation and usability of the particular sensors.

In the realm of sensing, optical fibre sensors have shown many advantages compared to conventional electrical sensors. The small size and thin design of the optical sensors along with their immunity to electromagnetic fields and high radiation environments makes them well suited for applications in harsh environments such as in high voltage, nuclear, high pressures, and at extremely high temperatures, where conventional sensors cannot be used. If we add the benefits of sensor multiplexing, the future for optical fibre sensors is highly promising. In addition, the optical sensors are capable of measuring more than one parameter at the same time, more notably are sensitive to strain, temperature, pressure, and humidity, whereas the measurement of acceleration and vibration is related to strain measurement. With this in mind, the development of optical sensor arrays in a single optical fibre cable for the measurement of broad range parameters is a tremendous advantage compared to the conventional sensors. While in the case of silica fibres the distance does not greatly influence the performance or the sensitivity of sensors and this single array of sensors could be used to cover hundreds of meters, enhancing this potential and the importance of optical sensors. Our work with POF sensors has opened the potential for FBGs in POF to offer an alternative solution for high resolution, short-range sensing.

The future direction of this research is currently focussed in three areas, the potential of gas sensing using TFBGs and MZIs, the development of apodised gratings and the inscription of gratings in earth-doped fibres for fibre laser applications. With these ideas in mind we note the following developments in each of the aforementioned areas.

There is great importance in developing accurate gas sensors for detecting harmful gases (to human health), such as the Methane (CH_4), Carbon Dioxide (CO_2), Sulfur dioxide (SO_2), Ammonia (NH_3), Nitrogen dioxide (NO_2), Nitric oxide (NO), Carbon monoxide (CO). All of these gases may be optically characterised by having distinct refractive index differences of $\sim 10^{-5}$ RIU. Thus, as shown in Chapter 6 and 7, we can achieve such a small RI sensitivity using TFBGs and MZI structures. Using higher order TFBGs we can significantly increase the cladding mode sensitivity, whereas MZI structures inscribed in the cladding of the fibre have also demonstrated a greater sensitivity to external index changes.

Apodised FBGs have a great importance in a range of applications, such as high and low reflectivity in-fibre mirrors for fibre lasers, high-temperature sensors, and WDM communication systems. Compared to uniform FBGs, the apodised gratings are characterised by clear spectral profiles without significant side lobe peaks in the reflection spectrum. By suppressing these side lobes complications such as crosstalk in WDM systems, and linewidth broadening in high power lasers can be limited. In Fig. 113(a) we observe the reflection spectrum of a Gaussian apodised FBG inscribed in a polyimide glass fibre. The grating isolation is more than 16dB, the FWHM is less than 0.4 nm, while the grating has a reflectivity >80%.

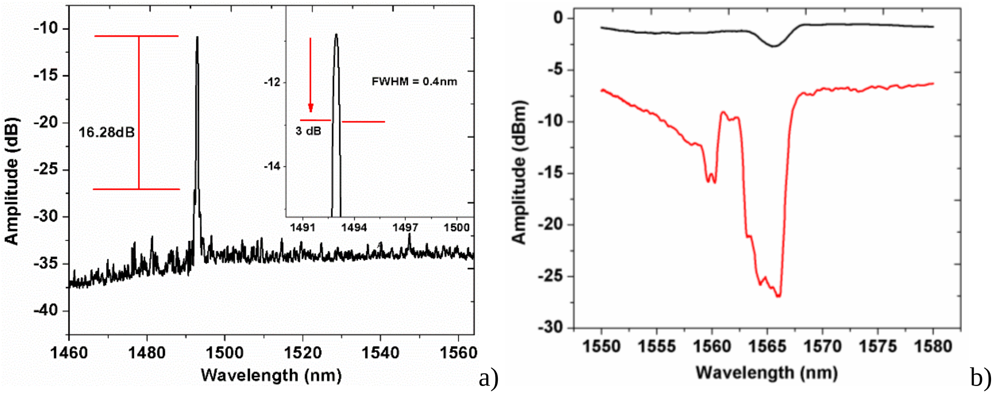

Figure 113: A) Gaussian apodised Bragg grating inscribed in a polyimide coated single mode fibre and through the coating, B) Chirped Bragg grating cavity inscribed directly in a Er/Yb doped fibre in order to create a monolithic fibre laser operating at 1560 nm.

Finally, we note that FBG inscription directly into active fibres as resonator mirrors would improve the laser compactness, and offer further flexibility in design, as the laser resonator is fully integrated into a monolithic structure. In addition, it potentially improves the durability of the fibre laser as there are no splices to the FBGs, which could generate failure under high optical pump and/or laser signal power. To address these points, we inscribed a chirped grating cavity directly in an Er/Yb doped fibre (Fig.31(b)) and characterised a fibre laser configuration. The results have shown a slope efficiency 100 times higher compared to other already published reports with lasing wavelength at 1560 nm using fs-laser inscribed FBGs. We are trying to further improve the laser efficiency whilst at the same time we are working with other rare-earth-doped fibres, such as Thulium doped fibres.

Appendix A Published Papers

Journal papers arise from the work described in this thesis:

1. **Antreas Theodosiou**, X. Hu, C. Caucheteur, K. Kalli, “Bragg gratings and Fabry-Perot cavities in low-loss multimode CYTOP polymer fibre”, IEEE Photonics Technology Letters, vol. 30, no. 9, pp. 857-860, 2018.
2. R. Ishikawa, H. Lee, A. Lacraz, **Antreas Theodosiou**, K. Kalli, Y. Mizuno, and K. Nakamura, "Strain dependence of perfluorinated polymer optical fiber Bragg grating measured at different wavelengths, " Jpn. J. Appl. Phys., vol. 57, no. 3, 038002, 2018.
3. Debora Vilarinho, **Antreas Theodosiou**, Caia Leitao, Arlando G. Leal-Junior, Maria de Fatima Domingues, Kyriacos Kalli, Paulo Andre, Paulo Antunes, Carlos Marques, “POFBG-Embedded Cork insole for plantar pressure monitoring”, Sensors, vo.17, no.12, pp.2924, 2017.
4. Andreas Ioannou, **Antreas Theodosiou**, Christophe Caucheteur, Kyriacos Kalli, “Direct writing of plane-by-plane tilted fiber Bragg gratings using femtosecond laser”, Optics Letters, vol.42, no.24, pp.5198-5201, 2017.
5. **Antreas Theodosiou**, Amedee Lacraz, Andreas Stassis, Charalambos Koutsides, Michael Komodromos, Kyriacos Kalli, “Plane-by-Plane femtosecond laser inscription method for single-peak Bragg gratings in multimode CYTOP polymer optical fibre”, Journal of Lightwave Technology, vol.35, no.24 pp. 5404-5410, 2017.
6. **Antreas Theodosiou**, Michael Komodromos, Kyriacos Kalli, “Carbon cantilever beam health inspection using a polymer fibre Bragg grating array”, Journal of Lightwave Technology, vol.36, no.4, pp.986-992, 2017.
7. Ryo Ishikawa, Heeyoung Lee, Amedee Lacraz, **Antreas Theodosiou**, Kyriacos Kalli, Yosuke Mizuno, Kentaro Nakamura, “Pressure dependence of fiber Bragg grating inscribed in perfluorinated polymer fiber”, IEEE Photonics Technology Letters, vo.29, no.24, pp.2167-2170, 2017.
8. **Antreas Theodosiou**, M. Komodromos, K. Kalli, “Accurate and fast demodulation algorithm for multipeak FBG reflection spectra using a combination of cross correlation and Holbert transformation”, Journal of Lightwave Technology, vol.35, no.18, pp.3956-3962, 2017.

9. Michael Fokine, **Antreas Theodosiou**, Seunghan Song, Thomas Hawkins, John Ballato, Kyriacos Kalli, Ursula J Gibson, “Laser structuring, stress modification and Bragg grating inscription in silicon-core glass fibers”, Optical Materials Express, vol.7, no.5, pp.1589-1597, 2017.
10. Amedee Lacraz, **Antreas Theodosiou**, Kyriacos Kalli, “Femtosecond laser inscribed Bragg grating arrays in long lengths of polymer optical fibres; a route to practical sensing with POF”, Electronics Letters, vol.52, no.19, pp.1626-1627, 2016.
11. **Antreas Theodosiou**, Amedee Lacraz, Michael Polis, Kyriacos Kalli, Maria Tsangari, Andreas Stassis, Michael Komodromos,“Modified fs-laser inscribed FBG array for rapid mode shape capture of free-free vibrating beams” ,IEEE Photonics Technology Letters, vol.28, no.14, pp. 1509-1512, 2016
12. Amedee Lacraz, Michael Polis, **Antreas Teodosiou**, Charalambos Koutsides, Kyriacos Kalli, “Femtosecond laser inscribed Bragg grating in low loss CYTOP polymer optical fiber”, IEEE Photonics Technology Letters, vol.27, no.7, pp.693-696, 2015.

Conference papers arise from the work described in this thesis:

1. **Antreas Theodosiou,** M. Polis, A. Lacraz, K. Kalli, M. Komodromos, A. Stassis, “Comparative study of multimode CYTOP graded index and single-mode silica fibre Bragg grating array for the mode shape capturing of a free-free metal beam”, SPIE Photonics Europe 2016.
2. A. Lacraz, M. Polis, **Antreas Theodosiou,** C. Koutsides, K. Kalli, “Bragg grating inscription in CYTOP polymer optical fibre using a femtosecond laser” Proc. Of SPIE, vol.9507, 2015.
3. **Antreas Theodosiou,** A. Ioannou, M. Pollis, A. Lacraz, “Femtosecond laser waveguide and FBG Inscription in four core optical fibre”, SPIE Photonics Europe 2016.
4. A. Ioannou, M. Polis, A. Lacraz, **Antreas Theodosiou,** K. Kalli, “Beam-shaping via femtosecond laser-modified optical fibre and faces”, SPIE Photonics Europe 2016.
5. A. Lacraz, **Antreas Theodosiou**, M. Polis, K. Kalli, “Fabrication and characterization of FBG sensors in low loss polymer optical fibre” EWOFs 2016.

6. K. Kalli, A. Lacraz, **Antreas Theodosiou,** M. Kofinas, “Modified femtosecond laser inscription method for tailored grating sensors in encapsulated silica and low-loss polymer optical fibres”, EWOFS 2016.
7. **Antreas Theodosiou**, K. Kalli, M. Komodromos, “Dynamic damage detection of a cantilever carbon beam using a FBG array inscribed in polymer gradient index multimode CYTOP fibre”, POF 2016.
8. A. Lacraz, M. Zubel, G. Demirci, **Antreas Theodosiou,** K. Kalli, K. Sugden, B. Gawdzik, “Embedding low loss polymer optical fibre Bragg gratings: Two different approaches”, POF 2016.
9. O. Palchik, N. Tal, E. Shafir, G. Berkovic, S. Zilberman, **Antreas Theodosiou,** K. Kalli, “Characteristics of photo polymerized polymer optical fibres, optical properties and femtosecond laser inscription of Bragg gratings”, POF 2016.
10. **Antreas Theodosiou,** K. Kalli, M. Komodromos, “Health monitoring of carbon cantilever using femtosecond laser inscribed FBG array in gradient-index CYTOP polymer fibre”, OFS 2017.
11. K. Kalli, **Antreas Theodosiou,** A. Ioannou, A. Lacraz, “Femtosecond laser processing of optical fibres for novel sensor development”, OFS 2017.
12. N. G. Boetti, D. Pugliese, **Antreas Theodosiou,** K. Kalli, E. Ceci-Ginistrelli, D. Janner, D. Milanese, “Bioresorbable phosphate glass optical fiber for biomedical applications”, WSOF 2017.
13. R. Ishikawa, H. Lee, A. Lacraz, **Antreas Theodosiou,** K. Kalli, Y. Mizuno, K. Nakamura, “Pressure dependence of Fiber Bragg grating inscribed in perfluorinated plastic optical fiber using femtosecond laser”, WSOF 2017.
14. P. Savva, **Antreas Theodosiou,** M. Petrou, K. Kalli, “Concrete RH monitoring using embedded FBG sensors inscribed in multimode CYTOP fibre”, WSOF, 2017.
15. M. Aressy, Y. B. Braouli, A. Lacraz, **Antreas Theodosiou,** K. Kalli, “Characterisation of a geosynthetic strip instrumented with FBG’s sensors in low loss polymer optical fibre”, WSOF, 2017.
16. **Antreas Theodosiou,** M. Fokine, S. Song, T. Hawkins, J. Ballato, U. J. Gibson, K. Kalli, “Fs laser inscription of FBGs in silicon core-silica clad optical fibres”, WSOF, 2017.
17. A. Ioannou, **Antreas Theodosiou**, C. Caucheteur, K. Kalli, “Femtosecond laser direct inscription of plane-by-plane tilted Bragg gratings”, WSOF 2017

18. **Antreas Theodosiou,** O. Palchik, N. Tal, E. Shafir, G. Berkovic, S. Zilberman, K. Kalli, “A new type of polymer fibre: Manufacturing, characterization, and FBG inscription using the *Pl-by-Pl* femtosecond laser inscription method”, WSOF 2017.
19. R. Ishikawa, H. Lee, A. Lacraz, **Antreas Theodosiou,** K. Kalli, Y. Mizumo, K. Nakamura, “Hydrostatic pressure dependence of FBG inscribed in perfluorinated GI-POF”, POF 2017.
20. **Antreas Theodosiou,** O. Palchik, N. Tal, E. Shafir, G. Berkovic, S. Zilberman, K. Kalli, “Measurements with an FBG inscribed on a new type of polymer fibre”, POF 2017.
21. A. Lacraz, **Antreas Theodosiou,** K. Kalli, “Low loss polymer fiber Bragg gratings sensors for effective optical sensing of strain and temperature”, Photonics Conference (IPC), 2016.
22. **Antreas Theodosiou,** A. Lacraz, K. Kalli, “Femtosecond laser inscription of multiplexed FBG sensors in CYTOP polymer optical fibres”, BGPP Photonics and Fiber Technology Congress, 2016.
23. D. Vilarinho, **Antreas Theodosiou,** F. Domingues, P. Antunes, K. Kalli, P.S. Andre, C.A.F. Marques, “Foot plantar pressure monitoring with CYTOP Bragg gratings sensing system” 11th International Conference on Biomedical Electronics and Devices 2018.

Appendix B Splicer Settings for Phosphate fibres

In this appendix presented the method of cleaving and splicing the Phosphate glass fibre samples presented earlier in this thesis. The Table 6 presents the modified splicing settings to splice single mode glass fibre with soft glass phosphate fibres using the Fujikura 100P+.

The Fig. 113(a) presents the bad cleaving of the phosphate fibre using the microscope camera of the fusion splicer. Figure 113(b) showing a good splicing performed after modified the setting of the splicer to those shown in Table 6 while Fig. 113(c) showing the resulting splicing using the default settings.

Table 6: Splicing settings for Phosphate fibre for Fujikura 100P+ fusion splicer.

Arc Power	-99 bits
Arc Time	100 ms
Gap	10 μm
Gapset position	R-400 μm
Cleaning Arc	OFF
Θ - alignment	OFF
Alignment mode	Cladding
Prefuse time	0 ms
Overlap	10 μm
Cleave angle limit	10°
Loss limit	1 dB
Cleave Shape error	OFF

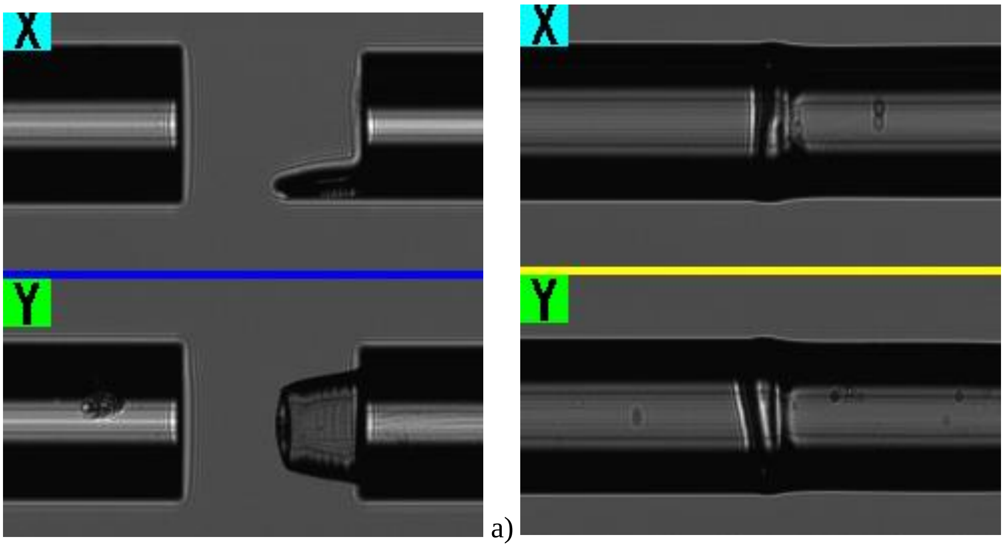

a) b)

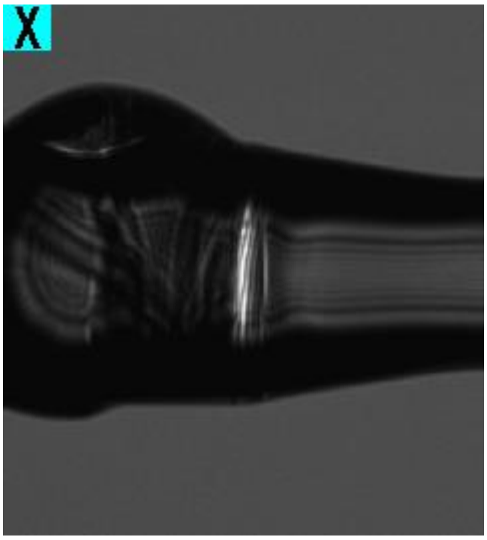

c)

Figure 114: a)Bad cleaving of the Phosphate fibre b)Splicing using the modified setting shown in Table 5 c) Splicing using the default setting of the Fushion splicer.

References

[1] G. Ma, A. P. Zhang, G. Yan, Y. Bai, Y. Hu, and X. Ye, “Label-free DNA biosensor based on cladding-etched thin-core fiber modal interferometer,” vol. 8421, p. 84215Q–84215Q–4, 2012.

[2] E. Field *et al.*, “Detecting Hybridization of DNA by Highly Sensitive Grating Sensors,” *Quantum*, vol. 11, no. 4, pp. 864–872, 2005.

[3] M. Dorrestijn *et al.*, “Polymer Optical Fibers as Gas Sensors,” pp. 448–449, 2012.

[4] E. Rochat, “Distributed Brillouin sensing : Applications to Oil & Gas Industries,” pp. 1–26, 2014.

[5] H. Y. Liu, G. D. Peng, and P. L. Chu, “Thermal tuning of polymer optical fiber Bragg gratings,” *IEEE Photonics Technol. Lett.*, vol. 13, no. 8, pp. 824–826, 2001.

[6] M. Okai, S. Tsuji, N. Chinone, and T. Harada, “Novel method to fabricate corrugation for a λ/4-shifted distributed feedback laser using a grating photomask,” *Appl. Phys. Lett.*, vol. 55, no. 5, pp. 415–417, Jul. 1989.

[7] K. O. Hill, B. Malo, K. a. Vineberg, F. Bilodeau, D. C. Johnson, and I. Skinner, “Efficient mode conversion in telecommunication fibre using externally written gratings,” *Electron. Lett.*, vol. 26, no. 16, pp. 1270–1272, 1990.

[8] N. Bohr, “I. On the constitution of atoms and molecules,” *Philos. Mag. Ser. 6*, vol. 26, no. 151, pp. 1–25, Jul. 1913.

[9] F. He *et al.*, “Femtosecond laser fabrication of monolithically integrated microfluidic sensors in glass,” *Sensors (Switzerland)*, vol. 14, no. 10, pp. 19402–19440, 2014.

[10] T. Krishnaswamy Subramaniam, “Erbium Doped Fiber Lasers for Long Distance Communication Using Network of Fiber Optics,” *Am. J. Opt. Photonics*, vol. 3, no. 3, p. 34, 2015.

[11] S. Kurtaran and M. S. Kılıçkaya, “The modelling of Fiber Bragg Grating,” *Opt. Quantum Electron.*, vol. 39, no. 8, pp. 643–650, 2007.

[12] J. Hongzhi and L. Yulin, “First- and second-order diffraction characteristics of fiber Bragg gratings,” *Opt. Commun.*, vol. 178, no. 4–6, pp. 339–343, May 2000.

[13] T. Erdogan, “Fiber grating spectra,” *J. Light. Technol.*, vol. 15, no. 8, pp. 1277–1294, 1997.

[14] A. Othonos and K. Kalli, *Fiber Bragg Gratings: Fundamentals and Applications in Telecommunications and Sensing*, 1st ed. Norward, 1999.

[15] D. N. Nikogosyan, “Multi-photon high-excitation-energy approach to fibre grating inscription,” *Meas. Sci. Technol.*, vol. 18, no. 1, pp. 1–29, 2007.

[16] Y. Liu, J. Lit, X. Gu, and L. Wei, “Fiber comb filters based on UV-writing Bragg gratings in graded-index multimode fibers,” *Opt. Express*, vol. 13, no. 21, pp. 8508–8513, 2005.

[17] G. Laffont *et al.*, “Tilted short-period fibre-Bragg-grating- induced coupling to cladding modes for accurate refractometry,” *Meas. Sci. Technol.*, vol. 12, no. JUNE, pp. 765–770, 2001.

[18] M. C. Phan Huy *et al.*, “Tilted Fiber Bragg Grating photowritten in microstructured optical fiber for improved refractive index measurement.,” *Opt. Express*, vol. 14, no. 22, pp. 10359–10370, 2006.

[19] J. Albert, L.-Y. Shao, and C. Caucheteur, “Tilted fiber Bragg grating sensors,” *Laser Photon. Rev.*, vol. 7, no. 1, pp. 83–108, 2013.

[20] E. Chehura, S. W. James, and R. P. Tatam, “Temperature and strain discrimination using a single tilted fibre Bragg grating,” *Opt. Commun.*, vol. 275, no. 2, pp. 344–347, Jul. 2007.
[21] X. Dong, H. Zhang, B. Liu, and Y. Miao, “Tilted fiber bragg gratings: Principle and sensing applications,” *Photonic Sensors*, vol. 1, no. 1, pp. 6–30, 2011.
[22] Y. Zhao, Q. I. Wang, and H. E. Huang, “Characteristics and applications of tilted fiber Bragg gratings,” *J. Optoelectrics Adv. Mater.*, vol. 12, no. 12, pp. 2343–2354, 2010.
[23] Y.-C. Wang, L.-H. Shyu, and C.-P. Chang, “The Comparison of Environmental Effects on Michelson and Fabry-Perot Interferometers Utilized for the Displacement Measurement,” *Sensors*, vol. 10, no. 12, pp. 2577–2586, Mar. 2010.
[24] T. Steinmetz *et al.*, “Stable fiber-based Fabry-Pérot cavity,” *Appl. Phys. Lett.*, vol. 89, no. 11, pp. 1–4, 2006.
[25] K. Ott *et al.*, “Millimeter-long fiber Fabry-Perot cavities,” *Opt. Express*, vol. 24, no. 9, p. 9839, 2016.
[26] W.-C. Du, X.-M. Tao, and H.-Y. Tam, “Fiber Bragg grating cavity sensor for simultaneous measurement of strain and temperature,” *IEEE Photonics Technol. Lett.*, vol. 11, no. 1, pp. 105–107, 1999.
[27] X. Li, Y. Shao, Y. Yu, Y. Zhang, and S. Wei, “A Highly Sensitive Fiber-Optic Fabry–Perot Interferometer Based on Internal Reflection Mirrors for Refractive Index Measurement,” *Sensors*, vol. 16, no. 6, p. 794, 2016.
[28] J. Xia, Q. Wang, X. Liu, and H. Luo, “Fiber Optic Fabry-Perot Current Sensor Integrated with Magnetic Fluid Using a Fiber Bragg Grating Demodulation,” *Sensors*, vol. 15, no. 7, pp. 16632–16641, 2015.
[29] J. Mathew *et al.*, “In-fiber Fabry-Perot cavity sensor for high-temperature applications,” *J. Light. Technol.*, vol. 33, no. 12, pp. 2419–2425, 2015.
[30] C. R. Liao, T. Y. Hu, and D. N. Wang, “Optical fiber Fabry-Perot interferometer cavity fabricated by femtosecond laser micromachining and fusion splicing for refractive index sensing,” *Opt. Express*, vol. 20, no. 20, p. 22813, 2012.
[31] A. Pospori and D. J. Webb, “Stress Sensitivity Analysis of Optical Fiber Bragg Grating-Based Fabry-Pérot Interferometric Sensors,” *J. Light. Technol.*, vol. 35, no. 13, pp. 2654–2659, 2017.
[32] W. Huang, W. Zhang, T. Zhen, F. Zhang, and F. Li, “π-phase-shifted FBG for high-resolution static-strain measurement based on wavelet threshold denoising algorithm,” *J. Light. Technol.*, vol. 32, no. 22, pp. 3692–3698, 2014.
[33] D. Gatti, G. Galzerano, D. Janner, S. Longhi, and P. Laporta, “Fiber strain sensor based on a π-phase-shifted Bragg grating and the Pound-Drever-Hall technique,” *Opt. Express*, vol. 16, no. 3, p. 1945, 2008.
[34] S. Cieszczyk, J. Klimek, K. Skorupski, and P. Kisala, “A study and modeling of Fabry-Perot cavities with rare earth doped fiber,” in *15th Conference on Optical Fibers and Their Applications*, 2014, p. 92280X.
[35] A. Wada, S. Tanaka, and N. Takahashi, “Optical Fiber Vibration Sensor Using FBG Fabry–Perot Interferometer With Wavelength Scanning and Fourier Analysis,” *IEEE Sens. J.*, vol. 12, no. 1, pp. 225–229, 2012.
[36] Y. Wu, Y. Yang, W. Jin, Y. Shen, and S. Jian, “Compact Mach–Zehnder interferometer-based no-core fiber hollow-core fiber no-core fiber structure,” *Opt. Eng.*, vol. 56, no. 3, p. 030501, 2017.
[37] D. Wu *et al.*, “Refractive index sensing based on Mach–Zehnder interferometer formed by three cascaded single-mode fiber tapers,” *Appl. Opt.*, vol. 50, no. 11,

p. 1548, 2011.

[38] W. W. Li, W. P. Chen, D. N. Wang, Z. K. Wang, and B. Xu, “Fiber inline Mach–Zehnder interferometer based on femtosecond laser inscribed waveguides,” *Opt. Lett.*, vol. 42, no. 21, p. 4438, 2017.

[39] P. Chen, X. Shu, and K. Sugden, “Ultra-compact all-in-fiber-core Mach–Zehnder interferometer,” *Opt. Lett.*, vol. 42, no. 20, pp. 4059–4062, 2017.

[40] P. Chen, X. Shu, and K. Sugden, “Compact assembly-free vector bend sensor based on all-in-fiber-core Mach–Zehnder interferometer,” *Opt. Lett.*, vol. 43, no. 3, pp. 531–534, 2018.

[41] D. Yuan, Y. Dong, Y. Liu, and T. Li, “Mach-Zehnder Interferometer Biochemical Sensor Based on Silicon-on-Insulator Rib Waveguide with Large Cross Section,” *Sensors*, vol. 15, no. 12, pp. 21500–21517, 2015.

[42] Y. K. T. Ishigure, M. Satoh, O. Takanashi, E. Nihei, T. Nyu, S. Yamazaki, “Formation of the refractive index profile in the graded index polymer optical fiber for gigabit data transmission,” *J. Light. Technol.*, vol. 15, no. 11, pp. 2095–2100, 1997.

[43] H. L. Dobb, “Fibre gratings in novel optical fibres for applications in sensing,” Aston University, 2007.

[44] O. Z. W. Daum, J. Krauser, P.E. Zamzow, *POF – polymer optical fiber for data communication applications*. Springer-Verlag Berlin Heidelberg GmbH, 2002.

[45] T. Ishigure, E. Nihei, S. Yamazaki, K. Kobayashi, and Y. Koike, “2.5-Gbit/s 100m Data-Transmission using Graded-Index Polymer Optical-Fiber and High-Speed Laser-Diode at 650 Nm Wavelength,” *Electron. Lett.*, vol. 31, no. 6, pp. 467–469, 1995.

[46] D. J. Webb and K. Kalli, “Polymer fiber Bragg gratings,” in *Fiber Bragg Grating Sensors: Recent Advancements, Industrial Applications and Market Exploitation*, A. C. and J. A. (Eds) Andrea Cusano, Ed. Bentham Science Publishers Ltd., 2011, pp. 292–312.

[47] G. Giaretta, W. White, M. Wegmuller, and T. Onishi, “High-speed (11 Gbit/s) data transmission using perfluorinated graded-index polymer optical fibers for short interconnects (<100 m),” *IEEE Photonics Technol. Lett.*, vol. 12, no. 3, pp. 347–349, 2000.

[48] E. N. Y. Koike, T. Ishigure, “High-bandwidth graded-index polymer optical fiber,” *J. Light. Technol.*, vol. 13, no. 7, pp. 1475–1489, 1995.

[49] J. Chen *et al.*, “High-Bandwidth and Large Coupling Tolerance Graded-Index Multimode Polymer Waveguides for On-Board High-Speed Optical Interconnects,” *J. Light. Technol.*, vol. 34, no. 12, pp. 2934–2940, 2016.

[50] J. Chen, N. Bamiedakis, P. Vasil’ev, R. Penty, and I. White, “Low-Loss and High-Bandwidth Multimode Polymer Waveguide Components Using Refractive Index Engineering,” in *Conference on Lasers and Electro-Optics*, 2016, p. SM2G.7.

[51] M. J. Schmid and M. S. Müller, “Measuring Bragg gratings in multimode optical fibers,” *Opt. Express*, vol. 23, no. 6, pp. 8087–8094, 2015.

[52] C. Lu and Y. Cui, “Fiber bragg grating spectra in multimode optical fibers,” *J. Light. Technol.*, vol. 24, no. 1, pp. 598–604, 2006.

[53] A. Stefani, “Bragg grating sensors in microstructured polymer optical fibres: Accelerometers and microphones,” Technical University of Denmark, 2011.

[54] G. D. Peng, P. L. Chu, Z. Xiong, T. W. Whitbread, and R. P. Chaplin, “Dye-doped step-index polymer optical fiber for broadband optical amplification,” *J. Light. Technol.*, vol. 14, no. 10, pp. 2215–2223, 1996.

[55] M. C. J. Large *et al.*, “Microstructured polymer optical fibers: progress and promise,” in *Proc. SPIE 4616*, 2002, pp. 105–116.

[56] N. A. Mortensen, “Semianalytical approach to short-wavelength dispersion and modal properties of photonic crystal fibers,” *Opt. Lett.*, vol. 30, no. 12, p. 1455, 2005.

[57] N. A. Mortensen, J. R. Folkenberg, M. D. Nielsen, and K. P. Hansen, “Modal cutoff and the V parameter in photonic crystal fibers,” *Opt. Lett.*, vol. 28, no. 20, p. 1879, 2003.

[58] G. D. Peng and P. L. Chu, “Polymer optical fiber photosensitivities and highly tunable fiber gratings,” *Fiber Integr. Opt.*, vol. 19, no. 4, pp. 277–293, 2000.

[59] Z. Xiong, G. D. Peng, B. Wu, and P. L. Chu, “Highly Tunable Bragg Gratings in Single-Mode Polymer Optical Fibers,” *IEEE Photonics Technol. Lett.*, vol. 11, no. 3, pp. 352–354, 1999.

[60] Z. X. P.-L. Chu, G. D. Peng, “Highly-tunable polymer optical fiber gratings,” in *8th international POF conference*, 1999, pp. 242–245.

[61] H. Y. Liu, G. D. Peng, and P. L. Chu, “Thermal tuning of polymer optical fiber Bragg gratings,” *IEEE Photonics Technol. Lett.*, vol. 13, no. 8, pp. 824–826, 2001.

[62] H. U. Hassan, K. Nielsen, S. Aasmul, and O. Bang, “Polymer optical fiber compound parabolic concentrator tip for enhanced coupling efficiency for fluorescence based glucose sensors,” *Biomed. Opt. Express*, vol. 6, no. 12, p. 5008, 2015.

[63] C. Zhang, W. Zhang, D. J. Webb, and G.-D. Peng, “Optical fibre temperature and humidity sensor,” *Electron. Lett.*, vol. 46, no. 9, p. 643, 2010.

[64] H. Ma, A. K. Y. Jen, and L. R. Dalton, “Polymer-based optical waveguides: Materials, processing, and devices,” *Adv. Mater.*, vol. 14, no. 19, pp. 1339–1365, 2002.

[65] A. Yeniay, R. Gao, K. Takayama, R. Gao, and A. F. Garito, “Ultra-Low-Loss Polymer Waveguides,” *J. Light. Technol.*, vol. 22, no. 1, pp. 154–158, 2004.

[66] J. Witt, M. Breithaupt, J. Erdmann, and K. Krebber, “Humidity sensing based on microstructured POF long period gratings,” in *International Conference on Plastic Optical Fibres*, 2011, no. 1, pp. 409–414.

[67] W. Zhang, D. J. Webb, and G. D. Peng, “Investigation into time response of polymer fiber bragg grating based humidity sensors,” *J. Light. Technol.*, vol. 30, no. 8, pp. 1090–1096, 2012.

[68] G. D. Peng, P. N. Ji, and T. Wang, “Development of special polymer optical fibres and devices,” *Proc. Soc. Photo-Optical Instrum. Eng.*, vol. 5595, pp. 138–152, 2004.

[69] A. Abang and D. J. Webb, “Demountable connection for polymer optical fiber grating sensors,” *Opt. Eng.*, vol. 51, no. 8, pp. 080503-1, 2012.

[70] D. J. Webb *et al.*, “Recent developments of Bragg gratings in PMMA and TOPAS polymer optical fibers,” in *Proceedings of SPIE*, 2008, vol. 6830, p. 683002.

[71] I. P. Johnson *et al.*, “Optical fibre Bragg grating recorded in TOPAS cyclic olefin copolymer,” *Electron. Lett.*, vol. 47, no. 4, p. 271, 2011.

[72] D. J. Webb *et al.*, “Temperature sensitivity of Bragg gratings in PMMA and TOPAS microstructured polymer optical fibres,” in *Photonic Crystal Fibers II*, 2008, vol. 6990, p. 69900L.

[73] W. Yuan *et al.*, “Humidity insensitive TOPAS polymer fiber Bragg grating sensor,” *Opt. Express*, vol. 19, no. 20, pp. 19731–19739, 2011.

[74] N. Yoshihara, “Low-loss, high-bandwidth fluorinated POF for visible to 1.3-μm wavelengths,” in *Optical Fiber Communication Conference and Exhibit*, 1998, p. 308-.

[75] N. Yoshihara, “Performance of perfluorinated POF,” in *POF conference*, 1997.

[76] Y. Koike, “Progress of low-loss GI polymer optical fiber from visible to 1.5-m wavelength,” in *11th International Conference on Integrated Optics and Optical Fibre Communications*, 1997, p. v1:59.

[77] Y. Koike and M. Asai, “The future of plastic optical fiber,” *NPG Asia Mater.*, vol. 1, no. 1, pp. 22–28, 2009.

[78] W. J. Tomlinson, I. P. Kaminow, E. A. Chandross, R. L. Fork, and W. T. Silfvast, “Photoinduced refractive index increase in poly(methylmethacrylate) and its applications,” *Appl. Phys. Lett.*, vol. 16, no. 12, pp. 486–489, 1970.

[79] I. P. Kaminow, H. P. Weber, and E. A. Chandross, “Poly(methyl methacrylate) dye laser with internal diffraction grating resonator,” *Appl. Phys. Lett.*, vol. 18, no. 11, pp. 497–499, 1971.

[80] J. M. Moran and I. P. Kaminow, “Properties of holographic gratings photoinduced in polymethyl methacrylate.,” *Appl. Opt.*, vol. 12, no. 8, pp. 1964–70, 1973.

[81] M. J. Bowden, E. A. Chandross, and I. P. Kaminow, “Mechanism of the photoinduced refractive index increase in polymethyl methacrylate,” *Appl. Opt.*, vol. 13, no. 1, pp. 112–117, 1974.

[82] J. Marotz, “Holographic storage in sensitized polymethyl methacrylate blocks,” *Appl. Phys. B Photophysics Laser Chem.*, vol. 37, no. 4, pp. 181–187, 1985.

[83] F. P. Laming, “Holographic grating formation in photopolymers-Polymethylmethacrylate,” *Polym. Eng. Sci.*, vol. 11, no. 5, pp. 421–425, 1971.

[84] T. Mitsuoka, A. Torikai, and K. Fueki, “Wavelength sensitivity of the photodegradation of poly(methyl methacrylate),” *J. Appl. Polym. Sci.*, vol. 47, no. 6, pp. 1027–1032, 1993.

[85] D. Sáez-Rodríguez, K. Nielsen, O. Bang, and D. J. Webb, “Photosensitivity mechanism of undoped poly(methyl methacrylate) under UV radiation at 325 nm and its spatial resolution limit,” *Opt. Lett.*, vol. 39, no. 12, pp. 3421–3424, 2014.

[86] J. Yu, X. Tao, and H. Tam, “Trans-4-stilbenemethanol-doped photosensitive polymer fibers and gratings.,” *Opt. Lett.*, vol. 29, no. 2, pp. 156–8, 2004.

[87] G. D. Peng, Z. Xiong, and P. L. Chu, “Photosensitivity and Gratings in Dye-Doped Polymer Optical Fibers,” *Opt. Fiber Technol.*, vol. 5, no. 2, pp. 242–251, 1999.

[88] H. Y. Liu, G. D. Peng, P. L. Chu, Y. Koike, and Y. Watanabe, “Photosensitivity in low-loss perfluoropolymer (CYTOP) fibre material,” *Electron. Lett.*, vol. 37, no. 6, pp. 347–348, 2001.

[89] L. R. Kawase, J. C. Santos, C. M. Gibo, H. Y. Liu, G. D. Peng, and P. L. Chu, “Study of Photosensitivity in Perfluorinated Polymer (CYTOP) Material,” in *POF 2001: 10th International Conference on Plastic Optical Fibers*, 2001.

[90] “An introduction to phase masks for FBG writing.” [Online]. Available: www.coherent.com.

[91] Z. Xiong, G. D. Peng, B. Wu, and P. L. Chu, “Effects of the zeroth-order diffraction of a phase mask on Bragg gratings,” *J. Light. Technol.*, vol. 17, no. 11, pp. 2361–2365, 1999.

[92] H. Dobb, D. J. Webb, K. Kalli, A. Argyros, M. C. J. Large, and M. A. van Eijkelenborg, “Continuous wave ultraviolet light-induced fiber Bragg gratings in few- and single-mode microstructured polymer optical fibers,” *Opt. Lett.*, vol.

30, no. 24, pp. 3296–3298, 2005.

[93] H. Dobb, D. J. Webb, and K. Kalli, “CW UV light induced fibre Bragg gratings in few- and single-moded microstructured polymer optical fibres,” *Opt. Lett.*, vol. 30, no. 24, pp. 3296–3298, 2005.

[94] I. Johnson, K. Kalli, and D. J. Webb, “827nm Bragg grating sensor in multimode microstructured polymer optical fibre,” *Electron. Lett.*, vol. 46, no. 17, pp. 3–4, 2010.

[95] Z. F. Zhang, C. Zhang, X. M. Tao, G. F. Wang, and G. D. Peng, “Inscription of polymer optical fiber Bragg grating at 962 nm and its potential in strain sensing,” *IEEE Photonics Technol. Lett.*, vol. 22, no. 21, pp. 1562–1564, 2010.

[96] H. Liu, G. D. Peng, and P. L. Chu, “Polymer fiber Bragg gratings with 28 dB transmission rejection,” *Opt. Commun.*, vol. 14, no. 7, pp. 935–937, 2002.

[97] G. Rajan, M. Y. M. Noor, E. Ambikairajah, and G.-D. Peng, “Inscription of Multiple Bragg Gratings in a Single-Mode Polymer Optical Fiber Using a Single Phase Mask and Its Analysis,” *IEEE Sens. J.*, vol. 14, no. 7, pp. 2384–2388, 2014.

[98] I. P. Johnson, D. J. Webb, K. Kalli, M. C. J. Large, and A. Argyros, “Multiplexed FBG sensor recorded in multimode microstructured polymer optical fibre,” vol. 7714, p. 77140D, 2010.

[99] X. Hu, D. Kinet, P. Mégret, and C. Caucheteur, “Control over photo-inscription and thermal annealing to obtain high-quality Bragg gratings in doped PMMA optical fibers,” *Opt. Lett.*, vol. 41, no. 13, pp. 2930–2933, 2016.

[100] H. B. Liu, H. Y. Liu, G. D. Peng, and P. L. Chu, “Novel Growth Behaviors of Fiber Bragg Gratings in Polymer Optical Fiber Under UV Irradiation With Low Power,” *IEEE Photonics Technol. Lett.*, vol. 16, no. 1, pp. 159–161, 2004.

[101] A. Stefani, M. Stecher, G. E. Town, and O. Bang, “Fiber design and realization of point-by-point written fiber Bragg gratings in polymer optical fibers,” in *Proceedings of SPIE, Microstructured and Specialty Optical Fibres*, 2012, pp. 842617-842617–7.

[102] I.-L. Bundalo, K. Nielsen, C. Markos, and O. Bang, “Bragg grating writing in PMMA microstructured polymer optical fibers in less than 7 minutes.,” *Opt. Express*, vol. 22, no. 5, pp. 5270–5276, 2014.

[103] R. Oliveira, L. Bilro, and R. Nogueira, “Bragg gratings in a few mode microstructured polymer optical fiber in less than 30 seconds,” *Opt. Express*, vol. 23, no. 8, p. 10181, 2015.

[104] X. Hu, D. Kinet, K. Chah, P. Mégret, and C. Caucheteur, “Bragg gratings inscription in step-index PMMA optical fiber by femtosecond laser pulses at 400 nm,” in *Sixth European Workshop on Optical Fibre Sensors*, 2016, vol. 9916, p. 99161X.

[105] B. Malo, K. O. Hill, F. Bilodeau, D. C. Johnson, and J. Albert, “Point-by-point fabrication of micro-Bragg gratings in photosensitive fibre using single excimer pulse refractive index modification techniques,” *Electron. Lett.*, vol. 29, no. 18, pp. 1668–1669, 1993.

[106] A. Martinez, M. Dubov, I. Khrushchev, and I. Bennion, “Direct writing of fibre Bragg gratings by femtosecond laser,” *Electron. Lett.*, vol. 40, no. 19, pp. 1170–1171, 2004.

[107] K. Peters, “Polymer optical fiber sensors - a review,” *Smart Mater. Struct.*, vol. 20, no. 1, pp. 1–17, 2011.

[108] W. Yuan *et al.*, “Improved thermal and strain performance of annealed polymer optical fiber Bragg gratings,” *Opt. Commun.*, vol. 284, no. 1, pp. 176–182, 2011.

[109] A. Abang and D. J. Webb, “Influence of mounting on the hysteresis of polymer fiber Bragg grating strain sensors,” *Opt. Lett.*, vol. 38, no. 9, pp. 1376–1378, 2013.

[110] A. Abang, D. J. Webb, and G.-D. Peng, “Strain response of POF sensors,” in *22nd International Conference on Optical Fiber Sensors*, 2012, vol. 8421, pp. 1–4.

[111] C. Markos, A. Stefani, K. Nielsen, H. K. Rasmussen, W. Yuan, and O. Bang, “High-Tg TOPAS microstructured polymer optical fiber for fiber Bragg grating strain sensing at 110 degrees,” *Opt. Express*, vol. 21, no. 4, pp. 4758–4765, 2013.

[112] G. Woyessa *et al.*, “Single mode step-index polymer optical fiber for humidity insensitive high temperature fiber Bragg grating sensors,” *Opt. Express*, vol. 24, no. 2, pp. 1253–1260, 2016.

[113] Y. Luo *et al.*, “Analysis of multimode BDK doped POF gratings for temperature sensing,” *Opt. Commun.*, vol. 285, no. 21–22, pp. 4353–4358, Oct. 2012.

[114] H. Y. Liu, G. D. Peng, and P. L. Chu, “Thermal stability of gratings in PMMA and CYTOP polymer fibers,” *Opt. Commun.*, vol. 204, no. 1–6, pp. 151–156, 2002.

[115] A. Ada and D. J. Webb, “Effects of annealing, pre-tension and mounting on the hysteresis of polymer strain sensors,” *Meas. Sci. Technol.*, vol. 25, no. 1, p. 15102, 2014.

[116] N. G. Harbach, “Fiber Bragg gratings in polymer optical fibers,” EPFL, 2008.

[117] W. Z. and D. J. Webb, “Humidity responsivity of poly(methyl methacrylate)-based optical fiber Bragg grating sensors,” *Opt. Lett.*, vol. 39, no. 10, pp. 3026–3029, 2014.

[118] L. Khan *et al.*, “Humidity sensitivity of topas optical fibre bragg grating,” in *20th International Conference on Plastic Optical Fibers*, 2011, pp. 179–183.

[119] M. a Davis, a D. Kersey, J. Sirkis, and E. J. Friebele, “Shape and vibration mode sensing using a fiber optic Bragg grating array,” *Smart Mater. Struct.*, vol. 5, no. 6, pp. 759–765, 1996.

[120] S. Javdani, M. Fabian, M. Ams, J. Carlton, T. Sun, and K. T. V Grattan, “Fiber bragg grating-based system for 2-D analysis of vibrational modes of a steel propeller blade,” *J. Light. Technol.*, vol. 32, no. 23, pp. 3991–3997, 2014.

[121] I.-B. Kwon and K.-S. Choi, “Fiber optic sensors and their applications on structural health monitoring in South Korea,” in *22nd International Conference on Optical Fiber Sensors;*, 2012, p. 84210I–84210I–8.

[122] Bai-Ou Guan, Hwa-Yaw Tam, Sien-Ting Lau, and H. L. W. Chan, “Ultrasonic hydrophone based on distributed Bragg reflector fiber laser,” *IEEE Photonics Technol. Lett.*, vol. 17, no. 1, pp. 169–171, 2005.

[123] L.-Y. Shao *et al.*, “High-Frequency Ultrasonic Hydrophone Based on a Cladding-Etched DBR Fiber Laser,” *IEEE Photonics Technol. Lett.*, vol. 20, no. 8, pp. 548–550, 2008.

[124] N. Cennamo, G. D’Agostino, M. Pesavento, and L. Zeni, “High selectivity and sensitivity sensor based on MIP and SPR in tapered plastic optical fibers for the detection of l-nicotine,” *Sensors Actuators B Chem.*, vol. 191, pp. 529–536, 2014.

[125] H. U. Hassan, A. Lacraz, K. Kalli, and O. Bang, “Femtosecond laser micromachining of compound parabolic concentrator fiber tipped glucose sensors,” *J. Biomed. Opt.*, vol. 22, no. 3, p. 037003, 2017.

[126] S. Poeggel *et al.*, “Recent improvement of medical optical fibre pressure and

temperature sensors," *Biosensors,* vol. 5, no. 3, pp. 432–449, 2015.

[127] C. Markos, W. Yuan, K. Vlachos, G. E. Town, and O. Bang, "Label-free biosensing with high sensitivity in dual-core microstructured polymer optical fibers," *Opt. Express,* vol. 19, no. 8, p. 7790, 2011.

[128] Y. Zhu, E. Simova, P. Berini, and C. P. Grover, "A comparison of wavelength dependent polarization dependent loss measurements in fiber gratings," *IEEE Trans. Instrum. Meas.*, vol. 49, no. 6, pp. 1231–1239, 2000.

[129] X. Hu *et al.*, "Polarization effects in polymer FBGs: study and use for transverse force sensing," *Opt. Express,* vol. 23, no. 4, pp. 4581–4590, 2015.

[130] T. Erdogan and V. Mizrahi, "Characterization of UV-induced birefringence in photosensitive Ge-doped silica optical fibers," *J. Opt. Soc. Am. B,* vol. 11, no. 10, pp. 2100–2105, 1994.

[131] M. G. Xu, L. Reekie, Y. T. Chow, and J. P. Dakin, "Optical in-fibre grating high pressure sensor," *Electron. Lett.*, vol. 29, no. 4, p. 398, 1993.

[132] K. Bhowmik *et al.*, "Experimental Study and Analysis of Hydrostatic Pressure Sensitivity of Polymer Fibre Bragg Gratings," *J. Light. Technol.*, vol. 33, no. 12, pp. 2456–2462, 2015.

[133] K. Johnson, Ian P.; Webb, David J. and Kalli, "Hydrostatic pressure sensing using a polymer optical fibre Bragg gratings," in *Asia Pacific optical sensors conference*, 2012, pp. 835106-1-835106–7.

[134] C. Caucheteur *et al.*, "Transverse Strain Measurements Using the Birefringence Effect in Fiber Bragg Gratings," *IEEE Photonics Technol. Lett.*, vol. 19, no. 13, pp. 966–968, 2007.

[135] S. Bette *et al.*, "Spectral characterization of differential group delay in uniform fiber Bragg gratings.," *Opt. Express,* vol. 13, no. 25, pp. 9954–9960, 2005.

[136] Y. O. Barmenkov, D. Zalvidea, S. Torres-Peiró, J. L. Cruz, and M. V. Andrés, "Effective length of short Fabry-Perot cavity formed by uniform fiber Bragg gratings," *Opt. Express,* vol. 14, no. 14, pp. 6394–6399, 2006.

[137] S. Huo, S. R. Short, and X. Xue, "FEM Based Modal Analysis of a Damaged Free-Free Beam," in *SEM X Int. Congr. Expo. Experim. Appl. Mech.*, 2004, vol. 2, no. 1, pp. 1–8.

[138] N. G. Jaiswal and D. W. Pande, "Sensitizing The Mode Shapes Of Beam Towards Damage Detection Using Curvature And Wavelet Transform," *Int. J. Sci. Technol. Res.*, vol. 4, no. 4, pp. 266–272, 2015.

[139] T. D. Burton, *Introduction To Dynamic Systems Analysis*. McGraw-Hill, 1994.

[140] D. J. Inman, *Engineering Vibration,* Third. Pearson, 2007.

[141] A. D. Dimarogonas, *Vibration for Engineers,* Second. Prentice Hall, 1996.

[142] C. Peterson and J. Korumpas, "Atmosphere detector for helicopter blades," US3795147A, 1972.

[143] M. C. T. G. P. Engels, "Helicopter blade crack detection system," US5205710A, 1993.

[144] R. A. Parr, "Blade inspection system and method," US3667862A, 1972.

[145] J. J. M. C. D. Sam, "Helicopter blade crack indicator," US3985318A, 1976.

[146] P. J. Schubel, R. J. Crossley, E. K. G. Boateng, and J. R. Hutchinson, "Review of structural health and cure monitoring techniques for large wind turbine blades," *Renew. Energy,* vol. 51, pp. 113–123, 2013.

[147] S. Song, Y. Hou, M. Guo, L. Wang, X. Tong, and J. Wu, "An investigation on the aggregate-shape embedded piezoelectric sensor for civil infrastructure health monitoring," *Constr. Build. Mater.*, vol. 131, pp. 57–65, 2017.

[148] W. Ecke, I. Latka, R. Willsch, A. Reutlinger, and R. Graue, "Fibre optic sensor

network for spacecraft health monitoring," *Meas. Sci. Technol.*, vol. 12, no. 7, p. 974, 2001.

[149] A. Theodosiou, K. Kalli, and M. Komodromos, "Health monitoring of carbon cantilever using femtosecond laser inscribed FBG array in gradient-index CYTOP polymer fibre," in *25th Optical Fibre Sensors Conference*, 2017, vol. 10323, pp. 4–7.

[150] A. Theodosiou, M. Komodromos, and K. Kalli, "Carbon cantilever beam health inspection using a polymer fibre Bragg grating array," *J. Light. Technol.*, vol. 36, no. 4, pp. 986–992, 2017.

[151] A. Theodosiou, K. Kalli, and M. Komodromos, "Dynamic damage detection of a cantilever carbon beam using a FBG array inscribed in polymer gradient index multimode CYTOP fibre," in *Conference on Polymer Optical fibers*, 2016, pp. 2–5.

[152] A. K. Pandey, M. Biswas, and M. M. Samman, "Damage detection from changes in curvature mode shapes," *J. Sound Vib.*, vol. 145, no. 2, pp. 321–332, 1991.

[153] J.-T. Kim, Y.-S. Ryu, H.-M. Cho, and N. Stubbs, "Damage identification in beam-type structures: frequency-based method vs mode-shape-based method," *Eng. Struct.*, vol. 25, no. 1, pp. 57–67, 2003.

[154] W. Yuan, A. Stefani, and O. Bang, "Tunable polymer fiber Bragg grating (FBG) inscription: Fabrication of dual-FBG temperature compensated polymer optical fiber strain sensors," *IEEE Photonics Technol. Lett.*, vol. 24, no. 5, pp. 401–403, 2012.

[155] C. A. F. Marques, D. J. Webb, and P. Andre, "Polymer optical fiber sensors in human life safety," *Opt. Fiber Technol.*, vol. 36, pp. 144–154, 2017.

[156] A. H. Abdul Razak, A. Zayegh, R. K. Begg, and Y. Wahab, "Foot plantar pressure measurement system: A review," *Sensors (Switzerland)*, vol. 12, no. 7. pp. 9884–9912, 2012.

[157] W. Tao, T. Liu, R. Zheng, and H. Feng, "Gait analysis using wearable sensors," *Sensors*, vol. 12, no. 2. pp. 2255–2283, 2012.

[158] E. Morag and P. R. Cavanagh, "Structural and functional predictors of regional peak pressures under the foot during walking," *J. Biomech.*, vol. 32, no. 4, pp. 359–370, 1999.

[159] C. M. Kim and J. J. Eng, "Symmetry in vertical ground reaction force is accompanied by symmetry in temporal but not distance variables of gait in persons with stroke," *Gait Posture*, vol. 18, no. 1, pp. 23–28, 2003.

[160] J. Taborri, E. Palermo, S. Rossi, and P. Cappa, "Gait partitioning methods: A systematic review," *Sensors*, vol. 16, no. 1, p. 66, 2016.

[161] O. Postolache *et al.*, "Smart walker solutions for physical rehabilitation," *IEEE Instrum. Meas. Mag.*, vol. 18, no. 5, pp. 21–30, 2015.

[162] L. De Vito, O. Postolache, and S. Rapuano, "Measurements and sensors for motion tracking in motor rehabilitation," *IEEE Instrum. Meas. Mag.*, vol. 17, no. 3, pp. 30–38, 2014.

[163] P. Roriz, L. Carvalho, O. Frazão, J. L. Santos, and J. A. Simões, "From conventional sensors to fibre optic sensors for strain and force measurements in biomechanics applications: A review," *Journal of Biomechanics*, vol. 47, no. 6. pp. 1251–1261, 2014.

[164] J. Z. Hao *et al.*, "Design of a foot-pressure monitoring transducer for diabetic patients based on FBG sensors," in *The 16th Annual Meeting of the IEEE Lasers and Electro-Optics Society*, 2003, vol. 1, pp. 23–24.

[165] T. C. Liang, J. J. Lin, and L. Y. Guo, "Plantar pressure detection with fiber bragg

gratings sensing system," *Sensors*, vol. 16, no. 10, p. 1766, 2016.
[166] R. Suresh, S. Bhalla, J. Hao, and C. Singh, "Development of a high resolution plantar pressure monitoring pad based on fiber Bragg grating (FBG) sensors," *Technol. Heal. Care*, vol. 23, no. 6, pp. 785–794, 2015.
[167] M. F. Domingues *et al.*, "Insole optical fiber Bragg grating sensors network for dynamic vertical force monitoring," *J. Biomed. Opt.*, vol. 22, no. 9, p. 091507, 2017.
[168] S. C. Wearing, S. Urry, J. E. Smeathers, and D. Battistutta, "A comparison of gait initiation and termination methods for obtaining plantar foot pressures," *Gait Posture*, vol. 10, no. 3, pp. 255–263, 1999.
[169] S. P. Silva, M. A. Sabino, E. M. Fernandes, V. M. Correlo, L. F. Boesel, and R. L. Reis, "Cork: properties, capabilities and applications," *Int. Mater. Rev.*, vol. 50, no. 6, pp. 345–365, 2005.
[170] W. M. dos Santos, G. A. P. Caurin, and A. A. G. Siqueira, "Design and control of an active knee orthosis driven by a rotary Series Elastic Actuator," *Control Eng. Pract.*, vol. 58, pp. 307–318, 2017.
[171] R. Osellame *et al.*, "Femtosecond writing of active optical waveguides with astigmatically shaped beams," *J. Opt. Soc. Am. B*, vol. 20, no. 7, p. 1559, 2003.
[172] H. Hosono, Y. Abe, D. L. Kinser, R. A. Weeks, K. Muta, and H. Kawazoe, "Nature and origin of the 5-eV band in SiO2:GeO2 glasses," *Phys. Rev. B*, vol. 46, no. 18, pp. 11445–11451, 1992.
[173] R. E. Silva, M. Becker, A. Hartung, M. Rothhardt, A. A. P. Pohl, and H. Bartelt, "Reflectivity and Bandwidth Modulation of Fiber Bragg Gratings in a Suspended Core Fiber by Tunable Acoustic Waves," *IEEE Photonics J.*, vol. 6, no. 6, pp. 1–8, 2014.
[174] K. Zhou, G. Simpson, X. Chen, L. Zhang, and I. Bennion, "45 ° tilted fiber Bragg gratings," *Opt. Lett.*, vol. 30, no. 11, pp. 1285–1287, 2005.
[175] Y. X. Jin, C. C. Chan, X. Y. Dong, and Y. F. Zhang, "Temperature-independent bending sensor with tilted fiber Bragg grating interacting with multimode fiber," *Opt. Commun.*, vol. 282, no. 19, pp. 3905–3907, 2009.
[176] X. Chen, K. Zhou, L. Zhang, and I. Bennion, "In-fiber twist sensor based on a fiber Bragg grating with 81o tilted structure," *IEEE Photonics Technol. Lett.*, vol. 18, no. 24, pp. 2596–2598, 2006.
[177] S. Maguis *et al.*, "Biofunctionalized tilted Fiber Bragg Gratings for label-free immunosensing.," *Opt. Express*, vol. 16, no. 23, pp. 19049–19062, 2008.
[178] T. Guo, C. Chen, A. Laronche, and J. Albert, "Power-referenced and temperature-calibrated optical fiber refractometer," *IEEE Photonics Technol. Lett.*, vol. 20, no. 8, pp. 635–637, 2008.
[179] W. Zhou, Y. Zhou, and J. Albert, "A true fiber optic refractometer," *Laser Photonics Rev.*, vol. 11, no. 1, pp. 1–10, 2017.
[180] Y. Shevchenko, G. Camci-Unal, D. F. Cuttica, M. R. Dokmeci, J. Albert, and A. Khademhosseini, "Surface plasmon resonance fiber sensor for real-time and label-free monitoring of cellular behavior," *Biosens. Bioelectron.*, vol. 56, pp. 359–367, 2014.
[181] V. Voisin, J. Pilate, P. Damman, P. Mégret, and C. Caucheteur, "Highly sensitive detection of molecular interactions with plasmonic optical fiber grating sensors," *Biosens. Bioelectron.*, vol. 51, pp. 249–254, 2014.
[182] C.-F. Chan, C. Chen, A. Jafari, A. Laronche, D. J. Thomson, and J. Albert, "Optical fiber refractometer using narrowband cladding-mode resonance shifts," *Appl. Opt.*, vol. 46, no. 7, p. 1142, 2007.

[183] C. Ribaut *et al.*, “Small biomolecule immunosensing with plasmonic optical fiber grating sensor,” *Biosens. Bioelectron.*, vol. 77, pp. 315–322, 2016.

[184] T. Guo, F. Liu, Y. Liu, N. K. Chen, B. O. Guan, and J. Albert, “In-situ detection of density alteration in non-physiological cells with polarimetric tilted fiber grating sensors,” *Biosens. Bioelectron.*, vol. 55, pp. 452–458, 2014.

[185] “https://www.fibercore.com/.” [Online]. Available: https://www.fibercore.com/.

[186] A. Theodosiou, M. Polis, A. Lacraz, K. Kalli, M. Komodromos, and A. Stassis, “Comparative study of multimode CYTOP graded index and single-mode silica fibre Bragg grating array for the mode shape capturing of a free-free metal beam,” in *Proc SPIE*, 2016, p. 98860O.

[187] C. Caucheteur, T. Guo, F. Liu, B.-O. Guan, and J. Albert, “Ultrasensitive plasmonic sensing in air using optical fibre spectral combs,” *Nat. Commun.*, vol. 7, 2016.

[188] C. Caucheteur, T. Guo, and J. Albert, “Polarization-assisted fiber Bragg grating sensors: tutorial and review,” *J. Light. Technol.*, vol. 35, no. 16, pp. 3311–3322, 2017.

[189] W. Zhou, Y. Zhou, and J. Albert, “A true fiber optic refractometer,” *Laser Photon. Rev.*, vol. 11, no. 1, p. 1600157, 2017.

[190] A. Dupuis *et al.*, “Prospective for biodegradable microstructured optical fibers,” *Opt. Lett.*, vol. 32, no. 2, p. 109, 2007.

[191] S. Kujala, A. Mannila, L. Karvonen, K. Kieu, and Z. Sun, “Natural Silk as a Photonics Component: a Study on Its Light Guiding and Nonlinear Optical Properties,” *Sci. Rep.*, vol. 6, no. 1, p. 22358, 2016.

[192] A. K. Yetisen *et al.*, “Photonic hydrogel sensors,” *Biotechnol. Adv.*, vol. 34, no. 3, pp. 250–271, 2016.

[193] M. Choi, J. W. Choi, S. Kim, S. Nizamoglu, S. K. Hahn, and S. H. Yun, “Light-guiding hydrogels for cell-based sensing and optogenetic synthesis in vivo,” *Nat. Photonics*, vol. 7, no. 12, pp. 987–994, 2013.

[194] S. Nizamoglu *et al.*, “Bioabsorbable polymer optical waveguides for deep-tissue photomedicine,” *Nat. Commun.*, vol. 7, p. 10374, 2016.

[195] E. Ceci-Ginistrelli *et al.*, “Novel biocompatible and resorbable UV-transparent phosphate glass based optical fiber,” *Opt. Mater. Express*, vol. 6, no. 6, p. 2040, 2016.

[196] J. Burnie, T. Gilchrist, S. Duff, C. Drake, N. Harding, and A. Malcolm, “Controlled release glasses (C.R.G.) for biomedical uses,” *Biomaterials*, vol. 2, no. 4, pp. 244–246, 1981.

[197] A. S. Monem, H. A. ElBatal, E. M. A. Khalil, M. A. Azooz, and Y. M. Hamdy, “In vivo behavior of bioactive phosphate glass-ceramics from the system P2O5–Na2O–CaO containing TiO2,” *J. Mater. Sci. Mater. Med.*, vol. 19, no. 3, pp. 1097–1108, 2008.

[198] N. J. Lakhkar, I.-H. Lee, H.-W. Kim, V. Salih, I. B. Wall, and J. C. Knowles, “Bone formation controlled by biologically relevant inorganic ions: Role and controlled delivery from phosphate-based glasses,” *Adv. Drug Deliv. Rev.*, vol. 65, no. 4, pp. 405–420, 2013.

[199] D. Milanese *et al.*, “Phosphate glass fibers for optical amplifiers and biomedical applications,” in *Optical Fiber Communication Conference*, 2017, p. M2F.2.

[200] L. Di Sieno *et al.*, “Towards the use of bioresorbable fibers in time-domain diffuse optics,” *J. Biophotonics*, vol. 11, pp. 1–12, 2017.

[201] M. Konstantaki, S. Pissadakis, D. Pugliese, E. Ceci-Ginistrelli, N. G. Boetti, and D. Milanese, “Bragg grating UV inscription in a bioresorbable phosphate glass

optical fiber," in *2016 18th International Conference on Transparent Optical Networks (ICTON)*, 2016, pp. 1–4.

[202] N. G. Boetti *et al.*, "High concentration Yb-Er co-doped phosphate glass for optical fiber amplification," *J. Opt.*, vol. 17, no. 6, p. 065705, 2015.

[203] Y. W. Lee, S. Sinha, M. J. F. Digonnet, R. L. Byer, and S. Jiang, "20 W single-mode Yb^3+-doped phosphate fiber laser," *Opt. Lett.*, vol. 31, no. 22, p. 3255, 2006.

[204] J. Guo *et al.*, "Highly Stretchable, Strain Sensing Hydrogel Optical Fibers," *Adv. Mater.*, vol. 28, no. 46, pp. 10244–10249, 2016.

[205] M. Konstantaki, S. Pissadakis, D. Pugliese, E. Ceci-Ginistrelli, N. Boetti, and D. Milanese, "Bragg Gratings in a Bioresorbable Phosphate Glass Optical Fiber," in *Photonics and Fiber Technology 2016 (ACOFT, BGPP, NP)*, 2016, vol. 1, p. BT2B.3.

[206] A. Theodosiou, M. Komodromos, and K. Kalli, "Accurate and Fast Demodulation Algorithm for Multipeak FBG Reflection Spectra Using a Combination of Cross Correlation and Hilbert Transformation," *J. Light. Technol.*, vol. 35, no. 18, pp. 3956–3962, 2017.

[207] K. Kalli, T. Allsop, C. Koutsides, E. Davies, D. Webb, and L. Zhang, "Femtosecond Laser Inscription of Fiber Bragg Gratings with Low Insertion Loss and Minor Polarization Dependence," in *Advanced Photonics & Renewable Energy*, 2010, p. BMA3.

[208] R. R. Thomson *et al.*, "Ultrafast laser inscription of a three dimensional fan-out device for multicore fiber coupling applications," *2008 Conf. Quantum Electron. Laser Sci. Conf. Lasers Electro-Optics, CLEO/QELS*, vol. 15, no. 18, pp. 11691–11697, 2008.

[209] G. N. Smith *et al.*, "Characterisation and performance of a Terfenol-D coated femtosecond laser inscribed optical fibre Bragg sensor with a laser ablated microslot for the detection of static magnetic fields," *Opt. Express*, vol. 19, no. 1, p. 363, 2011.

[210] C. Waltermann, A. Doering, M. Köhring, M. Angelmahr, and W. Schade, "Cladding waveguide gratings in standard single-mode fiber for 3D shape sensing," *Opt. Lett.*, vol. 40, no. 13, p. 3109, 2015.

[211] K. K. C. Lee, A. Mariampillai, M. Haque, B. A. Standish, V. X. D. Yang, and P. R. Herman, "Temperature-compensated fiber-optic 3D shape sensor based on femtosecond laser direct-written Bragg grating waveguides," *Opt. Express*, vol. 21, no. 20, p. 24076, 2013.

[212] S.-M. Tseng and C.-L. Chen, "Side-polished fibers," *Appl. Opt.*, vol. 31, no. 18, p. 3438, Jun. 1992.

[213] Q. Jiang, D. Hu, and M. Yang, "Simultaneous measurement of liquid level and surrounding refractive index using tilted fiber Bragg grating," *Sensors Actuators A Phys.*, vol. 170, no. 1–2, pp. 62–65, Nov. 2011.

[214] Y. Miao, B. Liu, and Q. Zhao, "Refractive index sensor based on measuring the transmission power of tilted fiber Bragg grating," *Opt. Fiber Technol.*, vol. 15, no. 3, pp. 233–236, 2009.

[215] J. H. Chong *et al.*, "Measurements of refractive index sensitivity using long-period grating refractometer," *Opt. Commun.*, vol. 229, no. 1–6, pp. 65–69, 2004.

[216] Z. Wang, "Tissue refractive index as marker of disease," *J. Biomed. Opt.*, vol. 16, no. 11, p. 116017, 2011.

[217] B. Kemper *et al.*, "Investigation of living pancreas tumor cells by digital

holographic microscopy," *J. Biomed. Opt.*, vol. 11, no. 3, p. 034005, 2006.

[218] B. Kemper *et al.*, "Integral refractive index determination of living suspension cells by multifocus digital holographic phase contrast microscopy.," *J. Biomed. Opt.*, vol. 12, no. 5, p. 054009, 2007.

[219] L. Yuan, Z. Liu, and J. Yang, "Coupling characteristics between single-core fiber and multicore fiber.," *Opt. Lett.*, vol. 31, no. 22, pp. 3237–3239, 2006.

[220] L. Yuan, Z. Liu, J. Yang, and C. Guan, "Bitapered fiber coupling characteristics between single-mode single-core fiber and single-mode multicore fiber.," *Appl. Opt.*, vol. 47, no. 18, pp. 3307–3312, 2008.

[221] B. Zhu *et al.*, "Seven-core multicore fiber transmissions for passive optical network," *Opt. Express*, vol. 18, no. 11, p. 11117, 2010.

[222] W. Klaus *et al.*, "Free-space coupling optics for multicore fibers," *IEEE Photonics Technol. Lett.*, vol. 24, no. 21, pp. 1902–1905, 2012.

[223] A. S. Kurkov, S. A. Babin, I. A. Lobach, and S. I. Kablukov, "New mechanism of the mode coupling in multi-core fiber lasers," vol. 6873, p. 68731Q, 2008.

[224] R. He *et al.*, "Silicon p-i-n Junction Fibers," *Adv. Mater.*, vol. 25, no. 10, pp. 1461–1467, 2013.

[225] F. A. Martinsen, B. K. Smeltzer, M. Nord, T. Hawkins, J. Ballato, and U. J. Gibson, "Silicon-core glass fibres as microwire radial-junction solar cells," *Sci. Rep.*, vol. 4, p. 6283, 2014.

[226] F. H. Suhailin *et al.*, "Kerr nonlinear switching in a hybrid silica-silicon microspherical resonator," *Opt. Express*, vol. 23, no. 13, p. 17263, 2015.

[227] P. J. Sazio *et al.*, "Microstructured optical fibers as high-pressure microfluidic reactors," *Science (80-.).*, vol. 311, no. 5767, pp. 1583–1586, 2006.

[228] J. Ballato *et al.*, "Silicon optical fiber," *Opt. Express*, vol. 16, no. 23, pp. 18675–18683, 2008.

[229] N. Healy *et al.*, "CO2 Laser-Induced Directional Recrystallization to Produce Single Crystal Silicon-Core Optical Fibers with Low Loss," *Adv. Opt. Mater.*, vol. 4, no. 7, pp. 1004–1008, 2016.

[230] F. H. Suhailin *et al.*, "Tapered polysilicon core fibers for nonlinear photonics," *Opt. Lett.*, vol. 41, no. 7, pp. 1360–1363, 2016.

[231] F. H. Suhailin *et al.*, "Tunable coaxial resonators based on silicon optical fibers," in *Advanced Photonics*, 2014, p. SoM2B.3.

[232] L. Xiao *et al.*, "Fusion splicing of silicon optical fibres," in *CLEO/Europe-EQEC '15*, 2015.

[233] S. Chaudhuri *et al.*, "Crystalline Silicon Optical Fibers with Low Optical Loss," *ACS Photonics*, vol. 3, no. 3, pp. 378–384, 2016.

[234] N. Healy *et al.*, "Extreme electronic bandgap modification in laser-crystallized silicon optical fibres," *Nat. Mater.*, vol. 13, no. 12, pp. 1122–1127, 2014.

[235] X. Ji *et al.*, "Single-Crystal Germanium Core Optoelectronic Fibers," *Adv. Opt. Mater.*, vol. 5, no. 1, p. 1600592, 2016.

[236] X. Ji *et al.*, "Single-Crystal Silicon Optical Fiber by Direct Laser Crystallization," *ACS Photonics*, vol. 4, no. 1, pp. 85–92, 2017.

[237] A. Suzuki and M. Ishihara, "Application of CO2 laser heating zone drawing and zone annealing to nylon 6 fibers," *J. Appl. Polym. Sci.*, vol. 83, no. 8, pp. 1711–1716, 2002.

[238] A. Heptonstall *et al.*, "Invited Article: CO2 laser production of fused silica fibers for use in interferometric gravitational wave detector mirror suspensions," *Rev. Sci. Instrum.*, vol. 82, no. 1, p. 011301, 2011.

[239] D. A. Coucheron *et al.*, "Laser recrystallization and inscription of compositional

microstructures in crystalline SiGe-core fibres," *Nat. Commun.*, vol. 7, p. 13265, 2016.

[240] G. N. Smith, K. Kalli, and K. Sugden, "Advances in Femtosecond Micromachining and Inscription of Micro and Nano Photonic Devices," in *Frontiers in Guided Wave Optics and Optoelectronics*, no. February, B. Pal, Ed. 2010, p. 674.

[241] T. E. Glover, "Hydrodynamics of particle formation following femtosecond laser ablation," *J. Opt. Soc. Am. B-Optical Phys.*, vol. 20, no. 1, pp. 125–131, 2003.

[242] P. Liu, R. Yen, N. Bloembergen, and R. Hodgson, "Picosecond Laser-Induced Melting and Resolidification Morphology on Si," *Appl. Phys. Lett.*, vol. 34, no. 12, pp. 864–866, 1979.

[243] Y. Nissim, J. Sapriel, and J. Oudar, "Microprobe Raman Analysis of Picosecond Laser Annealed Implanted Silicon," *Appl. Phys. Lett.*, vol. 42, no. 6, pp. 504–506, 1983.

[244] Y. Kanemitsu, I. Nakada, and H. Kuroda, "Picosecond Laser-Induced Anomalous Crystallization in Amorphous-Silicon," *Appl. Phys. Lett.*, vol. 47, no. 9, pp. 939–941, 1985.

[245] Y. Lai, K. Zhou, K. Sugden, and I. Bennion, "Point-By-Point Inscription of Sub-Micrometer Period Fiber Bragg Gratings," in *Lasers and Electro-Optics, 2008 and 2008 Conference on Quantum Electronics and Laser Science*, 2008.

[246] A. Theodosiou *et al.*, "Modified fs-Laser Inscribed FBG Array for Rapid Mode Shape Capture of Free-Free Vibrating Beams," *IEEE Photonics Technol. Lett.*, vol. 28, no. 14, pp. 1509–1512, 2016.

[247] A. Lacraz, M. Polis, A. Theodosiou, C. Koutsides, and K. Kalli, "Femtosecond Laser Inscribed Bragg Gratings in Low Loss CYTOP Polymer Optical Fiber," *IEEE Photonics Technol. Lett.*, vol. 27, no. 7, pp. 693–696, 2015.

[248] M. Green and M. Keevers, "Optical-Properties of Intrinsic Silicon at 300 K," *Prog. Photovoltaics*, vol. 3, no. 3, pp. 189–192, 1995.

[249] J. Komma, C. Schwarz, G. Hofmann, D. Heinert, and R. Nawrodt, "Thermo-optic coefficient of silicon at 1550 nm and cryogenic temperatures," *Appl. Phys. Lett.*, vol. 101, no. 4, pp. 4–8, 2012.

[250] A. Fasano *et al.*, "Fabrication and characterization of polycarbonate microstructured polymer optical fibers for high-temperature-resistant fiber Bragg grating strain sensors," *Opt. Mater. Express*, vol. 6, no. 2, pp. 649–659, 2016.

[251] W. Yuan *et al.*, "Humidity insensitive TOPAS polymer fiber Bragg grating sensor.," *Opt. Express*, vol. 19, no. 20, pp. 19731–9, 2011.

[252] G. Woyessa, A. Fasano, C. Markos, A. Stefani, H. K. Rasmussen, and O. Bang, "Zeonex microstructured polymer optical fiber: fabrication friendly fibers for high temperature and humidity insensitive Bragg grating sensing," *Opt. Mater. Express*, vol. 7, no. 1, p. 286, 2017.

[253] A. R. Prado *et al.*, "Polymethyl methacrylate (PMMA) recycling for the production of optical fiber sensor systems," *Opt. Express*, vol. 25, no. 24, p. 30051, 2017.

[254] A. Theodosiou *et al.*, "Measurements with an FBG inscribed on a new type of polymer fibre," in *26th International Conference on Plastic Optical Fibres*, 2017, pp. 1–4.

[255] O. Palchik and V. Palchik, "Thermoset and Thermoplastic fibers preparation thereof by UV curing," US 2014/0294917 A1, 2011.

[256] A. Badawi, "Characterization of the optical and mechanical properties of CdSe QDs/PMMA nanocomposite films," *J. Mater. Sci. Mater. Electron.*, vol. 26, no.

6, pp. 3450–3457, 2015.

[257] A. G. L. Junior, A. Frizera, and M. J. Pontes, “Analytical model for a polymer optical fiber under dynamic bending,” *Opt. Laser Technol.*, vol. 93, pp. 92–98, 2017.

[258] S. Ropers, M. Kardos, and T. A. Osswald, “A thermo-viscoelastic approach for the characterization and modeling of the bending behavior of thermoplastic composites,” *Compos. Part A Appl. Sci. Manuf.*, vol. 90, pp. 22–32, 2016.

[259] C. a. F. Marques, G.-D. Peng, and D. J. Webb, “Highly sensitive liquid level monitoring system utilizing polymer fiber Bragg gratings,” *Opt. Express*, vol. 23, no. 5, p. 6058, 2015.

[260] A. Stefani, S. Andresen, W. Yuan, N. Herholdt-Rasmussen, and O. Bang, “High sensitivity polymer optical fiber-bragg-grating-based accelerometer,” *IEEE Photonics Technol. Lett.*, vol. 24, no. 9, pp. 763–765, 2012.

[261] A. G. Leal-Junior, A. Frizera, and M. J. Pontes, “Dynamic Compensation Technique for POF Curvature Sensors,” *J. Light. Technol.*, vol. 36, no. 4, pp. 1112–1117, Feb. 2018.

[262] G. Woyessa, A. Fasano, C. Markos, H. K. Rasmussen, and O. Bang, “Low Loss Polycarbonate Polymer Optical Fiber for High Temperature FBG Humidity Sensing,” *IEEE Photonics Technol. Lett.*, vol. 29, no. 7, pp. 575–578, Apr. 2017.

[263] A. Theodosiou, M. Komodromos, and K. Kalli, “Carbon cantilever beam health inspection using a polymer fibre Bragg grating array,” *J. Light. Technol.*, vol. 36, no. 4, pp. 986–982, 2017.

[264] O. Ziemann, J. Krauser, P. E. Zamzow, and W. Daum, *POF Handbook: Optical Short Range Transmission Systems*. 2008.

[265] W. Zhang and D. J. Webb, “Humidity responsivity of poly (methyl methacrylate) - based optical fiber Bragg grating sensors,” vol. 39, no. 10, pp. 3026–3029, 2014.